

GNSS Localization and Attitude Determination via Optimization Techniques on Riemannian Manifolds

Dissertation by

Xing Liu

In Partial Fulfillment of the Requirements

For the Degree of

Doctor of Philosophy


King Abdullah University of Science and Technology

Thuwal, Kingdom of Saudi Arabia

©May, 2023

Xing Liu

All rights reserved

 <https://orcid.org/0000-0002-0506-6821>

ABSTRACT

GNSS Localization and Attitude Determination via Optimization Techniques on Riemannian Manifolds

Xing Liu

Global Navigation Satellite Systems (GNSS)-based localization and attitude determination are essential for many navigation and control systems widely used in aircrafts, spacecrafts, vessels, automobiles, and other dynamic platforms. A GNSS receiver can generate pseudo-range and carrier-phase observations based on the signals transmitted from the navigation satellites. Since the accuracy of the carrier phase is two orders of magnitude higher than that of the pseudo-range, it is crucial to employ the precise GNSS data, the carrier phase, to perform a high-accuracy position or/and attitude estimate. The main challenge to fully utilizing carrier-phase observations is to successfully resolve the unknown integer parts (number of whole cycles), a process usually referred to as integer ambiguity resolution. Many methods have been developed to resolve integer ambiguities with different performance offerings. Under challenging environments with insufficient tracked satellites, significant multipath interference, and severe atmospheric effects, the existing methods might not be up to par regarding reliability and efficiency.

First, we study the GNSS attitude determination problem in this thesis. A GNSS attitude model with nonlinear constraints about antenna-array geometry is used to incorporate a priori information rigorously. Given the characteristics of the employed nonlinear constraints, we formulate GNSS attitude determination as an optimization problem on a manifold. We propose three different attitude determination methods: the array-aided attitude determination based on an oriented

sphere manifold, the Riemannian-manifold-based orthonormality-constrained attitude determination (RieMOCAD), and the constrained wrapped least squares (C-WLS) method.

We also propose a joint solution for real-time kinematic positioning and attitude determination. Although without common parameters in the localization and attitude determination problems, the GNSS data of the two issues are correlated. We consider this correlation and treat GNSS localization and attitude determination as a joint problem instead of two independent issues, allowing us to leverage the prior information rigorously. Again, Riemannian optimization is applied to improve the performance of RTK positioning and attitude determination regarding the accuracy and ambiguity resolution.

ACKNOWLEDGEMENTS

First of all, I would like to give my sincere thanks to my supervisor, Dr. Tareq Y. Al-Naffouri, for offering me the opportunity to study as a Ph.D. student at KAUST and join his outstanding research group. It has been a great privilege to study under his supervision. I appreciate his guidance, support, and constructive advice on my thesis research.

I am also extremely grateful to Dr. Tarig Ballal, whose assistance and support are crucial in the course of preparing for this work. Thanks for being there to help and devoting much time to my research work.

I also would like to express my appreciation to all the people who have helped me with this thesis. Special thanks to Hui Chen and Mohanad Ahmed, who have greatly assisted me in my study.

Finally, my heartfelt gratitude goes to my family and friends for their love and continuous support.

Contents

| | |
|---|-----------|
| Abstract | 2 |
| Acknowledgements | 4 |
| Examination Committee Page | 8 |
| List of Figures | 9 |
| List of Tables | 11 |
| 1 Introduction | 13 |
| 1.1 Global Navigation Satellite System | 13 |
| 1.2 GNSS Positioning and Attitude Determination | 14 |
| 1.3 Related Works | 16 |
| 1.4 Challenge and Motivation | 19 |
| 1.5 Contributions | 20 |
| 1.6 Thesis Outline | 22 |
| 2 GNSS Observation Model and Existing Methods | 23 |
| 2.1 Observation Model | 23 |
| 2.2 Real-time Kinematic Positioning | 26 |
| 2.3 GNSS Attitude Determination Methods | 27 |
| 2.3.1 The Unconstrained Attitude Determination | 27 |
| 2.3.2 The Affine-constrained Attitude Determination | 29 |
| 2.3.3 The Orthonormality-Constrained Attitude Determination | 31 |
| 3 Overview of Riemannian Optimization | 33 |
| 3.1 Manifold Optimization: Definitions and Notation | 33 |
| 3.2 Euclidean and Riemannian Derivatives Operators | 34 |
| 3.3 First and Second Order Riemannian Algorithms | 35 |
| 4 Array-Aided Attitude Determination Based on Oriented Sphere Manifold | 38 |
| 4.1 System Model and Problem Formulation | 39 |
| 4.1.1 System Model | 39 |
| 4.1.2 Problem Formulation | 42 |

| | | |
|----------|---|------------|
| 4.2 | Optimization Over the Set of Unit Norm Oriented Vectors | 45 |
| 4.2.1 | Manifold Geometry and Tangent Bundle | 46 |
| 4.2.2 | Riemannian Gradient and Hessian Computation | 49 |
| 4.2.3 | Retraction of Tangent Vectors | 55 |
| 4.3 | 3-D GNSS Attitude Determination Using Riemannian Optimization | 60 |
| 4.3.1 | Proposed 3-D GNSS Attitude Determination Algorithm . . | 60 |
| 4.3.2 | Complexity Analysis and Rate of Convergence | 62 |
| 4.4 | Simulation Setup And Results | 62 |
| 4.4.1 | Simulation Setup | 63 |
| 4.4.2 | Numerical Results | 65 |
| 4.5 | Chapter Summary | 69 |
| 5 | Riemannian-manifold-based Ambiguity Resolution and Attitude Determination | 71 |
| 5.1 | The Intermediate Float Solution And Riemannian Algorithm Design | 73 |
| 5.1.1 | The Float Solution | 74 |
| 5.1.2 | Optimization Algorithm Design on Riemannian Manifolds | 75 |
| 5.2 | Ambiguity Resolution Aided by the Float Solution | 78 |
| 5.2.1 | Decomposition of the Objective Function | 78 |
| 5.2.2 | Integer Search Strategy | 81 |
| 5.3 | Performance Evaluation | 84 |
| 5.3.1 | Simulation Analysis | 84 |
| 5.3.2 | Experimental Evaluation | 94 |
| 5.4 | Chapter Summary | 97 |
| 6 | Constrained Wrapped Least-Squares Attitude Determination | 98 |
| 6.1 | Constrained Wrapped Least-Squares Method | 99 |
| 6.2 | Implementation of the Proposed C-WLS Method | 112 |
| 6.2.1 | Single-baseline Attitude Determination | 112 |
| 6.2.2 | Multi-baseline Attitude Determination | 118 |
| 6.3 | Performance Evaluation | 121 |
| 6.3.1 | Simulation Results | 121 |
| 6.3.2 | Experimental Results | 126 |
| 6.4 | Chapter Summary | 130 |
| 7 | Integrated Solution for Real-time Kinematic Positioning and Attitude Determination | 131 |
| 7.1 | System Model | 132 |
| 7.2 | Classical Unscented Kalman Filter | 136 |
| 7.3 | Unscented Kalman Filter on Riemannian Manifolds | 138 |

| | | |
|----------|--|------------|
| 7.3.1 | The Structure of RieMUKF | 138 |
| 7.3.2 | Required Riemannian Manifold-related Terminology | 141 |
| 7.4 | Performance Evaluation | 144 |
| 7.4.1 | Simulation | 144 |
| 7.4.2 | Experiment | 148 |
| 8 | Conclusion | 152 |
| 8.1 | Summary | 152 |
| 8.2 | Future Research Work | 154 |
| | References | 156 |
| | Appendices | 168 |

EXAMINATION COMMITTEE PAGE

Committee Chairperson: Prof. Tareq Y. Al-Naffouri

Committee Members: Prof. Peter Teunissen, Prof. Mohamed-Slim Alouini, Prof. Diogo Gomes, Prof. Shinkyu Park

LIST OF FIGURES

| | | |
|-----|--|-----|
| 1.1 | The Navigation Gap [1]. | 19 |
| 2.1 | RTK System Structure and Observation Model. | 26 |
| 4.1 | Receiver antenna configuration for ambiguity resolution. | 40 |
| 4.2 | Receiver antenna configuration for 3-D attitude determination. | 43 |
| 4.3 | Fraction of estimates with error less than ϵ . (a) and (b) indicate the results for GPS constellation on January 28, 2018. (c) and (d) represent the results for GPS constellation on April 29, 2018. | 66 |
| 4.4 | RMSE vs. Noise levels (29-Apr-2018) | 67 |
| 4.5 | RMSE vs. Number of Satellites (29-Apr-2018) | 67 |
| 4.6 | RMSE vs. Angle Between Two Baselines (29-Apr-2018) | 67 |
| 5.1 | Geometric illustration of the decomposition of the objective function. | 80 |
| 5.2 | RMSE of float ambiguity estimations (a single baseline to three baselines). | 89 |
| 5.3 | RMSE of float ambiguity estimations (four baselines to six baselines). | 90 |
| 5.4 | GNSS antenna set-up. | 95 |
| 5.5 | Satellite visibility during the tests. | 96 |
| 5.6 | Euler angle error distribution for the first experiment. | 96 |
| 5.7 | Euler angle error distribution for the second experiment. | 96 |
| 6.1 | Illustration of the wrapped least squares concept using complex values on the unit circle. | 103 |
| 6.2 | The relationship between \mathbf{r}_a and $\tilde{\mathbf{h}}_s$ | 113 |
| 6.3 | Distribution of potential candidate points for \mathbf{r}_a | 114 |
| 6.4 | Illustration of the intersection points. | 115 |
| 6.5 | Success rate with and without the angle constraint for dual-baseline set-up. | 123 |
| 6.6 | The number of tracked satellites and PDOP values. | 126 |
| 6.7 | Attitude angle error distribution for data 1. | 128 |
| 6.8 | Attitude angle error distribution for data 2. | 129 |
| 7.1 | Graphical illustration of the operators \boxplus and \boxminus | 139 |
| 7.2 | Position errors vs. epoch. | 146 |

| | | |
|-----|---|-----|
| 7.3 | Positioning RMSE of the float and fixed solutions. | 146 |
| 7.4 | Euler angle RMSE of the float and fixed solutions. | 147 |
| 7.5 | Experimental set-up. | 148 |
| 7.6 | The number of tracked satellites and the corresponding position dilution of precision. | 149 |
| 7.7 | Euler angle RMSE based on experimental data. | 150 |

LIST OF TABLES

| | | |
|------|---|----|
| 1.1 | GNSS comparison | 13 |
| 4.1 | Success rates over many GPS weeks for $d_{12} = d_{14} = 45$ cm, $\Delta = \Delta' = 8$ cm, $\sigma_\phi = 3$ mm, $\Theta = 90^\circ$ and $m = 4$ | 65 |
| 4.2 | RMSE ($^\circ$) over different GPS weeks for $d_{12} = d_{14} = 45$ cm, $\Delta = \Delta' = 8$ cm, $\sigma_\phi = 3$ mm, $\Theta = 90^\circ$ and $m = 4$ | 65 |
| 4.3 | Mean Running Time of the Different Algorithms. | 68 |
| 5.1 | RMSE of Different Estimators of \mathbf{R} Versus Observation Noise ($\#Sat = 6$, $\#BL = 3$ and $L = 1$ m). | 86 |
| 5.2 | Probability of Convergence to a Solution in The Constraints Set for Different Methods With Various Observation Noise ($\#Sat = 6$, $\#BL = 3$ and $L = 1$ m). | 86 |
| 5.3 | Number of Operations for Different Methods. | 86 |
| 5.4 | Computational Complexity Parameters for Different Methods Based on Simulations. | 86 |
| 5.5 | Total Number of Operations for Different Methods Based on Simulations. | 86 |
| 5.6 | Success rate (%) for different measurement precision σ_Ψ (mm), number of tracked satellites ($\#Sat$), and number of baselines. UC-AM/AC-AM RieMOCAD-LF | 91 |
| 5.7 | Success rate (%) for different measurement precision σ_Ψ (mm), number of tracked satellites ($\#Sat$), and number of baselines. UC-AM AC-AM RieMOCAD-LF | 91 |
| 5.8 | Success rate (%) for different measurement precision σ_Ψ (mm), number of tracked satellites ($\#Sat$), and number of baselines. MC-LAMBDA RieMOCAD-TF | 92 |
| 5.9 | Number of integers in the search space for different measurement precision σ_Ψ (mm), number of tracked satellites ($\#Sat$), and number of baselines. MC-LAMBDA RieMOCAD-TF | 93 |
| 5.10 | Success rate (%) based on experimental data. | 95 |
| 5.11 | Number of integers in the search space. | 96 |

| | | |
|-----|---|-----|
| 6.1 | Success rate (%) versus phase noise σ_ψ (mm), number of satellites (#Sat), and number of baselines. C-LAMBDA/MC-LAMBDA AFM Proposed | 122 |
| 6.2 | Average number of integers in the search space of the C-LAMBDA or MC-LAMBDA method versus phase noise σ_ψ (mm), number of satellites (#Sat), and number of baselines. | 122 |
| 6.3 | Computational Complexity of Different Algorithms. | 124 |
| 6.4 | Success rate (%) and RMSE (deg.) based on the experimental data. | 127 |
| 7.1 | Fix ratio (%) of ambiguity resolution and positioning RMSE (cm) of the fixed solutions based on experimental data. | 150 |

Chapter 1

Introduction

1.1 Global Navigation Satellite System

Global navigation satellite system (GNSS) encompasses a group of satellite navigation systems with global coverage, which allows the users to obtain their geospatial position using signals transmitted from satellites. Available GNSS constellations include Global Positioning System (GPS), GLONASS, BeiDou, Galileo, and so on. All of these constellations broadcast signals on multiple (dual or triple) frequencies. A comparison of these constellations is shown in TABLE 1.1.

GNSS consists of three segments, namely, space segment (satellites), control segment (ground stations), and user segment (rovers/receivers). The first GNSS constellation, GPS, developed by the United States government, became fully operational in 1995 [2]. After that, many researchers devoted their careers to enhancing the system's reliability, availability, and precision. The popular GNSS research areas involve atmospheric (ionospheric and tropospheric) delay modeling, multipath effect mitigating, satellite receiver and clocks synchronization, ambiguity resolution, etc.

Although millions of devices in the market have localization capabilities, GNSS remains one of the dominating techniques for absolute position estimation

Table 1.1: GNSS comparison

| | GPS | GLONASS | Galileo | BeiDou |
|-------------|--|---|---|---|
| Altitude | 20,180 km | 19,130 km | 23,222 km | 21,150 km |
| Period | 11 h 58 min | 11 h 16 min | 14 h 5 min | 12 h 38 min |
| Satellites | 31 | 24 | 30 (24 active + 6 spares) | 30 |
| Frequencies | 1575.42 MHz (L1) 1227.60 MHz (L2) 1176.45 MHz (L5) | 1602.00 MHz (L1) 1246.00 MHz (L2) 1202.025 MHz (L3) | 1575.42 MHz (E1) 1176.45/1207.14 MHz (E5a/b) 1278.75 MHz (E6) | 1561.098 MHz (B1) 1207.14 MHz (B2) 1268.52 MHz (B3) |

and is expected to play a critical role in various navigation and control systems. GNSS has been widely used for offering precise position and attitude information required by many types of applications like autonomous driving [3, 4, 5, 6], precision agriculture [7, 8], port automation [9], unmanned vehicles [10, 11, 12, 13, 14], etc. With the advent of next-generation GNSS [15, 16, 17, 18, 19], more potential applications are expected to emerge.

1.2 GNSS Positioning and Attitude Determination

Precise GNSS positioning techniques are widely used to achieve sub-meter localization accuracy [20, 21]. Real-time kinematic (RTK) is a popular precise GNSS positioning technique that estimates the receiver position with up to centimeter-level accuracy using pseudo-range and carrier-phase observations as well as real-time corrections from the reference station [22, 23]. The carrier-phase measurements have millimeter precision, but the ambiguities are unknown. The high precision of RTK positioning is dominated by the carrier-phase observations, which serve as ultraprecise pseudo-ranges after reliable ambiguity resolution. With the development of GNSS constellations and receivers, it is possible to resolve carrier-phase ambiguities with high probability, i.e., success rate [24, 25]. However, it is still a hot topic to improve the reliability of ambiguity resolution in some challenging scenarios, such as an urban canyon where only a small number of satellites are visible [26, 27, 28].

Nowadays, it is a common setup that a vehicle is equipped with more than one GNSS antenna, which enables GNSS-based attitude determination as an essential alternative to traditional techniques based on inertial navigation systems [29, 30, 31]. The goal of GNSS attitude determination is to estimate a vehicle's orientation with respect to a reference coordinate [32, 33], utilizing multiple GNSS antennas/receivers rigidly mounted on the body frame. Compared with the other sensors applied in attitude determination, such as gyroscopes or star-trackers, a GNSS receiver offers several advantages, including the driftless characteristic, low

power consumption, and minor maintenance requirements [34, 35]. Nowadays, GNSS localization and attitude determination have been ubiquitously explored in numerous land, airborne, and maritime scenarios [36, 37, 38, 39, 40, 33, 41, 42, 43, 44, 45, 46]. Furthermore, recent developments and interest in autonomous systems have resulted in even more attention drawn to this research area [47, 48, 49, 50].

The observations of GNSS receivers include pseudo-range and carrier phase. Depending on the assumptions on the system, GNSS observations can be pre-processed in numerous ways. In particular, GNSS measurements are processed as phase single, double, or even triple differences [51]. The single difference is defined as the difference between the simultaneous observations (from the same satellite) at two different antennas. The purpose of single difference is to eliminate the satellite clock bias. However, such approach would not solve the problem of receiver clock bias which still needs to be estimated. With common receiver clock technology, single-difference models can be used to simplify the complexity and reduce the influence of uncorrelated noise [52, 53]. The double difference refers to the instantaneous difference between the single-difference observations of two different satellites. By applying double-difference, the clock errors, instrumental delays, atmospheric parameters, and other unknown error sources are significantly mitigated or even removed [2]. As a result, many existing GNSS localization and attitude determination methods use the phase double-difference model to carry out baseline settlement. Finally, the triple difference is defined as the difference between the double-difference observations from two successive epochs [51]. Assuming that the integer ambiguity remains unchanged during the time interval between epochs, the use of triple-difference allows the total removal of the carrier phase integer ambiguity.

Although both kinds of measurements can be utilized for localization and attitude estimation, the high precision of GNSS solutions mainly derives from the accurate carrier phase measurements. Indeed, the noise level of the carrier phase

measurements is a couple of orders of magnitude lower than that of pseudo-range measurements[54]. On the downside, the primary challenge in GNSS localization and attitude determination stems from the fact that the phase observables are ambiguous by an unknown integer number of cycles ambiguity that needs to be resolved. Standard GNSS localization provided by mass-market devices uses only pseudo-range data, and its accuracy is 3-5 meters. Precise GNSS positioning techniques take advantage of both pseudo-range and carrier phase observations to achieve decimeter or even centimeter localization accuracy. The vehicle's attitude is determined by the relative position between the multiple GNSS antennas mounted on it. Since the distance between these antennas is usually small, a high-quality attitude (orientation) estimation can only be expected with a precise relative position given by high-precision observations, i.e., carrier phase. Hence, carrier phase ambiguity resolution, i.e., the process of resolving these unknown integer values, is a crucial step for GNSS positioning and attitude determination.

1.3 Related Works

A number of carrier phase ambiguity resolution methods have been proposed over the years, most of which belong to one of the following two classes: motion-based methods [55, 56, 57, 58] and search-based methods [59, 60, 61, 41, 62, 63, 64, 65]. Motion-based methods incorporate information about the dynamics of the vehicle into the estimation process and resolve the carrier phase ambiguities by exploiting the change in the receiver-satellite geometry with time [66, 56, 67]. These methods take advantage of multiple epochs of observations collected over a given period of time assuming that the integer ambiguities remain unchanged during this period. As a consequence of their design, these methods are not well-suited for real-time applications [68].

On the other hand, search-based methods, as their name suggests, search for the optimal solution in different domains. Indeed, the search-based methods are more diverse than the motion-based ones thanks to the use of various cost func-

tions and different information provided by the system. For example, there are search-based methods based on carrier phase only or carrier phase combined with pseudo-range, single frequency versus multi-frequency methods, with or without aid knowledge. As a result of their diversity, these methods differ widely in their efficiency depending on the adopted objective function and the search strategies [60, 69, 70, 62]. For instance, in [69], a constraint equation is used, and the search is carried out in the antenna positions domain. In contrast, the authors in [70] solve the ambiguity using an artificial neural network. For a limited number of GNSS observables, a search algorithm based on Gram-Schmidt orthonormalization (GSO) is developed in [62]. With only four GNSS observables, the algorithm constraints the search space to two dimensions so as to significantly improve the estimation efficiency.

While motion-based methods are not designed for real-time applications, their search-based counterparts are independent of the platform's motion, making them good candidates for instantaneous attitude determination. Among the search-based methods, the least-squares ambiguity decorrelation adjustment (LAMBDA) method [71, 72] and its modified versions [73, 63] received considerable attention in the literature. The main advantage of these methods is that the ambiguity resolution search is performed directly in the integer domain. The LAMBDA method solves an integer least squares problem through an ambiguity transformation that allows for an efficient search for the optimal estimates over a hyper-ellipsoidal region [71, 72].

The LAMBDA method has become the standard approach for GNSS ambiguity resolution with unconstrained or linearly constrained models [74, 54, 75]. For unconstrained or linearly constrained models, LAMBDA solutions are optimal in terms of the ambiguity resolution success rate, i.e., it offers the highest probability of resolving the ambiguities correctly [76].

The LAMBDA method is not designed for attitude determination and fails to take advantage of a priori knowledge of antenna geometry, which introduces

nonlinear (orthonormality) constraints to the optimization problem. The constrained LAMBDA (C-LAMBDA) [68] and multivariate constrained LAMBDA (MC-LAMBDA) methods [77] were proposed to leverage the priori knowledge about the antenna relative positions for single- and multi-baseline attitude models, respectively. The literature shows that these two techniques can significantly improve the success-rate performance compared to the LAMBDA method [68, 75]. Resolving the unknown carrier-phase ambiguities correctly allows for accurate attitude determination, whereas the orthonormality constraints facilitate high ambiguity resolution success rates and reliable attitude estimation [74]. Incorporating the nonlinear constraints into the optimization problem results in a more complex search space that is not ellipsoidal anymore, increasing the complexity of the search process significantly [78, 75]. The performance of the C-LAMBDA or MC-LAMBDA approaches relies upon the quality of the (initial) float solutions, that is, the least-squares estimations with the integer constraint of ambiguities ignored.

Based on a specific relaxation of the nonlinear constraints pertaining to the known antenna-array geometry, the affine-constrained attitude model (AC-AM) has been proposed as a compromise between the unconstrained LAMBDA and MC-LAMBDA methods [74, 54]. The AC-AM relaxes the orthonormality constraints to linear ones through an affine transformation. Therefore, if the number of baselines is greater than the dimension of their span, the AC-AM provides a better float solution compared to the unconstrained model such that it outperforms the standard LAMBDA in the terms of the ambiguity resolution success rate [74]. On the other hand, the AC-AM is less robust than the orthonormality-constrained attitude model (OC-AM) used in the MC-LAMBDA method; thus, high computational efficiency but lower success rates followed.

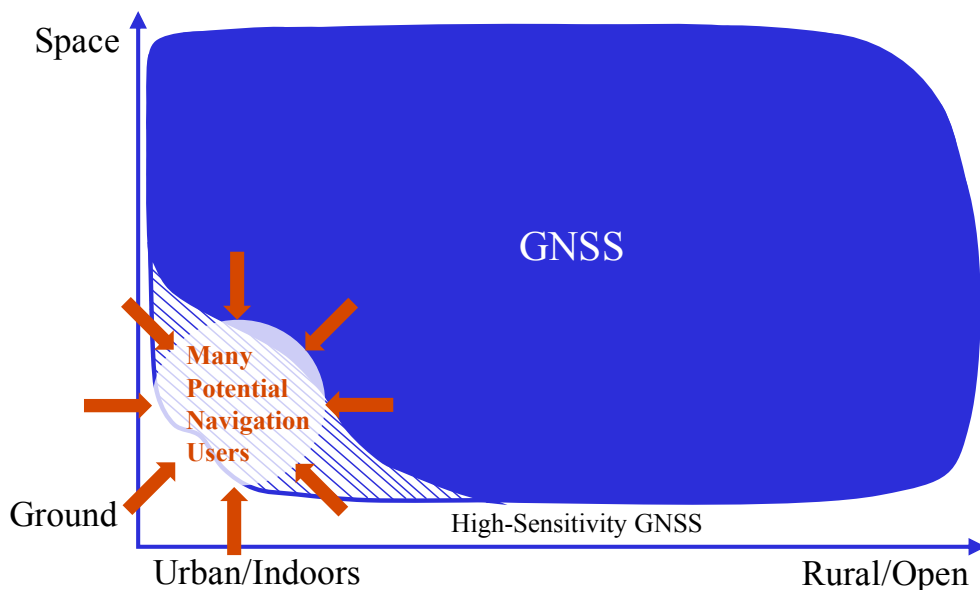


Figure 1.1: The Navigation Gap [1].

1.4 Challenge and Motivation

Carrier-phase-based GNSS techniques can provide seamless positioning solutions under good satellite visibility conditions, but their performance is limited in degraded environments. In urban areas, the performance is insufficient for the autonomous vehicle application as a consequence of blocked signals, multipath and non-line-of-sight (NLOS) signal reception [79]. A GNSS receiver can collect both the original and reflected signals, or worse, receiving only the reflected signals. Signal reflection introduces an extra propagation distance, leading to a huge positioning error. For a vehicle in deep urban areas, the localization errors can be as high as 50 meters or even higher because of multipath and NLOS effects. In these environments, GNSS alone cannot satisfy the rigorous requirements on continuity, accuracy, and reliability of positioning. The navigation gap distribution is shown in Fig. 1.1.

In addition to these general challenges on GNSS positioning, there are specific problems for RTK. One drawback of RTK is that the validity of the correction message provided by the reference station decreases rapidly when the user-to-reference separation is over 20 km. Multiple local reference stations and communications link are needed all around an urban area. Vehicles in regions equipped

with the required infrastructures would receive local corrections through cellular links to achieve high accuracy location information. However, accuracy degrades near edges of the local reference station network. When multiple reference stations are used, the individual local reference station may produce significantly different corrections, resulting in severe ionospheric and tropospheric decorrelation [80]. Depending on the distance between the rovers/receivers and reference station, the quality of the correction streams coming from the reference stations, the number of tracked satellites, and the environment surrounding the vehicle, it may take a few minutes to 30 minutes to achieve the reliable ambiguities. Fast convergence is still a big challenge for precise GNSS localization.

For GNSS attitude determination, the existing methods can provide excellent solutions in ideal environments, with the ambiguities resolved instantaneously with high success rate. However, these methods are faced with some challenges under satellite-deprived environments such as urban canyons. For example, the computational efficiency of the C-LAMBDA and MC-LAMBDA methods might be inadequate in challenging environments with significant multipath effects or an adverse view of satellites, such as in urban canyon scenarios [81]. Given a large number of baselines, the AC-AM can generally provide high success rate, allowing it to be a fast alternative to the MC-LAMBDA method [54]. However, with a limited number of baselines, there is still much room for success rate improvement.

1.5 Contributions

We propose several novel methods to solve the remaining challenging issues for GNSS applications. These contributions are summarized in the following:

1. We propose a novel 3-D GNSS attitude determination method based on Riemannian optimization techniques. The proposed method first exploits the antenna geometry and baseline lengths to reformulate the 3-D GNSS attitude determination problem as an optimization over a non-convex set. A particular

receiver configuration leads to a simple solution for the ambiguity resolution. Since the solution set is a manifold, in this manuscript we formulate the problem as an optimization over a Riemannian manifold. The study of the geometry of the manifold allows the design of efficient first and second order Riemannian algorithms to solve the 3-D GNSS attitude determination problem. Despite the non-convexity of the problem, the proposed algorithms are guaranteed to globally converge to a critical point of the optimization problem.

2. We present an ambiguity resolution method for Global Navigation Satellite System (GNSS)-based attitude determination. A GNSS attitude model with nonlinear constraints is used to rigorously incorporate a priori information. Given the characteristics of the employed nonlinear constraints, we formulate GNSS attitude determination as an optimization problem on a manifold. Then, Riemannian manifold optimization algorithms are utilized to aid ambiguity resolution based on a proposed decomposition of the objective function. The application of manifold geometry enables high-quality float solutions that are critical to reinforcing search-based integer ambiguity resolution in terms of efficiency, availability, and reliability. The proposed approach is characterized by a low computational complexity and a high probability of resolving the ambiguities correctly.

3. We develop a constrained wrapped least-squares (C-WLS) method for high-accuracy attitude determination. This approach is built on an optimization model that leverages prior information related to the antenna array and the integer nature of the carrier-phase ambiguities in an innovative way. The proposed approach adopts an efficient search strategy to estimate the vehicle's attitude parameters using ambiguous carrier-phase observations directly, without requiring prior carrier-phase ambiguity fixing.

4. We propose a joint solution for GNSS localization and attitude determination. Although without common parameters in the localization and attitude determination problems, the GNSS data of the two issues are correlated. We consider this correlation and treat GNSS localization and attitude determination

as a joint problem instead of two independent issues, allowing us to leverage the prior information rigorously. Again, Riemannian optimization is applied to aid the process of ambiguity resolution, which improves the accuracy and accelerates the convergence of the positioning and attitude solution.

1.6 Thesis Outline

The following chapter describes the GNSS observation models and the related work in the literature. In Chapter 3, an overview of Riemannian optimization methods over matrix manifolds is presented. Chapter 4 introduces the proposed oriented spheres manifold and applies it to precise attitude determination with carrier-phase ambiguities resolved based on a designed antenna geometry. In chapter 5, Riemannian manifold optimization algorithms are utilized to aid ambiguity resolution for attitude determination based on a proposed decomposition of the objective function, which works on an arbitrary antenna array. In chapter 6, a constrained wrapped least squares method is presented to determine a vehicle's attitude through a search procedure in the solution space (manifolds). Chapter 7 addressed a joint solution for GNSS localization and attitude determination, which uses an unscented Kalman filter on the Riemannian manifold to improve the accuracy and accelerate the convergence of the positioning and attitude solution. In the last chapter, some potential future research directions are proposed.

Chapter 2

GNSS Observation Model and Existing Methods

2.1 Observation Model

For the GNSS antenna a that tracks $\mathcal{S} + 1$ satellites, the original observations from the s -th satellite's signal ($s = 0, 1, 2, \dots, \mathcal{S}$) can be modelled as

$$\begin{aligned}\psi_a^s &= P_a^s + n_a^s - i_a^s + \tau_a^s + \frac{c}{\lambda}(\delta t_a - \delta t^s) + \eta_a^s, \\ \rho_a^s &= P_a^s + i_a^s + \tau_a^s + \frac{c}{\lambda}(\delta t_a - \delta t^s) + \varepsilon_a^s,\end{aligned}\tag{2.1}$$

with

$$P_a^s = \frac{1}{\lambda} \|\mathbf{x}^s - \mathbf{x}_a\|_2.\tag{2.2}$$

Without loss of generality, we assume that the observations and all distances are measured in units of wavelength. The variables in (2.1)–(2.2) are defined as follows: ψ_a^s and ρ_a^s are the carrier-phase and pseudo-range observables (respectively), P_a^s denotes the distance between the s -th satellite and the a -th antenna, n_a^s is the carrier-phase ambiguity, i_a^s is the ionospheric delay, τ_a^s is the tropospheric delay, λ represents the wavelength for the given frequency, c is the speed of light, δt_a denotes the receiver clock bias, δt^s is the satellite clock bias, \mathbf{x}^s is the satellite location, \mathbf{x}_a is the antenna position, η_a^s and ε_a^s account for unmodelled errors and noise, and $\eta_a^s \ll \varepsilon_a^s$.

For a configuration with multiple antennas, let us denote the baseline direction vector between antenna a and antenna b represented in the reference coordinate by $\mathbf{x}_{ab} \in \mathbb{R}^3$. To eliminate the satellite clock biases, we calculate the difference of observations at antenna a and antenna b , with the latter being the reference

antenna. This operation is usually denoted as *single difference* (SD), and it results in the the observation model

$$\begin{aligned}\psi_{ab}^s &= \psi_a^s - \psi_b^s = P_{ab}^s + n_{ab}^s - i_{ab}^s + \tau_{ab}^s + \frac{c}{\lambda}\delta t_{ab} + \eta_{ab}^s, \\ \rho_{ab}^s &= \rho_a^s - \rho_b^s = P_{ab}^s + i_{ab}^s + \tau_{ab}^s + \frac{c}{\lambda}\delta t_{ab} + \varepsilon_{ab}^s.\end{aligned}\quad (2.3)$$

Since the baseline length is far smaller than the distance from the satellite to the antennas, P_{ab}^s can be represented as [82]

$$P_{ab}^s = P_a^s - P_b^s = \frac{1}{\lambda} (\mathbf{h}^s)^T \mathbf{x}_{ab}, \quad (2.4)$$

where $\mathbf{h}^s \in \mathbb{R}^3$ is the unit line-of-sight vector between the receiver and satellite s , and T denotes the matrix transpose.

Another difference operation is carried out on the SD observations over pairs of satellites to cancel out the receiver clock bias. By designating satellite 0 as a reference, the difference process results in the so-called *double-difference* (DD) model, which is given by

$$\begin{aligned}\psi_{ab}^{s0} &= \psi_{ab}^s - \psi_{ab}^0 = \frac{1}{\lambda} (\mathbf{h}^s - \mathbf{h}^0)^T \mathbf{x}_{ab} + n_{ab}^{s0} - i_{ab}^{s0} + \tau_{ab}^{s0} + \eta_{ab}^{s0}, \\ \rho_{ab}^{s0} &= \rho_{ab}^s - \rho_{ab}^0 = \frac{1}{\lambda} (\mathbf{h}^s - \mathbf{h}^0)^T \mathbf{x}_{ab} + i_{ab}^{s0} + \tau_{ab}^{s0} + \varepsilon_{ab}^{s0}.\end{aligned}\quad (2.5)$$

The DD operation eliminates both the receiver and satellites clock errors. If the distance between the antennas is small, the atmospheric delays are highly correlated such that i_{ab}^{s0} and τ_{ab}^{s0} can be ignored. As the baseline length rise, one needs to consider the effects of the ionospheric and the tropospheric delays, that is, i_{ab}^{s0} and τ_{ab}^{s0} should be treated as unknowns together with the other parameters.

For the baseline \mathbf{x}_{ab} , we can arrange the double-difference observations from various satellites in the vectors

$$\boldsymbol{\psi}_{ab} = \begin{bmatrix} \psi_{ab}^{10} & \cdots & \psi_{ab}^{S0} \end{bmatrix}^T, \quad \boldsymbol{\rho}_{ab} = \begin{bmatrix} \rho_{ab}^{10} & \cdots & \rho_{ab}^{S0} \end{bmatrix}^T. \quad (2.6)$$

By arranging the other parameters in (2.5) in a vector or a matrix to match (2.6), the standard double-difference model is given by the following linear observation equations:

$$\begin{aligned}\boldsymbol{\psi}_{ab} &= \mathbf{H}\mathbf{x}_{ab} + \mathbf{n}_{ab} - \mathbf{i}_{ab} + \boldsymbol{\tau}_{ab} + \boldsymbol{\eta}_{ab}, \\ \boldsymbol{\rho}_{ab} &= \mathbf{H}\mathbf{x}_{ab} + \mathbf{i}_{ab} + \boldsymbol{\tau}_{ab} + \boldsymbol{\epsilon}_{ab},\end{aligned}\tag{2.7}$$

with the design (non-singular) matrix

$$\mathbf{H} = \frac{1}{\lambda} \begin{bmatrix} (\mathbf{h}^1 - \mathbf{h}^0)^\top \\ \vdots \\ (\mathbf{h}^S - \mathbf{h}^0)^\top \end{bmatrix} = \begin{bmatrix} \tilde{\mathbf{h}}_1 \\ \vdots \\ \tilde{\mathbf{h}}_S \end{bmatrix},\tag{2.8}$$

where $\mathbf{n}_{ab} \in \mathbb{Z}^S$ is the unknown integer ambiguity vector, $\mathbf{i}_{ab} \in \mathbb{R}^S$ consists of the DD ionospheric delays, $\boldsymbol{\tau}_{ab} \in \mathbb{R}^S$ denotes the DD tropospheric delay vector, and $\boldsymbol{\eta}_{ab}, \boldsymbol{\epsilon}_{ab} \in \mathbb{R}^S$ are the unmodeled error and noise vectors.

Let $\mathbf{y}_{ab} = [\boldsymbol{\psi}_{ab}^\top, \boldsymbol{\rho}_{ab}^\top]^\top$, the compact form of (2.7) is given by

$$\mathbf{y}_{ab} = \mathbf{A}\mathbf{x}_{ab} + \mathbf{B}\mathbf{n}_{ab} + \mathbf{c} \otimes \mathbf{i}_{ab} + \mathbf{1}_2 \otimes \boldsymbol{\tau}_{ab} + \mathbf{e}_{ab}\tag{2.9}$$

with

$$\mathbf{A} = \begin{bmatrix} \mathbf{H} \\ \mathbf{H} \end{bmatrix}, \mathbf{B} = \begin{bmatrix} \mathbf{I}_S \\ \mathbf{O} \end{bmatrix}, \mathbf{c} = \begin{bmatrix} -1 \\ 1 \end{bmatrix}, \mathbf{e}_{ab} = \begin{bmatrix} \boldsymbol{\eta}_{ab} \\ \boldsymbol{\epsilon}_{ab} \end{bmatrix},$$

where \mathbf{I}_S is an identity matrix of size S , and $\mathbf{1}_2$ is a 2-dimensional all-one vector.

Assume that the pseudo-range and carrier-phase are uncorrelated. The covariance matrices of $\boldsymbol{\psi}_{ab}$ and $\boldsymbol{\rho}_{ab}$ are given by

$$\mathbf{Q}_{\boldsymbol{\psi}_{ab}\boldsymbol{\psi}_{ab}} = \text{cov}(\boldsymbol{\psi}_{ab}) = \text{E}[(\boldsymbol{\psi}_{ab} - \text{E}(\boldsymbol{\psi}_{ab}))(\boldsymbol{\psi}_{ab} - \text{E}(\boldsymbol{\psi}_{ab}))^\top],$$

$$\mathbf{Q}_{\boldsymbol{\rho}_{ab}\boldsymbol{\rho}_{ab}} = \text{cov}(\boldsymbol{\rho}_{ab}) = \text{E}[(\boldsymbol{\rho}_{ab} - \text{E}(\boldsymbol{\rho}_{ab}))(\boldsymbol{\rho}_{ab} - \text{E}(\boldsymbol{\rho}_{ab}))^\top],$$

where $\text{E}(\cdot)$ denotes the expectation operator, and $\text{cov}(\cdot)$ produces the covariance

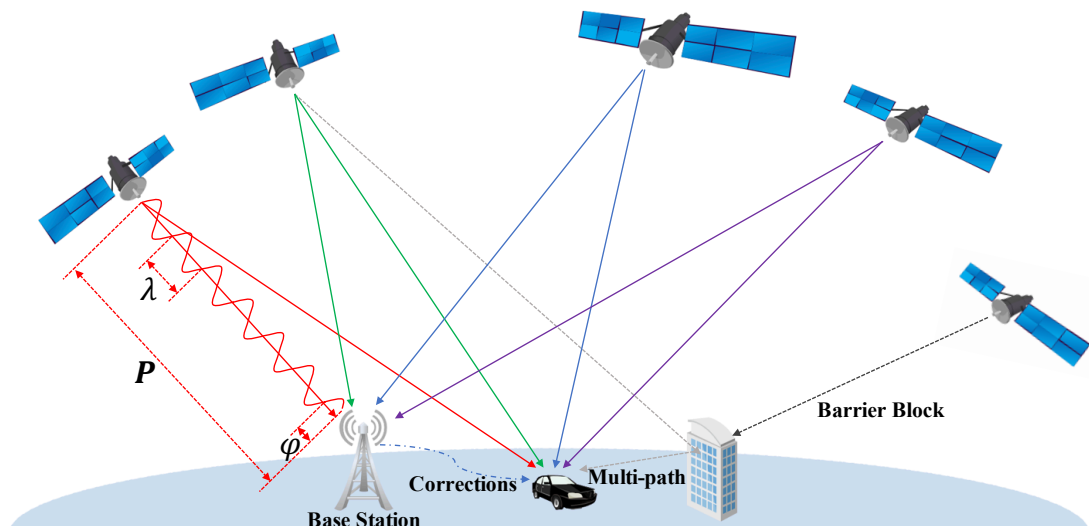


Figure 2.1: RTK System Structure and Observation Model.

matrix. Then, the covariance matrix of \mathbf{y}_{ab} is expressed as

$$\mathbf{Q}_{\mathbf{y}_{ab}\mathbf{y}_{ab}} = \text{cov}(\mathbf{y}_{ab}) = \begin{bmatrix} \mathbf{Q}_{\psi_{ab}\psi_{ab}} & \mathbf{O} \\ \mathbf{O} & \mathbf{Q}_{\rho_{ab}\rho_{ab}} \end{bmatrix}.$$

2.2 Real-time Kinematic Positioning

In RTK positioning, the fixed reference station transmits its pseudo-range and carrier phase data to the vehicle via a suitable communication link [83]. The simultaneous measurements of both the reference station and the vehicle are then linearly combined using the DD operation to remove symmetrical errors and processed in real-time manner [33].

Considering only a single vehicle and a single reference station as shown in Fig. 2.1, the RTK problem can be expressed using the DD model as

$$\mathbf{y}_{vr} = \mathbf{A}\mathbf{x}_{vr} + \mathbf{B}\mathbf{n}_{vr} + \mathbf{c} \otimes \mathbf{i}_{vr} + \mathbf{1}_2 \otimes \boldsymbol{\tau}_{vr} + \mathbf{e}_{vr}, \quad (2.10)$$

where the subscripts v and r represent the vehicle and the reference station, respectively.

The validity of the above model hinges on the distance between the vehicle

and reference station, i.e., the baseline length. Generally, for short baselines, the atmospheric delay terms are considerably reduced and can be basically ignored. So the unknowns are only relative position and integer ambiguities. For short baselines, the model is highly accurate; Whereas for long baselines, the atmospheric delay terms can be considerably different resulting in residual errors which be modeled and estimated as parameters [84].

The carrier-phase ambiguities are constant values over time, as long as there are no cycle slips. A cycle slip will lead to a jump of ambiguity, which can be detected based on the standard hypothesis testing theory [85]. If a cycle slip occurs, one needs to adjust the corresponding ambiguity so that the time constancy is no longer violated.

One usually needs a long observation time to estimate position and ambiguities accurately. The multi-epoch observations can be processed using a Kalman type filter, ignoring the integer constraint of ambiguities. Once the float solutions are precise enough, the integer ambiguities can be resolved correctly using ambiguity resolution methods, where the LAMBDA method is the standard approach. Then, the vehicle's relative position with respect to the reference station, \mathbf{x}_{vr} , can be accurately. Note that the position of the reference station should be precisely known; that is, the RTK technique can offer the accurate absolute position of the vehicle.

2.3 GNSS Attitude Determination Methods

In this section, we describe the various GNSS attitude models and the related work in the literature.

2.3.1 The Unconstrained Attitude Determination

Consider a vehicle equipped with $\mathcal{A} + 1$ GNSS antennas (named as 0-th, 1-st, \dots , and \mathcal{A} -th antennas) that track $\mathcal{S} + 1$ satellites simultaneously. The double-difference (DD) operation is applied to cancel out the common-mode errors. The

antenna 0 is selected as the reference one. The GNSS attitude observation equations are given by

$$\mathbf{Y} = \mathbf{A}\mathbf{X} + \mathbf{B}\mathbf{N} + \mathbf{E}, \quad (2.11)$$

where

$$\begin{aligned} \mathbf{Y} &= \begin{bmatrix} \mathbf{y}_{10} & \cdots & \mathbf{y}_{A0} \end{bmatrix}, \\ \mathbf{X} &= \begin{bmatrix} \mathbf{x}_{10} & \cdots & \mathbf{x}_{A0} \end{bmatrix}, \\ \mathbf{N} &= \begin{bmatrix} \mathbf{n}_{10} & \cdots & \mathbf{n}_{A0} \end{bmatrix}, \\ \mathbf{E} &= \begin{bmatrix} \mathbf{e}_{10} & \cdots & \mathbf{e}_{A0} \end{bmatrix}. \end{aligned}$$

In the attitude determination problem, the baseline length is usually quite short (meter-level or shorter) [86]. This makes the atmospheric delays for two antennas highly correlated and can almost be eliminated by the difference operation.

The model (2.11) is called the unconstrained attitude model (UC-AM) since it disregards the prior knowledge of the baseline matrix. Note that “unconstrained” is only in terms of the antenna-array geometry; the integer constraints are given full consideration. To estimate the unknown baseline coordinates and integer ambiguities, the problem can be formulated as

$$\min_{\mathbf{X} \in \mathbb{R}^{3 \times A}, \mathbf{N} \in \mathbb{Z}^{S \times A}} \|\text{vec}(\mathbf{Y} - \mathbf{A}\mathbf{X} - \mathbf{B}\mathbf{N})\|_{\mathbf{Q}_{\mathbf{Y}\mathbf{Y}}^{-1}}^2, \quad (2.12)$$

where the notation $\text{vec}(\cdot)$ represents the vectorization operation, $\|(\cdot)\|_{\mathbf{Q}_{\mathbf{Y}\mathbf{Y}}^{-1}}^2 = (\cdot)^T \mathbf{Q}_{\mathbf{Y}\mathbf{Y}}^{-1} (\cdot)$, and $\mathbf{Q}_{\mathbf{Y}\mathbf{Y}}$ is the covariance matrix of $\text{vec}(\mathbf{Y})$, that is

$$\mathbf{Q}_{\mathbf{Y}\mathbf{Y}} = \mathbb{E} \left[\text{vec}(\mathbf{Y} - \mathbb{E}(\mathbf{Y})) [\text{vec}(\mathbf{Y} - \mathbb{E}(\mathbf{Y}))]^T \right].$$

To determine the solution of (2.12), the following orthogonal decomposition

can be applied to simplify the problem [54]:

$$\begin{aligned} & \min_{\mathbf{X} \in \mathbb{R}^{3 \times A}, \mathbf{N} \in \mathbb{Z}^{S \times A}} \|\text{vec}(\mathbf{Y} - \mathbf{A}\mathbf{X} - \mathbf{B}\mathbf{N})\|_{\mathbf{Q}_{\mathbf{Y}\mathbf{Y}}^{-1}}^2 \\ & = \|\text{vec}(\mathbf{E}_{\text{UC}})\|_{\mathbf{Q}_{\mathbf{Y}\mathbf{Y}}^{-1}}^2 + \min_{\mathbf{N} \in \mathbb{Z}^{S \times A}} \left(\left\| \text{vec}(\mathbf{N} - \hat{\mathbf{N}}_{\text{UC}}) \right\|_{\mathbf{Q}_{\hat{\mathbf{N}}_{\text{UC}}\hat{\mathbf{N}}_{\text{UC}}}^{-1}}^2 + \min_{\mathbf{X} \in \mathbb{R}^{3 \times A}} \left\| \text{vec}(\mathbf{X} - \hat{\mathbf{X}}_{\text{UC}}(\mathbf{N})) \right\|_{\mathbf{Q}_{\hat{\mathbf{X}}_{\text{UC}}(\mathbf{N})\hat{\mathbf{X}}_{\text{UC}}(\mathbf{N})}^{-1}}^2 \right). \end{aligned} \quad (2.13)$$

In (2.13), $\mathbf{E}_{\text{UC}} = \mathbf{Y} - \mathbf{A}\hat{\mathbf{X}}_{\text{UC}} - \mathbf{B}\hat{\mathbf{N}}_{\text{UC}}$ is the residual matrix of the least-squares solution, i.e., the float solution without the integer constraints given by

$$\hat{\mathbf{X}}_{\text{UC}}, \hat{\mathbf{N}}_{\text{UC}} = \arg \min_{\mathbf{X} \in \mathbb{R}^{3 \times A}, \mathbf{N} \in \mathbb{R}^{S \times A}} \|\text{vec}(\mathbf{Y} - \mathbf{A}\mathbf{X} - \mathbf{B}\mathbf{N})\|_{\mathbf{Q}_{\mathbf{Y}\mathbf{Y}}^{-1}}^2, \quad (2.14)$$

whose covariance matrixes are $\mathbf{Q}_{\hat{\mathbf{N}}_{\text{UC}}\hat{\mathbf{N}}_{\text{UC}}}$, $\mathbf{Q}_{\hat{\mathbf{X}}_{\text{UC}}\hat{\mathbf{X}}_{\text{UC}}}$, $\mathbf{Q}_{\hat{\mathbf{N}}_{\text{UC}}\hat{\mathbf{X}}_{\text{UC}}}$, and $\mathbf{Q}_{\hat{\mathbf{X}}_{\text{UC}}\hat{\mathbf{N}}_{\text{UC}}}$. The other variables in (2.13) are expressed as

$$\begin{aligned} \text{vec}(\hat{\mathbf{X}}_{\text{UC}}(\mathbf{N})) &= \text{vec}(\hat{\mathbf{X}}_{\text{UC}}) - \mathbf{Q}_{\hat{\mathbf{X}}_{\text{UC}}\hat{\mathbf{N}}_{\text{UC}}} \mathbf{Q}_{\hat{\mathbf{N}}_{\text{UC}}\hat{\mathbf{N}}_{\text{UC}}}^{-1} \text{vec}(\hat{\mathbf{N}}_{\text{UC}} - \mathbf{N}), \\ \mathbf{Q}_{\hat{\mathbf{X}}_{\text{UC}}(\mathbf{N})\hat{\mathbf{X}}_{\text{UC}}(\mathbf{N})} &= \mathbf{Q}_{\hat{\mathbf{X}}_{\text{UC}}\hat{\mathbf{X}}_{\text{UC}}} - \mathbf{Q}_{\hat{\mathbf{X}}_{\text{UC}}\hat{\mathbf{N}}_{\text{UC}}} \mathbf{Q}_{\hat{\mathbf{N}}_{\text{UC}}\hat{\mathbf{N}}_{\text{UC}}}^{-1} \mathbf{Q}_{\hat{\mathbf{N}}_{\text{UC}}\hat{\mathbf{X}}_{\text{UC}}}. \end{aligned} \quad (2.15)$$

For further details, refer to [54].

The residual term is independent of the parameters. Since the UC-AM disregards the constraints on \mathbf{X} , we can let $\mathbf{X} = \hat{\mathbf{X}}_{\text{UC}}(\mathbf{N})$ so that the third term on the right-hand side of (2.13) is equal to zero, i.e., minimizing (2.13). Hence, the original optimization in (2.12) is equivalent to the following integer least-squares (ILS) problem

$$\min_{\mathbf{N} \in \mathbb{Z}^{S \times A}} \left\| \text{vec}(\mathbf{N} - \hat{\mathbf{N}}_{\text{UC}}) \right\|_{\mathbf{Q}_{\hat{\mathbf{N}}_{\text{UC}}\hat{\mathbf{N}}_{\text{UC}}}^{-1}}^2. \quad (2.16)$$

The LAMBDA method can solve (2.16) efficiently, with $\hat{\mathbf{N}}_{\text{UC}}$ being the center of the search space (an ellipsoidal set). Once the integer ambiguities are resolved, the recovered DD carrier phase can be utilized to estimate the baseline coordinates.

2.3.2 The Affine-constrained Attitude Determination

One can accurately measure the antenna-array geometry because the GNSS antennas are firmly mounted on the vehicle. Therefore, the antenna-array coor-

ordinates in the body frame can be considered as known parameters that can be incorporated in GNSS attitude determination. In [74, 54], to leverage the priori knowledge, the authors take advantage of an affine transformation, which converts the baseline coordinates from the body frame to the reference frame through

$$\mathbf{X} = \mathbf{R}\mathbf{X}_b, \quad \mathbf{R} \in \mathbb{R}^{3 \times q}, \quad (2.17)$$

where $\mathbf{X}_b \in \mathbb{R}^{q \times \mathcal{A}}$, and $q = \min(3, \mathcal{A})$. Then, (2.11) and (2.17) establish the affine-constrained attitude model (AC-AM).

Based on the affine transformation, the attitude determination problem can be expressed as

$$\min_{\mathbf{R} \in \mathbb{R}^{3 \times q}, \mathbf{N} \in \mathbb{Z}^{S \times \mathcal{A}}} \|\text{vec}(\mathbf{Y} - \mathbf{A}\mathbf{R}\mathbf{X}_b - \mathbf{B}\mathbf{N})\|_{\mathbf{Q}_{\mathbf{Y}\mathbf{Y}}^{-1}}^2. \quad (2.18)$$

Similar to (2.13), the following orthogonal decomposition is used

$$\begin{aligned} & \min_{\mathbf{R} \in \mathbb{R}^{3 \times q}, \mathbf{N} \in \mathbb{Z}^{S \times \mathcal{A}}} \|\text{vec}(\mathbf{Y} - \mathbf{A}\mathbf{R}\mathbf{X}_b - \mathbf{B}\mathbf{N})\|_{\mathbf{Q}_{\mathbf{Y}\mathbf{Y}}^{-1}}^2 = \|\text{vec}(\mathbf{E}_{\text{AC}})\|_{\mathbf{Q}_{\mathbf{Y}\mathbf{Y}}^{-1}}^2 \\ & + \min_{\mathbf{N} \in \mathbb{Z}^{S \times \mathcal{A}}} \left(\left\| \text{vec}(\mathbf{N} - \hat{\mathbf{N}}_{\text{AC}}) \right\|_{\mathbf{Q}_{\hat{\mathbf{N}}_{\text{AC}}\hat{\mathbf{N}}_{\text{AC}}}^{-1}}^2 + \min_{\mathbf{R} \in \mathbb{R}^{3 \times q}} \left\| \text{vec}(\mathbf{R} - \hat{\mathbf{R}}_{\text{AC}}(\mathbf{N})) \right\|_{\mathbf{Q}_{\hat{\mathbf{R}}_{\text{AC}}(\mathbf{N})\hat{\mathbf{R}}_{\text{AC}}(\mathbf{N})}^{-1}}^2 \right), \end{aligned} \quad (2.19)$$

where $\mathbf{E}_{\text{AC}} = \mathbf{Y} - \mathbf{A}\hat{\mathbf{R}}_{\text{AC}}\mathbf{X}_b - \mathbf{B}\hat{\mathbf{N}}_{\text{AC}}$ is the least-squares residual matrix of the float solution given by

$$\hat{\mathbf{R}}_{\text{AC}}, \hat{\mathbf{N}}_{\text{AC}} = \arg \min_{\mathbf{R} \in \mathbb{R}^{3 \times q}, \mathbf{N} \in \mathbb{R}^{S \times \mathcal{A}}} \|\text{vec}(\mathbf{Y} - \mathbf{A}\mathbf{R}\mathbf{X}_b - \mathbf{B}\mathbf{N})\|_{\mathbf{Q}_{\mathbf{Y}\mathbf{Y}}^{-1}}^2, \quad (2.20)$$

with the covariance matrix $\mathbf{Q}_{\hat{\mathbf{N}}_{\text{AC}}\hat{\mathbf{N}}_{\text{AC}}}$, $\mathbf{Q}_{\hat{\mathbf{R}}_{\text{AC}}\hat{\mathbf{R}}_{\text{AC}}}$, $\mathbf{Q}_{\hat{\mathbf{N}}_{\text{AC}}\hat{\mathbf{R}}_{\text{AC}}}$, and $\mathbf{Q}_{\hat{\mathbf{R}}_{\text{AC}}\hat{\mathbf{N}}_{\text{AC}}}$. The other variables in (2.19) are given by

$$\begin{aligned} \text{vec}(\hat{\mathbf{R}}_{\text{AC}}(\mathbf{N})) &= \text{vec}(\hat{\mathbf{R}}_{\text{AC}}) - \mathbf{Q}_{\hat{\mathbf{R}}_{\text{AC}}\hat{\mathbf{N}}_{\text{AC}}} \mathbf{Q}_{\hat{\mathbf{N}}_{\text{AC}}\hat{\mathbf{N}}_{\text{AC}}}^{-1} \text{vec}(\hat{\mathbf{N}}_{\text{AC}} - \mathbf{N}), \\ \mathbf{Q}_{\hat{\mathbf{R}}_{\text{AC}}(\mathbf{N})\hat{\mathbf{R}}_{\text{AC}}(\mathbf{N})} &= \mathbf{Q}_{\hat{\mathbf{R}}_{\text{AC}}\hat{\mathbf{R}}_{\text{AC}}} - \mathbf{Q}_{\hat{\mathbf{R}}_{\text{AC}}\hat{\mathbf{N}}_{\text{AC}}} \mathbf{Q}_{\hat{\mathbf{N}}_{\text{AC}}\hat{\mathbf{N}}_{\text{AC}}}^{-1} \mathbf{Q}_{\hat{\mathbf{N}}_{\text{AC}}\hat{\mathbf{R}}_{\text{AC}}}. \end{aligned} \quad (2.21)$$

Finally, the optimization problem in (2.18) is identical to the following minimiza-

tion [74]

$$\min_{\mathbf{N} \in \mathbb{Z}^{S \times A}} \left\| \text{vec}(\mathbf{N} - \hat{\mathbf{N}}_{AC}) \right\|_{\mathbf{Q}_{\hat{\mathbf{N}}_{AC} \hat{\mathbf{N}}_{AC}}^{-1}}^2. \quad (2.22)$$

Since $\mathbf{Q}_{\hat{\mathbf{N}}_{AC} \hat{\mathbf{N}}_{AC}} < \mathbf{Q}_{\hat{\mathbf{N}}_{UC} \hat{\mathbf{N}}_{UC}}$, the AC-AM can improve the float solution such that it can provide better ambiguity estimations compared with the UC-AM [54].

2.3.3 The Orthonormality-Constrained Attitude Determination

The AC-AM does not rigorously integrate the known geometry of the GNSS antenna configuration into the objective function. To fully leverage the nonlinear constraints of antenna-array geometry, an orthonormal matrix \mathbf{R} is used to link \mathbf{X} and \mathbf{X}_b through

$$\mathbf{X} = \mathbf{R}\mathbf{X}_b, \quad \mathbf{R} \in \mathbb{O}^{3 \times q}, \quad (2.23)$$

where $\mathbf{R}^T \mathbf{R} = \mathbf{I}_q$, and \mathbf{I}_q represents an identity matrix of size q . The matrix \mathbf{R} indicates the orientation of the platform's body frame relative to the reference coordinate. The combination of (2.11) and (2.23) yields the orthonormality-constrained attitude model (OC-AM).

The OC-AM involves two kinds of constraints, namely, the integer constraints for the ambiguities and the orthonormality constraints for matrix \mathbf{R} . The optimization for the OC-AM can be expressed as

$$\min_{\mathbf{R} \in \mathbb{O}^{3 \times q}, \mathbf{N} \in \mathbb{Z}^{S \times A}} \left\| \text{vec}(\mathbf{Y} - \mathbf{A}\mathbf{R}\mathbf{X}_b - \mathbf{B}\mathbf{N}) \right\|_{\mathbf{Q}_{\mathbf{Y}\mathbf{Y}}^{-1}}^2, \quad (2.24)$$

which can be decomposed into three terms [77, 75]

$$\begin{aligned} & \min_{\mathbf{R} \in \mathbb{O}^{3 \times q}, \mathbf{N} \in \mathbb{Z}^{S \times A}} \left\| \text{vec}(\mathbf{Y} - \mathbf{A}\mathbf{R}\mathbf{X}_b - \mathbf{B}\mathbf{N}) \right\|_{\mathbf{Q}_{\mathbf{Y}\mathbf{Y}}^{-1}}^2 = \left\| \text{vec}(\mathbf{E}_{AC}) \right\|_{\mathbf{Q}_{\mathbf{Y}\mathbf{Y}}^{-1}}^2 \\ & + \min_{\mathbf{N} \in \mathbb{Z}^{S \times A}} \left(\left\| \text{vec}(\mathbf{N} - \hat{\mathbf{N}}_{AC}) \right\|_{\mathbf{Q}_{\hat{\mathbf{N}}_{AC} \hat{\mathbf{N}}_{AC}}^{-1}}^2 + \min_{\mathbf{R} \in \mathbb{O}^{3 \times q}} \left\| \text{vec}(\mathbf{R} - \hat{\mathbf{R}}_{AC}(\mathbf{N})) \right\|_{\mathbf{Q}_{\hat{\mathbf{R}}_{AC}(\mathbf{N}) \hat{\mathbf{R}}_{AC}(\mathbf{N})}^{-1}}^2 \right). \end{aligned} \quad (2.25)$$

Both (2.19) and (2.25) use the same float solution. The only difference between (2.19) and (2.25) is the solution space for the matrix \mathbf{R} . Due to the orthonormality

constraint, one has to take the last term of (2.25) into account. For the OC-AM, the optimization in (2.24) is equivalent to [77]

$$\min_{\mathbf{N} \in \mathbb{Z}^{S \times A}} \left(\left\| \text{vec}(\mathbf{N} - \hat{\mathbf{N}}_{\text{AC}}) \right\|_{\mathbf{Q}_{\hat{\mathbf{N}}_{\text{AC}} \hat{\mathbf{N}}_{\text{AC}}}^{-1}}^2 + \min_{\mathbf{R} \in \mathbb{O}^{3 \times q}} \left\| \text{vec}(\mathbf{R} - \hat{\mathbf{R}}_{\text{AC}}(\mathbf{N})) \right\|_{\mathbf{Q}_{\hat{\mathbf{R}}_{\text{AC}}(\mathbf{N}) \hat{\mathbf{R}}_{\text{AC}}(\mathbf{N})}^{-1}}^2 \right). \quad (2.26)$$

The OC-AM is more robust than the UC-AM and AC-AM. Nowadays, the MC-LAMBDA method is the most notable approach to solve (2.26), which takes advantage of the search-and-shrink or search-and-expand algorithms to speed up the integer search procedures [78]. However, the search space of (2.26) is no longer an ellipsoidal set, which leads to more complexity than that of (2.16) and (2.22). It is challenging to solve the complicated non-convex optimization (2.26), especially to satisfy the requirements of real-time applications. Therefore, it is essential to develop a more efficient method to alleviate the high computational burden of ambiguity resolution encountered in many practical situations.

Chapter 3

Overview of Riemannian Optimization

This chapter presents an overview of Riemannian optimization methods over matrix manifolds. The first part of the section briefly introduces manifold terminology, definitions, and notations. Afterward, the optimization techniques are presented and the Riemannian derivatives introduced. Finally, section 3.3 presents the templates of first and second order algorithms on Riemannian manifolds.

3.1 Manifold Optimization: Definitions and Notation

Let \mathcal{M} be a manifold of dimension d , i.e., the set \mathcal{M} (or a smoothly overlapping partition of the set) is in bijection with an open space of \mathbb{R}^d . In the same spirit that functions can be locally approximated with their derivatives, at each point $\mathbf{x} \in \mathcal{M}$, the manifold \mathcal{M} can be approximated by a d -dimensional linear space referred to as the tangent space $\mathcal{T}_{\mathbf{x}}\mathcal{M}$ at the point \mathbf{x} . The next section presents a lemma for deriving the expression of such tangent space for the manifold of interest in this paper.

Given that the tangent space $\mathcal{T}_{\mathbf{x}}\mathcal{M}$ is a linear space, one can endow it with an inner product $\langle \cdot, \cdot \rangle_{\mathbf{x}}$, also known as the Riemannian metric. Furthermore, assuming that the manifold \mathcal{M} is a matrix manifold, i.e., embedded in the space of matrices, a canonical Riemannian metric is the canonical inner product of the matrix space. Such a choice is motivated by the fact that it would greatly simplify the expression of the Riemannian gradient and Hessian as illustrated in the next section.

Consider a smooth function $F : \mathcal{E} \rightarrow \mathbb{R}$ from the Euclidean space \mathcal{E} to \mathbb{R} . The directional derivative of $F(\mathbf{X})$ in the direction $\xi \in \mathcal{E}$, denoted by $D(F(\mathbf{X}))[\xi]$,

is defined as

$$D(F(\mathbf{X}))[\xi] = \lim_{t \rightarrow 0} \frac{F(\mathbf{X} + t\xi) - F(\mathbf{X})}{t}. \quad (3.1)$$

For a smooth function $f : \mathcal{M} \rightarrow \mathbb{R}$ over a Riemannian manifold \mathcal{M} , the directional derivative of f at the point \mathbf{x} in the direction $\xi_{\mathbf{x}}$ is defined in a similar fashion as in (3.1). However, only directions $\xi_{\mathbf{x}}$ in the tangent space $\mathcal{T}_{\mathbf{x}}\mathcal{M}$ are permitted. In fact, for a small t , the expression $f(\mathbf{x} + t\xi_{\mathbf{x}})$ is well-defined only for tangent vectors $\xi_{\mathbf{x}}$ as the tangent space $\mathcal{T}_{\mathbf{x}}\mathcal{M}$ linearly approximates the manifold at \mathbf{x} .

The operator $D(f(\mathbf{X})) : \mathcal{T}_{\mathbf{x}}\mathcal{M} \rightarrow \mathbb{R}$ which associates to each $\xi_{\mathbf{x}}$ the directional derivative $D(f(\mathbf{X}))[\xi_{\mathbf{x}}]$ is referred to as the indefinite directional derivative of f at \mathbf{X} .

3.2 Euclidean and Riemannian Derivatives Operators

Riemannian optimization extends unconstrained optimization methods to Riemannian manifolds by approximating the curvature of the manifold at each point by a linear space. As stated earlier, the dimension d of the tangent space corresponds to the dimension of the manifold which is embedded in a Euclidean space of higher dimension n . While the Euclidean gradient of a function is defined on the original high-dimensional space, the Riemannian gradient is a derivative operator that is defined only on the tangent space. In other words, the Riemannian gradient of f at the point $\mathbf{x} \in \mathcal{M}$ is the unique element of $\mathcal{T}_{\mathbf{x}}\mathcal{M}$ that is related to the directional derivative through the following equation

$$\langle \text{grad } f(\mathbf{x}), \xi_{\mathbf{x}} \rangle_{\mathbf{x}} = D(f(\mathbf{x}))[\xi_{\mathbf{x}}]. \quad (3.2)$$

Similar to the Euclidean Hessian, the Riemannian Hessian is defined as the directional derivative of the Riemannian gradient. However, as the directional

derivative may not be contained in the tangent space, one needs to project the directional derivative of the Riemannian gradient onto the tangent space in order to obtain the Riemannian Hessian, i.e.,

$$\text{hess } f(\mathbf{x})[\xi_{\mathbf{x}}] = \Pi_{\mathbf{x}}(\text{D}(\text{grad } f(\mathbf{x}))[\xi_{\mathbf{x}}]), \quad (3.3)$$

where $\Pi_{\mathbf{x}}$ is the orthogonal projection from the ambient space to the tangent space $\mathcal{T}_{\mathbf{x}}\mathcal{M}$.

3.3 First and Second Order Riemannian Algorithms

As stated earlier, Riemannian optimization considers the constrained optimization problem as an unconstrained optimization over a constrained set. As such, the optimization algorithms on Riemannian manifolds follow similar steps as the unconstrained ones with few exceptions.

Given a point \mathbf{x} on a manifold, the first step is to approximate the manifold linearly around the point to obtain a Euclidean space. This is accomplished by deriving the expression of the tangent space $\mathcal{T}_{\mathbf{x}}\mathcal{M}$ and equipping it with the Riemannian metric. Thanks to the fact that the tangent space is a linear space of finite dimension, one can perform a step of unconstrained optimization using the Riemannian gradient and Hessian instead of their Euclidean counterpart. After completing the optimization step, the newly found point, although contained in the tangent space, is not a feasible solution as it does not belong to the manifold. Hence, the final step to obtain the updated point is to project the point from the tangent space to the manifold by using a retraction operator $R_{\mathbf{x}}$. The next section provides a lemma for computing an efficient retraction for our oriented sphere manifold.

According to the algorithm outlined above, the Riemannian version of the gradient descent algorithms requires three ingredients, viz., the tangent space, the Riemannian gradient, and the retraction operator. Similar to its Euclidean

Algorithm 3.1 Gradient Descent on Riemannian Manifold

- 1: Initialize $\mathbf{x} \in \mathcal{M}$.
- 2: **while** $\|\text{grad } f(\mathbf{x})\|_{\mathbf{x}} \neq 0$ **do**
- 3: Find the search direction $\xi_{\mathbf{x}} \in \mathcal{T}_{\mathbf{x}}\mathcal{M}$ by solving

$$\xi_{\mathbf{x}} = -\text{grad } f(\mathbf{x}). \quad (3.4)$$

- 4: Compute the step size α using backtracking.
 - 5: Retract $\mathbf{x} = R_{\mathbf{x}}(\alpha\xi_{\mathbf{x}})$.
 - 6: **end while**
-

Algorithm 3.2 Newton's method on Riemannian Manifold

- 1: **while** $\|\text{grad } f(\mathbf{x})\|_{\mathbf{x}} \neq 0$ **do**
- 2: Find the search direction $\xi_{\mathbf{x}} \in \mathcal{T}_{\mathbf{x}}\mathcal{M}$ such that:

$$\text{hess } f(\mathbf{x})[\xi_{\mathbf{x}}] = -\text{grad } f(\mathbf{x}), \quad (3.5)$$

- 3: Compute the step size α using backtracking.
 - 4: Retract $\mathbf{x} = R_{\mathbf{x}}(\alpha\xi_{\mathbf{x}})$.
 - 5: **end while**
-

counterpart, The Riemannian algorithm chooses the steepest descent direction by setting the search direction to $\xi_{\mathbf{x}} = -\text{grad } f(\mathbf{x})$. The steps of the Gradient Descent on Riemannian manifolds are available in Algorithm 3.1. As stated earlier, first-order algorithms are only guaranteed to converge to an extreme point. To check whether the extreme point is a local minimum, one can check if the Hessian is positive definite, i.e., $\langle \text{hess } f(\mathbf{x})[\xi_{\mathbf{x}}], \xi_{\mathbf{x}} \rangle_{\mathbf{x}} > 0$ for a set of directions $\xi_{\mathbf{x}}$ forming an orthogonal basis of the embedding space.

Newton's method on Riemannian manifolds follows a similar logic as the gradient descent algorithm with the exception that the search direction is performed while using information about the second order derivative. In other words, the search direction $\xi_{\mathbf{x}}$ is computed by solving the following equation:

$$\text{hess } f(\mathbf{x})[\xi_{\mathbf{x}}] = -\text{grad } f(\mathbf{x}).$$

After getting the search direction and computing the step size, the point is retracted to the manifold as previously. The steps of Newton's method on Riemannian

nian manifolds can be found in Algorithm 3.2.

Chapter 4

Array-Aided Attitude Determination Based on Oriented Sphere Manifold

In this chapter, we draw on the ambiguity resolution method proposed in [87, 88, 64] where a particular receiver configuration leads to a simple solution for the ambiguity problem. The search space is reduced to only three candidate integer values, guaranteeing that the search is highly efficient and performs well even with a minimal number of satellites. A single-difference model is adopted with all the antennas operating using a single common clock, which means that the receiver clock bias is automatically canceled [89]. In [87, 88], a triple-antenna configuration is considered, and a solution for the single baseline line pointing direction is developed. We consider a more complex configuration of five antennas to obtain the pointing direction vectors of non-parallel baselines for more accurate 3-D attitude determination, using only the carrier phase measurements.

The main contribution of this work is to provide a highly accurate 3-D GNSS attitude determination by rigorously solving the underlying optimization problem. As pointed out in [90], the inclusion of the information about the receiver geometry and baseline length as non-linear constraints in the optimization problem improves the quality of the attitude estimate. While previous works, e.g., [91, 68], use regularization to deal with the non-convexity indirectly, this paper proposes a more direct method by solving the non-convex optimization problem using a Riemannian optimization approach. The efficiency of the proposed scheme is tested through extensive simulation with a particular focus on the most challenging case of GNSS attitude determination, i.e., the single-epoch single-frequency case. In contrast with previous works that use Riemannian optimization over well-

investigated manifolds to solve the attitude determination problem, e.g., [92, 93], this chapter introduces a new manifold and thoroughly investigates its geometry. To the best of the authors' knowledge, the proposed manifold has not been introduced nor studied in the literature.

The rest of this chapter is organized as follows. Firstly, the ambiguity resolution method of [87, 88, 64] is exploited to formulate the 3-D GNSS attitude determination problem as a non-convex optimization problem. Then the manifold of interest is introduced and its geometry is derived. Furthermore, the Riemannian optimization tools, along with the geometry of the manifold, allow the design of efficient first and second-order 3-D attitude determination algorithms that are presented. Finally, we present and discuss numerical results comparing the proposed algorithm with non-convex generic solvers, the least squares, and LAMBDA methods.

4.1 System Model and Problem Formulation

4.1.1 System Model

Common receiver clock technology can be realized using the multi-antenna synchronized GNSS receiver. It means that these antennas share identical receiver clock bias and initial phase offset, which can be eliminated by single difference operation. The SD carrier phase between antenna a and b is

$$\bar{\psi}_{ab} = \bar{\mathbf{H}}\mathbf{x}_{ab} + \bar{\mathbf{n}}_{ab} + \bar{\boldsymbol{\eta}}_{ab}, \quad (4.1)$$

where

$$\bar{\mathbf{H}} = \frac{1}{\lambda} \begin{bmatrix} (\mathbf{h}^0)^T \\ \vdots \\ (\mathbf{h}^S)^T \end{bmatrix}, \quad (4.2)$$

$\bar{\mathbf{n}}_{ab}$ is the SD ambiguity vector, and $\bar{\boldsymbol{\eta}}_{ab}$ is the SD carrier-phase noise.

Let d_{ab} be the baseline length and \mathbf{x} be the unit direction vector of the an-

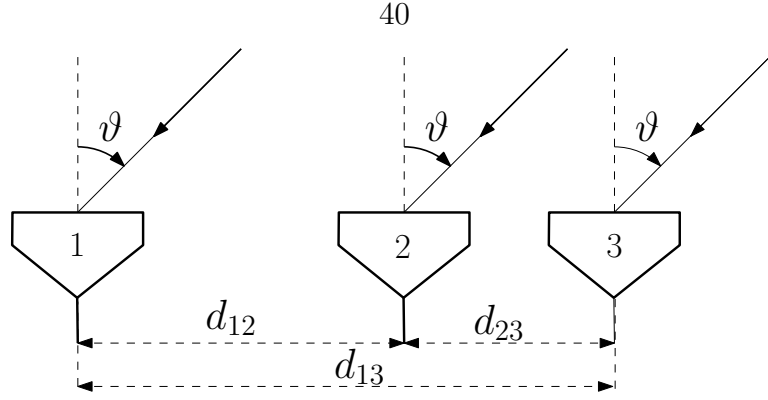


Figure 4.1: Receiver antenna configuration for ambiguity resolution.

tenna baseline, that is, $\mathbf{x}_{ab} = d_{ab}\mathbf{x}$. Attitude determination can be achieved by estimating two unit vectors (or pointing directions) using two non-collinear baselines. The integer ambiguity problem, i.e., the fact that the integer vector $\bar{\mathbf{n}}_{ab}$ is unknown, is the main source of difficulty in applying GNSS carrier phase difference based attitude determination. This section tailors the phase difference ambiguity resolution method for the specific antenna configuration in [64, 87, 88] to the antenna configuration of interest herein, depicted in Fig. 4.1. Once $\bar{\mathbf{n}}_{ab}$ is resolved correctly, the genuine carrier phase differences can be modelled as

$$\phi_{ab} = \bar{\psi}_{ab} - \bar{\mathbf{n}}_{ab}. \quad (4.3)$$

More details and a rigorous analysis of the integer ambiguity resolution method presented in this section can be found in [87] and [88].

Three collinearly positioned antennas are configured such that the lengths of the shortest two baselines are different, i.e., $d_{12} \neq d_{23}$. The difference between these two baselines, $\Delta = d_{23} - d_{12}$, satisfies the criterion suggested in [88] for ambiguity resolution. In other words, we have the following:

$$0 < |\Delta| \leq \frac{1}{2|\sin(\vartheta)|}, \quad (4.4)$$

wherein $\vartheta \in [-\frac{\pi}{2}, \frac{\pi}{2}]$ is the angle of arrival (AOA) of the signal from one satellite through the line-of-sight path, i.e., the angle between the line-of-sight and the plane perpendicular to the antenna baselines. For the sake of simplicity, a fixed

value is used in practice. It can readily be noted that when the AOA approaches $\pm\frac{\pi}{2}$, the above inequality simplifies to the following

$$0 < |\Delta| \leq \frac{1}{2}. \quad (4.5)$$

Given the above antenna configuration, there are only three candidate values for the unwrapped phase difference [87]. These candidate phase differences are related to the difference of two carrier phase observables as follows:

$$\phi_{12,s}(k) = \frac{d_{12}}{\Delta}(\bar{\psi}_{23,s} - \bar{\psi}_{12,s} + k), \quad k = -1, 0, 1, \quad (4.6)$$

where $\phi_{ab,s}$ and $\bar{\psi}_{ab,s}$ denote the s -th elements of $\boldsymbol{\phi}_{ab}$ and $\bar{\boldsymbol{\psi}}_{ab}$, respectively. It is demonstrated in [87] that the desired unwrapped phase difference is the unique one that satisfies $\phi_{12,s}(k) \in [-d_{12}, d_{12}]$. Furthermore, according to the results of [64] and given the unique candidate phase difference, the unique solution of the phase unwrapping problem is the candidate with minimum absolute value, i.e., $\hat{\phi}_{12,s} = \phi_{12,s}(\hat{k})$ for \hat{k} satisfying

$$\hat{k} = \arg \min_{k \in \{-1, 0, 1\}} |\phi_{12,s}(k)|. \quad (4.7)$$

Finally, due to the impact of noise, the recovered integer ambiguity and the unwrapped phase difference can be refined in practice using

$$\begin{aligned} \hat{n}_{12,s} &= \text{round} \left(\bar{\psi}_{12,s} - \hat{\phi}_{12,s} \right), \\ \hat{\phi}_{12,s} &= \bar{\psi}_{12,s} - \hat{n}_{12,s}, \end{aligned} \quad (4.8)$$

with $\text{round}(\cdot)$ being a special rounding function that works exactly like a standard rounding function except that for $N \in \mathbb{Z}$, $\text{round}(N + 0.5) = N$.

4.1.2 Problem Formulation

This subsection formulates the 3-D GNSS attitude determination problem. The first part describes the single baseline pointing vector estimation approach. This is done by adapting the least squares approach proposed in [64] for the configuration of interest in this paper. Afterward, a second non-collinear baseline pointing vector is considered to obtain precise 3-D GNSS attitude estimation.

Single Baseline Pointing Vector Estimation

This part concerns in determining the single baseline pointing vector which is a unit vector that indicates the pointing direction of the baseline in a reference coordinate system. Given the ambiguity resolution process and the system equations described previously, the single baseline pointing vector determination can be expressed as the following minimization problem

$$\min_{\mathbf{x} \in \mathbb{R}^3} \|\hat{\phi}_{12} - d_{12}\mathbf{H}\mathbf{x}\|_2^2, \quad (4.9)$$

which has the least squares (LS) solution

$$\hat{\mathbf{x}} = \frac{1}{d_{12}}(\mathbf{H}^T\mathbf{H})^{-1}\mathbf{H}^T\hat{\phi}_{12}. \quad (4.10)$$

It can be noted from (4.10) that under the same phase noise, the longer the baseline is, the more precise the pointing vector is. In other words, the accuracy of the pointing vector estimation is proportional to the length of the antenna baseline. Hence, the longest baseline, d_{13} herein, should be exploited to acquire a more precise pointing vector which can be realized using the upcoming operations

$$\begin{aligned} \hat{\mathbf{n}}_{13} &= \text{round}(\varphi_{13} - d_{13}\mathbf{H}\hat{\mathbf{x}}), \\ \hat{\phi}_{13} &= \varphi_{13} - \hat{\mathbf{n}}_{13}, \\ \hat{\mathbf{x}} &= \frac{1}{d_{13}}(\mathbf{H}^T\mathbf{H})^{-1}\mathbf{H}^T\hat{\phi}_{13}. \end{aligned} \quad (4.11)$$

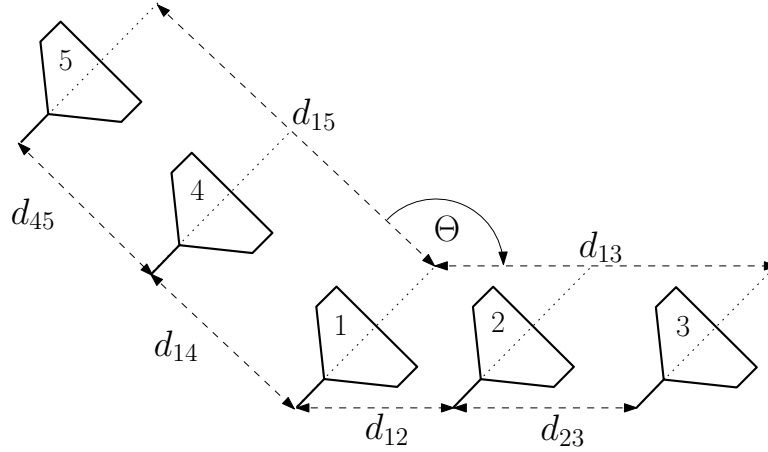


Figure 4.2: Receiver antenna configuration for 3-D attitude determination.

Two Baselines Attitude Determination

Single pointing vector estimation is the first step in 3-D attitude measurement. Indeed, in order to obtain 3-D attitude information, one needs at least another baseline which is not parallel to the first one. A natural extension of the configuration in Fig. 4.1 that can tackle the 3-D attitude determination and ambiguity resolution is shown in Fig. 4.2. One antenna is shared by the two baselines so as to reduce the number of required antennas. As a consequence, only 5 antennas are required instead of 6. The angle between the two baseline directions is denoted by Θ . Similar to the first baseline direction, the difference between the two shorter baselines of the antenna configuration of antenna 1, 4, and 5 satisfies the criterion

$$0 < |\Delta'| = |d_{45} - d_{14}| \leq \frac{1}{2}, \quad (4.12)$$

In a similar fashion as for (4.9)-(4.11), the carrier phase difference vectors $\hat{\phi}_{14}$ and $\hat{\phi}_{15}$, the integer ambiguity vector $\hat{\mathbf{n}}_{14}$ and $\hat{\mathbf{n}}_{15}$, and the corresponding pointing vector $\hat{\mathbf{y}}$ can be estimated. In other words, the two baseline pointing vectors are estimated independently by solving the minimization problem (4.9) for each of the two baselines separately. Once the two baseline vectors have been estimated, two non-parallel pointing vectors are known in the reference

coordinate and the 3-D attitude of platform can be calculated by transferring these two pointing vectors to an attitude matrix in a straightforward manner. However, the described method does not take the antenna geometry and baseline length into consideration which can greatly reduce the precision of the estimation. We suggest instead to use two baselines jointly to incorporate all the available information. After recovering the unambiguous phase differences, the 3-D GNSS attitude determination problem can be formulated as

$$\min_{\mathbf{x}, \mathbf{y} \in \mathbb{R}^3} \|\phi_{12} - d_{12}\mathbf{H}\mathbf{x}\|_2^2 + \|\phi_{14} - d_{14}\mathbf{H}\mathbf{y}\|_2^2 \quad (4.13a)$$

$$\text{s.t. } \|\mathbf{x}\|_2^2 = 1 \quad (4.13b)$$

$$\|\mathbf{y}\|_2^2 = 1 \quad (4.13c)$$

$$\langle \mathbf{x}, \mathbf{y} \rangle = \cos(\Theta). \quad (4.13d)$$

This is a non-convex optimization problem as indicated by the three quadratic equality constraints. More generally, let \mathbf{a} and \mathbf{b} be two m -dimensional vectors, let \mathbf{A} and \mathbf{B} be two $m \times n$ matrices and consider a scalar $-1 < c < 1$. This work focuses on solving the following optimization problem:

$$\min_{\mathbf{x}, \mathbf{y} \in \mathbb{R}^n} \|\mathbf{a} - \mathbf{A}\mathbf{x}\|_2^2 + \|\mathbf{b} - \mathbf{B}\mathbf{y}\|_2^2 \quad (4.14a)$$

$$\text{s.t. } \|\mathbf{x}\|_2^2 = 1 \quad (4.14b)$$

$$\|\mathbf{y}\|_2^2 = 1 \quad (4.14c)$$

$$\langle \mathbf{x}, \mathbf{y} \rangle = c, \quad (4.14d)$$

wherein constraint (4.14b) underlines the fact that \mathbf{x} is a unit norm vector and constraint (4.14c) corresponds to the fact that \mathbf{y} is also a unit norm vector. Finally, constraint (4.14d) insists that the cosine of the angle between \mathbf{x} and \mathbf{y} is c . Notice that the strict inequalities in $-1 < c < 1$ comes without loss of generality. Indeed, if we set $c = 1$, then $\mathbf{x} = \mathbf{y}$ which allows to reformulate the optimization problem in a convex, single-variable program. The same is valid for

$c = -1$ for which $\mathbf{x} = -\mathbf{y}$.

Despite the convexity of the objective function (4.14a), the optimization problem in (4.14) is not convex due to the coupling of variables in constraint (4.14d). However, the set \mathcal{M} of potential solutions given by

$$\mathcal{M} = \{(\mathbf{x}, \mathbf{y}) \in (\mathbb{R}^n)^2 \mid \mathbf{x}^T \mathbf{x} = \mathbf{y}^T \mathbf{y} = 1, \mathbf{x}^T \mathbf{y} = c\} \quad (4.15)$$

forms a compact, i.e., closed and bounded, manifold embedded in the Euclidean space $(\mathbb{R}^n)^2 = \mathbb{R}^n \times \mathbb{R}^n$. Therefore, one can take advantage of Riemannian optimization algorithms over manifolds to efficiently solve the above problem. Indeed, thanks to the compactness of the manifold \mathcal{M} and the convexity of the objective function (4.14a), first-order Riemannian methods are guaranteed to converge to a critical point of the optimization problem [94], i.e., a saddle point, local minimum or local maximum. However, it has been observed in the literature that first-order methods converge to a local minimum unless the initialization is specifically crafted, e.g., see [94]. Furthermore, second-order methods are always guaranteed to converge to a local minimum due to the instability of saddle points and local maxima for these methods. This paper solves the non-convex optimization problem (4.14) by designing both first and second order Riemannian algorithms over \mathcal{M} , called herein the oriented spheres manifold.

4.2 Optimization Over the Set of Unit Norm Oriented Vectors

This section describes the geometry of the oriented spheres manifold \mathcal{M} defined in (4.15) in order to design efficient Riemannian optimization algorithms. The first part of this section derives the expression of the tangent bundle and endows it with a Riemannian metric to turn \mathcal{M} into a Riemannian manifold. The rest of the section derive expressions of the Riemannian gradient and Hessian and designs a computationally efficient retraction. Section 4.3 uses the geometry of

the oriented spheres manifold \mathcal{M} to derive efficient algorithms for the 3-D GNSS attitude determination problem of interest.

4.2.1 Manifold Geometry and Tangent Bundle

Recall that the tangent space $\mathcal{T}_{(\mathbf{x}, \mathbf{y})}\mathcal{M}$ at the point $(\mathbf{x}, \mathbf{y}) \in \mathcal{M}$ is a linear space that approximates \mathcal{M} around (\mathbf{x}, \mathbf{y}) . The tangent space can be computed using the following lemma [94].

Lemma 4.1. *Let \mathcal{M} be an embedded manifold with a Euclidean ambient space \mathcal{E} . Assume that \mathcal{M} is the level-set of a constant-rank function $F : \mathcal{E} \rightarrow \mathcal{E}'$ with \mathcal{E}' being a linear space, then we have*

$$\text{Ker}(D(F(\mathbf{X}))) = \mathcal{T}_{\mathbf{x}}\mathcal{M}. \quad (4.16)$$

Using the result of this lemma, the following theorem derives the expression of the tangent bundle $\mathcal{T}\mathcal{M}$ of the oriented spheres manifold \mathcal{M} .

Theorem 4.1. *The tangent space $\mathcal{T}_{(\mathbf{x}, \mathbf{y})}\mathcal{M}$ at the point $(\mathbf{x}, \mathbf{y}) \in \mathcal{M}$ is given by the following $(2n - 3)$ -dimensional Euclidean space*

$$\mathcal{T}_{(\mathbf{x}, \mathbf{y})}\mathcal{M} = \left\{ (\xi_{\mathbf{x}}, \eta_{\mathbf{y}}) \in (\mathbb{R}^n)^2 \mid \mathbf{x}^T \xi_{\mathbf{x}} = \mathbf{y}^T \eta_{\mathbf{y}} = 0, \mathbf{x}^T \eta_{\mathbf{y}} + \mathbf{y}^T \xi_{\mathbf{x}} = 0 \right\}. \quad (4.17)$$

Proof. Let \mathcal{S}^n be the set of $n \times n$ symmetric matrices and consider the function $F : (\mathbb{R}^n)^2 \rightarrow \mathcal{S}^2$ given by

$$F(\mathbf{x}, \mathbf{y}) = \begin{pmatrix} \mathbf{x}^T \mathbf{x} & \mathbf{x}^T \mathbf{y} \\ \mathbf{y}^T \mathbf{x} & \mathbf{y}^T \mathbf{y} \end{pmatrix} \quad (4.18)$$

The set of symmetric matrices \mathcal{S}^n is a linear set as mandated by the conditions of Lemma 4.1. Furthermore, from the definition of the function F , it is clear that the oriented spheres manifold \mathcal{M} is the level set of $\mathbf{C} = \begin{pmatrix} 1 & c \\ c & 1 \end{pmatrix}$ by the continuous

and smooth function F . Indeed, the manifold can be expressed as $\mathcal{M} = F^{-1}(\mathbf{C})$. In order to show that the map F is a constant-rank function, it is sufficient to show that \mathbf{C} is a regular value of F , i.e., the rank of each $(\mathbf{x}, \mathbf{y}) \in F^{-1}(\mathbf{C}) = \mathcal{M}$ is equal to $\text{Dim}(\mathcal{S}^2) = \frac{2(2+1)}{2} = 3$. In other words, we need to show that the indefinite directional derivative of F is a surjective map.

The directional derivative of F at (\mathbf{x}, \mathbf{y}) in the direction $(\xi_{\mathbf{x}}, \eta_{\mathbf{y}}) \in (\mathbb{R}^n)^2$ is given by

$$D(F(\mathbf{x}, \mathbf{y}))[\xi_{\mathbf{x}}, \eta_{\mathbf{y}}] = \begin{pmatrix} 2\mathbf{x}^T \xi_{\mathbf{x}} & \mathbf{x}^T \eta_{\mathbf{y}} + \mathbf{y}^T \xi_{\mathbf{x}} \\ \mathbf{x}^T \eta_{\mathbf{y}} + \mathbf{y}^T \xi_{\mathbf{x}} & 2\mathbf{y}^T \eta_{\mathbf{y}} \end{pmatrix} \quad (4.19)$$

Let $\mathbf{S} = \begin{pmatrix} \mathbf{S}_{11} & \mathbf{S}_{12} \\ \mathbf{S}_{21} & \mathbf{S}_{22} \end{pmatrix} \in \mathcal{S}^n$ be an arbitrary 2×2 symmetric matrix, i.e., $\mathbf{S}_{21} = \mathbf{S}_{12}$. Finding $(\xi_{\mathbf{x}}, \eta_{\mathbf{y}})$ such that $D(F(\mathbf{x}, \mathbf{y}))[\xi_{\mathbf{x}}, \eta_{\mathbf{y}}] = \mathbf{S}$ can be reduced to solving the following linear system of equations

$$\mathbf{A} \begin{pmatrix} \xi_{\mathbf{x}} \\ \eta_{\mathbf{y}} \end{pmatrix} = \begin{pmatrix} 2\mathbf{x}^T & \mathbf{0} \\ \mathbf{0} & 2\mathbf{y}^T \\ \mathbf{y}^T & \mathbf{x}^T \end{pmatrix} \begin{pmatrix} \xi_{\mathbf{x}} \\ \eta_{\mathbf{y}} \end{pmatrix} = \begin{pmatrix} \mathbf{S}_{11} \\ \mathbf{S}_{22} \\ \mathbf{S}_{12} \end{pmatrix}. \quad (4.20)$$

With the obvious assumption that $n \geq 2$, the linear system has a fat matrix \mathbf{A} with dimension $3 \times 2n$. Furthermore, the matrix \mathbf{A} is full-row rank. Indeed, assume that some linear combination of the rows with the scalars α , β , and γ , respectively, gives a zero vector. In other words, we have the following system of equations:

$$2\alpha\mathbf{x}^T + \gamma\mathbf{y}^T = \mathbf{0}^T, \quad (4.21)$$

$$2\beta\mathbf{y}^T + \gamma\mathbf{x}^T = \mathbf{0}^T. \quad (4.22)$$

Multiplying each equation in the above system of equations by \mathbf{x} and \mathbf{y} , and

rearranging the expressions yields

$$\begin{pmatrix} 2 & 0 & c \\ 2c & 0 & 1 \\ 0 & 2 & c \\ 0 & 2c & 1 \end{pmatrix} \begin{pmatrix} \alpha \\ \beta \\ \gamma \end{pmatrix} = \begin{pmatrix} 0 \\ 0 \\ 0 \\ 0 \end{pmatrix}. \quad (4.23)$$

To attest that the matrix above has trivial Null space, one can notice that the determinant of the first 3×3 block is $4c^2 - 4$ which does not have solutions for $c \in (-1, 1)$. Therefore, we conclude that the matrix \mathbf{A} is full-row rank and thus the map $D(F(\mathbf{x}, \mathbf{y}))$ is surjective which concludes that F is a rank-constant function.

Exploiting the result of Lemma 4.1, the tangent space of \mathcal{M} can be expressed as the set of directions that annihilate the directional derivative of the function F . In other words, we obtain the following characterization of the tangent space

$$\begin{aligned} \mathcal{T}_{(\mathbf{x}, \mathbf{y})}\mathcal{M} &= \text{Ker}(D(F(\mathbf{x}, \mathbf{y}))) \\ &= \left\{ (\xi_{\mathbf{x}}, \eta_{\mathbf{y}}) \in (\mathbb{R}^n)^2 \mid D(F(\mathbf{x}, \mathbf{y}))[\xi_{\mathbf{x}}, \eta_{\mathbf{y}}] = \mathbf{0} \right\} \\ &= \left\{ (\xi_{\mathbf{x}}, \eta_{\mathbf{y}}) \in (\mathbb{R}^n)^2 \mid \mathbf{x}^T \xi_{\mathbf{x}} = \mathbf{y}^T \eta_{\mathbf{y}} = 0, \mathbf{x}^T \eta_{\mathbf{y}} + \mathbf{y}^T \xi_{\mathbf{x}} = 0 \right\}. \end{aligned} \quad (4.24)$$

Finally, assuming $n \geq 2$ and using the submersion theorem of Riemannian manifold [94], we conclude that $\mathcal{M} = F^{-1}(\mathbf{C})$ is a manifold of dimension $\text{Dim}((\mathbb{R}^n)^2) - \text{Dim}(\mathcal{S}^2) = 2n - 3$. The dimension of the manifold can also be concluded from the expression of the tangent space derived above. \square

Let the embedding space $(\mathbb{R}^n)^2$ be equipped with the Frobenius inner product, defined as $\langle (\mathbf{x}, \mathbf{y}), (\mathbf{x}', \mathbf{y}') \rangle = \mathbf{x}^T \mathbf{x}' + \mathbf{y}^T \mathbf{y}'$ for all vectors (\mathbf{x}, \mathbf{y}) and $(\mathbf{x}', \mathbf{y}')$ in $((\mathbb{R}^n)^2)$. This paper considers that the embedded manifold inherits the inner product of the embedding space. In other words, the induced inner product

$\langle \cdot, \cdot \rangle_{(\mathbf{x}, \mathbf{y})}$ on the tangent space $\mathcal{T}_{(\mathbf{x}, \mathbf{y})}\mathcal{M}$ for $(\mathbf{x}, \mathbf{y}) \in \mathcal{M}$ is given by

$$\langle (\xi_{\mathbf{x}}, \eta_{\mathbf{y}}), (\xi'_{\mathbf{x}}, \eta'_{\mathbf{y}}) \rangle_{(\mathbf{x}, \mathbf{y})} = \xi_{\mathbf{x}}^T \xi'_{\mathbf{x}} + \eta_{\mathbf{y}}^T \eta'_{\mathbf{y}}, \quad (4.25)$$

for all tangent vectors $(\xi_{\mathbf{x}}, \eta_{\mathbf{y}})$ and $(\xi'_{\mathbf{x}}, \eta'_{\mathbf{y}})$ in $\mathcal{T}_{(\mathbf{x}, \mathbf{y})}\mathcal{M}$.

4.2.2 Riemannian Gradient and Hessian Computation

This part computes the Riemannian gradient and Hessian for the introduced oriented spheres manifold \mathcal{M} . Let $f : \mathcal{M} \rightarrow \mathbb{R}$ be a smooth function defined on the Riemannian manifold \mathcal{M} . As stated before, the Riemannian gradient of f at the point $(\mathbf{x}, \mathbf{y}) \in \mathcal{M}$ is the unique element of $\mathcal{T}_{(\mathbf{x}, \mathbf{y})}\mathcal{M}$ that relates to the directional derivative through the following equation

$$\langle \text{grad } f(\mathbf{x}, \mathbf{y}), (\xi_{\mathbf{x}}, \eta_{\mathbf{y}}) \rangle_{(\mathbf{x}, \mathbf{y})} = D(f(\mathbf{x}, \mathbf{y}))[\xi_{\mathbf{x}}, \eta_{\mathbf{y}}]. \quad (4.26)$$

Recall that the paper considers the induced inner product from the ambient space $(\mathbb{R}^n)^2$. Therefore, the expression of the Riemannian metric simplifies to $\text{grad } f(\mathbf{x}, \mathbf{y}) = \Pi_{(\mathbf{x}, \mathbf{y})}(\text{Grad } f(\mathbf{x}, \mathbf{y}))$ with $\Pi_{(\mathbf{x}, \mathbf{y})} : (\mathbb{R}^n)^2 \rightarrow \mathcal{T}_{(\mathbf{x}, \mathbf{y})}\mathcal{M}$ being the orthogonal projection from the ambient space to the tangent one [95]. In the rest of this section, the first and second components of the Riemannian gradient are denoted by $\text{grad}_{\mathbf{x}}f(\mathbf{x}, \mathbf{y})$ and $\text{grad}_{\mathbf{y}}f(\mathbf{x}, \mathbf{y})$, respectively. The same notation is used for the Euclidean gradient, i.e., $\text{Grad}_{\mathbf{x}}f(\mathbf{x}, \mathbf{y})$ and $\text{Grad}_{\mathbf{y}}f(\mathbf{x}, \mathbf{y})$ for the derivative with respect to \mathbf{x} and \mathbf{y} , respectively. The following theorem relates the expression of the Riemannian gradient $\text{grad } f(\mathbf{x}, \mathbf{y}) = \Pi_{(\mathbf{x}, \mathbf{y})}(\text{Grad } f(\mathbf{x}, \mathbf{y}))$ to its Euclidean counterpart $\text{Grad } f(\mathbf{x}, \mathbf{y})$ by providing the expression of the orthogonal projection $\Pi_{(\mathbf{x}, \mathbf{y})}$.

Theorem 4.2. *The orthogonal projection $\Pi_{(\mathbf{x}, \mathbf{y})}$ from the ambient space $(\mathbb{R}^n)^2$ to*

the tangent space $\mathcal{T}_{(\mathbf{x}, \mathbf{y})}\mathcal{M}$ is given by

$$\Pi_{(\mathbf{x}, \mathbf{y})}(\mathbf{u}, \mathbf{v}) = \begin{pmatrix} \mathbf{u} - \frac{1}{2(1-c^2)}(\alpha\mathbf{x} + \gamma\mathbf{y}) \\ \mathbf{v} - \frac{1}{2(1-c^2)}(\gamma\mathbf{x} + \beta\mathbf{y}) \end{pmatrix}, \quad (4.27)$$

where the scalars α , β , and γ are given by the following equations

$$\begin{pmatrix} \alpha \\ \beta \\ \gamma \end{pmatrix} = \begin{pmatrix} (2-c^2)\mathbf{x}^T\mathbf{u} + c^2\mathbf{y}^T\mathbf{v} - c(\mathbf{x}^T\mathbf{v} + \mathbf{y}^T\mathbf{u}) \\ (2-c^2)\mathbf{y}^T\mathbf{v} + c^2\mathbf{x}^T\mathbf{u} - c(\mathbf{y}^T\mathbf{u} + \mathbf{x}^T\mathbf{v}) \\ \mathbf{x}^T(\mathbf{v} - c\mathbf{u}) + \mathbf{y}^T(\mathbf{u} - c\mathbf{v}) \end{pmatrix}. \quad (4.28)$$

Proof. In order to derive the expression of the Riemannian gradient, one needs to compute the orthogonal projection from the ambient space to the tangent bundle. Such orthogonal projection is obtained by first expressing the orthogonal complement of the tangent space in the below lemma.

Lemma 4.2. *The orthogonal complement of $\mathcal{T}_{(\mathbf{x}, \mathbf{y})}^\perp\mathcal{M}$ of the tangent space $\mathcal{T}_{(\mathbf{x}, \mathbf{y})}\mathcal{M}$ at $(\mathbf{x}, \mathbf{y}) \in \mathcal{M}$ is given by*

$$\mathcal{T}_{(\mathbf{x}, \mathbf{y})}^\perp\mathcal{M} = \left\{ (\zeta_{\mathbf{x}}, \psi_{\mathbf{y}}) \in (\mathbb{R}^n)^2 \mid \zeta_{\mathbf{x}} = \alpha\mathbf{x} + \gamma\mathbf{y}, \psi_{\mathbf{y}} = \gamma\mathbf{x} + \beta\mathbf{y}, \alpha, \beta, \gamma \in \mathbb{R} \right\}. \quad (4.29)$$

Proof. The proof of this lemma is obtained by double inclusion of the orthogonal complement of the tangent space and the proposed set in the lemma. The first inclusion is asserted by direct computation of the inner product between the tangent space and its orthogonal complement. A dimension counting argument concludes the proof.

Recall that the tangent vector $(\xi_{\mathbf{x}}, \eta_{\mathbf{y}}) \in \mathcal{T}_{(\mathbf{x}, \mathbf{y})}\mathcal{M}$ satisfies the following equal-

ity

$$\begin{aligned}\mathbf{x}^T \xi_{\mathbf{x}} &= \mathbf{y}^T \eta_{\mathbf{y}} = 0, \\ \mathbf{x}^T \eta_{\mathbf{y}} + \mathbf{y}^T \xi_{\mathbf{x}} &= 0.\end{aligned}\tag{4.30}$$

Now, consider the vector $(\zeta_{\mathbf{x}}, \psi_{\mathbf{y}})$ satisfying $\zeta_{\mathbf{x}} = \alpha \mathbf{x} + \gamma \mathbf{y}$ and $\psi_{\mathbf{y}} = \gamma \mathbf{x} + \beta \mathbf{y}$ for some real numbers α , β , and γ . The inner product can be expressed as

$$\begin{aligned}\langle (\xi_{\mathbf{x}}, \eta_{\mathbf{y}}), (\zeta_{\mathbf{x}}, \psi_{\mathbf{y}}) \rangle_{(\mathbf{x}, \mathbf{y})} &= \xi_{\mathbf{x}}^T \zeta_{\mathbf{x}} + \eta_{\mathbf{y}}^T \psi_{\mathbf{y}} \\ &= \xi_{\mathbf{x}}^T (\alpha \mathbf{x} + \gamma \mathbf{y}) + \eta_{\mathbf{y}}^T (\gamma \mathbf{x} + \beta \mathbf{y}) \\ &= \gamma (\xi_{\mathbf{x}}^T \mathbf{y} + \eta_{\mathbf{y}}^T \mathbf{x}) = 0.\end{aligned}\tag{4.31}$$

Therefore, we obtain the inclusion

$$\mathcal{T}_{(\mathbf{x}, \mathbf{y})}^{\perp} \mathcal{M} \subseteq \left\{ (\zeta_{\mathbf{x}}, \psi_{\mathbf{y}}) \in (\mathbb{R}^n)^2 \mid \zeta_{\mathbf{x}} = \alpha \mathbf{x} + \gamma \mathbf{y}, \psi_{\mathbf{y}} = \gamma \mathbf{x} + \beta \mathbf{y}, \alpha, \beta, \gamma \in \mathbb{R} \right\}.\tag{4.32}$$

Now notice that the dimension of the ambient space is $2n$ and the dimension of the tangent space is $2n - 3$ which concludes that $\mathcal{T}_{(\mathbf{x}, \mathbf{y})}^{\perp} \mathcal{M}$ is of dimension 3 which matches the dimension of the set in the left-hand side of (4.29). Therefore, we conclude the equality of both sets. \square

With the characterization of the orthogonal complement of the tangent space in the previous lemma, we now compute the orthogonal projection from the ambient space to the tangent one. Consider a vector $(\mathbf{u}, \mathbf{v}) \in (\mathbb{R}^n)^2$ in the ambient space. Such vector can be decomposed into a tangent and an orthogonal component as follows:

$$(\mathbf{u}, \mathbf{v}) = \Pi_{(\mathbf{x}, \mathbf{y})}(\mathbf{u}, \mathbf{v}) + \Pi_{(\mathbf{x}, \mathbf{y})}^{\perp}(\mathbf{u}, \mathbf{v}),\tag{4.33}$$

where $\Pi_{(\mathbf{x}, \mathbf{y})}^{\perp}(\mathbf{u}, \mathbf{v})$ is the projection onto the orthogonal complement of the tan-

gent space that can be expressed as

$$\Pi_{(\mathbf{x}, \mathbf{y})}^\perp(\mathbf{u}, \mathbf{v}) = \begin{pmatrix} \alpha \mathbf{x} + \gamma \mathbf{y} \\ \gamma \mathbf{x} + \beta \mathbf{y} \end{pmatrix} \quad (4.34)$$

for some real numbers α , β , and γ . Recall that the tangent vector $\Pi_{(\mathbf{x}, \mathbf{y})}(\mathbf{u}, \mathbf{v})$ satisfies the following three equations

$$\langle \Pi_{(\mathbf{x}, \mathbf{y})}(\mathbf{u}, \mathbf{v}), (\mathbf{x}, \mathbf{0}) \rangle_{(\mathbf{x}, \mathbf{y})} = \mathbf{0} \quad (4.35)$$

$$\langle \Pi_{(\mathbf{x}, \mathbf{y})}(\mathbf{u}, \mathbf{v}), (\mathbf{0}, \mathbf{y}) \rangle_{(\mathbf{x}, \mathbf{y})} = \mathbf{0}$$

$$\langle \Pi_{(\mathbf{x}, \mathbf{y})}(\mathbf{u}, \mathbf{v}), (\mathbf{y}, \mathbf{x}) \rangle_{(\mathbf{x}, \mathbf{y})} = \mathbf{0}.$$

Combining the equations in (4.33) with the tangent space characterization in (4.35) and using the expression of the orthogonal projection in (4.27), we obtain the following three equations

$$\mathbf{x}^T(\alpha \mathbf{x} + \gamma \mathbf{y}) = \mathbf{x}^T \mathbf{u} \quad (4.36)$$

$$\mathbf{y}^T(\gamma \mathbf{x} + \beta \mathbf{y}) = \mathbf{y}^T \mathbf{v} \quad (4.37)$$

$$\mathbf{y}^T(\alpha \mathbf{x} + \gamma \mathbf{y}) + \mathbf{x}^T(\gamma \mathbf{x} + \beta \mathbf{y}) = \mathbf{x}^T \mathbf{v} + \mathbf{y}^T \mathbf{u}. \quad (4.38)$$

Now using the manifold equations, the above equations can be simplified to the following linear system in the variables α , β , and γ .

$$\begin{pmatrix} 1 & 0 & c \\ 0 & 1 & c \\ c & c & 2 \end{pmatrix} \begin{pmatrix} \alpha \\ \beta \\ \gamma \end{pmatrix} = \begin{pmatrix} \mathbf{x}^T \mathbf{u} \\ \mathbf{y}^T \mathbf{v} \\ \mathbf{x}^T \mathbf{v} + \mathbf{y}^T \mathbf{u} \end{pmatrix}. \quad (4.39)$$

Finally, noticing that

$$\begin{pmatrix} 1 & 0 & c \\ 0 & 1 & c \\ c & c & 2 \end{pmatrix}^{-1} = \frac{1}{2(1-c^2)} \begin{pmatrix} 2-c^2 & c^2 & -c \\ c^2 & 2-c^2 & -c \\ -c & -c & 1 \end{pmatrix}, \quad (4.40)$$

and rearranging the terms concludes the proof. \square

The fact that the manifold \mathcal{M} is an embedded manifold in a Euclidean ambient space allows us to simplify the expression of the Riemannian Hessian. Indeed, as stated earlier, the expression of the Riemannian Hessian can be simplified to a directional derivative followed by an orthogonal projection, i.e.,

$$\begin{aligned} \text{hess } f(\mathbf{x}, \mathbf{y})[\xi_{\mathbf{x}}, \eta_{\mathbf{y}}] &= \Pi_{(\mathbf{x}, \mathbf{y})}(\text{D}(\text{grad } f(\mathbf{x}, \mathbf{y}))[\xi_{\mathbf{x}}, \eta_{\mathbf{y}}]) \\ &= \Pi_{(\mathbf{x}, \mathbf{y})} \begin{pmatrix} \text{D}(\text{grad}_{\mathbf{x}} f(\mathbf{x}, \mathbf{y}))[\xi_{\mathbf{x}}, \eta_{\mathbf{y}}] \\ \text{D}(\text{grad}_{\mathbf{y}} f(\mathbf{x}, \mathbf{y}))[\xi_{\mathbf{x}}, \eta_{\mathbf{y}}] \end{pmatrix}. \end{aligned} \quad (4.41)$$

Using the above characterization of the Riemannian Hessian, the next proposition establishes the relation between the Riemannian Hessian and its Euclidean Hessian counterpart.

Proposition 4.1. *The Riemannian Hessian (denoted by $\text{hess } f(\mathbf{x}, \mathbf{y})[\xi_{\mathbf{x}}, \eta_{\mathbf{y}}]$) of the function f at the point $(\mathbf{x}, \mathbf{y}) \in \mathcal{M}$ and in the direction $[\xi_{\mathbf{x}}, \eta_{\mathbf{y}}]$ is given by the following expression*

$$\text{hess } f(\mathbf{x}, \mathbf{y}) = \begin{pmatrix} \text{hess}_{\mathbf{x}} f(\mathbf{x}, \mathbf{y}) \\ \text{hess}_{\mathbf{y}} f(\mathbf{x}, \mathbf{y}) \end{pmatrix} = \Pi_{(\mathbf{x}, \mathbf{y})} \begin{pmatrix} \overline{\Delta}_{\mathbf{x}} \\ \overline{\Delta}_{\mathbf{y}} \end{pmatrix}, \quad (4.42)$$

where the components of the vector are given by

$$\bar{\Delta}_{\mathbf{x}} = \Delta_{\mathbf{x}} - \frac{1}{2(1-c^2)} (\dot{\alpha}\mathbf{x} + \alpha\xi_{\mathbf{x}} + \dot{\gamma}\mathbf{y} + \gamma\eta_{\mathbf{y}}), \quad (4.43)$$

$$\bar{\Delta}_{\mathbf{y}} = \Delta_{\mathbf{y}} - \frac{1}{2(1-c^2)} (\dot{\gamma}\mathbf{x} + \gamma\xi_{\mathbf{x}} + \dot{\beta}\mathbf{y} + \beta\eta_{\mathbf{y}}). \quad (4.44)$$

The scalars α , β , and γ are given by

$$\begin{pmatrix} \alpha \\ \beta \\ \gamma \end{pmatrix} = \mathbf{A} \begin{pmatrix} \mathbf{x}^T \text{Grad}_{\mathbf{x}} f(\mathbf{x}, \mathbf{y}) \\ \mathbf{y}^T \text{Grad}_{\mathbf{y}} f(\mathbf{x}, \mathbf{y}) \\ \mathbf{x}^T \text{Grad}_{\mathbf{y}} f(\mathbf{x}, \mathbf{y}) + \mathbf{y}^T \text{Grad}_{\mathbf{x}} f(\mathbf{x}, \mathbf{y}) \end{pmatrix}, \quad (4.45)$$

where \mathbf{A} is the constant matrix $\begin{pmatrix} 2-c^2 & c^2 & -c \\ c^2 & 2-c^2 & -c \\ -c & -c & 1 \end{pmatrix}$ and the derivatives $\dot{\alpha}$, $\dot{\beta}$, and $\dot{\gamma}$ are given by the following equations:

$$\begin{pmatrix} \dot{\alpha} \\ \dot{\beta} \\ \dot{\gamma} \end{pmatrix} = \mathbf{A} \begin{pmatrix} \xi_{\mathbf{x}}^T & \mathbf{0}^T & \mathbf{x}^T & \mathbf{0}^T \\ \mathbf{0}^T & \eta_{\mathbf{y}}^T & \mathbf{0}^T & \mathbf{y}^T \\ \eta_{\mathbf{y}}^T & \xi_{\mathbf{x}}^T & \mathbf{y}^T & \mathbf{x}^T \end{pmatrix} \begin{pmatrix} \text{Grad}_{\mathbf{x}} f(\mathbf{x}, \mathbf{y}) \\ \text{Grad}_{\mathbf{y}} f(\mathbf{x}, \mathbf{y}) \\ \Delta_{\mathbf{x}} \\ \Delta_{\mathbf{y}} \end{pmatrix}, \quad (4.46)$$

with the Euclidean Hessian $\Delta_{\mathbf{x}} = \text{Hess}_{\mathbf{x}} f(\mathbf{x}, \mathbf{y})[\xi_{\mathbf{x}}, \eta_{\mathbf{y}}]$ and $\Delta_{\mathbf{y}} = \text{Hess}_{\mathbf{y}} f(\mathbf{x}, \mathbf{y})[\xi_{\mathbf{x}}, \eta_{\mathbf{y}}]$ being the directional derivative of the Euclidean gradient components. In other words,

$$\begin{aligned} \Delta_{\mathbf{x}} &= \text{Hess}_{\mathbf{x}} f(\mathbf{x}, \mathbf{y})[\xi_{\mathbf{x}}, \eta_{\mathbf{y}}] = D(\text{Grad}_{\mathbf{x}} f(\mathbf{x}, \mathbf{y}))[\xi_{\mathbf{x}}, \eta_{\mathbf{y}}] \\ \Delta_{\mathbf{y}} &= \text{Hess}_{\mathbf{y}} f(\mathbf{x}, \mathbf{y})[\xi_{\mathbf{x}}, \eta_{\mathbf{y}}] = D(\text{Grad}_{\mathbf{y}} f(\mathbf{x}, \mathbf{y}))[\xi_{\mathbf{x}}, \eta_{\mathbf{y}}]. \end{aligned}$$

Proof. The proof of this proposition is omitted herein as it follows directly from the expression of the Riemannian gradient and the definition of the Riemannian

Hessian for a manifold \mathcal{M} embedded in a Euclidean space endowed with the induced canonical inner product, i.e., the Riemannian Hessian characterization in (4.41) and the Riemannian gradient expression in Theorem 4.2. \square

4.2.3 Retraction of Tangent Vectors

This subsection designs a computationally efficient retraction $R_{(\mathbf{x}, \mathbf{y})}$ on the tangent space $\mathcal{T}_{(\mathbf{x}, \mathbf{y})}\mathcal{M}$ of the manifold \mathcal{M} by exploiting the vector space structure of the embedding space $(\mathbb{R}^n)^2$. Given a Euclidean ambient space, the following lemma [94] provides a way to construct a retraction.

Lemma 4.3. *Let \mathcal{M} be an embedded manifold of the Euclidean space \mathcal{E} and let \mathcal{N} be an abstract manifold such that $\dim(\mathcal{M}) + \dim(\mathcal{N}) = \dim(\mathcal{E})$. Assume that there is a diffeomorphism*

$$\begin{aligned} \phi : \mathcal{M} \times \mathcal{N} &\longrightarrow \mathcal{E}^* \\ (\mathbf{F}, \mathbf{G}) &\longmapsto \phi(\mathbf{F}, \mathbf{G}) \end{aligned} \tag{4.47}$$

where \mathcal{E}^* is an open subset of \mathcal{E} , with an element $\mathbf{I} \in \mathcal{N}$ satisfying $\phi(\mathbf{F}, \mathbf{I}) = \mathbf{F}$, $\forall \mathbf{F} \in \mathcal{M}$. Under the above assumption, the mapping

$$\begin{aligned} R_{\mathbf{X}} : \mathcal{T}_{\mathbf{X}}\mathcal{M} &\longrightarrow \mathcal{M} \\ \xi_{\mathbf{X}} &\longmapsto R_{\mathbf{X}}(\xi_{\mathbf{X}}) = \pi_1(\phi^{-1}(\mathbf{X} + \xi_{\mathbf{X}})), \end{aligned} \tag{4.48}$$

where $\pi_1 : \mathcal{M} \times \mathcal{N} \longrightarrow \mathcal{M} : (\mathbf{F}, \mathbf{G}) \longmapsto \mathbf{F}$ is the projection onto the first component, defines a retraction on the manifold \mathcal{M} for all $\mathbf{X} \in \mathcal{M}$ and tangent vector $\xi_{\mathbf{X}} \in \mathcal{T}_{\mathbf{X}}\mathcal{M}$.

Recall that the dimension of the manifold coincides with the dimension of its tangent space. Therefore, from the expression of the tangent space in Theorem 4.1, one can conclude that the manifold \mathcal{M} has a dimension equal to $(2n - 3)$. Let $\mathcal{N} = \mathbb{R}_* \times \mathbb{R}_* \times \mathbb{R}$ be a manifold of dimension 3. Therefore, we have $\dim(\mathcal{M})$

+ $\dim(\mathcal{N}) = \dim((\mathbb{R}^n)^2)$. Now consider the mapping ϕ defined by

$$\begin{aligned} \phi : \quad \mathcal{M} \times \mathcal{N} &\longrightarrow \mathcal{E}^* \subset (\mathbb{R}^n)^2 \\ \begin{pmatrix} \mathbf{x} \\ \mathbf{y} \end{pmatrix} \times \begin{pmatrix} \alpha \\ \beta \\ \gamma \end{pmatrix} &\longmapsto \begin{pmatrix} \alpha\mathbf{x} + \gamma\mathbf{y} \\ \gamma\mathbf{x} + \beta\mathbf{y} \end{pmatrix}, \end{aligned} \quad (4.49)$$

with $\mathcal{E}^* = (\mathbb{R}_*^n)^2$ representing the open subset of $(\mathbb{R}^n)^2$ containing only non-zero vectors in each of the two components. Note that the function ϕ is a continuous and differentiable function for all input parameters. Furthermore, for any input parameters $(\mathbf{x}, \mathbf{y}) \in \mathcal{M}$, notice that

$$\phi \left(\begin{pmatrix} \mathbf{x} \\ \mathbf{y} \end{pmatrix}, \begin{pmatrix} 1 \\ 1 \\ 0 \end{pmatrix} \right) = \begin{pmatrix} \mathbf{x} \\ \mathbf{y} \end{pmatrix}. \quad (4.50)$$

In other words, the element $\begin{pmatrix} 1 \\ 1 \\ 0 \end{pmatrix} \in \mathcal{N}$ is a neutral element for ϕ as mandated by Lemma 4.3. Finally, the following theorem provides the expression of the proposed retraction.

Theorem 4.3. *The mapping $R : \mathcal{T}\mathcal{M} \rightarrow \mathcal{M}$ whose restriction $R_{(\mathbf{x}, \mathbf{y})}$ to $\mathcal{T}_{(\mathbf{x}, \mathbf{y})}\mathcal{M}$ is given by*

$$R_{(\mathbf{x}, \mathbf{y})}(\xi_{\mathbf{x}}, \eta_{\mathbf{y}}) = (\mathbf{v}, \mathbf{w}), \quad (4.51)$$

with the vector (\mathbf{v}, \mathbf{w}) being expressed as

$$\begin{pmatrix} \mathbf{v} \\ \mathbf{w} \end{pmatrix} = \begin{pmatrix} \cos(\theta)\mathbf{I}_n & -\sin(\theta)\mathbf{I}_n \\ \cos(\varphi)\mathbf{I}_n & \sin(\varphi)\mathbf{I}_n \end{pmatrix} \begin{pmatrix} \mathbf{e}_1 \\ \mathbf{e}_2 \end{pmatrix}, \quad (4.52)$$

where the angles θ and φ , the basis vectors \mathbf{e}_1 and \mathbf{e}_2 , and the constants c_1 , c_2 , and c_3 are given by

$$\begin{aligned}\theta &= \cos^{-1}(c) - \varphi \\ \varphi &= \tan^{-1} \left(\frac{c_1 \sqrt{1 - c^2} + c_3}{c_2 + c_1 c} \right) \\ c_1 &= \|\mathbf{x} + \xi_{\mathbf{x}}\|_2 \\ \mathbf{e}_1 &= \frac{\mathbf{x} + \xi_{\mathbf{x}}}{c_1} \\ c_2 &= (\mathbf{y} + \eta_{\mathbf{y}})^T \mathbf{e}_1 \\ c_3 &= \|(\mathbf{y} + \eta_{\mathbf{y}}) - c_2 \mathbf{e}_1\|_2 \\ \mathbf{e}_2 &= \frac{(\mathbf{y} + \eta_{\mathbf{y}}) - c_2 \mathbf{e}_1}{c_3}.\end{aligned}$$

Proof. This theorem is demonstrated by applying the result of Lemma 4.3 to the mapping ϕ . Given the preliminary results above, the expression of the retraction is proven by showing that ϕ is a diffeomorphism and by computing its inverse. In other words, the retraction is derived by showing that ϕ is a bijection from $\mathcal{M} \times \mathcal{N}$ to $\mathcal{E}^* = \phi(\mathcal{M}, \mathcal{N})$ and by obtaining the expression of the inverse.

Let (\mathbf{v}, \mathbf{w}) with $\mathbf{v} \neq \mathbf{0}$ and $\mathbf{w} \neq \mathbf{0}$ be a vector in \mathcal{E}^* . It can readily be seen that, up to the permutation of (\mathbf{x}, \mathbf{y}) and (α, β) , there exists a unique $(\mathbf{x}, \mathbf{y}) \in \mathcal{M}$ and unique reals α , β , and γ such that

$$\phi \left(\left(\begin{array}{c} \mathbf{x} \\ \mathbf{y} \end{array} \right), \left(\begin{array}{c} \alpha \\ \beta \\ \gamma \end{array} \right) \right) = \left(\begin{array}{c} \mathbf{v} \\ \mathbf{w} \end{array} \right). \quad (4.53)$$

The rest of the proof derives a closed form expression of the inverse map ϕ^{-1} . First, using the Gram-Schmidt basis orthogonalization theorem, the family (\mathbf{v}, \mathbf{w})

can be expressed as

$$\begin{pmatrix} \mathbf{v} \\ \mathbf{w} \end{pmatrix} = \begin{pmatrix} c_1 \mathbf{e}_1 \\ c_2 \mathbf{e}_1 + c_3 \mathbf{e}_2 \end{pmatrix} = \begin{pmatrix} c_1 \mathbf{I}_n & 0 \mathbf{I}_n \\ c_2 \mathbf{I}_n & c_3 \mathbf{I}_n \end{pmatrix} \begin{pmatrix} \mathbf{e}_1 \\ \mathbf{e}_2 \end{pmatrix} \quad (4.54)$$

with $c_1, c_3 > 0$ and $\|\mathbf{e}_1\|_2 = \|\mathbf{e}_2\|_2 = 1$ and $\mathbf{e}_1^T \mathbf{e}_2 = 0$. The expression of these basis vectors and constants obtained from the Gram-Schmidt basis orthogonalization theorem are given by

$$\begin{aligned} c_1 &= \|\mathbf{v}\|_2 \\ \mathbf{e}_1 &= \frac{\mathbf{v}}{c_1} \\ c_2 &= \mathbf{w}^T \mathbf{e}_1 \\ c_3 &= \|\mathbf{w} - c_2 \mathbf{e}_1\|_2 \\ \mathbf{e}_2 &= \frac{\mathbf{w} - c_2 \mathbf{e}_1}{c_3}. \end{aligned}$$

Now, let $\mathbf{O} = \begin{pmatrix} \cos(\theta) \mathbf{I}_n & -\sin(\theta) \mathbf{I}_n \\ \cos(\varphi) \mathbf{I}_n & \sin(\varphi) \mathbf{I}_n \end{pmatrix}$ be an $2n \times 2n$ matrix for some angles θ and φ . Consider the non-isometric transformation of the basis vectors

$$\begin{pmatrix} \mathbf{x} \\ \mathbf{y} \end{pmatrix} = \mathbf{O} \begin{pmatrix} \mathbf{e}_1 \\ \mathbf{e}_2 \end{pmatrix}. \quad (4.55)$$

Notice that thanks to the structure of the matrix \mathbf{O} , the constraint $\mathbf{x}^T \mathbf{x} = \mathbf{y}^T \mathbf{y} = 1$. Indeed, we have $\mathbf{x}^T \mathbf{x} = \cos^2(\theta) + \sin^2(\theta) = 1$. The constraint $\mathbf{x}^T \mathbf{y} = c$ implies the following

$$\cos(\theta) \cos(\varphi) - \sin(\theta) \sin(\varphi) = c \Rightarrow \cos(\theta + \varphi) = c.$$

Now, combining (4.55) and (4.54) gives the following change of basis

$$\begin{pmatrix} \mathbf{v} \\ \mathbf{w} \end{pmatrix} = \begin{pmatrix} c_1 \mathbf{I}_n & 0 \mathbf{I}_n \\ c_2 \mathbf{I}_n & c_3 \mathbf{I}_n \end{pmatrix} \frac{1}{\det \mathbf{O}} \begin{pmatrix} \sin(\varphi) \mathbf{I}_n & \sin(\theta) \mathbf{I}_n \\ -\cos(\varphi) \mathbf{I}_n & \cos(\theta) \mathbf{I}_n \end{pmatrix} \begin{pmatrix} \mathbf{x} \\ \mathbf{y} \end{pmatrix}.$$

Multiplying the above matrices and insisting that the component along \mathbf{y} of the first vector matches the component along \mathbf{x} of the second vector, i.e., the scalar γ is the same in (4.54), generate the following equality:

$$\begin{aligned} c_1 \sin(\theta) &= c_2 \sin(\varphi) - c_3 \cos(\varphi) \\ c_1 \frac{\sin(\theta)}{\cos(\varphi)} &= c_2 \frac{\sin(\varphi)}{\cos(\varphi)} - c_3 \\ c_1 \frac{\sin(\theta)}{\cos(\varphi)} &= c_2 \tan(\varphi) - c_3. \end{aligned} \tag{4.56}$$

Recall that $\theta = \cos^{-1}(c) - \varphi$. Therefore, we have

$$\sin(\theta) = \sin(\cos^{-1}(c) - \varphi) = \sqrt{1 - c^2} \cos(\varphi) - c \sin(\varphi). \tag{4.57}$$

Substituting the previous equality in (4.56) and rearranging the terms gives $c_1(\sqrt{1 - c^2} - c \tan(\varphi)) = c_2 \tan(\varphi) - c_3$ and allows to conclude that

$$\tan(\varphi) = \frac{c_1 \sqrt{1 - c^2} + c_3}{c_2 + c_1 c}. \tag{4.58}$$

The scalars α , β , and γ can be obtained by expanding (4.55). However, it is omitted herein as the retraction is only interested in the first component of the inverse map ϕ^{-1} .

Finally, the retraction is obtained by applying the above algorithm to the vector $(\mathbf{x} + \xi_{\mathbf{x}}, \mathbf{y} + \eta_{\mathbf{y}})$. In other words, the retraction is given by the following

expression:

$$R_{(\mathbf{x}, \mathbf{y})}(\xi_{\mathbf{x}}, \eta_{\mathbf{y}}) = \pi_1 \left(\phi^{-1} \left(\begin{pmatrix} \mathbf{x} + \xi_{\mathbf{x}} \\ \mathbf{y} + \eta_{\mathbf{y}} \end{pmatrix} \right) \right). \quad (4.59)$$

□

Remark 4.1. *Note that the arc-tangent function \tan^{-1} in Theorem 4.3 is defined from $[0, \pi)$ instead of the usual $[-\pi/2, \pi/2)$ in order to obtain a positive scalar α , i.e., a positive sine.*

4.3 3-D GNSS Attitude Determination Using Riemannian Optimization

4.3.1 Proposed 3-D GNSS Attitude Determination Algorithm

This section describes the proposed method for 3-D GNSS attitude determination using the above derived first and second order Riemannian optimization algorithms. First, the ambiguity resolution method presented in (4.6) and (4.7) of Section 4.1 is applied to resolve the integer ambiguities. It should be noted that the antenna configuration shown in Fig. 4.2 is utilized instead of the one in Fig. 4.1. The estimations of the phase differences $\hat{\phi}_{12}$ and $\hat{\phi}_{14}$ are recovered. These phase differences can be used directly to obtain an estimate of the desired attitude. However, as pointed in [64], the unambiguous phase estimates usually suffer in terms of accuracy due to the accumulation of phase error. In addition, it is not guaranteed that the correct integer value is recovered by (4.7), i.e., the ambiguity resolution may actually fail. Therefore, these factors dictate that some processing should be performed before these phase estimates can be used for attitude determination.

Since the processes of ambiguity resolution for two baselines are independent, the geometry information of the antenna configuration is not respected. The

Algorithm 4.1 Proposed 3-D GNSS Attitude Determination Algorithm

- 1: Recover $\hat{\phi}_{12}$ and $\hat{\phi}_{14}$ independently using (4.6)–(4.8).
 - 2: Estimate the pointing vectors $\hat{\mathbf{x}}$ and $\hat{\mathbf{y}}$ using $\hat{\phi}_{12}$ and $\hat{\phi}_{14}$ by the least squares solution (4.10).
 - 3: **while** $|\hat{\mathbf{x}}^T \hat{\mathbf{y}} - \cos(\Theta)| > \epsilon$ **do**
 - 4: Adjust the integer ambiguities to the closest integer.
 - 5: Re-compute $\hat{\phi}_{12}$ and $\hat{\phi}_{14}$ using the adjusted integer ambiguities.
 - 6: Re-compute $\hat{\mathbf{x}}$ and $\hat{\mathbf{y}}$ based on (4.10).
 - 7: **end while**
 - 8: Estimate the pointing vectors $\hat{\mathbf{x}}$ and $\hat{\mathbf{y}}$ using the RieOpt method initialized using $\hat{\mathbf{x}}$ and $\hat{\mathbf{y}}$.
 - 9: Compute $\hat{\phi}_{13}$ and $\hat{\phi}_{15}$ from $\hat{\mathbf{x}}$ and $\hat{\mathbf{y}}$ using (4.11).
 - 10: Re-compute $\hat{\mathbf{x}}$ and $\hat{\mathbf{y}}$ using $\hat{\phi}_{13}$ and $\hat{\phi}_{15}$ through the RieOpt method described in Section 4.2.
-

prior knowledge of the angle between the two baselines can act as a constraint to judge the resolved integer ambiguities. If the angle condition isn't satisfied, a correction is performed to the resulting integer ambiguities by changing them to the closest integer until reaching a reasonable result. For a short baseline case, the bias of wrong integer ambiguity is usually very small.

Now, we are in a position to precisely estimate the pointing vectors using Riemannian Optimization (RieOpt method) developed in Section 4.2. The optimization problem in (4.14) is solved by the proposed RieOpt method initializing $\hat{\mathbf{x}}$ and $\hat{\mathbf{y}}$ with the LS solutions $\hat{\mathbf{x}}$ and $\hat{\mathbf{y}}$ as computed in (4.10). As mentioned before, the constraints in (4.14) strictly integrate the antennas geometry and baseline lengths into the cost function. Thus, as the optimization problem is ensured to converge to a critical point of the objective function, it is guaranteed that the geometry and the angles are satisfied.

In order to further improve the results, the phase difference between the longest baselines should be exploited. This can be done by applying the correction operation as in (4.11), and the step of integer ambiguity check and correction can be repeated again. Finally, the RieOpt method is carried out again for the largest baselines to refine the results of attitude determination. The integral process of the proposed method can be found in Algorithm 4.1.

4.3.2 Complexity Analysis and Rate of Convergence

The proposed Riemannian steepest descent method in Algorithm 3.1 requires the computation of the Riemannian gradient and the retraction at each step. As shown previously, the Riemannian gradient is obtained by simply projecting the Euclidean gradient. Given that the derived orthogonal projection in Theorem 4.2 only involves inner products, its complexity is linear in the dimension of the system. Likewise, from the expression of the retraction in Theorem 4.3, the most expensive step is the matrix multiplication in (4.52) which is quadratic in n . However, given the tri-diagonal structure of the matrix, the multiplication can be done in linear time which results in a retraction with linear complexity. Finally, it can be concluded that the per iteration complexity of the proposed Riemannian steepest descent method is linear in the dimension of the problem. Furthermore, thanks to the compactness of the manifold, first-order Riemannian methods are shown to exhibit a linear convergence rate [94].

The complexity analysis of the proposed Riemannian Newton's method follows similar steps as for the steepest descent. Indeed, from Algorithm 3.2, it can easily be seen that the most complex step is to compute the Hessian and solve for the search direction. From the expression of the Hessian in Proposition 4.1, it can easily be seen that it can be computed in $\mathcal{O}(n)$ steps. However, solving for the search direction $\xi_{\mathbf{x}}$ that satisfies $\text{hess } f(\mathbf{x})[\xi_{\mathbf{x}}] = -\text{grad } f(\mathbf{x})$ requires solving a system of n linear equations which can be done in n^3 . However, the use of iterative methods can reduce the complexity to n^2 resulting in an algorithm with quadratic complexity. Thanks to the use of second-order derivatives, the proposed Newton's method exhibits a convergence rate that is at least quadratic [94].

4.4 Simulation Setup And Results

This section presents the simulation results in order to evaluate the performance of the proposed approach under a noise-controlled environment. The first part of the section presents an overview of the simulation environment and parameters. The

second part plots the performance of the proposed method against benchmarks methods in the literature, namely, the least squares, LAMBDA method [60], and generic non-convex solvers. The LAMBDA method is the standard method for attitude determination and has found success in different attitude scenarios. The LS method resolves the integer ambiguity and estimates the attitude using the (4.6)–(4.11) for each baseline separately. Its objective function has similar formulation with (4.9)) for both baselines. The proposed RieOpt method applies the procedure summarised in Algorithm 3. The objective function is formulated as (4.14). While the LS and the proposed approach utilizes only carrier phase, the LAMBDA method takes advantage of both the carrier phase and pseudo-range. Besides, the LAMBDA method does not consider the priori knowledge about antenna array. So the comparison with the LAMBDA method is not exactly fair.

4.4.1 Simulation Setup

The simulations are implemented using Matlab and the libraries of the visual simulation software [96]. The basic parameters are produced based on the libraries of this software using the receiver location or antenna baseline and real GPS constellation information. Furthermore, the MATLAB version 3.0 of the LAMBDA software [97] is used.

The presence of trees, buildings and other high rising structures, natural or artificial, around the receivers may hamper the view of the satellites. GNSS observations below 15 degrees are usually disturbed by multi-path and other problems, e.g., cycle slips, and low signal to noise ratio [51]. The elevation mask allows us to set an elevation angle such that we can discard the data below that angle. This parameter has a great influence on dilution of precision (DOP), so it needs to be chosen carefully. In our simulations, an elevation mask of 15 degrees is applied.

The proposed method can be easily modified and extended to multi-epoch and multi-frequency cases. However, in our simulations, only the challenging single-

epoch, single-frequency case is considered using the GPS L1 frequency, which has a wavelength equal to 19cm approximately. The antenna configuration is similar to Fig. 4.2 with $\Delta = \Delta' = 8$ cm and different values of the angle Θ between the two baselines are considered. According to this setup, both conditions (4.5) and (4.12) are satisfied. This contribution takes advantage of a specific antenna array. We apply this configuration for this sep-up for all the methods. It should be noted that the setting will simplify the process of integer ambiguity resolution, but this is not necessary for other algorithms. Besides, the proposed Riemannian manifold optimization can also combine with other integer ambiguity resolution methods.

To demonstrate the performance of the proposed method in multiple possible scenarios, simulations are carried out over different GPS weeks, noise levels and number of satellites. For each simulation setup, the tests are repeated 10^5 times with random Gaussian noise and random baseline pointing vectors. For the carrier phase observables, the Gaussian noise has zero mean and standard deviation σ_ϕ , ranging from 1 mm to 7 mm. Unlike other non-convex methods, the proposed Riemannian method is guaranteed to always reach an extreme point of the problem. Furthermore, for moderate to high noise variance, non-convex solvers return different results due to the existence of multiple local minima. Typical GPS phase measurements have phase standard deviation in the range of 1-3 mm [98]. For GPS, the pseudo-range and phase variance ratio is around 10^4 [74], i.e., $\frac{\sigma_p^2}{\sigma_\phi^2} = 10^4$. For pseudo-range measurements, according to the above ratio, the Gaussian noises with zero mean and standard deviation σ_p are used.

To test the performance of the proposed approach, we evaluate the success rate and root mean square error (RMSE) of the baseline pointing direction. Success rate is defined as the percentage of occurrences that the integer vectors are correctly fixed over 10^5 simulation trials. The baseline pointing vector error refers to the deviation of the resulting direction vector from the true pointing direction. Finally, the RMSE is evaluated only for the configurations resulting in a successful

Table 4.1: Success rates over many GPS weeks for $d_{12} = d_{14} = 45$ cm, $\Delta = \Delta' = 8$ cm, $\sigma_\phi = 3$ mm, $\Theta = 90^\circ$ and $m = 4$

| Date | GPS week | LS | | RieOpt | | LAMBDA | |
|-------------|----------|-------|-------|--------|-------|--------|-------|
| | | x | y | x | y | x | y |
| 03-Sep-2017 | 941 | 0.960 | 0.960 | 0.961 | 0.962 | 0.973 | 0.974 |
| 01-Oct-2017 | 945 | 0.982 | 0.984 | 0.984 | 0.985 | 0.998 | 0.998 |
| 19-Nov-2017 | 952 | 0.987 | 0.988 | 0.988 | 0.989 | 0.999 | 0.988 |
| 28-Jan-2018 | 962 | 0.988 | 0.988 | 0.988 | 0.988 | 0.999 | 0.999 |
| 04-Feb-2018 | 963 | 0.985 | 0.987 | 0.984 | 0.987 | 0.999 | 0.999 |
| 01-Apr-2018 | 971 | 0.981 | 0.982 | 0.983 | 0.984 | 0.998 | 0.998 |
| 08-Apr-2018 | 972 | 0.980 | 0.981 | 0.983 | 0.984 | 0.998 | 0.998 |
| 22-Apr-2018 | 974 | 0.969 | 0.970 | 0.972 | 0.973 | 0.991 | 0.992 |
| 29-Apr-2018 | 975 | 0.982 | 0.983 | 0.984 | 0.985 | 0.999 | 0.999 |
| 06-May-2018 | 976 | 0.983 | 0.984 | 0.985 | 0.985 | 0.998 | 0.998 |

Table 4.2: RMSE ($^\circ$) over different GPS weeks for $d_{12} = d_{14} = 45$ cm, $\Delta = \Delta' = 8$ cm, $\sigma_\phi = 3$ mm, $\Theta = 90^\circ$ and $m = 4$

| Date | GPS week | LS | | RieOpt | | LAMBDA | |
|-------------|----------|-------|-------|--------|-------|--------|-------|
| | | x | y | x | y | x | y |
| 03-Sep-2017 | 941 | 0.465 | 0.458 | 0.338 | 0.331 | 0.651 | 0.637 |
| 01-Oct-2017 | 945 | 0.338 | 0.367 | 0.268 | 0.280 | 0.478 | 0.519 |
| 19-Nov-2017 | 952 | 0.521 | 0.536 | 0.359 | 0.382 | 0.734 | 0.755 |
| 28-Jan-2018 | 962 | 0.734 | 0.746 | 0.489 | 0.498 | 1.035 | 1.052 |
| 04-Feb-2018 | 963 | 0.555 | 0.637 | 0.416 | 0.541 | 0.783 | 0.900 |
| 01-Apr-2018 | 971 | 0.349 | 0.343 | 0.265 | 0.263 | 0.491 | 0.483 |
| 08-Apr-2018 | 972 | 0.304 | 0.307 | 0.251 | 0.252 | 0.428 | 0.433 |
| 22-Apr-2018 | 974 | 0.301 | 0.317 | 0.253 | 0.256 | 0.424 | 0.447 |
| 29-Apr-2018 | 975 | 0.330 | 0.331 | 0.271 | 0.271 | 0.465 | 0.467 |
| 06-May-2018 | 976 | 0.379 | 0.394 | 0.284 | 0.287 | 0.532 | 0.555 |

estimation.

4.4.2 Numerical Results

Table 4.1 shows the success rates of the proposed and the two benchmark approaches for 10 different GPS weeks on specific days and time 00 : 00. In this result set, the same setup is used with $d_{12} = d_{14} = 45$ cm, $\Delta = \Delta' = 8$ cm, $\sigma_\phi = 3$ mm, $\Theta = 90^\circ$ and number of satellites $m = 4$. Such a small number of satellites is meant to provide a challenging scenario to compare the performance of three methods. Table 4.1 indicates that all the three methods have very high success rates. The RieOpt method and LS method have similar success rates

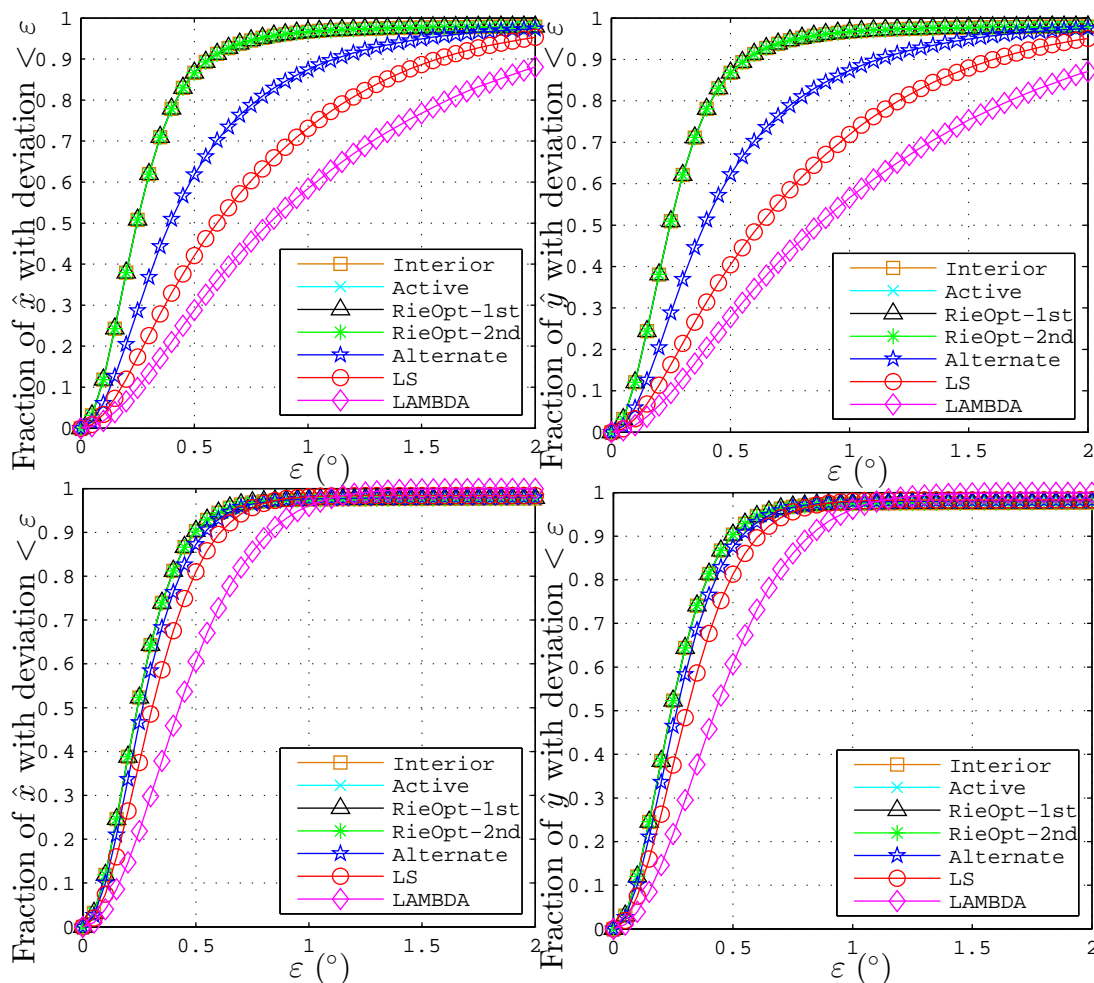


Figure 4.3: Fraction of estimates with error less than ϵ . (a) and (b) indicate the results for GPS constellation on January 28, 2018. (c) and (d) represent the results for GPS constellation on April 29, 2018.

since the Rieopt method is based on the unwrapped phase obtained from the LS method. However, the success rate of the LAMBDA method is a little higher than the other two methods, which may come from the fact that the LAMBDA method also takes advantage of pseudo-range data. Even though the success rates are slightly different, all the three methods offer excellent performance in satellite-deprived environments.

Table 4.2 lists the RMSE of the three methods over the 10 GPS weeks of Table 4.1. It is clear that the RieOpt method provides the best accuracy in almost all simulated cases except few instances wherein the Active set method provides better results. The RieOpt method rigorously integrates the antenna geometry and baseline lengths to its objective function so that it produces more

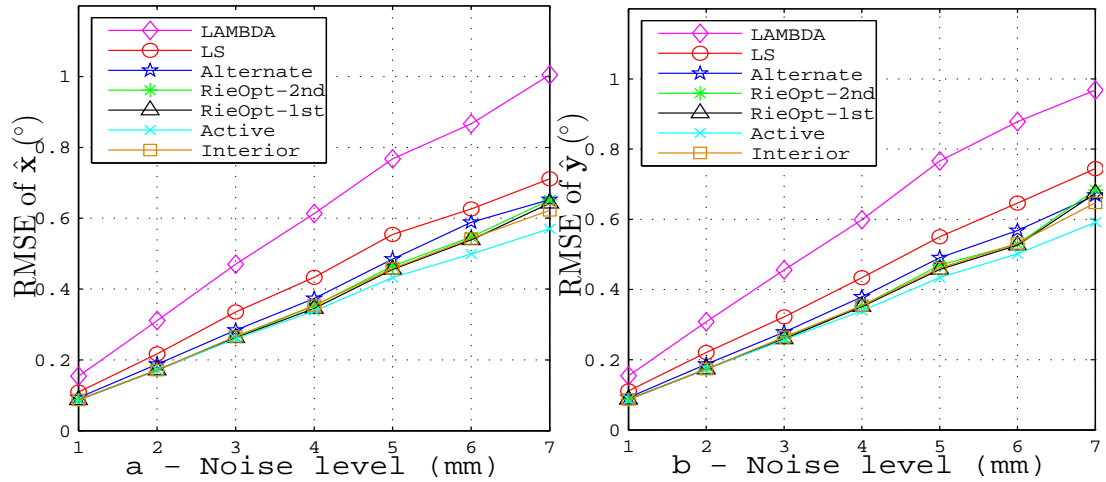


Figure 4.4: RMSE vs. Noise levels (29-Apr-2018)

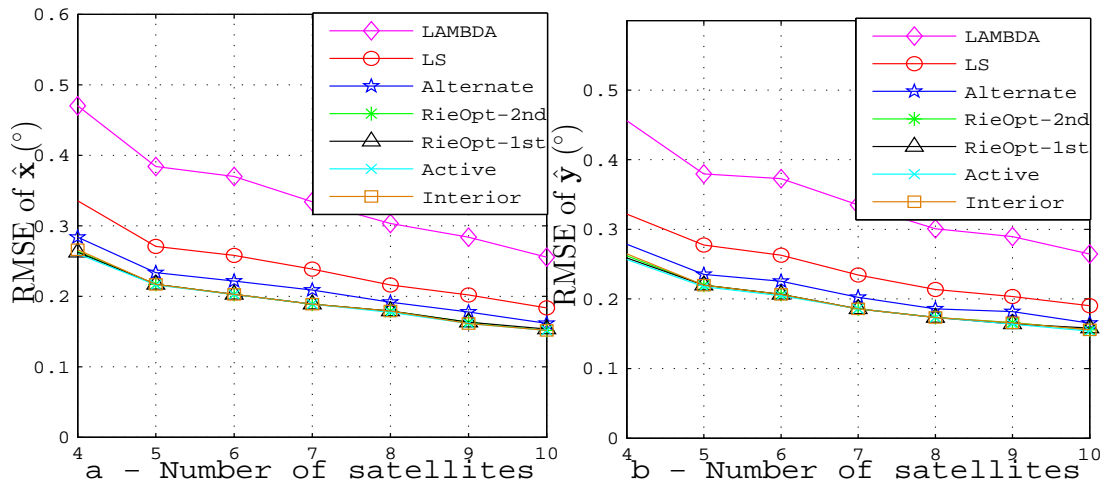


Figure 4.5: RMSE vs. Number of Satellites (29-Apr-2018)

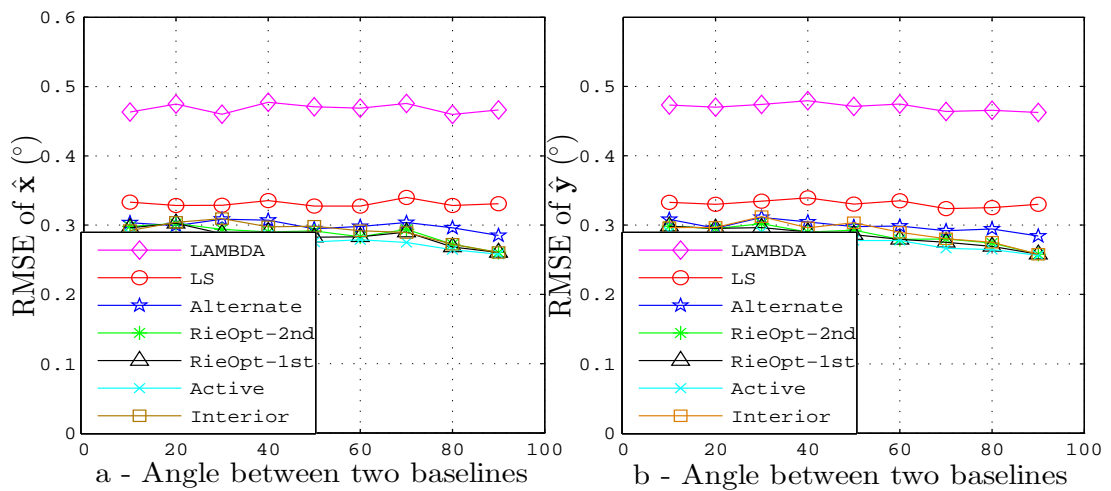


Figure 4.6: RMSE vs. Angle Between Two Baselines (29-Apr-2018)

Table 4.3: Mean Running Time of the Different Algorithms.

| Method | Alt. | Int. | Act. | Rie-1st | Rie-2nd |
|----------|--------|--------|--------|---------|---------|
| Time (s) | 0.1278 | 0.0269 | 0.0180 | 0.0054 | 0.0147 |

accurate results than the other methods. However, it is worth mentioning that the LS method also outperforms the LAMBDA method.

Fig. 4.3 shows the fraction of simulation trials with RMSE below different values on two different dates, January 28, 2018 and April 29, 2018. These plots depict the success rates and attitude estimation accuracy of the seven methods in a different way. These four plots show that the RieOpt method can enhance the accuracy of the resulting pointing vectors while offering similar success rates to those of the LS. Comparing the plots of these two GPS weeks, we can find out that the improvement is more evident for the case in which the LS method and LAMBDA method have less accurate results.

To test the effect of carrier phase noise on the proposed method, a set of simulations is carried out for GPS week 975. The standard deviation of carrier phase, σ_ϕ , varies from 1 mm to 7 mm, and the standard deviation of pseudo-range adjusted according to the ratio $\sigma_p^2/\sigma_\phi^2 = 10^4$. All the other setting parameters are kept unchanged. Fig. 4.4 plots the corresponding RMSE of the three methods under different noise levels. Although the errors of all the methods increase as the noises increase, the RieOpt method consistently offers the best performance in almost all scenarios. The LS method outperforms the LAMBDA method over the different scenarios. Besides, the larger the noise is, the more obvious the accuracy improvement of the RieOpt method is. Fig. 4.5 shows the RMSE of all methods when different numbers of satellites are used. As expected, the accuracy of all the methods improves as the the number of satellites increases. The results prove that the RieOpt method provides the best performance in almost all situations regardless of the number of satellites. The LAMBDA method jointly utilizes carrier phase and pseudo-range of the two co-linear baselines such that its success

rate is a bit higher than the rest methods. However, using the short and long baselines together leads to that its RMSEs is worse than the LS method (the baseline length will influence the results). Otherwise, its accuracy should be similar to the LS approach, but still poorer than the RieOpt method.

While the above mentioned simulations assume orthogonal baselines, Fig. 4.6 attest the performance of the proposed algorithm using a more general configuration, i.e., with different angle values between two baselines. From the numerical results, it appears that the angle between two baselines does not show any visible effect on the results. Finally, considering all the aforementioned simulations, it can be concluded that the RieOpt approach is able to significantly improve the accuracy of attitude estimation over that offered by the LS, the LAMBDA methods, and generic non-convex solvers. Furthermore, the proposed method is faster than its generic non-convex counterparts as shown in Table 4.3. For example, the proposed first-order Riemannian algorithm is on average 3 times as fast as the active set method and 5 times as fast as the interior point method. This further emphasizes the clever exploitation of the geometry of the problem by the proposed Riemannian methods.

4.5 Chapter Summary

This chapter proposes a novel Riemannian optimization based scheme for precise 3-D GNSS attitude determination. Given a specific antenna configuration, the unwrapped phase difference is recovered by an efficient state-of-the-art ambiguity resolution method. Subsequently, this unwrapped phase difference is used to formulate 3-D attitude determination as a non-convex optimization problem that incorporates all the available baseline length and angle constraints. The non-convex problem is solved by introducing a novel Riemannian manifold and investigating its geometry. The resulting first and second order optimization algorithms are not only efficient for their clever use of the geometry of the problem, but are also guaranteed to converge to an extreme point. The performance of the

proposed framework is assessed through extensive numerical simulations under various setup conditions, with particular a focus on challenging scenarios. Simulation results demonstrate that the proposed Riemannian optimization based scheme largely outperforms the least squares and the LAMBDA benchmark approaches in all test scenarios with a lower complexity than generic non-convex solvers.

Chapter 5

Riemannian-manifold-based Ambiguity Resolution and Attitude Determination

For the integer search-based methods discussed in Chapter 2, ambiguity resolution is carried out via searching around the float solution in the integer domain; that is, the float solution acts as an intermediate to simplify the integer search. As a consequence, the performance of ambiguity resolution profoundly relies on the quality of the float solution. Hence, it is critical to ensure that the float solution is of sufficient accuracy. Indeed, the more accurate the float solution, the better. To facilitate resolving the carrier-phase ambiguities more efficiently and reliably, we propose an approach based on optimization techniques on Riemannian manifolds to enhance the float solution. Subsequently, we develop an efficient integer search algorithm based on the improved float solution.

The proposed method employs the OC-AM with (2.24) being the objective function incorporating both the orthonormality and integer constraints, which is named as Riemannian-manifold-based orthonormality-constrained attitude determination (RieMOCAD). We improve the computational efficiency of the MC-LAMBDA method in two ways. First, we improve the float solution by enforcing the constraints. Using the prior knowledge of the geometric constraints is expected to improve the float solution and make it closer to the true solution. This can further enhance the integer search. Since the search strategy of the MC-LAMBDA depends on the float solution being at the global minimum of the unconstrained objective function, using the improved float solution requires a modified integer search strategy. We develop such a strategy based on a new proposed decomposition of the objective function.

As we will see in the following sections, the float solution needs to be computed not only once at the initialization stage but also repetitively as part of the integer search routine. Hence, as a second way to improve the computational efficiency of attitude estimation using orthonormality constraints, we employ a more efficient solver to compute the constrained float solution. The nonlinearly constrained least-squares problem can be solved, for example, through parameterization [99, 100, 101] or using the Lagrange multipliers method [102, 103]. The solution is usually implemented using an iterative technique such as the Newton's or Gauss-Newton methods [102, 90]. In this paper, we apply Riemannian optimization to solve the nonlinearly constrained least-squares problem. Riemannian optimization treats the constrained optimization problem in the Euclidean space as an *unconstrained* optimization on a Riemannian manifold. This simplifies our perception of the problem and allows us to apply tools from unconstrained optimization to solve the problem on the manifold [104]. Additionally, the transformation of the constrained optimization into an unconstrained optimization on a manifold offers the following advantages:

1. Since the iterates execute on the manifold where all the constraints are satisfied, Riemannian optimization does not need to consider Lagrange multipliers or penalty functions, inherently maintaining convergence properties of unconstrained optimization algorithms [104].
2. The dimension of the manifold is smaller than or equal to that of the original Euclidean space [105]. The (possibly) reduced dimensionality, as well as exploiting the underlying geometric structure of the manifold, allows Riemannian optimization algorithms to be more efficient than their (constrained) Euclidean counterparts [106].
3. Another benefit of Riemannian algorithms lies in their flexibility with respect to changing or modifying the objective function without requiring a substantial change in the whole algorithm. The Riemannian algorithm

design is largely dictated by the manifold, i.e., the constraints, not the objective function. This can be particularly useful when the objective function needs to be modified to cope with changes in the noise model or incorporate new measurements, etc. [104].

To differentiate between the proposed method and existing methods, we have summarized our main contributions as:

1. Enforcing the orthonormality constraints in the (initial) float solution to improve the integer search.
2. Proposing a decomposition of the objective function that allows us to employ the constrained float solution to accelerate the search process.
3. Developing a Riemannian optimization algorithm to efficiently compute the constrained float solution and improve the computational efficiency of the overall attitude determination algorithm.

The rest of this chapter is structured as follows. Firstly, we present the proposed attitude determination algorithm, including the problem formulation and the proposed method to obtain the constrained float solution using Riemannian manifold optimization. Secondly, we describe how to apply the constrained float solution to solve the ambiguity resolution problem using a proposed objective-function decomposition. Then, we present numerical results, comparing the performance of the proposed approach and a number of benchmark methods using different evaluation criteria. Finally, we draw the conclusion of the chapter.

5.1 The Intermediate Float Solution And Riemannian Algorithm Design

In this section, we first formulate the float solution used in this work. Then, we study and characterize the geometry of the manifolds of interest and present Riemannian optimization algorithms employed to achieve the float solution.

5.1.1 The Float Solution

The key principle behind the proposed method is to maintain the orthonormality constraint $\mathbf{R} \in \mathbb{O}^{3 \times q}$ when pursuing the initial float solution. The motivation here is that preserving this constraint is expected to provide a better float solution (than the one obtained with the constraint ignored). Incorporating the constrained, however, usually leads to an increased computational complexity. To develop a computationally efficient solution, we leverage advanced tools from *manifold optimization* [107, 94, 108].

Due to the orthonormality characteristics, the solution set of \mathbf{R} is a manifold, which allows us to solve the problem using efficient Riemannian algorithms. In other words, we calculate the float solution by using Riemannian manifold optimization, which gives us

$$\hat{\mathbf{R}}_{\text{RM}}, \hat{\mathbf{N}}_{\text{RM}} = \arg \min_{\mathbf{R} \in \mathbb{O}^{3 \times q}, \mathbf{N} \in \mathbb{R}^{S \times A}} \|\text{vec}(\mathbf{Y} - \mathbf{A}\mathbf{R}\mathbf{X}_b - \mathbf{B}\mathbf{N})\|_{\mathbf{Q}_{\mathbf{Y}\mathbf{Y}}^{-1}}^2. \quad (5.1)$$

The incorporation of the orthonormality constraint $\mathbf{R} \in \mathbb{O}^{3 \times q}$ can improve the estimation of \mathbf{R} using (5.1) compared to (2.20). We can generally expect $\hat{\mathbf{R}}_{\text{RM}}$ to be more accurate than $\hat{\mathbf{R}}_{\text{AC}}$. Given the convexity of the objective functions (2.20) and (5.1) in the unconstrained ambiguities, the float solutions obtained from these optimizations should satisfy

$$\hat{\mathbf{N}}_{\text{AC}} = (\mathbf{B}^T \mathbf{Q}_{\mathbf{Y}\mathbf{Y}}^{-1} \mathbf{B}) \mathbf{B}^T \mathbf{Q}_{\mathbf{Y}\mathbf{Y}}^{-1} \text{vec}(\mathbf{Y} - \mathbf{A}\hat{\mathbf{R}}_{\text{AC}} \mathbf{X}_b), \quad (5.2)$$

$$\hat{\mathbf{N}}_{\text{RM}} = (\mathbf{B}^T \mathbf{Q}_{\mathbf{Y}\mathbf{Y}}^{-1} \mathbf{B}) \mathbf{B}^T \mathbf{Q}_{\mathbf{Y}\mathbf{Y}}^{-1} \text{vec}(\mathbf{Y} - \mathbf{A}\hat{\mathbf{R}}_{\text{RM}} \mathbf{X}_b). \quad (5.3)$$

Given that $\hat{\mathbf{R}}_{\text{RM}}$ is less erroneous than $\hat{\mathbf{R}}_{\text{AC}}$, we can expect $\hat{\mathbf{N}}_{\text{RM}}$ to be of higher quality than $\hat{\mathbf{N}}_{\text{AC}}$.

Note that the LS solutions $\hat{\mathbf{R}}_{\text{AC}}$ and $\hat{\mathbf{N}}_{\text{AC}}$ are also required in the integer search process (presented later). Hence, the first step is to compute the LS solution $\hat{\mathbf{R}}_{\text{AC}}$ and $\hat{\mathbf{N}}_{\text{AC}}$, which allows us to obtain $\hat{\mathbf{R}}_{\text{RM}}$ and $\hat{\mathbf{N}}_{\text{RM}}$ based on $\hat{\mathbf{R}}_{\text{AC}}$ and $\hat{\mathbf{N}}_{\text{AC}}$ rather

than solving (5.1) directly. To determine the solution of (5.1), we reformulate the objective function as a sum of several squares terms. This reformulation helps us in exploiting Riemannian optimization with an easy-compute form.

Lemma 5.1. *Let $\hat{\mathbf{R}}_{AC}$ and $\hat{\mathbf{N}}_{AC}$ be the LS solutions given in (2.20). Then, we have*

$$\begin{aligned} & \|\text{vec}(\mathbf{Y} - \mathbf{A}\mathbf{R}\mathbf{X}_b - \mathbf{B}\mathbf{N})\|_{\mathbf{Q}_{\mathbf{Y}\mathbf{Y}}^{-1}}^2 \\ &= \|\text{vec}(\mathbf{E}_{AC})\|_{\mathbf{Q}_{\mathbf{Y}\mathbf{Y}}^{-1}}^2 + \left\| \text{vec}(\mathbf{R} - \hat{\mathbf{R}}_{AC}) \right\|_{\mathbf{Q}_{\hat{\mathbf{R}}_{AC}\hat{\mathbf{R}}_{AC}}^{-1}}^2 + \left\| \text{vec}(\mathbf{N} - \hat{\mathbf{N}}_{AC}(\mathbf{R})) \right\|_{\mathbf{Q}_{\hat{\mathbf{N}}_{AC}(\mathbf{R})\hat{\mathbf{N}}_{AC}(\mathbf{R})}^{-1}}^2, \end{aligned} \quad (5.4)$$

with

$$\text{vec}(\hat{\mathbf{N}}_{AC}(\mathbf{R})) = \text{vec}(\hat{\mathbf{N}}_{AC}) - \mathbf{Q}_{\hat{\mathbf{N}}_{AC}\hat{\mathbf{R}}_{AC}} \mathbf{Q}_{\hat{\mathbf{R}}_{AC}\hat{\mathbf{R}}_{AC}}^{-1} \text{vec}(\hat{\mathbf{R}}_{AC} - \mathbf{R}). \quad (5.5)$$

Proof. See Appendix A. □

According to Lemma 5.1, the optimization problem in (5.1) is equivalent to

$$\hat{\mathbf{R}}_{RM} = \arg \min_{\mathbf{R} \in \mathbb{O}^{3 \times q}} \left\| \text{vec}(\mathbf{R} - \hat{\mathbf{R}}_{AC}) \right\|_{\mathbf{Q}_{\hat{\mathbf{R}}_{AC}\hat{\mathbf{R}}_{AC}}^{-1}}^2, \quad (5.6)$$

$$\hat{\mathbf{N}}_{RM} = \hat{\mathbf{N}}_{AC}(\hat{\mathbf{R}}_{RM}). \quad (5.7)$$

That is to say, solving (5.6) is where Riemannian optimization comes into play.

5.1.2 Optimization Algorithm Design on Riemannian Manifolds

As stated in Section 2.3.3, the attitude matrix \mathbf{R} is an orthonormal matrix whose columns are orthogonal regarding the inner product. Here, for the sake of simplicity and avoiding confusion, we still utilize the symbol \mathbf{X} to denote the point on the manifold rather than symbol \mathbf{R} . Then, we can use the terminologies discussed in Section 3 and present the required elements for Riemannian algorithms.

The potential solution set \mathcal{M} is an embedded submanifold of $\mathbb{R}^{3 \times q}$ ($q = 1, 2, 3$),

which is well known as the Stiefel manifold given by [104]

$$\mathcal{M} = \{\mathbf{X} \in \mathbb{R}^{3 \times q} \mid \mathbf{X}^T \mathbf{X} = \mathbf{I}_q\}. \quad (5.8)$$

The dimension of the the Stiefel manifold \mathcal{M} is

$$\dim \mathcal{M} = \dim \mathbb{R}^{3 \times q} - \dim \text{Sym}(q) = 3q - \frac{q(q+1)}{2}, \quad (5.9)$$

where $\text{Sym}(q)$ represents the linear space of symmetric matrices of size q .

The tangent spaces of the the Stiefel manifold \mathcal{M} , a subspace of $\mathbb{R}^{3 \times q}$, is given by

$$\mathcal{T}_{\mathbf{x}} \mathcal{M} = \{\mathbf{V} \in \mathbb{R}^{3 \times q} \mid \mathbf{X}^T \mathbf{V} + \mathbf{V}^T \mathbf{X} = \mathbf{0}\}. \quad (5.10)$$

Alternatively, one can also express the tangent vectors in an explicit form as

$$\mathcal{T}_{\mathbf{x}} \mathcal{M} = \{\mathbf{X}\mathbf{S} + \mathbf{X}_{\perp} \mathbf{K} \mid \mathbf{S} \in \text{Skew}(q), \mathbf{K} \in \mathbb{R}^{(3-q) \times q}\}, \quad (5.11)$$

where \mathbf{X} and \mathbf{X}_{\perp} constitute the orthonormal basis of $\mathbb{R}^{3 \times 3}$, and

$$\text{Skew}(q) = \{\mathbf{S} \in \mathbb{R}^{q \times q} \mid \mathbf{S}^T = -\mathbf{S}\} \quad (5.12)$$

denotes the set of skew-symmetric matrices of size q .

At a point \mathbf{X} on the Stiefel manifold \mathcal{M} , the orthogonal projection to the tangent space $\mathcal{T}_{\mathbf{x}} \mathcal{M}$ can be formulated as

$$\begin{aligned} \Pi_{\mathbf{x}}(\mathbf{U}) &= \mathbf{U} - \mathbf{X} \frac{\mathbf{X}^T \mathbf{U} + \mathbf{U}^T \mathbf{X}}{2} \\ &= (\mathbf{I} - \mathbf{X}\mathbf{X}^T) \mathbf{U} + \mathbf{X} \frac{\mathbf{X}^T \mathbf{U} - \mathbf{U}^T \mathbf{X}}{2}. \end{aligned} \quad (5.13)$$

Note that the orthogonal projector $\Pi_{\mathbf{x}}$ guarantees that $\mathbf{U} - \Pi_{\mathbf{x}}(\mathbf{U})$ falls into the normal space $\mathcal{T}_{\mathbf{x}}^{\perp} \mathcal{M}$ of the tangent space $\mathcal{T}_{\mathbf{x}} \mathcal{M}$. According to (3.2) and (3.3),

we can compute the Riemannian gradient $\bar{\nabla}_{\mathbf{x}} f$ and Riemannian Hessian $\bar{\nabla}_{\mathbf{x}}^2 f$. Then, we obtain

$$\bar{\nabla}_{\mathbf{x}} f = \nabla_{\mathbf{x}} f - \mathbf{X} \frac{\mathbf{X}^T \nabla_{\mathbf{x}} f + (\nabla_{\mathbf{x}} f)^T \mathbf{X}}{2}, \quad (5.14)$$

$$\bar{\nabla}_{\mathbf{x}}^2 f[\boldsymbol{\xi}_{\mathbf{x}}] = \Pi_{\mathbf{x}}(\nabla_{\mathbf{x}}^2 f[\boldsymbol{\xi}_{\mathbf{x}}]) - \boldsymbol{\xi}_{\mathbf{x}} \frac{\mathbf{X}^T \nabla_{\mathbf{x}} f + (\nabla_{\mathbf{x}} f)^T \mathbf{X}}{2}. \quad (5.15)$$

After finding a new point in $\mathcal{T}_{\mathbf{x}} \mathcal{M}$ using $\bar{\nabla}_{\mathbf{x}} f$ and/or $\bar{\nabla}_{\mathbf{x}}^2 f$, retraction is required to turn the new point into the manifold \mathcal{M} . For the the Stiefel manifold, multiple retraction operators exist. For instance, the Q-factor retraction is an efficient operator to retract the updated point to the manifold [104]:

$$R_{\mathbf{x}}(\mathbf{V}) = \mathbf{Q}, \quad (5.16)$$

in which the QR decomposition is employed such that $\mathbf{Q}\mathbf{R}_{ut} = \mathbf{X} + \mathbf{V}$ with $\mathbf{Q} \in \mathcal{M}$ and $\mathbf{R}_{ut} \in \mathbb{R}^{q \times q}$. Here, \mathbf{R}_{ut} represents an upper triangular with nonnegative diagonal entries. On the other hand, the polar retraction can also be used [104], which is expressed as

$$\begin{aligned} R_{\mathbf{x}}(\mathbf{V}) &= (\mathbf{X} + \mathbf{V}) \left((\mathbf{X} + \mathbf{V})^T (\mathbf{X} + \mathbf{V}) \right)^{-\frac{1}{2}} \\ &= (\mathbf{X} + \mathbf{V}) (\mathbf{I}_q + \mathbf{V}^T \mathbf{V})^{-\frac{1}{2}}, \end{aligned} \quad (5.17)$$

where $(\cdot)^{-\frac{1}{2}}$ represents the inverse matrix square root. For both retraction operators, it readily seen that $R_{\mathbf{x}}(\mathbf{0}) = \mathbf{X}$. In this work, we employ the polar retraction.

5.2 Ambiguity Resolution Aided by the Float Solution

5.2.1 Decomposition of the Objective Function

As stated in Chapter 2, decomposing the objective function to a few more simple terms plays a crucial part in ambiguity resolution in the sense of defining the search space and simplifying the search process. However, the orthogonal decomposition (2.13) and (2.19) rely on an essential fact that the first-order and high-order (higher than two) derivatives of the objective function at the LS solution are zero [90]. There is no doubt that the orthogonal decomposition is not feasible at any other point except for the point where the gradient vanishes corresponding to the LS solution, prompting us to develop a decomposition method to use the float solution $\hat{\mathbf{R}}_{\text{RM}}$ and $\hat{\mathbf{N}}_{\text{RM}}$.

In order to utilize the high-quality float solution $\hat{\mathbf{R}}_{\text{RM}}$ and $\hat{\mathbf{N}}_{\text{RM}}$, we first consider decomposing (2.24) at an arbitrary point, as shown in Lemma 5.2.

Lemma 5.2. *For $\forall \bar{\mathbf{R}} \in \mathbb{R}^{3 \times q}$ and $\forall \bar{\mathbf{N}} \in \mathbb{R}^{S \times A}$, we can rewrite the objective function of (2.24) as a sum of five terms expressed by $\bar{\mathbf{R}}$ and $\bar{\mathbf{N}}$ as*

$$\begin{aligned}
& \|\text{vec}(\mathbf{Y} - \mathbf{A}\mathbf{R}\mathbf{X}_b - \mathbf{B}\mathbf{N})\|_{\mathbf{Q}_{\mathbf{Y}\mathbf{Y}}^{-1}}^2 \\
= & \|\text{vec}(\bar{\mathbf{E}})\|_{\mathbf{Q}_{\mathbf{Y}\mathbf{Y}}^{-1}}^2 + \|\text{vec}(\mathbf{N} - \bar{\mathbf{N}})\|_{\mathbf{Q}_{\hat{\mathbf{N}}_{AC}\hat{\mathbf{N}}_{AC}}^{-1}}^2 + \|\text{vec}(\mathbf{R} - \bar{\mathbf{R}}(\mathbf{N}))\|_{\mathbf{Q}_{\hat{\mathbf{R}}_{AC}(\mathbf{N})\hat{\mathbf{R}}_{AC}(\mathbf{N})}^{-1}}^2 \\
& + 2\text{vec}(\mathbf{N} - \bar{\mathbf{N}})^T \mathbf{Q}_{\hat{\mathbf{N}}_{AC}\hat{\mathbf{N}}_{AC}}^{-1} \text{vec}(\bar{\mathbf{N}} - \hat{\mathbf{N}}_{AC}) \\
& + 2\text{vec}(\mathbf{R} - \bar{\mathbf{R}}(\mathbf{N}))^T \mathbf{Q}_{\hat{\mathbf{R}}_{AC}(\mathbf{N})\hat{\mathbf{R}}_{AC}(\mathbf{N})}^{-1} \text{vec}(\bar{\mathbf{R}} - \hat{\mathbf{R}}_{AC}(\bar{\mathbf{N}}))
\end{aligned} \tag{5.18}$$

with $\bar{\mathbf{E}} = \mathbf{Y} - \mathbf{A}\bar{\mathbf{R}}\mathbf{X}_b - \mathbf{B}\bar{\mathbf{N}}$.

Proof. See Appendix B. □

Compared with (2.25), (5.18) contains five terms on the right-hand side, among which the first represents the squares norm of the residual corresponding to $\bar{\mathbf{R}}$ and $\bar{\mathbf{N}}$, the second measures the the distance from the integer matrix \mathbf{N} to $\bar{\mathbf{N}}$ in the metric of $\mathbf{Q}_{\hat{\mathbf{N}}_{AC}\hat{\mathbf{N}}_{AC}}^{-1}$, the third weighs the distance from the orthonormal matrix \mathbf{R} to $\bar{\mathbf{R}}(\mathbf{N})$ in the metric of $\mathbf{Q}_{\hat{\mathbf{R}}_{AC}(\mathbf{N})\hat{\mathbf{R}}_{AC}(\mathbf{N})}^{-1}$, and the last two terms are

related to distance from the selected points $\bar{\mathbf{R}}$ and $\bar{\mathbf{N}}$ to the LS solution $\hat{\mathbf{R}}_{AC}$ and $\hat{\mathbf{N}}_{AC}$. Note that the covariance matrixes of the LS solution are used in (5.18), and we can always compute these matrixes using a close form. If $\bar{\mathbf{R}} = \hat{\mathbf{R}}_{AC}$ and $\bar{\mathbf{N}} = \hat{\mathbf{N}}_{AC}$, the last two terms in (5.18) equal to zero, leading to the identical expression as (2.25).

Figure 5.1 shows a geometric illustration of the decomposition of the objective function. The essence of the optimization (2.24) is to seek for the solution that minimizes d^2 in Figure 5.1. Decomposing d^2 into a few easy-evaluated terms allows the full usage of the float solutions as an intermediate to simplify the search process. This figure depicts one of the most simple cases and indicates the difference between the two decomposition methods.

To simplify ambiguity resolution, we try to reformulate (5.18) as an alternative form that is easy to be bounded and evaluate.

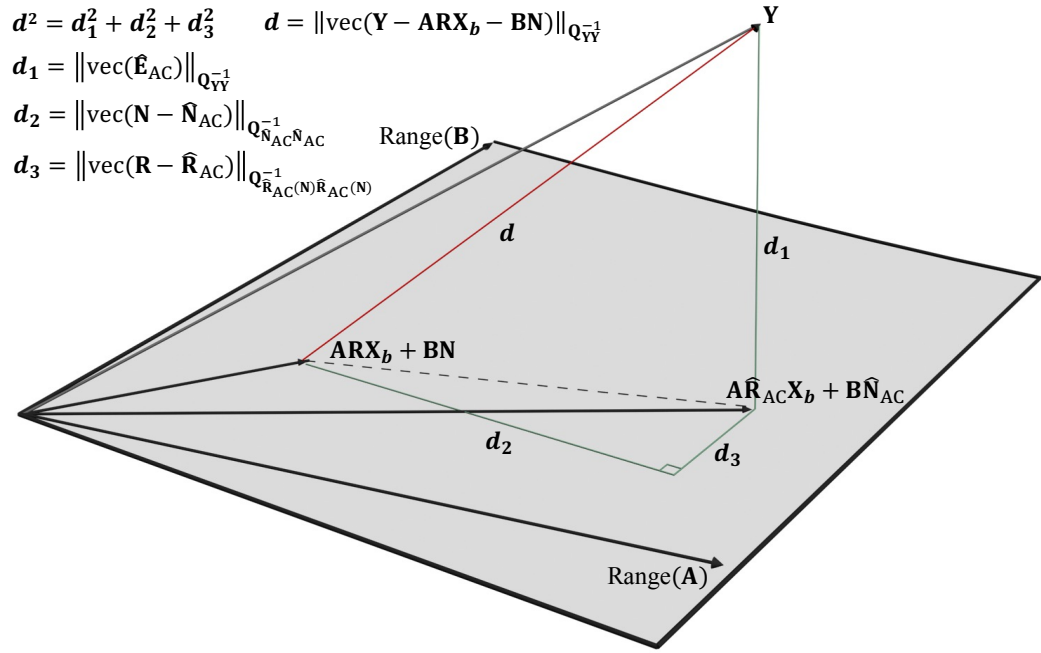
Lemma 5.3. *For $\forall \bar{\mathbf{R}} \in \mathbb{R}^{3 \times q}$ and $\forall \bar{\mathbf{N}} \in \mathbb{R}^{S \times A}$, the following relationship is an alternative form of (5.18)*

$$\begin{aligned} & \|\text{vec}(\mathbf{Y} - \mathbf{A}\mathbf{R}\mathbf{X}_b - \mathbf{B}\mathbf{N})\|_{\mathbf{Q}_{\mathbf{Y}\mathbf{Y}}^{-1}}^2 \\ = & \|\text{vec}(\bar{\mathbf{E}})\|_{\mathbf{Q}_{\mathbf{Y}\mathbf{Y}}^{-1}}^2 + \|\text{vec}(\mathbf{N} - \bar{\mathbf{N}})\|_{\mathbf{Q}_{\hat{\mathbf{N}}_{AC}\hat{\mathbf{N}}_{AC}}^{-1}}^2 + \left\| \text{vec}\left(\bar{\mathbf{R}} - \hat{\mathbf{R}}_{AC}(\mathbf{N})\right) \right\|_{\mathbf{Q}_{\hat{\mathbf{R}}_{AC}(\mathbf{N})\hat{\mathbf{R}}_{AC}(\mathbf{N})}^{-1}}^2 \\ & + 2\text{vec}(\mathbf{N} - \bar{\mathbf{N}})^T \mathbf{Q}_{\hat{\mathbf{N}}_{AC}\hat{\mathbf{N}}_{AC}}^{-1} \text{vec}(\bar{\mathbf{N}} - \hat{\mathbf{N}}_{AC}) - \left\| \text{vec}\left(\bar{\mathbf{R}} - \hat{\mathbf{R}}_{AC}(\bar{\mathbf{N}})\right) \right\|_{\mathbf{Q}_{\hat{\mathbf{R}}_{AC}(\bar{\mathbf{N}})\hat{\mathbf{R}}_{AC}(\bar{\mathbf{N}})}^{-1}}^2. \end{aligned} \quad (5.19)$$

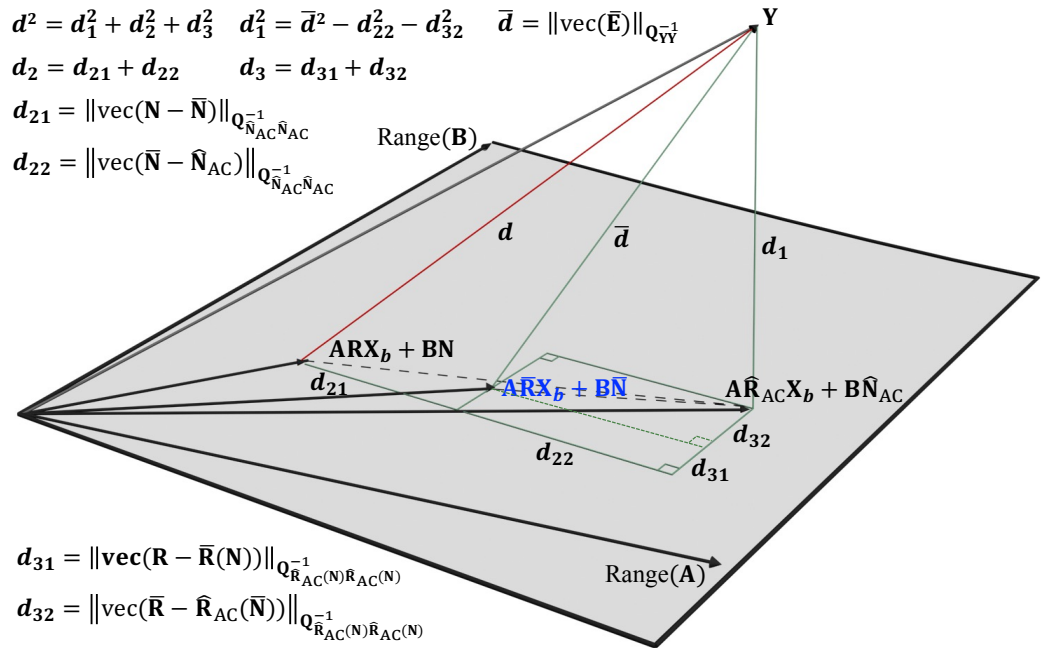
Proof. See Appendix C. □

Lemma 5.2 and Lemma 5.3 hold for an arbitrary point, so as to $\hat{\mathbf{R}}_{RM}$ and $\hat{\mathbf{N}}_{RM}$. If we replace $\bar{\mathbf{R}}$ and $\bar{\mathbf{N}}$ using $\hat{\mathbf{R}}_{RM}$ and $\hat{\mathbf{N}}_{RM}$, the first and last terms on the right-hand side of (5.19) are independent of the parameters. Then we achieve the equivalent form of (2.24) as follows

$$\min_{\mathbf{N} \in \mathbb{Z}^{S \times A}} \mathcal{C}(\mathbf{N}), \quad (5.20)$$



(a) Orthogonal decomposition [82]



(b) Proposed decomposition

Figure 5.1: Geometric illustration of the decomposition of the objective function.

with

$$\mathcal{C}(\mathbf{N}) = \left\| \text{vec}(\mathbf{N} - \hat{\mathbf{N}}_{\text{RM}}) \right\|_{\mathbf{Q}_{\hat{\mathbf{N}}_{\text{AC}} \hat{\mathbf{N}}_{\text{AC}}}}^{-1}{}^2 + 2 \text{vec}(\mathbf{N} - \hat{\mathbf{N}}_{\text{RM}})^{\text{T}} \mathbf{Q}_{\hat{\mathbf{N}}_{\text{AC}} \hat{\mathbf{N}}_{\text{AC}}}^{-1} \text{vec}(\hat{\mathbf{N}}_{\text{RM}} - \hat{\mathbf{N}}_{\text{AC}}) + \min_{\mathbf{R} \in \mathbb{O}^{3 \times q}} \left\| \text{vec}(\mathbf{R} - \hat{\mathbf{R}}_{\text{AC}}(\mathbf{N})) \right\|_{\mathbf{Q}_{\hat{\mathbf{R}}_{\text{AC}}(\mathbf{N})} \hat{\mathbf{R}}_{\text{AC}}(\mathbf{N})}}^{-1}{}^2. \quad (5.21)$$

The function $\mathcal{C}(\mathbf{N})$ includes three coupled terms.

If we ignore the last two terms in (5.21), we can define a loose-form solution of RieMOCAD (RieMOCAD-LF); that is, we calculate the closest integer estimations to the float solution $\hat{\mathbf{N}}_{\text{RM}}$ in the metric of the associated weight matrix

$$\min_{\mathbf{N} \in \mathbb{Z}^{S \times A}} \left\| \text{vec}(\mathbf{N} - \hat{\mathbf{N}}_{\text{RM}}) \right\|_{\mathbf{Q}_{\hat{\mathbf{N}}_{\text{AC}} \hat{\mathbf{N}}_{\text{AC}}}}^{-1}{}^2. \quad (5.22)$$

RieMOCAD-LF, (5.22), only partially employs the orthonormality constraint, which can be used as a low-complexity option in many practical applications. To fully incorporate this constraint, one needs to achieve the tight-form solution of RieMOCAD (RieMOCAD-TF), i.e., minimizing (5.20). Section 5.2.2 presents the details to solve the optimization problem (5.20). Note that (5.20) provides only one possible tight-form solution of the OC-AM, and (2.26) is another alternative. In this contribution, (5.20) is applied rather than (2.26) to accelerate the process of the integer ambiguity resolution.

5.2.2 Integer Search Strategy

To seek for the optimal integer matrix that minimizes (5.20), a search process is required and the search space is defined as

$$\Omega(\chi) = \{ \mathbf{N} \in \mathbb{Z}^{S \times A} \mid \mathcal{C}(\mathbf{N}) < \chi \}. \quad (5.23)$$

It requires high computational load to evaluate the integer matrix in $\Omega(\chi)$ due to the complex optimization caused by the presence of the orthonormality constraint. In other words, we need to evaluate every candidate in $\Omega(\chi)$ by solving the orthonormality-constrained optimization using the methods discussed in Sec-

tion 5.1.2. Similar to the MC-LAMBDA method, the cost function $\mathcal{C}(\mathbf{N})$ is also bounded by two easier-to-evaluate functions, which are formulated as

$$\begin{aligned}\mathcal{C}_L(\mathbf{N}) &= \left\| \text{vec}(\mathbf{N} - \hat{\mathbf{N}}_{\text{RM}}) \right\|_{\mathbf{Q}_{\hat{\mathbf{N}}_{\text{AC}} \hat{\mathbf{N}}_{\text{AC}}}^{-1}}^2 + 2 \text{vec}(\mathbf{N} - \hat{\mathbf{N}}_{\text{RM}})^T \mathbf{Q}_{\hat{\mathbf{N}}_{\text{AC}} \hat{\mathbf{N}}_{\text{AC}}}^{-1} \text{vec}(\hat{\mathbf{N}}_{\text{RM}} - \hat{\mathbf{N}}_{\text{AC}}) + \xi_{\min} \sum_{i=1}^q (\|\hat{\mathbf{r}}_i(\mathbf{N})\| - 1)^2, \\ \mathcal{C}_U(\mathbf{N}) &= \left\| \text{vec}(\mathbf{N} - \hat{\mathbf{N}}_{\text{RM}}) \right\|_{\mathbf{Q}_{\hat{\mathbf{N}}_{\text{AC}} \hat{\mathbf{N}}_{\text{AC}}}^{-1}}^2 + 2 \text{vec}(\mathbf{N} - \hat{\mathbf{N}}_{\text{RM}})^T \mathbf{Q}_{\hat{\mathbf{N}}_{\text{AC}} \hat{\mathbf{N}}_{\text{AC}}}^{-1} \text{vec}(\hat{\mathbf{N}}_{\text{RM}} - \hat{\mathbf{N}}_{\text{AC}}) + \xi_{\max} \sum_{i=1}^q (\|\hat{\mathbf{r}}_i(\mathbf{N})\| - 1)^2,\end{aligned}\tag{5.24}$$

with

$$\mathcal{C}_L(\mathbf{N}) \leq \mathcal{C}(\mathbf{N}) \leq \mathcal{C}_U(\mathbf{N})\tag{5.25}$$

where $\hat{\mathbf{r}}_i(\mathbf{N})$ is the i -th column of $\hat{\mathbf{R}}_{\text{AC}}(\mathbf{N})$, and ξ_{\min} and ξ_{\max} denote the smallest and largest eigenvalues of $\mathbf{Q}_{\hat{\mathbf{R}}_{\text{AC}}(\mathbf{N}) \hat{\mathbf{R}}_{\text{AC}}(\mathbf{N})}^{-1}$, respectively.

Based on the lower and upper bounds of $\mathcal{C}(\mathbf{N})$, we can define the corresponding search space as

$$\begin{aligned}\Omega_L(\chi) &= \{ \mathbf{N} \in \mathbb{Z}^{S \times A} \mid \mathcal{C}_L(\mathbf{N}) < \chi \}, \\ \Omega_U(\chi) &= \{ \mathbf{N} \in \mathbb{Z}^{S \times A} \mid \mathcal{C}_U(\mathbf{N}) < \chi \},\end{aligned}\tag{5.26}$$

with

$$\Omega_U(\chi) \subseteq \Omega(\chi) \subseteq \Omega_L(\chi).\tag{5.27}$$

Then, two search approaches, namely the search-and-shrink and search-and-expand strategies, can be applied to adjust the size of the search space adaptively so as to reduce the computational complexity significantly.

The search-and-shrink strategy takes advantage of the upper bound $\mathcal{C}_U(\mathbf{N})$ and the corresponding set $\Omega_U(\chi)$. Initially, a large $\chi_0 > 0$ is chosen to initialize χ such that $\Omega_U(\chi)$ and $\Omega(\chi)$ are nonempty. Find an integer matrix $\mathbf{N}_1 \in \Omega_U(\chi)$ with $\mathcal{C}_U(\mathbf{N}_1) = \chi_1 < \chi$. Then, shrink the search space by replacing $\chi = \chi_1$ and continue to look for an integer matrix $\mathbf{N}_2 \in \Omega_U(\chi)$ with $\mathcal{C}_U(\mathbf{N}_2) = \chi_2 < \chi$. Iterate the search procedures until there is only one integer matrix \mathbf{N}_k in the search space $\Omega_U(\chi)$ (assume k iterations and $\chi = \chi_k$). $\mathbf{N} = \mathbf{N}_k$ minimizes $\mathcal{C}_U(\mathbf{N})$ and $\chi = \mathcal{C}_U(\mathbf{N}_k)$. Note that $\mathbf{N} = \mathbf{N}_k$ does have to minimize $\mathcal{C}(\mathbf{N})$. Therefore, we need to evaluate $\Omega(\chi)$ using Riemannian optimization algorithms. Finally, we seek for

Algorithm 5.1 RieMOCAD using the search-and-shrink strategy.

- 1: Compute $\hat{\mathbf{R}}_{AC}$ and $\hat{\mathbf{N}}_{AC}$ based on (2.20).
 - 2: Solve (5.6) to obtain $\hat{\mathbf{R}}_{RM}$ using the Riemannian algorithms.
 - 3: Compute $\hat{\mathbf{N}}_{RM}$ using (5.5) and (5.7).
 - 4: Initialize $k = 0$ and $\chi = \chi_0 > 0$ such that $\Omega_U(\chi) \neq \emptyset$ and $\Omega(\chi) \neq \emptyset$.
 - 5: **while** $\text{card}\{\Omega_U(\chi)\} > 1$ **do**
 - 6: $k = k + 1$.
 - 7: Find $\mathbf{N}_k \in \Omega_U(\chi)$ with $\mathcal{C}_U(\mathbf{N}_k) = \chi_k < \chi$.
 - 8: $\chi = \chi_k$.
 - 9: Update $\Omega_U(\chi)$ based on (5.24) and (5.26).
 - 10: **end while**
 - 11: Establish $\Omega(\chi)$ using the Riemannian algorithms.
 - 12: Choose $\mathbf{N} \in \Omega(\chi)$ that minimizes $\mathcal{C}(\mathbf{N})$.
-

$\mathbf{N} \in \Omega(\chi)$ that minimizes $\mathcal{C}(\mathbf{N})$ as the estimation.

In contrast, the search-and-expand strategy utilizes the lower bound $\mathcal{C}_L(\mathbf{N})$ and the associated search space $\Omega_L(\chi)$. Initially, a small $\chi_0 > 0$ is chosen to initialize χ . If $\Omega_L(\chi)$ is empty, replace χ using a larger value χ_1 and check $\Omega_L(\chi)$ again. Iterate the search procedures (assume k steps) until $\Omega_L(\chi)$ with $\chi = \chi_k$ is nonempty. Then, evaluate all the candidates in $\Omega_L(\chi)$ using $\mathcal{C}(\mathbf{N})$, that is

$$\Omega(\chi) = \{\mathbf{N} \in \Omega_L(\chi) \mid \mathcal{C}(\mathbf{N}) < \chi\}. \quad (5.28)$$

If $\Omega(\chi)$ is nonempty, we extract $\mathbf{N} \in \Omega(\chi)$ that minimizes $\mathcal{C}(\mathbf{N})$ as the final estimation. Otherwise, let $\chi = \chi_{k+1} > \chi_k$, $k = k + 1$ and repeat the search procedures until $\Omega(\chi)$ is nonempty.

Algorithm 5.1 and Algorithm 5.2 summarize the RieMOCAD method (tight form) using the search-and-shrink and search-and-expand strategies, respectively. Compared with the existing methods, the major differences of the proposed approach are as follows. The RieMOCAD method requires the float solutions Least Squares and Riemannian optimization, whereas the MC-LAMBDA method requires only the Least Squares. The decomposition of the objective function is different between the RieMOCAD and MC-LAMBDA methods, leading to different cost functions used in the feasible set. Instead of solving the orthonormality-constrained least-squares problem through the gradient descent techniques, the

Algorithm 5.2 RieMOCAD using the search-and-expand strategy.

- 1: Compute $\hat{\mathbf{R}}_{AC}$ and $\hat{\mathbf{N}}_{AC}$ based on (2.20).
 - 2: Solve (5.6) to obtain $\hat{\mathbf{R}}_{RM}$ using the Riemannian algorithms.
 - 3: Compute $\hat{\mathbf{N}}_{RM}$ using (5.5) and (5.7).
 - 4: Initialize $\chi = \chi_0 > 0$ and $k = 0$.
 - 5: Let $\Omega(\chi) = \emptyset$.
 - 6: **while** $\Omega(\chi) = \emptyset$ **do**
 - 7: Set $\Omega_L(\chi)$ based on (5.24) and (5.26).
 - 8: **for all** $\mathbf{N} \in \Omega_L(\chi)$ **do**
 - 9: Calculate $\mathcal{C}(\mathbf{N})$ using the Riemannian algorithms.
 - 10: **if** $\mathcal{C}(\mathbf{N}) < \chi$ **then**
 - 11: $\Omega(\chi) = \Omega(\chi) \cup \mathbf{N}$.
 - 12: **end if**
 - 13: **end for**
 - 14: **if** $\Omega(\chi) = \emptyset$ **then**
 - 15: $\chi = \chi_{k+1} > \chi_k$.
 - 16: $k = k + 1$.
 - 17: **end if**
 - 18: **end while**
 - 19: Choose $\mathbf{N} \in \Omega(\chi)$ that minimizes $\mathcal{C}(\mathbf{N})$.
-

RieMOCAD method employs the optimization over the Riemannian manifold in the search process.

5.3 Performance Evaluation

This section tests the proposed RieMOCAD method and compares it with several benchmarks using simulations as well as experimental data. For different scenarios, we analyze performance in terms of the quality of the float solution, success rate, and computational efficiency in the single-epoch and single-frequency case, with only GPS satellites utilized. Riemannian optimization algorithms are implemented based on the Manopt toolbox [109]

5.3.1 Simulation Analysis

Simulated data is used to test different methods under error-controlled conditions. The simulations are implemented using the assumed platform's attitude and the actual satellite orbit information in the GPS Yuma Almanacs file on November 7, 2021. Several scenarios are simulated with a different number of tracked satellites,

a different number of antennas, and various measurement noises. The number of satellites is varied from four to eight, i.e., from the satellite-deprived situations to satellite-sufficient environments, by randomly choosing the satellites from the visible ones. The noise level is controlled by adding a zero-mean Gaussian noise with a specified standard deviation to the undifferenced GNSS observations. We assume that the noise of pseudo-range data is two orders of magnitude higher than that of the carrier phase, that is, $\sigma_P = 100\sigma_\psi$. For each simulated scenario, a set of 10^4 data is generated, with a random rotation and random antenna positions in the body frame in each trial. We let the baseline length be 1 meter and guarantee the antenna position matrix to be full row rank.

Comparison of Different Optimization Techniques in Estimating \mathbf{R}

Note that in addition to Riemannian optimization, (5.6) can be solved using a plethora of methods such as the solutions based on the Lagrange multipliers and parameterization [102, 101]. Before studying the constrained float solution's impact on ambiguity resolution, we first compare the Riemannian algorithm with the Lagrange multipliers method and a nonlinear estimation of a quaternion. The orthonormal matrix form and its quaternion parameterization are used to formulate the problem, with the nonlinear constraints incorporated by the Lagrange multiplier. Newton's method is applied to solve the Lagrange functions. For more details on these methods, the readers are referred to [102]. The comparison is performed in terms of the estimation accuracy of the orthonormal matrix, algorithm convergence characteristics, and computational complexity based on simulated data ($\hat{\mathbf{R}}_{AC}$ and $\mathbf{Q}_{\hat{\mathbf{R}}_{AC}\hat{\mathbf{R}}_{AC}}$).

The estimation accuracy of different methods is evaluated using the root-mean-square error (RMSE) to measure the average accuracy of estimating the

Table 5.1: RMSE of Different Estimators of \mathbf{R} Versus Observation Noise (#Sat = 6, #BL = 3 and L = 1 m).

| σ_{Ψ} (mm) \n Methods | 1 | 2 | 3 | 4 |
|---------------------------------|-------|-------|-------|-------|
| Unconstrained Least Squares | 0.076 | 0.441 | 0.743 | 1.006 |
| Lagrange Multiplier | 0.017 | 0.179 | 0.355 | 0.458 |
| Quaternion | 0.047 | 0.293 | 0.465 | 0.523 |
| Riemannian Optimization | 0.017 | 0.153 | 0.321 | 0.415 |

Table 5.2: Probability of Convergence to a Solution in The Constraints Set for Different Methods With Various Observation Noise (#Sat = 6, #BL = 3 and L = 1 m).

| σ_{Ψ} (mm) \ Methods | 1 | 2 | 3 | 4 |
|--------------------------------|------|-------|-------|-------|
| Lagrange Multiplier | 1.00 | 0.998 | 0.971 | 0.964 |
| Quaternion | 1.00 | 0.987 | 0.911 | 0.841 |
| Riemannian Optimization | 1.00 | 1.00 | 1.00 | 1.00 |

Table 5.3: Number of Operations for Different Methods.

| Method | Number of Operations |
|-------------------------|---|
| Lagrange Multiplier | $\frac{L_l}{6} (4K_l^3 + 21K_l^2 - 7K_l)$ |
| Quaternion | $\frac{L_q}{6} (4K_q^3 + 15K_q^2 + 17K_q + 12K_r^2 + 12K_q^2 K_r - 24K_q K_r + 18K_r - 24)$ |
| Riemannian Optimization | $L_r \left[\frac{14}{81} K_r^3 + \frac{71}{9} K_r^2 + \frac{22}{9} K_r + 12L_{\alpha} (K_r^2 + K_r) - 2 \right]$ |

Table 5.4: Computational Complexity Parameters for Different Methods Based on Simulations.

| Parameter | L_l | L_q | L_r | L_{α} |
|---------------|-------|-------|-------|--------------|
| Average Value | 19.91 | 62.25 | 7.39 | 2.07 |

Table 5.5: Total Number of Operations for Different Methods Based on Simulations.

| Method | Number of Operations |
|-------------------------|----------------------|
| Lagrange Multiplier | 60128.20 |
| Quaternion | 38283.75 |
| Riemannian Optimization | 22322.23 |

elements of the unknown matrix \mathbf{R} . We define this RMSE as follows:

$$\text{RMSE}(\hat{\mathbf{X}}) = \sqrt{\frac{\sum_{i=1}^T \left\| \text{vec}(\hat{\mathbf{X}}_i - \mathbf{X}_i) \right\|_2^2 / (mn)}{T}},$$

where $\hat{\mathbf{X}}_i \in \mathbb{R}^{m \times m}$ denotes the matrix estimate from the i -th epoch, \mathbf{X}_i represents the ground truth, and T is the total number of epochs.

Table 5.1 presents the RMSE values of estimations of \mathbf{R} for the Riemannian optimization, Lagrange multipliers, and the quaternion methods. For reference, we also include the unconstrained least squares method. The results in Table 5.1 demonstrate that the constrained estimators offer smaller RMSEs than the unconstrained least squares. Riemannian optimization clearly outperforms the other two constrained optimization methods. Riemannian algorithms execute the iterates on the manifold such that the solutions always satisfy all the constraints. Although the Lagrange multipliers method is used to incorporate the nonlinear constraints (the orthonormality constraint or unit norm constraint for a quaternion), it is not guaranteed to converge to a solution in the constraints set. Hence, it occasionally produces substandard results.

To investigate how various constrained optimization methods fare when it comes to satisfying the constraints, Table 5.2 evaluates the probability of each method converging to a solution in the constraints set. These probability values are estimated using the same setup of Table 5.1. From Table 5.2, we can infer that the Riemannian optimization algorithm always converges to a solution in the constraints set. The same cannot be said about the two other constrained optimization methods, as they occasionally produce results that are inconsistent with the constraints. This kind of divergence (from the constraints set) might result in severe estimation errors, which explains the results in Table 5.1. Therefore, it can be said that the inherent ability of Riemannian optimization to consistently and systematically converge to solutions in the desired constraints set presents a significant advantage compared with the other two methods.

To evaluate the computational complexity, the number of computations for different methods is summarized in Table 5.3. The symbols L_l , L_q and L_r denote the number of iterations required to reach a pre-defined precision level for the Lagrange Multiplier, quaternion, and Riemannian optimization methods, respectively. The symbol K_l is the number of unknown parameters for the Lagrange multiplier method, which is the number of elements of the orthonormal matrix and the number of Lagrange multipliers. Since $\mathbf{R} \in \mathbb{O}^{3 \times q}$, $K_l = 3q + q(q + 1)/2$. The parameter K_q represents to the number of elements of a quaternion plus one Lagrange multiplier, that is, $K_q = 5$. The parameter K_r is equal to the number of elements of the orthonormal matrix, i.e., $K_r = 3q$. The symbol L_α denotes the number of iterations required to find the search direction in the tangent space. Table 5.4 shows the average values of L_l , L_q , L_r and L_α to solve (5.6) based on simulated data generated using three baselines with random length (0 to 3 m), random observation noise (0 to 7 mm), and random number of satellites (4 to 8). Subsequently, we obtain the total number of operations for the Lagrange Multiplier, quaternion, and Riemannian optimization methods as presented in Table 5.5. According to Table 5.5, re-parameterizing the orthonormal matrix with a quaternion estimation reduces computational complexity significantly. However, Riemannian optimization reduces the computational complexity even more.

Attitude Determination Performance Evaluation

Firstly, we will study the quality of various float ambiguity solutions, i.e., $\hat{\mathbf{N}}_{\text{UC}}$, $\hat{\mathbf{N}}_{\text{AC}}$ and $\hat{\mathbf{N}}_{\text{RM}}$ obtained by (2.14), (2.20), and (5.1), respectively. We characterize the quality of the float solution in terms of two metrics. The first metric is the root-mean-square error (RMSE) that captures the differences between the float ambiguity solutions and the ground truth integer ambiguities. The second metric is defined as the success rate of the optimal integers of (2.16), (2.22), and (5.22), which gives us an idea about how good the closest integer estimations to different float solutions in the metric of the associated weight matrix.

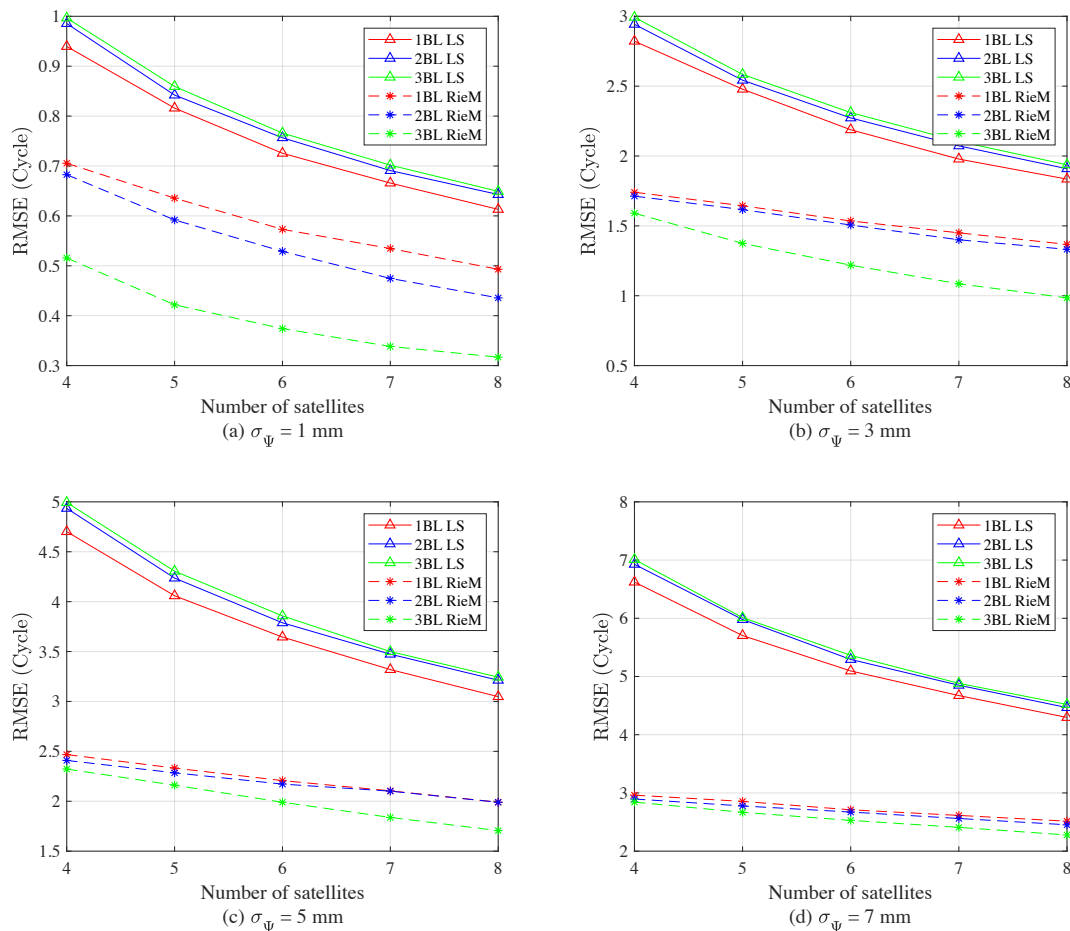


Figure 5.2: RMSE of float ambiguity estimations (a single baseline to three baselines).

Figure 5.2 and Figure 5.3 demonstrate the RMSE of the float ambiguities in various simulated environments. When the number of baselines (BL) is less or equal to the dimension of the range of the baseline matrix, the UC-AM and AC-AM have exactly the same float solution, that is, $\hat{\mathbf{N}}_{\text{UC}} = \hat{\mathbf{N}}_{\text{AC}}$, resulting in the same fixed integer solutions of (2.16) and (2.22). Hence, Figure 5.2 shows only the LS solutions and Riemannian-manifold-based (RieM) solutions. According to Figure 5.2, the more baselines we use, the larger the error of the LS estimation. On the contrary, the RieM-based errors decrease as the number of baselines increases. The reason why multi-baseline configuration improves the RieM-based float solution is that the set-up benefits from more antenna-array geometry information.

As shown in Figure 5.3, when the number of baselines is greater than the

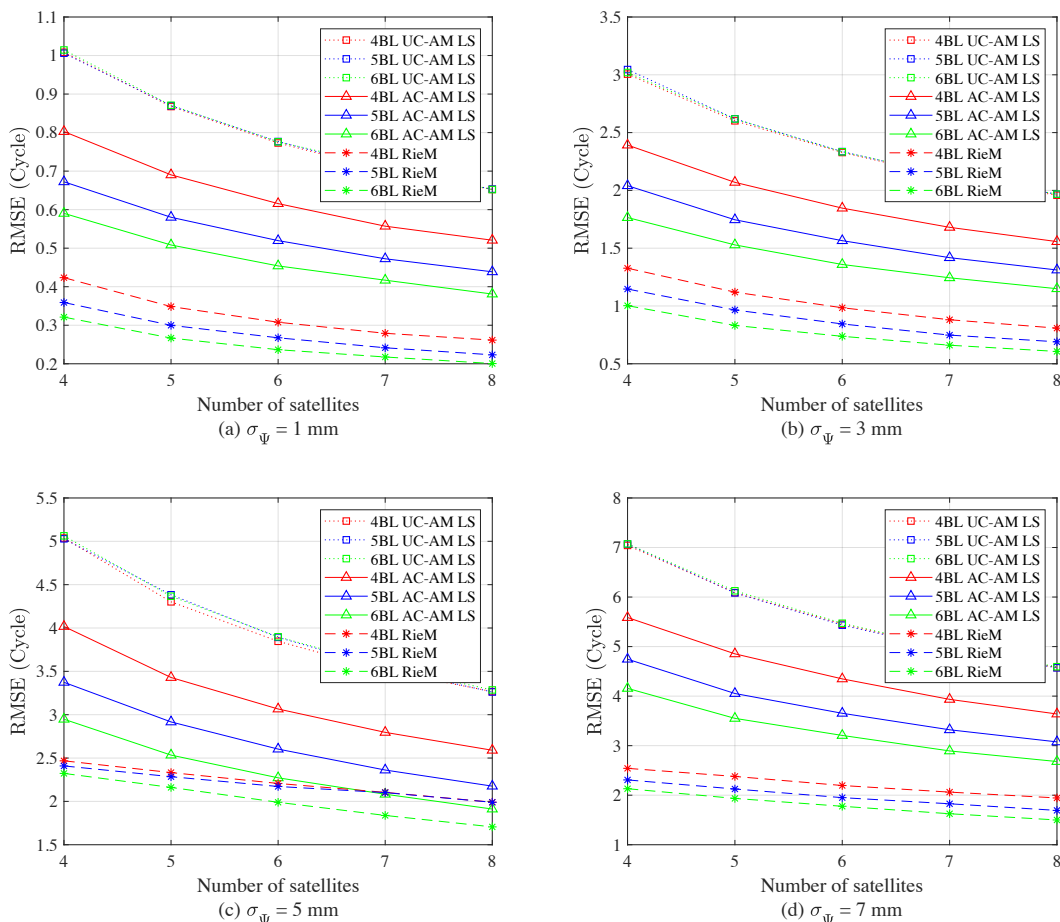


Figure 5.3: RMSE of float ambiguity estimations (four baselines to six baselines).

dimension of the range of the baseline matrix, the quality of the float solutions for the UC-AM tends to converge to a stable level. However, the AC-AM demonstrates its advantage compared with the UC-AM since the affine transformation (linear constraint) can take advantage of the redundancy of the GNSS data. To elaborate, we can analyze each model's number of observations and unknowns. For the UC-AM, there are $2\mathcal{A}\mathcal{S}$ observations and $\mathcal{A}\mathcal{S} + 3\mathcal{A}$ unknown parameters. The AC-AM involves the same measurements as the UC-AM, with only $\mathcal{A}\mathcal{S} + 9$ unknowns ($9 < 3\mathcal{A}$). The RieMOCAD-LF has the same number of observables and unknowns as the AC-AM. However, the additional nonlinear constraint explains why the RieMOCAD-LF outperforms the other two benchmarks. Unlike the UC-AM, the performance of the AC-AM and RieMOCAD-LF improves as the number of baselines rises.

Table 5.6: Success rate (%) for different measurement precision σ_Ψ (mm), number of tracked satellites (#Sat), and number of baselines.

UC-AM/AC-AM

RieMOCAD-LF

| #Sat | σ_Ψ | Single Baseline | | | | Two Baselines | | | | Three Baselines | | | |
|------|---------------|-----------------|--------------|--------------|--------------|---------------|--------------|--------------|--------------|-----------------|--------------|--------------|--------------|
| | | 7 | 5 | 3 | 1 | 7 | 5 | 3 | 1 | 7 | 5 | 3 | 1 |
| 4 | | 0.01 | 0.06 | 0.30 | 6.84 | 0 | 0 | 0 | 0.75 | 0 | 0 | 0 | 0.11 |
| | | 2.74 | 3.76 | 6.00 | 22.53 | 0.35 | 0.45 | 1.14 | 11.63 | 0.06 | 0.16 | 0.92 | 18.07 |
| 5 | | 0.19 | 0.54 | 3.29 | 61.60 | 0 | 0 | 0.18 | 48.85 | 0 | 0 | 0.02 | 40.66 |
| | | 2.94 | 5.20 | 13.26 | 73.74 | 0.22 | 0.75 | 3.84 | 68.75 | 0.19 | 0.20 | 3.11 | 76.01 |
| 6 | | 0.83 | 3.90 | 25.07 | 99.11 | 0 | 0.24 | 9.83 | 99.19 | 0 | 0.02 | 4.45 | 99.50 |
| | | 5.73 | 13.75 | 43.48 | 99.35 | 0.67 | 3.95 | 29.25 | 99.54 | 0.26 | 2.38 | 29.92 | 99.96 |
| 7 | | 4.13 | 16.70 | 68.34 | 99.98 | 0.38 | 5.38 | 60.07 | 99.99 | 0.04 | 1.74 | 56.75 | 100 |
| | | 13.47 | 33.43 | 79.78 | 99.98 | 3.76 | 18.67 | 76.64 | 99.99 | 1.85 | 14.77 | 81.03 | 100 |
| 8 | | 13.41 | 46.71 | 94.62 | 100 | 3.90 | 33.86 | 94.51 | 100 | 1.35 | 26.85 | 94.84 | 100 |
| | | 29.06 | 63.78 | 96.75 | 100 | 16.29 | 57.14 | 97.14 | 100 | 11.60 | 56.91 | 98.03 | 100 |

Table 5.7: Success rate (%) for different measurement precision σ_Ψ (mm), number of tracked satellites (#Sat), and number of baselines.

UC-AM

AC-AM

RieMOCAD-LF

| #Sat | σ_Ψ | Four Baselines | | | | Five Baselines | | | | Six Baselines | | | |
|------|---------------|----------------|--------------|--------------|--------------|----------------|--------------|--------------|--------------|---------------|--------------|--------------|--------------|
| | | 7 | 5 | 3 | 1 | 7 | 5 | 3 | 1 | 7 | 5 | 3 | 1 |
| 4 | | 0 | 0 | 0 | 0.01 | 0 | 0 | 0 | 0.01 | 0 | 0 | 0 | 0 |
| | | 0 | 0 | 0.03 | 40.78 | 0 | 0.02 | 4.10 | 96.48 | 0.03 | 1.68 | 54.60 | 99.89 |
| | | 0.03 | 0.17 | 2.82 | 75.91 | 0.13 | 1.64 | 23.67 | 98.41 | 1.38 | 13.40 | 73.47 | 99.89 |
| 5 | | 0 | 0 | 0 | 35.26 | 0 | 0 | 0 | 30.96 | 0 | 0 | 0 | 27.91 |
| | | 0 | 0.13 | 13.33 | 96.44 | 0.56 | 14.42 | 81.12 | 99.97 | 15.34 | 74.92 | 97.59 | 100 |
| | | 0.33 | 3.54 | 38.26 | 98.72 | 6.02 | 37.51 | 88.72 | 99.99 | 37.71 | 83.80 | 98.71 | 100 |
| 6 | | 0 | 0.02 | 1.98 | 99.47 | 0 | 0 | 1.19 | 99.59 | 0 | 0 | 0.73 | 99.62 |
| | | 0.72 | 16.78 | 88.09 | 100 | 31.20 | 91.65 | 99.70 | 100 | 91.70 | 99.54 | 99.99 | 100 |
| | | 7.22 | 42.51 | 93.96 | 100 | 57.96 | 95.46 | 99.82 | 100 | 95.28 | 99.63 | 99.99 | 100 |
| 7 | | 0 | 0.78 | 51.69 | 100 | 0 | 0.38 | 49.41 | 100 | 0 | 0.14 | 46.86 | 100 |
| | | 17.78 | 80.22 | 99.12 | 100 | 91.81 | 99.28 | 100 | 100 | 99.72 | 99.96 | 100 | 100 |
| | | 43.27 | 89.35 | 99.69 | 100 | 96.08 | 99.61 | 100 | 100 | 99.79 | 99.96 | 100 | 100 |
| 8 | | 0.56 | 23.75 | 94.35 | 100 | 0.29 | 20.29 | 94.32 | 100 | 0.09 | 17.24 | 94.11 | 100 |
| | | 73.20 | 97.80 | 99.99 | 100 | 99.55 | 99.99 | 100 | 100 | 99.98 | 100 | 100 | 100 |
| | | 86.13 | 98.84 | 100 | 100 | 99.69 | 99.99 | 100 | 100 | 99.99 | 100 | 100 | 100 |

Table 5.8: Success rate (%) for different measurement precision σ_Ψ (mm), number of tracked satellites (#Sat), and number of baselines.

MC-LAMBDA
RieMOCAD-TF

| #Sat | σ_Ψ | Single Baseline | | | | Two Baselines | | | | Three Baselines | | | |
|------|---------------|-----------------|--------------|--------------|--------------|---------------|--------------|--------------|--------------|-----------------|--------------|--------------|--------------|
| | | 7 | 5 | 3 | 1 | 7 | 5 | 3 | 1 | 7 | 5 | 3 | 1 |
| 4 | | 8.39 | 14.46 | 28.00 | 81.18 | 0 | 0 | 4.45 | 97.91 | 0 | 0 | 0.12 | 50.43 |
| | | 10.19 | 14.82 | 28.01 | 81.18 | 6.39 | 12.88 | 39.32 | 98.39 | 2.25 | 6.88 | 16.55 | 92.22 |
| 5 | | 21.80 | 37.74 | 70.79 | 99.20 | 1.76 | 11.78 | 79.99 | 100 | 0 | 0.29 | 20.11 | 100 |
| | | 21.91 | 37.77 | 70.81 | 99.19 | 20.90 | 44.89 | 92.21 | 100 | 3.99 | 15.38 | 67.75 | 100 |
| 6 | | 46.54 | 71.67 | 95.41 | 99.98 | 18.44 | 71.96 | 99.85 | 100 | 0.88 | 16.79 | 97.36 | 100 |
| | | 46.55 | 71.67 | 95.42 | 99.98 | 55.56 | 91.77 | 99.85 | 100 | 17.99 | 61.80 | 99.09 | 100 |
| 7 | | 72.80 | 92.10 | 99.42 | 100 | 66.12 | 98.72 | 100 | 100 | 16.55 | 84.63 | 100 | 100 |
| | | 72.80 | 92.10 | 99.42 | 100 | 89.55 | 99.11 | 100 | 100 | 56.31 | 97.01 | 100 | 100 |
| 8 | | 88.19 | 98.00 | 99.92 | 100 | 96.37 | 100 | 100 | 100 | 73.26 | 100 | 100 | 100 |
| | | 88.19 | 98.00 | 99.92 | 100 | 99.23 | 100 | 100 | 100 | 93.11 | 100 | 100 | 100 |

Table 5.6 and Table 5.7 list the success rate of the UC-AM, AC-AM and RieMOCAD-LF, that is, the optimums of (2.16), (2.22), and (5.22). The success rate of the UC-AM continuously decreases as the number of baselines increases caused by the low-quality float solution coupled with the growth of dimension of the integer space. Generally, the AC-AM and RieMOCAD-LF tend to achieve a higher success rate when more baselines are considered since the improved float solutions are offered. However, the performance in some setups may not follow the trend. It depends on which factor, the quality of the float solution, or the dimension of the integer space, dominates the results. As shown in Table 5.7, the AC-AM and RieMOCAD-LF can offer acceptable results in many scenarios (except for the extreme ones, where the tight-form solutions of the OC-AM are required) when using a large number of baselines. Figure 5.2, Figure 5.3, Table 5.6 and Table 5.7 indicate the significant improvement of the RieM-based float solution compared with the LS solution.

According to Table 5.6 and Table 5.7, the estimations of the UC-AM, AC-AM, and RieMOCAD-LF are not up to par in many challenging environments, especially when the number of baselines is less than the dimension of the range space of baseline matrix. Therefore, the robust model OC-AM is required to improve the results. Both (2.26) and (5.20) are just two alternative forms of the

Table 5.9: Number of integers in the search space for different measurement precision σ_Ψ (mm), number of tracked satellites (#Sat), and number of baselines.

MC-LAMBDA
RieMOCAD-TF

| σ_Ψ \#Sat | Single Baseline | | | | Two Baselines | | | | Three Baselines | | | |
|---------------------|-----------------|---------------|---------------|--------------|----------------|----------------|----------------|----------------|-----------------|----------------|----------------|----------------|
| | 7 | 5 | 3 | 1 | 7 | 5 | 3 | 1 | 7 | 5 | 3 | 1 |
| 4 | 4268.66 | 2164.82 | 595.79 | 39.13 | 10000 | 9992.12 | 9990.35 | 3097.07 | 10000 | 10000 | 10000 | 9640.19 |
| | 420.28 | 277.91 | 140.19 | 23.37 | 9960.78 | 9914.55 | 9776.32 | 1607.71 | 10000 | 10000 | 10000 | 7163.28 |
| 5 | 1403.85 | 498.66 | 97.43 | 3.75 | 9987.01 | 9865.44 | 6726.23 | 12.09 | 10000 | 10000 | 9977.65 | 52.43 |
| | 253.20 | 149.77 | 51.17 | 3.08 | 9873.52 | 9285.21 | 4614.93 | 7.22 | 10000 | 9998.11 | 9314.99 | 30.11 |
| 6 | 496.25 | 137.22 | 17.29 | 2.03 | 9761.09 | 7260.33 | 415.42 | 2.04 | 10000 | 9915.11 | 3838.67 | 2.07 |
| | 153.19 | 64.16 | 10.98 | 2.00 | 8892.29 | 4888.82 | 187.58 | 2.00 | 9971.03 | 9098.00 | 1391.81 | 2.01 |
| 7 | 177.78 | 32.46 | 3.53 | 2.00 | 7238.69 | 1414.66 | 10.01 | 2.00 | 9914.09 | 6567.13 | 34.27 | 2.00 |
| | 74.23 | 18.09 | 2.85 | 2.00 | 5321.99 | 692.21 | 5.90 | 2.00 | 9158.31 | 3335.94 | 12.12 | 2.00 |
| 8 | 58.86 | 7.91 | 2.20 | 2.00 | 2679.34 | 82.03 | 2.31 | 2.00 | 7650.06 | 469.38 | 2.74 | 2.00 |
| | 30.22 | 5.60 | 2.01 | 2.00 | 1338.81 | 32.24 | 2.07 | 2.00 | 4607.26 | 116.35 | 2.45 | 2.00 |

optimization (2.24). Therefore, if the search space is large enough, (2.24), (2.26) and (5.20) should achieve identical optima.

This work aims to speed up the search using the proposed intermediate solution to shrink the search space required. To avoid an enormous search space caused by the adaptive adjustment procedures discussed in Section 5.2.2, we set up 10^4 integer candidates as the limit to evaluate. Table 5.8 demonstrates the success rate for the MC-LAMBDA method and RieMOCAD-TF, i.e., (2.26) and (5.20), under different simulated environments. Table 5.9 summarizes the corresponding number of integer candidates that need to evaluate. In a single-baseline configuration, RieMOCAD-TF and the MC-LAMBDA method have a comparable success rate, except for the extremely challenging set-up with $\sigma_\Psi = 7$ mm, $\sigma_P = 70$ cm and 4 satellites, where RieMOCAD-TF offers a better success-rate performance. However, the required search space of RieMOCAD-TF is smaller than that of the MC-LAMBDA method, indicating an improvement in computational efficiency. In dual- or triple-baseline cases, it is more difficult to resolve the integer ambiguities due to the high dimensionality of the integer space. In such situations, the advantages of the proposed approach become more notable. As stated above, the different success rate derives from the limit of the size of the search space, which also verifies the low complexity of RieMOCAD-TF. In summary, integrating Riemannian algorithms into the process of ambiguity res-

olution can shrink the search space in the integer domain at the expense of just an additional nonlinear optimization.

5.3.2 Experimental Evaluation

In addition to the simulations, we evaluate the proposed method’s performance using experimental data and compare it with other benchmarks. To estimate the ground truth precisely, we carried out two static experiments using three ANAVS multi-sensor modules. The receivers were arranged in an equilateral triangle with a 0.63-meter side, as shown in Figure 5.4. The receivers were firmly mounted on the platform, which remained stationary at positions (N22°18'34", E39°6'16") and (N22°18'32", E39°6'27") during the two experiments, respectively. These receivers can collect GNSS data at a 5 Hz sampling rate. The first experiment was performed from 18:35 to 19:03 (UTC) on 6 April 2021, with 8500 epochs of GNSS data collected. The other experiment was carried out from 20:34 to 21:50 (UTC) on 25 May 2021 to acquire 25500 epochs of GNSS measurements. The satellite visibility during the tests is shown in Figure 5.5, with a 10-degree cut-off angle. We estimate the ground truth by using the data of the entire test period and fusing data from multiple sensors, including GNSS observations (GPS+GLONASS) and data from an inertial measurement unit (IMU).

Table 5.10 shows the success rate of ambiguity resolution for both experiments. The estimations in the second experiment are much better since we fixed the platform at a place with good satellite visibility. The location of the first experiment was surrounded by obstacles, such as trees and buildings. We can also see that the AC-AM (the same as UC-AM) shows a poor success rate. As expected, RieMOCAD-LF offers a higher success rate compared to the AC-AM. The two tight-form implementations of the OC-AM, i.e., the MC-LAMBDA method and RieMOCAD-TF, beat other techniques in ambiguity resolution success rate, with RieMOCAD-TF performing the best. As aforesaid, the constrained search space in the integer domain decides the difference in ambiguity resolution perfor-

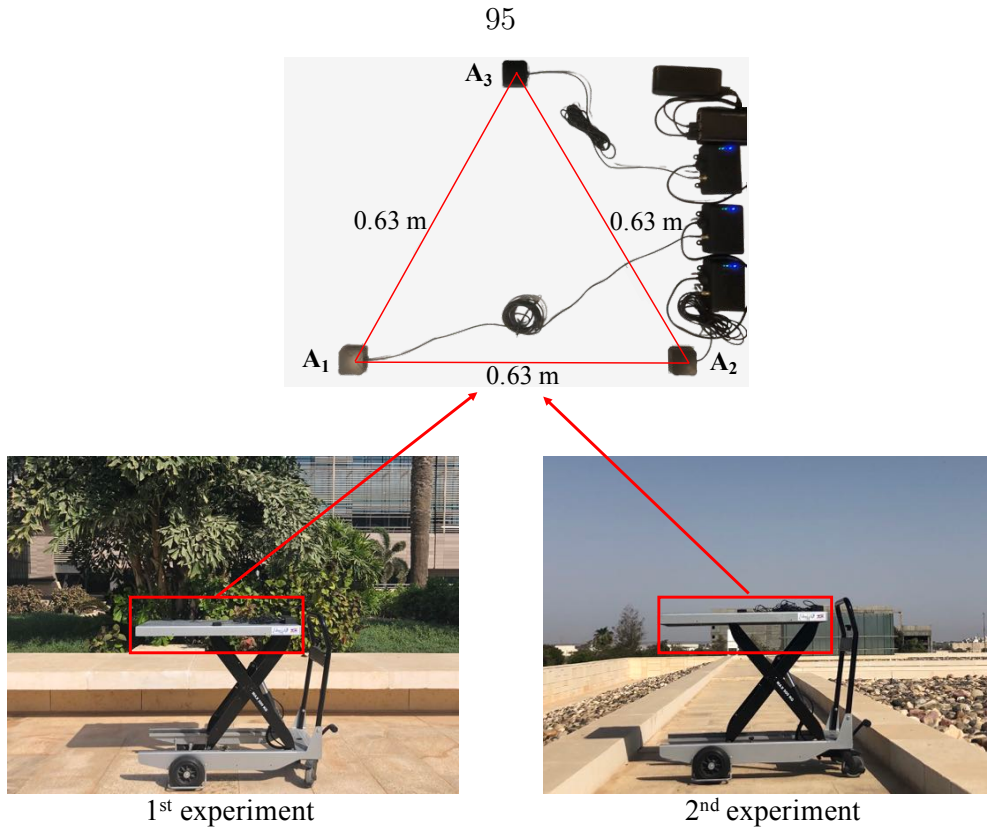


Figure 5.4: GNSS antenna set-up.

Table 5.10: Success rate (%) based on experimental data.

| | 1st experiment | 2nd experiment |
|-------------|----------------|----------------|
| UC-AM/AC-AM | 0.01 | 50.06 |
| RieMOCAD-LF | 5.83 | 86.81 |
| MC-LAMBDA | 6.75 | 99.28 |
| RieMOCAD-TF | 72.07 | 99.33 |

mance between RieMOCAD-TF and the MC-LAMBDA method. The size of the search space, i.e., the number of integer candidates as summarized in Table 5.11, reveals the low complexity of RieMOCAD-TF.

Figure 5.6 and Figure 5.7 show the cumulative errors of the attitude angles (Euler angles). Consistent with the success-rate performance described above, RieMOCAD-LF outperforms the AC-AM. On the other hand, RieMOCAD-TF outperforms the corresponding benchmark, the MC-LAMBDA method. The success rate, size of the search space, and the angle error distribution prove the reliability and feasibility of the proposed method.

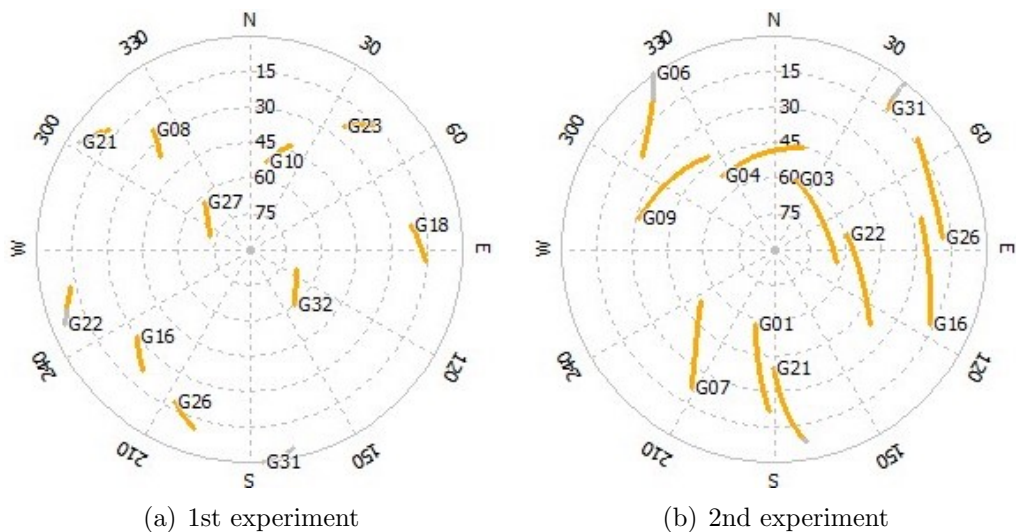


Figure 5.5: Satellite visibility during the tests.

Table 5.11: Number of integers in the search space.

| | 1st experiment | 2nd experiment |
|-------------|----------------|----------------|
| MC-LAMBDA | 9891.17 | 1118.65 |
| RieMOCAD-TF | 8649.51 | 795.02 |

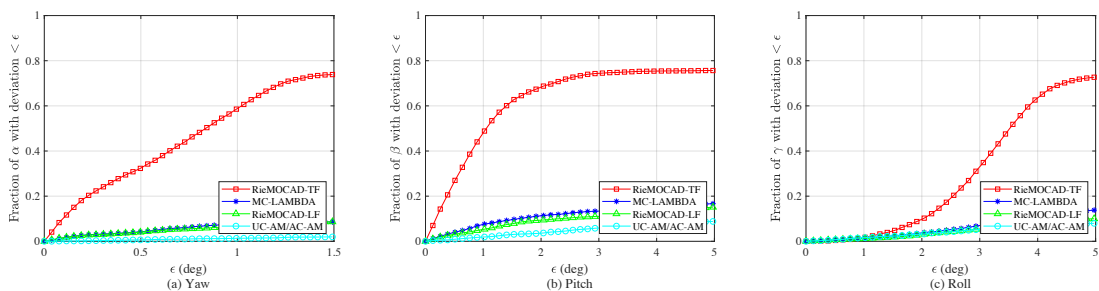


Figure 5.6: Euler angle error distribution for the first experiment.

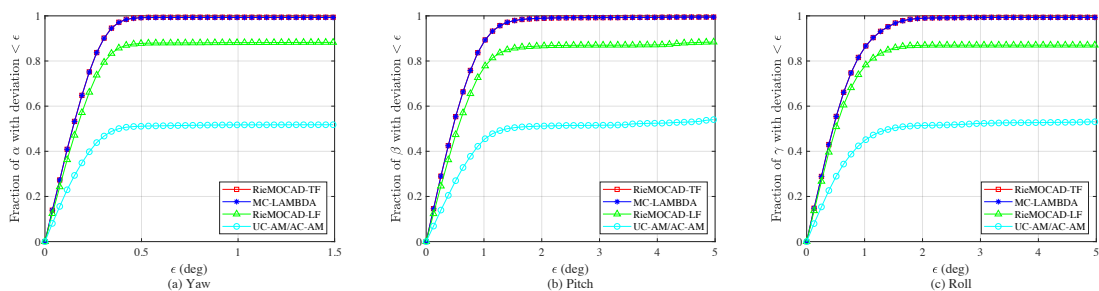


Figure 5.7: Euler angle error distribution for the second experiment.

5.4 Chapter Summary

We proposed an ambiguity resolution method for GNSS attitude determination. By modeling the GNSS attitude problem as an optimization on the Stiefel manifold, we alleviate the difficulties to resolve the unknown carrier-phase ambiguities. First, to replace the widely used least-squares solution, we calculate a high-quality float solution using Riemannian manifold optimization as an improved starting point for the integer search process. To take advantage of the improved intermediate solution, we propose decomposing the objective function at an arbitrary point instead of the widely used orthogonal decomposition. By leveraging Riemannian optimization, the improved float solution, and the proposed decomposition, we are able to search for the carrier-phase ambiguities in the integer domain with high efficiency and reliability. The presented algorithm has two variants: a loose form and a tight form known as RieMOCAD-LF and RieMOCAD-TF, respectively. They are compared to relevant state-of-the-art methods using both simulation and experimental data. We evaluate performance in terms of key performance indicators such as success rate, search space size, and attitude error distribution. The results confirm the feasibility and effectiveness of the proposed approach.

Chapter 6

Constrained Wrapped Least-Squares Attitude Determination

Based on the OC-AM, search-based approaches in the integer domain can significantly enhance the performance of ambiguity resolution at the cost of requiring a more sophisticated search algorithm to meet the nonlinear constraints on the antenna array geometry [110, 54]. Despite the resounding success of these LAMBDA variants, their computational efficiency might be inadequate in challenging environments with significant multipath effects or an adverse view of satellites, such as in urban canyon scenarios.

To avoid the complex process of resolving the carrier-phase integer ambiguities, we propose a novel optimization model to estimate the rotation matrix directly and recover the unambiguous phase as a by-product. This model leads to a very efficient approach to solve the attitude determination problem.

The main contribution of this work lies in developing a novel GNSS attitude determination method based on a proposed *constrained wrapped least-squares* (C-WLS) optimization criterion. The designed approach incorporates the antenna array information, the ambiguity integer characteristics, and residual phase constraints into the optimization model. The proposed approach belongs to the search-based category. The method considers the attitude parameters as the only unknown variables and rigorously assimilates all the available constraints. Compared with existing algorithms in the float domain [111, 112, 113], the computational complexity of the proposed method is kept low by reducing the search space to a subset that most likely contains the correct solution. This is done without sacrificing any prior information or constraints. Instead of performing integer

ambiguity resolution and attitude estimation in two separate steps, as is done in most traditional approaches [114, 115], we use the ambiguous carrier-phase measurements directly to estimate the attitude information. We demonstrate the effectiveness of our approach in different scenarios. As shown by our simulation and experimental results, the main benefit of the proposed method is improving the success rate and computational complexity, especially in challenging situations with a limited number of satellites or large measurement noise.

In this chapter, we first present the proposed constraint wrapped least-squares method and theoretically analyzes various aspects of the proposed approach. Then, we describe the adopted search strategy to find the attitude solution. Simulation and experimental results are presented, demonstrating the feasibility of the proposed approach. Finally, we draw the conclusion of this chapter.

6.1 Constrained Wrapped Least-Squares Method

To strengthen the attitude model, additional constraints (prior information) will be exploited. Given carrier-phase observations, the unknown matrices \mathbf{R} and \mathbf{N} can be estimated by applying the C-ILS optimization

$$\min_{\mathbf{R} \in \mathbb{O}^{3 \times q}, \mathbf{N} \in \mathbb{Z}^{S \times \mathcal{A}}} \|\text{vec}[\boldsymbol{\xi}(\mathbf{R}, \mathbf{N})]\|_{\mathbf{Q}_{\Psi}^{-1}}^2, \quad (6.1)$$

where $\boldsymbol{\xi}(\mathbf{R}, \mathbf{N})$ is the residual phase error defined as

$$\boldsymbol{\xi}(\mathbf{R}, \mathbf{N}) \triangleq \boldsymbol{\Psi} - \mathbf{H}\mathbf{R}\mathbf{X}_b - \mathbf{N}, \quad (6.2)$$

$$\boldsymbol{\Psi} = \begin{bmatrix} \psi_{10} & \cdots & \psi_{\mathcal{A}0} \end{bmatrix}. \quad (6.3)$$

Let N_{ij} and $\xi_{ij}(\mathbf{R}, N_{ij})$ be the entries in the i -th row and j -th column of \mathbf{N} and $\boldsymbol{\xi}(\mathbf{R}, \mathbf{N})$, respectively. Considering the observation error distribution, we can

apply an upper-bound to restrict the residual phase, i.e.,

$$|\xi_{ij}(\mathbf{R}, N_{ij})| \leq \delta, \quad i = 1, 2, \dots, \mathcal{S}; \quad j = 1, 2, \dots, \mathcal{A}; \quad (6.4)$$

where $|\cdot|$ denotes the absolute value, and δ is an upper bound that can be related to the noise level. In what follows we will state our main assumption concerning this upper bound. This assumption significantly simplifies the process of estimating the rotation matrix, as will be shown subsequently.

Assumption 6.1. *Double-difference carrier-phase observation noise is confined to an interval bounded by minus and plus a half wavelength. That is*

$$|\eta_{a0}^{s0}| \leq \frac{1}{2}, \quad s = 1, 2, \dots, \mathcal{S}; \quad a = 1, 2, \dots, \mathcal{A}. \quad (6.5)$$

This assumption is essential to the development of the proposed attitude determination method. Therefore, we examine the validity of this assumption before proceeding further. We analyze the assumption from two points of view, as follows.

- **Measurement noise level**

To analyze the double-difference observation noise level, we apply the Gaussian model to the original carrier-phase measurement noise, that is, we assume the noise of the undifferenced phase follows a Gaussian distribution $\mathcal{N}(0, \sigma_0^2)$. By the rules of error propagation, the noise of the double-difference phase also follows a Gaussian distribution $\mathcal{N}(0, \sigma^2)$ with $\sigma = 2\sigma_0$. The possibility that the double-difference carrier phase noise exceeds half of a cycle is

$$P_{\frac{1}{2}} = 2Q\left(\frac{1}{2}\right), \quad (6.6)$$

where $Q(\cdot)$ is the Q-function. As reported in [32], the carrier-phase observations can be measured to better than 0.01 wavelength. By setting $\sigma_0 = 0.01$ and $\sigma = 0.02$, we find out that $P_{\frac{1}{2}} \approx 0$. Thus, it is generally reasonable to

regard $P_{\frac{1}{2}}$ as small enough to be ignored.

- **Phase observation nature**

In the context of attitude determination, only the fractional part of the double-difference phase data is meaningful. This particular property of phase measurements is due to the presence of integer ambiguities. Based on (2.7), for two different observed noise vectors $\boldsymbol{\eta}_a$ and $\boldsymbol{\eta}_a + \Delta\mathbf{N}_a$, $\Delta\mathbf{N}_a \in \mathbb{Z}^S$, the double-difference phase observations $\boldsymbol{\psi}_a$ will have identical fractional parts. This results in the same estimations of the rotation matrix and the unambiguous double-difference carrier phase based on (2.24). The integer $\Delta\mathbf{N}_a$ will be absorbed in the integer ambiguity estimation. Therefore, it is impossible to distinguish whether the phase noise is $\boldsymbol{\eta}_a$ or $\boldsymbol{\eta}_a + \Delta\mathbf{N}_a$. Given that achieving the optimal attitude information is the real goal, we can make an assumption about the integer part of phase noise to restrict the possible solutions in a way that is beneficial in improving the estimation of the rotation matrix. Hence, we can select the integer to minimize the absolute value of phase noise, which will lead the phase noise to fall in $[-1/2, 1/2]$; that is, we consider only the estimations corresponding to observations with the lowest possible noise. In other words, double-difference carrier-phase observation noise can be assumed to be no greater than a half wavelength.

Based on Assumption 6.1, we obtain the following constraint on the residual phase:

$$|\xi_{ij}(\mathbf{R}, N_{ij})| \leq \frac{1}{2}, \quad i=1, 2, \dots, \mathcal{S}; \quad j=1, 2, \dots, \mathcal{A}. \quad (6.7)$$

Note that $|\xi_{ij}(\mathbf{R}, N_{ij})| = 1/2$ will result in N_{ij} having multiple solutions for the same \mathbf{R} . To facilitate obtaining an interesting form of the proposed method, we introduce a minor technical trick to modify (6.7) by limiting the range of $\xi_{ij}(\mathbf{R}, N_{ij})$ to $(-1/2, 1/2]$, that is

$$-\frac{1}{2} < \xi_{ij}(\mathbf{R}, N_{ij}) \leq \frac{1}{2}, \quad i=1, 2, \dots, \mathcal{S}; \quad j=1, 2, \dots, \mathcal{A}. \quad (6.8)$$

Combining (6.1) with (6.8), we obtain the following version of the minimization problem for attitude determination:

$$\min_{\mathbf{R} \in \mathbb{O}^{3 \times q}, \mathbf{N} \in \mathbb{Z}^{S \times \mathcal{A}}} \|\text{vec}[\boldsymbol{\xi}(\mathbf{R}, \mathbf{N})]\|_{\mathbf{Q}_{\Psi}^{-1}}^2, \quad (6.9a)$$

$$\text{s.t. } -\frac{1}{2} < \xi_{ij}(\mathbf{R}, N_{ij}) \leq \frac{1}{2}, \quad (6.9b)$$

$$i = 1, 2, \dots, S; \quad j = 1, 2, \dots, \mathcal{A}.$$

We can rewrite (6.9a) in an alternative form as

$$\min_{\mathbf{R} \in \mathbb{O}^{3 \times q}} \left(\min_{\mathbf{N} \in \mathbb{Z}^{S \times \mathcal{A}}} \|\text{vec}[\boldsymbol{\xi}(\mathbf{R}, \mathbf{N})]\|_{\mathbf{Q}_{\Psi}^{-1}}^2 \right). \quad (6.10)$$

Given any value of \mathbf{R} , the corresponding value of \mathbf{N} is

$$\tilde{\mathbf{N}}(\mathbf{R}) = \text{round}(\boldsymbol{\Psi} - \mathbf{H}\mathbf{R}\mathbf{X}_b). \quad (6.11)$$

Using (6.11), (6.10) can be rewritten as a single optimization

$$\min_{\mathbf{R} \in \mathbb{O}^{3 \times q}} \left\| \text{vec} \left[\boldsymbol{\Psi} - \mathbf{H}\mathbf{R}\mathbf{X}_b - \tilde{\mathbf{N}}(\mathbf{R}) \right] \right\|_{\mathbf{Q}_{\Psi}^{-1}}^2. \quad (6.12)$$

Based on (6.12), a more compact form of the attitude determination problem formulated by (6.9a) and (6.9b) is given in the following lemma.

Lemma 6.1. *Based on Assumption 6.1, the rotation matrix \mathbf{R} can be estimated by solving the minimization*

$$\min_{\mathbf{R} \in \mathbb{O}^{3 \times q}} \|\text{wrap}[\text{vec}(\boldsymbol{\Psi} - \mathbf{H}\mathbf{R}\mathbf{X}_b)]\|_{\mathbf{Q}_{\Psi}^{-1}}^2, \quad (6.13)$$

where $\text{wrap}(\cdot)$ is defined as

$$\text{wrap}(\cdot) = (\cdot) - \text{round}(\cdot).$$

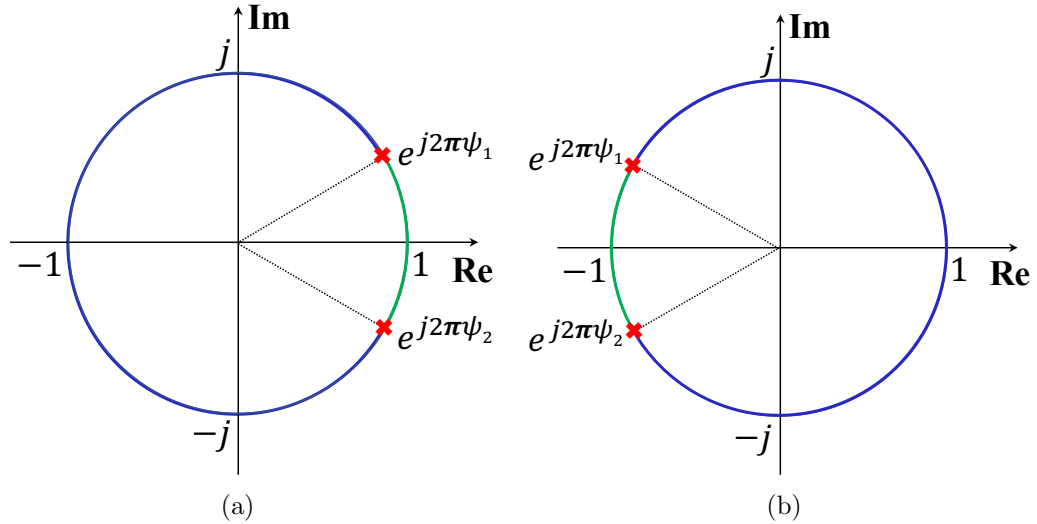


Figure 6.1: Illustration of the wrapped least squares concept using complex values on the unit circle.

We refer to (6.13) as the *constrained wrapped least-squares* (C-WLS) problem. Here, the rotation matrix \mathbf{R} is the only unknown. Once \mathbf{R} is known, the corresponding integer vector \mathbf{N} can be determined from (6.11).

A geometric interpretation of the WLS concept is given in Fig. 6.1. The absolute difference between a phase value ϕ_1 , which is an unwrapped version of an element of Ψ , and the corresponding value in \mathbf{HRX}_b (ϕ_2), can be represented by the distance between two points $e^{j2\pi\phi_1}$ and $e^{j2\pi\phi_2}$ on the unit circle. Since $e^{j2\pi\psi_i} = e^{j2\pi\phi_i}$, where ψ_i is the wrapped version of ϕ_i , the absolute difference between ϕ_1 and ϕ_2 (on the unit circle) can be measured as the distance between the complex values $e^{j2\pi\psi_1}$ and $e^{j2\pi\psi_2}$ on the unit circle, i.e.,

$$|\text{wrap}(\psi_1 - \psi_2)| = |\text{wrap}(\phi_1 - \phi_2)|. \quad (6.14)$$

The caveat here is that representing phase values on the unit circle automatically removes the effect of their integer parts. The distance of interest is always measured over the shorter (green) arc, which corresponds to respecting the half-cycle residual constraint (6.8). Given that only the fractional part of phase data is available, we can still measure the distance (on the unit circle) between the computed phase and the observed unwrapped phase (the observed wrapped phase plus the

true integer value) using the fraction parts of the two phases, as emphasized by (6.14).

Based on the above discussion, estimating unknowns using phase measurements can be achieved by matching the fractional part of the phase observations and those of the corresponding predictions. If we consider a scalar phase observation ψ_1 and the prediction $\psi_2 = \psi(x)$ for an unknown parameter x , the estimation of x can be carried out using

$$\min_x |\text{wrap}(\psi_1 - \psi_2)|. \quad (6.15)$$

Extending the results to the vector/matrix case while considering the available set of constraints yields the proposed C-WLS optimization in (6.13).

As compared with the C-ILS method, the C-WLS model maintains the integer constraint on the carrier-phase ambiguities (implicitly) and adds an additional constraint to limit the range of residual phase errors. Note that the C-WLS model keeps only the integer ambiguities satisfying the residual constraint, instead of the entire integer space. The effect of the residual restriction on the rotation matrix estimations can be demonstrated by comparing the solutions of (6.1) and (6.13), which is the subject of the following lemma.

Lemma 6.2. *A sufficient and necessary condition for (6.1) and (6.13) to have the same global optimum regarding \mathbf{R} is that the residual phase errors corresponding to the global minimum of (6.1) satisfy*

$$\left| \xi_{ij}(\hat{\mathbf{R}}, \hat{N}_{ij}) \right| \leq \frac{1}{2}, \quad i=1, 2, \dots, \mathcal{S}; \quad j=1, 2, \dots, \mathcal{A}, \quad (6.16)$$

where $\hat{\mathbf{R}}$ and $\hat{\mathbf{N}}$ are the globally optimal solutions of (6.1), and \hat{N}_{ij} is the entry in the i -th row and j -th column of $\hat{\mathbf{N}}$.

Proof. Suppose that $\hat{\mathbf{R}}$ and $\hat{\mathbf{N}}$ minimize (6.1), and they satisfy (6.16). We can

calculate the integer matrix based on $\hat{\mathbf{R}}$ using

$$\tilde{\mathbf{N}}(\hat{\mathbf{R}}) = \text{round}(\boldsymbol{\Psi} - \mathbf{H}\hat{\mathbf{R}}\mathbf{X}_b). \quad (6.17)$$

When the residual phase errors satisfy

$$\left| \xi_{ij}(\hat{\mathbf{R}}, \hat{N}_{ij}) \right| < \frac{1}{2}, \quad i=1, 2, \dots, \mathcal{S}; \quad j=1, 2, \dots, \mathcal{A}, \quad (6.18)$$

we obtain $\hat{\mathbf{N}} = \tilde{\mathbf{N}}(\hat{\mathbf{R}})$. If there is some residual error $\left| \xi_{ij}(\hat{\mathbf{R}}, \hat{N}_{ij}) \right| = 1/2$, $\hat{\mathbf{N}}$ will have multiple possible values, and $\tilde{\mathbf{N}}(\hat{\mathbf{R}})$ is one of the solutions. Anyway, $\hat{\mathbf{R}}$ and $\tilde{\mathbf{N}}(\hat{\mathbf{R}})$ will minimize (6.1). Hence, $\hat{\mathbf{R}}$ will be the global optimum of (6.12), which is equivalent to (6.13).

In contrast, we assume that $\hat{\mathbf{R}}$ and $\hat{\mathbf{N}}$ minimize (6.1), and $\hat{\mathbf{R}}$ minimizes (6.13). Given the fact that (6.12) and (6.13) are equivalent, $\hat{\mathbf{R}}$ will also minimize (6.12). Then, we have $\hat{\mathbf{N}} = \tilde{\mathbf{N}}(\hat{\mathbf{R}})$ or $\tilde{\mathbf{N}}(\hat{\mathbf{R}})$ is one of the possible values of $\hat{\mathbf{N}}$. Otherwise, $\hat{\mathbf{R}}$ cannot minimize (6.1) anymore. Therefore, $\hat{\mathbf{R}}$ and $\hat{\mathbf{N}}$ will satisfy (6.16). \square

The structure of the weight matrix $\mathbf{Q}_{\boldsymbol{\Psi}}$ is related to whether (6.16) holds or not. Likewise, the relationship between (6.1) and (6.13) might differ for a various weight matrix $\mathbf{Q}_{\boldsymbol{\Psi}}$. For double-difference observations, $\mathbf{Q}_{\boldsymbol{\Psi}}$ is not diagonal. With common clock technology, multiple antennas can use a synchronized clock such that the single-difference model is applicable in attitude determination. In that case, $\mathbf{Q}_{\boldsymbol{\Psi}}$ is a diagonal matrix. We obtain Lemma 6.3 as a special case to establish (6.16).

Lemma 6.3. *A sufficient condition for (6.16) to hold, and hence for (6.1) and (6.13) to have the same global optimum for \mathbf{R} , is that $\mathbf{Q}_{\boldsymbol{\Psi}}$ is a diagonal matrix.*

Proof. In (6.1), for $\forall \mathbf{R} \in \mathbb{O}^{3 \times q}$, we can figure out the optimal integer ambiguities by minimizing

$$F = \min_{\mathbf{N} \in \mathbb{Z}^{\mathcal{S} \times \mathcal{A}}} \|\text{vec}[\boldsymbol{\xi}(\mathbf{R}, \mathbf{N})]\|_{\mathbf{Q}_{\boldsymbol{\Psi}}^{-1}}^2. \quad (6.19)$$

The diagonal matrix \mathbf{Q}_Ψ results in the following expression

$$\begin{aligned} F &= \min_{N_{11} \in \mathbb{Z}, \dots, N_{S,A} \in \mathbb{Z}} \left(\sum_{i=1}^S \sum_{j=1}^A \frac{[\xi_{ij}(\mathbf{R}, N_{ij})]^2}{\sigma_{\Psi, kk}^2} \right) \\ &= \sum_{i=1}^S \sum_{j=1}^A \left(\min_{N_{ij} \in \mathbb{Z}} \frac{[\xi_{ij}(\mathbf{R}, N_{ij})]^2}{\sigma_{\Psi, kk}^2} \right), \quad k = (j-1)\mathcal{A} + i, \end{aligned} \quad (6.20)$$

where $\sigma_{\Psi, kk}$ is the k -th diagonal entry of \mathbf{Q}_Ψ .

Since the sum entries are uncorrelated, we obtain the optimal by minimizing each entry independently. It is apparent that $N_{ij} \in \mathbb{Z}$ satisfying $|\xi_{ij}(\mathbf{R}, N_{ij})| \leq 1/2$ will minimize $[\xi_{ij}(\mathbf{R}, N_{ij})]^2$. Therefore, $\hat{\mathbf{R}}$ and $\hat{\mathbf{N}}$, the global optimums of (6.1), always satisfy (6.16) when \mathbf{Q}_Ψ is a diagonal matrix. According to Lemma 6.2, we conclude that (6.1) and (6.13) have the same global optimum for \mathbf{R} . \square

To precisely explain the effect of the residual constraint, the results based on the unambiguous phase can be used as a benchmark to appreciate the difference between (6.1) and (6.13). Assuming Φ is the unambiguous double-different phase, we define \mathbb{S} , \mathbb{S}_1 and \mathbb{S}_2 as

$$\begin{aligned} \mathbb{S} &= \mathbb{O}^{3 \times q}, \\ \mathbb{S}_1 &= \{\mathbf{R} | \mathbf{R} \in \mathbb{O}^{3 \times q}, \boldsymbol{\xi} = \Phi - \mathbf{H}\mathbf{R}\mathbf{X}_b, |\xi_{ij}| \leq \frac{1}{2}, i=1, \dots, \mathcal{S}; j=1, \dots, \mathcal{A}\}, \\ \mathbb{S}_2 &= \mathbb{S} - \mathbb{S}_1. \end{aligned}$$

An *oracle* estimator (that has access to the correct integer ambiguities) can be formulated as

$$\mathbf{R}_{\text{or}} = \arg \min_{\mathbf{R} \in \mathbb{S}_1} \|\text{vec}(\Phi - \mathbf{H}\mathbf{R}\mathbf{X}_b)\|_{\mathbf{Q}_\Psi^{-1}}^2. \quad (6.21)$$

Contrast this with the C-WLS estimator

$$\mathbf{R}_{\text{CWLS}} = \arg \min_{\mathbf{R} \in \mathbb{S}} \|\text{wrap}[\text{vec}(\Psi - \mathbf{H}\mathbf{R}\mathbf{X}_b)]\|_{\mathbf{Q}_\Psi^{-1}}^2, \quad (6.22)$$

and the C-ILS estimator

$$\mathbf{R}_{\text{CILS}}, \mathbf{N}_{\text{CILS}} = \arg \min_{\mathbf{R} \in \mathbb{S}, \mathbf{N} \in \mathbb{Z}^{S \times A}} \|\text{vec}(\Psi - \mathbf{H}\mathbf{R}\mathbf{X}_b - \mathbf{N})\|_{\mathbf{Q}_\Psi^{-1}}^2. \quad (6.23)$$

Corollary 6.1, Corollary 6.2, and Corollary 6.3 summarize the relationships between these three estimators.

Corollary 6.1. *If the C-ILS estimator (6.23) and the oracle estimator (6.21) have the same global optimum for \mathbf{R} , the C-WLS estimator (6.22) will also have the identical global optimum as the oracle estimator (6.21), i.e.,*

$$\mathbf{R}_{\text{CILS}} = \mathbf{R}_{\text{or}} \Rightarrow \mathbf{R}_{\text{CWLS}} = \mathbf{R}_{\text{or}}.$$

Proof. We can readily see that

$$\begin{aligned} & \min_{\mathbf{R} \in \mathbb{S}_1} \|\text{wrap}[\text{vec}(\Psi - \mathbf{H}\mathbf{R}\mathbf{X}_b)]\|_{\mathbf{Q}_\Psi^{-1}}^2 \\ &= \min_{\mathbf{R} \in \mathbb{S}_1} \|\text{vec}(\Phi - \mathbf{H}\mathbf{R}\mathbf{X}_b)\|_{\mathbf{Q}_\Psi^{-1}}^2, \end{aligned} \quad (6.24)$$

and

$$\begin{aligned} & \min_{\mathbf{R} \in \mathbb{S}_2} \|\text{wrap}[\text{vec}(\Psi - \mathbf{H}\mathbf{R}\mathbf{X}_b)]\|_{\mathbf{Q}_\Psi^{-1}}^2 \\ & \geq \min_{\mathbf{R} \in \mathbb{S}_2, \mathbf{N} \in \mathbb{Z}^{S \times A}} \|\text{vec}(\Psi - \mathbf{H}\mathbf{R}\mathbf{X}_b - \mathbf{N})\|_{\mathbf{Q}_\Psi^{-1}}^2. \end{aligned} \quad (6.25)$$

If (6.23) converges to the oracle estimator, i.e., $\mathbf{R}_{\text{CILS}} \in \mathbb{S}_1$ and $\mathbf{R}_{\text{CILS}} = \mathbf{R}_{\text{or}}$, we obtain

$$\begin{aligned} & \min_{\mathbf{R} \in \mathbb{S}_1, \mathbf{N} \in \mathbb{Z}^{S \times A}} \|\text{vec}(\Psi - \mathbf{H}\mathbf{R}\mathbf{X}_b - \mathbf{N})\|_{\mathbf{Q}_\Psi^{-1}}^2 \\ & < \min_{\mathbf{R} \in \mathbb{S}_2, \mathbf{N} \in \mathbb{Z}^{S \times A}} \|\text{vec}(\Psi - \mathbf{H}\mathbf{R}\mathbf{X}_b - \mathbf{N})\|_{\mathbf{Q}_\Psi^{-1}}^2, \end{aligned} \quad (6.26)$$

and

$$\begin{aligned} & \min_{\mathbf{R} \in \mathbb{S}_1, \mathbf{N} \in \mathbb{Z}^{S \times A}} \|\text{vec}(\Psi - \mathbf{H}\mathbf{R}\mathbf{X}_b - \mathbf{N})\|_{\mathbf{Q}_\Psi^{-1}}^2 \\ &= \min_{\mathbf{R} \in \mathbb{S}_1} \|\text{vec}(\Phi - \mathbf{H}\mathbf{R}\mathbf{X}_b)\|_{\mathbf{Q}_\Psi^{-1}}^2. \end{aligned} \quad (6.27)$$

From (6.24)-(6.27), it follows that

$$\begin{aligned} & \min_{\mathbf{R} \in \mathbb{S}_1} \|\text{wrap}[\text{vec}(\Psi - \mathbf{H}\mathbf{R}\mathbf{X}_b)]\|_{\mathbf{Q}_\Psi^{-1}}^2 \\ & < \min_{\mathbf{R} \in \mathbb{S}_2} \|\text{wrap}[\text{vec}(\Psi - \mathbf{H}\mathbf{R}\mathbf{X}_b)]\|_{\mathbf{Q}_\Psi^{-1}}^2. \end{aligned} \quad (6.28)$$

Note that

$$\begin{aligned} & \arg \min_{\mathbf{R} \in \mathbb{S}_1} \|\text{vec}(\Phi - \mathbf{H}\mathbf{R}\mathbf{X}_b)\|_{\mathbf{Q}_\Psi^{-1}}^2 \\ & = \arg \min_{\mathbf{R} \in \mathbb{S}_1} \|\text{wrap}[\text{vec}(\Psi - \mathbf{H}\mathbf{R}\mathbf{X}_b)]\|_{\mathbf{Q}_\Psi^{-1}}^2, \end{aligned} \quad (6.29)$$

then (6.22) will also have the same global optimum as (6.21), i.e., $\mathbf{R}_{\text{CWLS}} \in \mathbb{S}_1$ and $\mathbf{R}_{\text{CWLS}} = \mathbf{R}_{\text{CILS}} = \mathbf{R}_{\text{or}}$. Hence, $\mathbf{R}_{\text{CILS}} = \mathbf{R}_{\text{or}} \Rightarrow \mathbf{R}_{\text{CWLS}} = \mathbf{R}_{\text{or}}$, but not vice versa. \square

Corollary 6.2. *If the C-WLS estimator (6.22) and the oracle estimator (6.21) have different global optimums, the global optimum (with respect to \mathbf{R}) of the C-ILS estimator (6.23) will also differ from that of the oracle estimator (6.21). That is*

$$\mathbf{R}_{\text{CWLS}} \neq \mathbf{R}_{\text{or}} \Rightarrow \mathbf{R}_{\text{CILS}} \neq \mathbf{R}_{\text{or}}.$$

Proof. If $\mathbf{R}_{\text{CWLS}} \neq \mathbf{R}_{\text{or}}$, then $\mathbf{R}_{\text{CWLS}} \in \mathbb{S}_2$, and

$$\begin{aligned} & \min_{\mathbf{R} \in \mathbb{S}_1} \|\text{wrap}[\text{vec}(\Psi - \mathbf{H}\mathbf{R}\mathbf{X}_b)]\|_{\mathbf{Q}_\Psi^{-1}}^2 \\ & > \min_{\mathbf{R} \in \mathbb{S}_2} \|\text{wrap}[\text{vec}(\Psi - \mathbf{H}\mathbf{R}\mathbf{X}_b)]\|_{\mathbf{Q}_\Psi^{-1}}^2. \end{aligned} \quad (6.30)$$

According to (6.25) and (6.30), we have

$$\begin{aligned} & \min_{\mathbf{R} \in \mathbb{S}, \mathbf{N} \in \mathbb{Z}^{S \times A}} \|\text{vec}(\Psi - \mathbf{H}\mathbf{R}\mathbf{X}_b - \mathbf{N})\|_{\mathbf{Q}_\Psi^{-1}}^2 \\ & \leq \min_{\mathbf{R} \in \mathbb{S}_2, \mathbf{N} \in \mathbb{Z}^{S \times A}} \|\text{vec}(\Psi - \mathbf{H}\mathbf{R}\mathbf{X}_b - \mathbf{N})\|_{\mathbf{Q}_\Psi^{-1}}^2 \\ & \leq \min_{\mathbf{R} \in \mathbb{S}_2} \|\text{wrap}[\text{vec}(\Psi - \mathbf{H}\mathbf{R}\mathbf{X}_b)]\|_{\mathbf{Q}_\Psi^{-1}}^2 \\ & < \left\| \text{wrap} \left[\text{vec} \left(\Psi - \mathbf{H}\hat{\mathbf{R}}_{\text{or}} \right) \right] \right\|_{\mathbf{Q}_\Psi^{-1}}^2 \\ & = \|\text{vec}(\Psi - \mathbf{H}\hat{\mathbf{x}}_{\text{or}} - \mathbf{N}_{\text{or}})\|_{\mathbf{Q}_\Psi^{-1}}^2, \end{aligned} \quad (6.31)$$

with

$$\mathbf{N}_{\text{or}} = \mathbf{\Psi} - \mathbf{\Phi}, \quad (6.32)$$

then $\mathbf{R}_{\text{CILS}} \neq \mathbf{R}_{\text{or}}$ and $\mathbf{N}_{\text{CILS}} \neq \mathbf{N}_{\text{or}}$. As a result, $\mathbf{R}_{\text{CWLS}} \neq \mathbf{R}_{\text{or}} \Rightarrow \mathbf{R}_{\text{CILS}} \neq \mathbf{R}_{\text{or}}$. \square

Using the results of Corollary 6.1 and Corollary 6.2, the following corollary holds.

Corollary 6.3. *Compared with the C-ILS estimator (6.23), the C-WLS estimator (6.22) is more likely to have the equivalent global optimum for \mathbf{R} as the oracle estimator (6.21), i.e.,*

$$P(\mathbf{R}_{\text{CWLS}} = \mathbf{R}_{\text{or}}) \geq P(\mathbf{R}_{\text{CILS}} = \mathbf{R}_{\text{or}}),$$

where $P(\cdot)$ denotes the probability.

Proof. Since

$$\mathbf{R}_{\text{CILS}} = \mathbf{R}_{\text{or}} \Rightarrow \mathbf{R}_{\text{CWLS}} = \mathbf{R}_{\text{or}},$$

$$\mathbf{R}_{\text{CWLS}} \neq \mathbf{R}_{\text{or}} \Rightarrow \mathbf{R}_{\text{CILS}} \neq \mathbf{R}_{\text{or}},$$

it can be readily seen that $P(\mathbf{R}_{\text{CWLS}} = \mathbf{R}_{\text{or}}) \geq P(\mathbf{R}_{\text{CILS}} = \mathbf{R}_{\text{or}})$. \square

When only carrier-phase measurements are utilized to jointly estimate the ambiguities and attitude, there are more unknowns than the number of equations. Corollary 6.3 illuminates the advantage of the C-WLS approach compared to the C-ILS method. However, the pseudo-range observations are still required to improve the solutions.

Lemma 6.4. *Including both pseudo-range and carrier-phase data, the proposed C-WLS method can be formulated as*

$$\min_{\mathbf{R} \in \mathcal{S}} \left\| \begin{bmatrix} \text{wrap}[\text{vec}(\mathbf{\Psi} - \mathbf{H}\mathbf{R}\mathbf{X}_b)] \\ \text{vec}(\mathbf{P} - \mathbf{H}\mathbf{R}\mathbf{X}_b) \end{bmatrix} \right\|_{\mathbf{Q}^{-1}}^2. \quad (6.33)$$

It is readily seen that (6.33) will achieve the same global minimum and optimal solution of \mathbf{R} as

$$\min_{\mathbf{R} \in \mathcal{S}, \mathbf{N} \in \mathbb{Z}^{\mathcal{S} \times \mathcal{A}}} \|\text{vec}(\mathbf{Y} - \mathbf{A}\mathbf{R}\mathbf{X}_b - \mathbf{B}\mathbf{N})\|_{\mathbf{Q}_Y^{-1}}^2 \quad (6.34a)$$

$$\text{s.t. } -\frac{1}{2} < \xi_{ij}(\mathbf{R}, N_{ij}) \leq \frac{1}{2}, \quad (6.34b)$$

$$i = 1, 2, \dots, \mathcal{S}; \quad j = 1, 2, \dots, \mathcal{A}.$$

To compare (6.33) with (2.24), we assume that

$$\tilde{\mathbf{R}}_{\text{or}} = \arg \min_{\mathbf{R} \in \mathcal{S}_1} \left\| \text{vec} \left(\begin{bmatrix} \Phi \\ \mathbf{P} \end{bmatrix} - \begin{bmatrix} \mathbf{H} \\ \mathbf{H} \end{bmatrix} \mathbf{R}\mathbf{X}_b \right) \right\|_{\mathbf{Q}^{-1}}^2, \quad (6.35)$$

$$\tilde{\mathbf{R}}_{\text{CWLS}} = \arg \min_{\mathbf{R} \in \mathcal{S}} \left\| \begin{bmatrix} \text{wrap}[\text{vec}(\Psi - \mathbf{H}\mathbf{R}\mathbf{X}_b)] \\ \text{vec}(\mathbf{P} - \mathbf{H}\mathbf{R}\mathbf{X}_b) \end{bmatrix} \right\|_{\mathbf{Q}^{-1}}^2, \quad (6.36)$$

$$\tilde{\mathbf{R}}_{\text{CILS}}, \tilde{\mathbf{N}}_{\text{CILS}} = \arg \min_{\mathbf{R} \in \mathcal{S}, \mathbf{N} \in \mathbb{Z}^{\mathcal{S} \times \mathcal{A}}} \|\text{vec}(\mathbf{Y} - \mathbf{A}\mathbf{R}\mathbf{X}_b - \mathbf{B}\mathbf{N})\|_{\mathbf{Q}_Y^{-1}}^2. \quad (6.37)$$

Given the structure of \mathbf{Q} , we have

$$\tilde{\mathbf{R}}_{\text{or}} = \arg \min_{\mathbf{R} \in \mathcal{S}_1} \{ \|\text{vec}(\Phi - \mathbf{H}\mathbf{R}\mathbf{X}_b)\|_{\mathbf{Q}_\Psi^{-1}}^2 + \|\text{vec}(\mathbf{P} - \mathbf{H}\mathbf{R}\mathbf{X}_b)\|_{\mathbf{Q}_\mathbf{P}^{-1}}^2 \}, \quad (6.38)$$

$$\tilde{\mathbf{R}}_{\text{CWLS}} = \arg \min_{\mathbf{R} \in \mathcal{S}} \{ \|\text{wrap}[\text{vec}(\Psi - \mathbf{H}\mathbf{R}\mathbf{X}_b)]\|_{\mathbf{Q}_\Psi^{-1}}^2 + \|\text{vec}(\mathbf{P} - \mathbf{H}\mathbf{R}\mathbf{X}_b)\|_{\mathbf{Q}_\mathbf{P}^{-1}}^2 \}, \quad (6.39)$$

$$\tilde{\mathbf{R}}_{\text{CILS}}, \tilde{\mathbf{N}}_{\text{CILS}} = \arg \min_{\mathbf{R} \in \mathcal{S}, \mathbf{N} \in \mathbb{Z}^{\mathcal{S} \times \mathcal{A}}} \{ \|\text{vec}(\Psi - \mathbf{H}\mathbf{R}\mathbf{X}_b - \mathbf{N})\|_{\mathbf{Q}_\Psi^{-1}}^2 + \|\text{vec}(\mathbf{P} - \mathbf{H}\mathbf{R}\mathbf{X}_b)\|_{\mathbf{Q}_\mathbf{P}^{-1}}^2 \}. \quad (6.40)$$

Incorporating pseudo-range will introduce the same terms ($\|\text{vec}(\mathbf{P} - \mathbf{H}\mathbf{R}\mathbf{X}_b)\|_{\mathbf{Q}_\mathbf{P}^{-1}}^2$) to (6.38)-(6.40). So all the results in Corollary 6.1, Corollary 6.2, and Corollary 6.3 are still true. As a consequence, we establish the following corollary.

Corollary 6.4. *For the estimators in (6.38), (6.39) and (6.40), the global opti-*

mums with respect to \mathbf{R} satisfy the following relationships

$$\tilde{\mathbf{R}}_{CILS} = \tilde{\mathbf{R}}_{or} \Rightarrow \tilde{\mathbf{R}}_{CWLS} = \tilde{\mathbf{R}}_{or},$$

$$\tilde{\mathbf{R}}_{CWLS} \neq \tilde{\mathbf{R}}_{or} \Rightarrow \tilde{\mathbf{R}}_{CILS} \neq \tilde{\mathbf{R}}_{or},$$

$$P(\tilde{\mathbf{R}}_{CWLS} = \tilde{\mathbf{R}}_{or}) \geq P(\tilde{\mathbf{R}}_{CILS} = \tilde{\mathbf{R}}_{or}).$$

Corollary 6.4 demonstrates the advantage of the C-WLS model. The proposed method imposes a constraint on the residual errors, which shrinks the solution space and remove spurious solutions. This results in an improvement over the C-ILS method. To give insight into all the results discussed in this section, we summarize the significance of various lemmas and corollaries in Remark 6.1.

Remark 6.1. *The significance of various lemmas and corollaries is as follows.*

Lemma 6.1 and Lemma 6.4 formulate the proposed C-WLS optimization model.

- *Lemma 6.1 based on only carrier phase data.*
- *Lemma 6.4 based on pseudo-range and carrier phase data.*

Lemma 6.2 – 6.3 discuss the conditions for the C-WLS and the C-ILS optimization to have equivalent global optimum for \mathbf{R} when using only carrier phase observations.

- *Lemma 6.2 provides a sufficient and necessary condition.*
- *Lemma 6.3 proves a diagonal \mathbf{Q}_Ψ as a sufficient condition.*

Corollary 6.1 – 6.4 indicate the advantage of the C-WLS model compared with the C-ILS model; namely, the C-WLS estimator is more likely to have the same global optimum for \mathbf{R} as the oracle estimator.

- *Corollary 6.1 – 6.3 based on only carrier phase data.*
- *Corollary 6.4 based on pseudo-range and carrier phase data.*

6.2 Implementation of the Proposed C-WLS Method

In the C-WLS problem (6.33), the rotation matrix \mathbf{R} is the only unknown. For $q = 3$, \mathbf{R} includes 9 elements that are uniquely determined by 3 independent variables. The Euler angles are usually used to define \mathbf{R} and represent the orientation of the rigid body with respect to the three axes in reference coordinate system. The rotation matrix \mathbf{R} can be expressed in the following form:

$$\mathbf{R} = \begin{bmatrix} \cos \alpha \cos \beta & \cos \alpha \sin \beta \sin \gamma - \sin \alpha \cos \gamma & \cos \alpha \sin \beta \cos \gamma + \sin \alpha \sin \gamma \\ \sin \alpha \cos \beta & \sin \alpha \sin \beta \sin \gamma + \cos \alpha \cos \gamma & \sin \alpha \sin \beta \cos \gamma - \cos \alpha \sin \gamma \\ -\sin \beta & \cos \beta \sin \gamma & \cos \beta \cos \gamma \end{bmatrix},$$

where α , β and γ are the yaw, pitch, and roll angles, respectively. An optimal of (6.33) can be found by searching over the range of the Euler angles. However, such a 3-D search leads to a high computational complexity. Given the prior knowledge of the antenna-array configuration and the integer characteristics of phase ambiguities, we can efficiently reduce the search space to a few possible estimates of \mathbf{R} (instead of searching through the whole range of the Euler angles). In the following subsections, we will develop the search strategies for the single-baseline and multi-baseline cases separately.

6.2.1 Single-baseline Attitude Determination

In a single-baseline set-up, $\mathbf{R} \in \mathbb{R}^3$ is a unit column vector, uniquely determined by yaw and pitch angles. To facilitate the discussion of the multi-baseline case (presented later), we replace \mathbf{R} with \mathbf{r}_a , which will later be used to indicate the a -th (single) baseline in a multi-baseline configuration. The vector \mathbf{r}_a represents the unit direction vector of a single baseline. Based on (6.33), we can write

$$\min_{\mathbf{r}_a \in \mathbb{R}^3, \|\mathbf{r}_a\|_2=1} \left\| \begin{bmatrix} \text{wrap}(\psi_a - d_a \mathbf{H} \mathbf{r}_a) \\ \boldsymbol{\rho}_a - d_a \mathbf{H} \mathbf{r}_a \end{bmatrix} \right\|_{\mathbf{Q}_a^{-1}}^2, \quad (6.41)$$

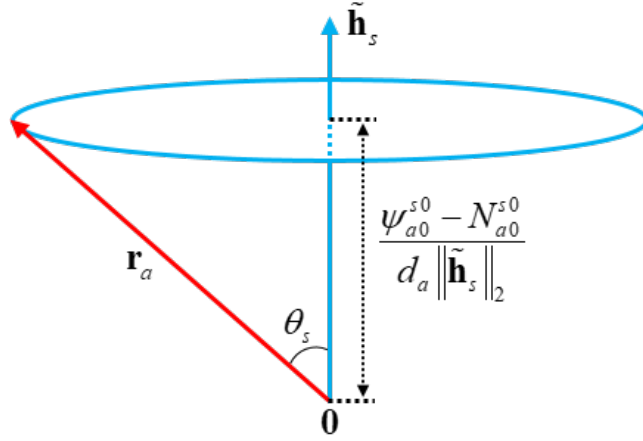


Figure 6.2: The relationship between \mathbf{r}_a and $\tilde{\mathbf{h}}_s$.

where d_a is the baseline length, and \mathbf{Q}_a is the covariance matrix. The baseline vector in the reference frame is given by

$$\mathbf{x}_a = d_a \mathbf{r}_a. \quad (6.42)$$

According to (2.5), (2.8) and (6.42), we have

$$\psi_{a0}^{s0} - N_{a0}^{s0} = d_a \tilde{\mathbf{h}}_s \mathbf{r}_a + \eta_{a0}^{s0}. \quad (6.43)$$

As shown in Fig. 6.2, we draw the vector \mathbf{r}_a and $\tilde{\mathbf{h}}_s$ starting from the origin. \mathbf{r}_a is the unknown unit vector which makes an angle θ_s with $\tilde{\mathbf{h}}_s$. Hence, the candidate terminal points (coordinates) for \mathbf{r}_a represent a circle on the sphere centered around the radial line of $\tilde{\mathbf{h}}_s$. If we ignore phase noise, the angle θ_s satisfies

$$\cos \theta_s = \frac{\psi_{a0}^{s0} - N_{a0}^{s0}}{d_a \|\tilde{\mathbf{h}}_s\|_2}. \quad (6.44)$$

For the s -th element of $\boldsymbol{\psi}_a$, the possible integer ambiguities should be confined to

$$-d_a \|\tilde{\mathbf{h}}_s\|_2 \leq \psi_{a0}^{s0} - N_{a0}^{s0} \leq d_a \|\tilde{\mathbf{h}}_s\|_2. \quad (6.45)$$

Considering all the possible N_{a0}^{s0} , the candidate terminal points for \mathbf{r}_a will be on a set of parallel circles on the spherical surface.

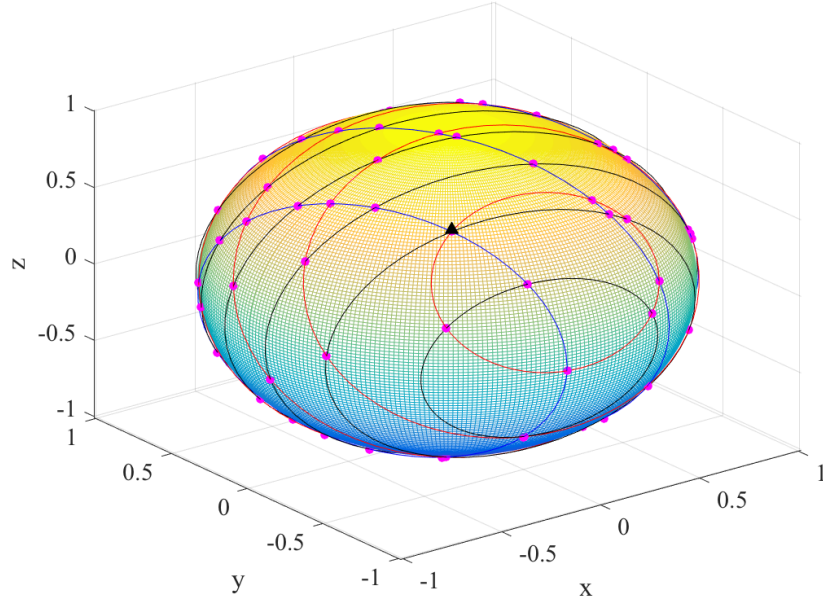


Figure 6.3: Distribution of potential candidate points for \mathbf{r}_a .

Fig. 6.3 shows an example of the distribution of possible candidate points for \mathbf{r}_a with four satellites under consideration (circles of the same color corresponding to one double-difference phase observation). The intersections between the circles of different colors indicate possible estimates of \mathbf{r}_a . The intersection points between two circles exist if the following system of equations has a solution:

$$\begin{cases} \psi_{a0}^{s0} - N_{a0}^{s0} = d_a \tilde{\mathbf{h}}_s \mathbf{r}_a, \\ \psi_{a0}^{m0} - N_{a0}^{m0} = d_a \tilde{\mathbf{h}}_m \mathbf{r}_a. \end{cases} \quad (6.46)$$

In the noise-free case, there is one combination of the integers

$$\mathbf{N}_a = \begin{bmatrix} N_{a0}^{10} & \dots & N_{a0}^{S0} \end{bmatrix}^T, \quad (6.47)$$

whose corresponding circles have a joint intersection point, that is, (6.47) satisfies

$$\begin{cases} \psi_{a0}^{10} - N_{a0}^{10} = d_a \tilde{\mathbf{h}}_1 \mathbf{r}_a, \\ \psi_{a0}^{20} - N_{a0}^{20} = d_a \tilde{\mathbf{h}}_2 \mathbf{r}_a, \\ \vdots \\ \psi_{a0}^{S0} - N_{a0}^{S0} = d_a \tilde{\mathbf{h}}_S \mathbf{r}_a. \end{cases} \quad (6.48)$$

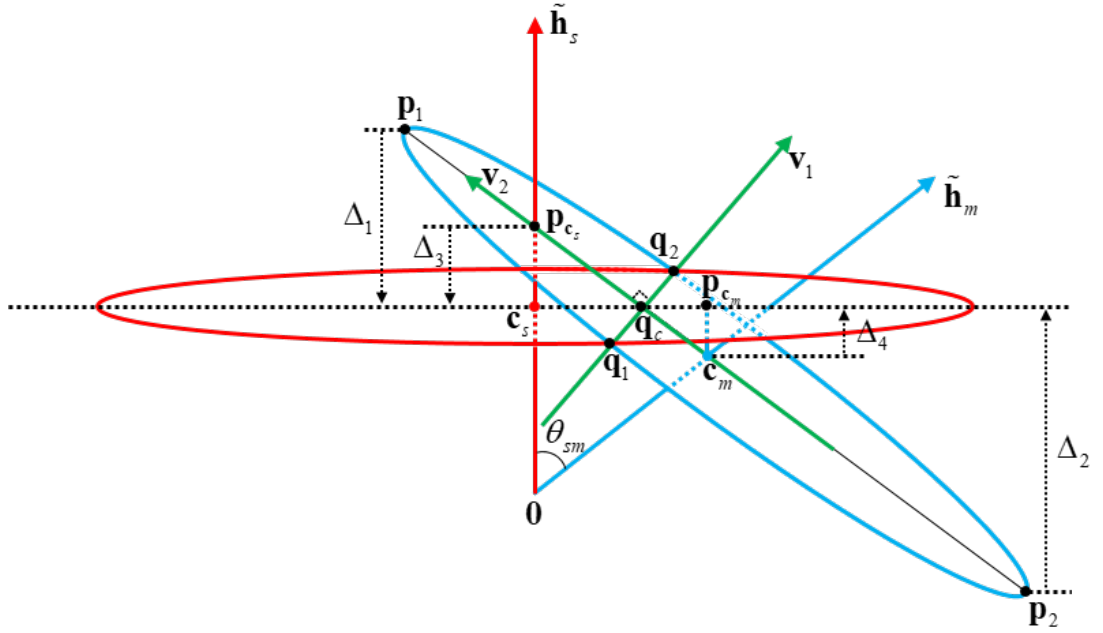


Figure 6.4: Illustration of the intersection points.

Due to the measurement noise, we may have only pairwise circle intersect, that is, a solution of (6.48) may not exist. However, we can calculate the intersection points for all the circle pairs of different observations. The baseline vector can be determined by evaluating (6.41) (only) at these intersections.

Instead of solving the system of equations (6.46), we can achieve the intersections by applying the geometry relationships between two circles on the sphere. To calculate the intersection points, we need to define some intermediate vectors, such as the normal vector \mathbf{v}_1 of the plane determined by $\tilde{\mathbf{h}}_s$ and $\tilde{\mathbf{h}}_m$, and the normal vector \mathbf{v}_2 of the plane on which \mathbf{v}_1 and $\tilde{\mathbf{h}}_m$ lie. \mathbf{v}_1 and \mathbf{v}_2 are given by

$$\mathbf{v}_1 = \frac{\tilde{\mathbf{h}}_s \times \tilde{\mathbf{h}}_m}{\|\tilde{\mathbf{h}}_s \times \tilde{\mathbf{h}}_m\|_2}, \quad \mathbf{v}_2 = \frac{\mathbf{v}_1 \times \tilde{\mathbf{h}}_m}{\|\mathbf{v}_1 \times \tilde{\mathbf{h}}_m\|_2}. \quad (6.49)$$

In Fig. 6.4, the centers of the circle s and circle m are

$$\mathbf{c}_s = \frac{\cos \theta_s \tilde{\mathbf{h}}_s}{\|\tilde{\mathbf{h}}_s\|_2}, \quad \mathbf{c}_m = \frac{\cos \theta_m \tilde{\mathbf{h}}_m}{\|\tilde{\mathbf{h}}_m\|_2}, \quad (6.50)$$

where the cosines can be computed based on (6.44).

To check whether the two circles intersect, we define the peak points (the

closest or farthest points from the other circle) of circle m with respect to circle s as follows

$$\mathbf{p}_1 = \mathbf{c}_m - \sin \theta_m \mathbf{v}_2, \quad \mathbf{p}_2 = \mathbf{c}_m + \sin \theta_m \mathbf{v}_2. \quad (6.51)$$

The directed distances (positive or negative) between the peak points and circle s plane are given by

$$\Delta_1 = (\mathbf{p}_1 - \mathbf{c}_s)^T \frac{\tilde{\mathbf{h}}_s}{\|\tilde{\mathbf{h}}_s\|_2}, \quad \Delta_2 = (\mathbf{p}_2 - \mathbf{c}_s)^T \frac{\tilde{\mathbf{h}}_s}{\|\tilde{\mathbf{h}}_s\|_2}. \quad (6.52)$$

If $\Delta_1 \Delta_2 \leq 0$, circle s will intersect with circle m . Otherwise, there is no intersection. When $\Delta_1 = 0$, the two circles intersect at \mathbf{p}_1 . Similarly, if $\Delta_2 = 0$, \mathbf{p}_2 is the intersection point. When $\Delta_1 \Delta_2 < 0$, there are two intersection points between circle s and circle m . A procedure to calculate these intersection points is as follows. The directed distance between \mathbf{c}_m and circle s plane is

$$\Delta_3 = (\mathbf{c}_m - \mathbf{c}_s)^T \frac{\tilde{\mathbf{h}}_s}{\|\tilde{\mathbf{h}}_s\|_2}. \quad (6.53)$$

The projected point of \mathbf{c}_m on circle s plane is expressed as

$$\mathbf{p}_{\mathbf{c}_m} = \mathbf{c}_m - \frac{\Delta_3 \tilde{\mathbf{h}}_s}{\|\tilde{\mathbf{h}}_s\|_2}. \quad (6.54)$$

As shown in Fig. 6.4, $\tilde{\mathbf{h}}_s$ intersects with the circle m plane at

$$\mathbf{p}_{\mathbf{c}_s} = \frac{\cos \theta_m}{\cos \theta_{sm}} \frac{\tilde{\mathbf{h}}_s}{\|\tilde{\mathbf{h}}_s\|_2}, \quad (6.55)$$

where θ_{sm} is the angle between $\tilde{\mathbf{h}}_s$ and $\tilde{\mathbf{h}}_m$. The directed distance between $\mathbf{p}_{\mathbf{c}_s}$ and circle s plane is given by

$$\Delta_4 = (\mathbf{p}_{\mathbf{c}_s} - \mathbf{c}_s)^T \frac{\tilde{\mathbf{h}}_s}{\|\tilde{\mathbf{h}}_s\|_2}. \quad (6.56)$$

Based on the basic proportionality theorem of similar triangles, we have

$$\frac{\mathbf{p}_c - \mathbf{c}_s}{\mathbf{p}_c - \mathbf{p}_{c_m}} = \frac{\Delta_4}{\Delta_3}, \quad (6.57)$$

where \mathbf{p}_c is the center point on the intersection line. Therefore, we have

$$\mathbf{p}_c = \frac{\Delta_3 \mathbf{c}_s - \Delta_4 \mathbf{p}_{c_m}}{\Delta_3 - \Delta_4}. \quad (6.58)$$

The two intersection points can be represented as

$$\mathbf{q}_1 = \mathbf{p}_c - \sqrt{1 - \|\mathbf{p}_c\|_2^2} \mathbf{v}_1, \quad \mathbf{q}_2 = \mathbf{p}_c + \sqrt{1 - \|\mathbf{p}_c\|_2^2} \mathbf{v}_1. \quad (6.59)$$

We consider all the intersection points as candidates for being an estimate of \mathbf{r}_a . When there is no intersection, if Δ_1 or Δ_2 is close to zero, some points around the corresponding peak point should also be selected as the potential candidates as the lack of intersection might be due to noise. We define a threshold δ_Δ for Δ_1 and Δ_2 . If $|\Delta_1| < \delta_\Delta$, we can select \mathbf{p}_1 as a candidate; if $|\Delta_2| < \delta_\Delta$, we can choose \mathbf{p}_2 as a candidate. We can create a pool ($\mathbb{S}_{\mathbf{r}_a}$) of all candidate points from the intersections of all possible circle pair combinations. Algorithm 6.1 summarizes the procedure to determine $\mathbb{S}_{\mathbf{r}_a}$. We keep the best K estimations of \mathbf{r}_a (coarse solutions) using

$$\min_{\mathbf{r}_a \in \mathbb{S}_{\mathbf{r}_a}} \left\| \begin{bmatrix} \text{wrap}(\boldsymbol{\psi}_a - d_a \mathbf{H} \mathbf{r}_a) \\ \boldsymbol{\rho}_a - d_a \mathbf{H} \mathbf{r}_a \end{bmatrix} \right\|_{\mathbf{Q}_a^{-1}}^2. \quad (6.60)$$

To achieve a high-quality solution, a refinement of the coarse results is necessary. When the unambiguous phase $\boldsymbol{\phi}_a$ is available, we consider the following optimization

$$\min_{\mathbf{r}_a \in \mathbb{R}^3, \|\mathbf{r}_a\|_2=1} \left\| \begin{bmatrix} \boldsymbol{\phi}_a - d_a \mathbf{H} \mathbf{r}_a \\ \boldsymbol{\rho}_a - d_a \mathbf{H} \mathbf{r}_a \end{bmatrix} \right\|_{\mathbf{Q}_a^{-1}}^2, \quad (6.61)$$

which leads to a general constraint least-squares solution. Many strategies, generally iterative schemes, can be utilized to solve the nonlinear system in (6.61).

Algorithm 6.1 Procedure to search baseline vector candidates.

```

1:  $\mathbb{S}_{\mathbf{r}_a} = \emptyset$ 
2: for all Circle pairs do
3:   Compute  $\mathbf{p}_1$ ,  $\mathbf{p}_2$ ,  $\Delta_1$  and  $\Delta_2$  using (6.49)–(6.52).
4:   if  $\Delta_1\Delta_2 < 0$  then
5:     Compute  $\mathbf{q}_1$  and  $\mathbf{q}_2$  using (6.53)–(6.59).
6:      $\mathbb{S}_{\mathbf{r}_a} = \mathbb{S}_{\mathbf{r}_a} \cup \{\mathbf{q}_1, \mathbf{q}_2\}$ .
7:   else
8:     When  $|\Delta_1| < \delta_\Delta$ ,  $\mathbb{S}_{\mathbf{r}_a} = \mathbb{S}_{\mathbf{r}_a} \cup \{\mathbf{p}_1\}$ .
9:     When  $|\Delta_2| < \delta_\Delta$ ,  $\mathbb{S}_{\mathbf{r}_a} = \mathbb{S}_{\mathbf{r}_a} \cup \{\mathbf{p}_2\}$ .
10:  end if
11: end for

```

Algorithm 6.2 C-WLS Single-baseline Attitude Determination.

```

1: Determine  $\mathbb{S}_{\mathbf{r}_a}$  based on Algorithm 6.1.
2: Select the best  $K$  estimations from  $\mathbb{S}_{\mathbf{r}_a}$  using (6.60).
3: Use the coarse results as the initial solutions.
4: Final results after refinement based on (6.61)–(6.62).

```

We can directly utilize the ambiguous carrier phase as long as we substitute the following term in (6.61):

$$\phi_a = \psi_a + \text{round}(d_a \mathbf{H} \mathbf{r}_a - \psi_a). \quad (6.62)$$

We use the coarse results as the initial solutions and achieve the final estimation based on (6.61)–(6.62). The entire procedures are summarized in Algorithm 6.2.

6.2.2 Multi-baseline Attitude Determination

For multi-baseline configurations, we can estimate the rotation matrix by refining single-baseline solutions to avoid high complexity, rather than searching the solution directly. Single-baseline attitude determination applies only the baseline length constraint. To fully integrate the geometry constraints, we need to consider the relative direction of different baselines. This can be realized by checking the angle between estimations of baseline vectors.

For each baseline, we keep the best K estimations of the direction vector based on the intersection points and potential candidates. For the a -th and k -th

Algorithm 6.3 C-WLS Multi-baseline Attitude Determination.

- 1: Find the best K estimations for each baseline using step 1–2 of Algorithm 6.2.
 - 2: Keep the estimations that satisfy the angle criteria (6.63) for every baseline pair.
 - 3: Combine pointing vectors to create the baseline matrix using (6.64).
 - 4: Convert the baseline matrix to a rotation matrix using (6.66).
 - 5: Initialize the orthogonal rotation matrix using Wahba's problem as in (6.67).
 - 6: Final results after refinement via (6.70)–(6.71).
-

baseline, we choose the estimations that satisfy

$$|\arccos(\mathbf{r}_a^T \mathbf{r}_k) - \Theta_{ak}| < \delta_\Theta, \quad (6.63)$$

where Θ_{ak} is the angle between two baselines, and δ_Θ is the threshold of angle difference. The selected baseline vectors constitute the possible baseline matrix in the reference coordinate, that is

$$\widehat{\mathbf{X}} = \begin{bmatrix} d_1 \mathbf{r}_1 & \cdots & d_{\mathcal{A}} \mathbf{r}_{\mathcal{A}} \end{bmatrix}. \quad (6.64)$$

For $\mathcal{A} = 2$, we can add a column to $\widehat{\mathbf{X}}$ and \mathbf{X}_b , that is

$$\tilde{\mathbf{X}} = \begin{bmatrix} d_1 \mathbf{r}_1 & d_2 \mathbf{r}_2 & \frac{\mathbf{r}_1 \times \mathbf{r}_2}{\|\mathbf{r}_1 \times \mathbf{r}_2\|_2} \end{bmatrix}, \mathbf{X}_b = \begin{bmatrix} \mathbf{x}_b^1 & \mathbf{x}_b^2 & \frac{\mathbf{x}_b^1 \times \mathbf{x}_b^2}{\|\mathbf{x}_b^1 \times \mathbf{x}_b^2\|_2} \end{bmatrix}. \quad (6.65)$$

According to the relationship between the baseline matrix in the body frame and reference frame, the coarse solution of the rotation matrix can be calculated using

$$\tilde{\mathbf{R}} = \tilde{\mathbf{X}} \mathbf{X}_b^T (\mathbf{X}_b \mathbf{X}_b^T)^{-1}. \quad (6.66)$$

To satisfy the antenna array constraints, we have to transform the rotation matrix to an orthogonal matrix, that is, to solve the following optimization problem:

$$\widehat{\mathbf{R}} = \arg \min_{\mathbf{R} \in \mathbb{O}^{3 \times 3}} \left\| \mathbf{R} - \tilde{\mathbf{R}} \right\|_2. \quad (6.67)$$

This is the Wahba's problem for which an analytical solution exists [116, 117]. The solution goes as follows. First, apply singular-value decomposition to the coarse rotation matrix

$$\tilde{\mathbf{R}} = \tilde{\mathbf{U}}\tilde{\mathbf{\Sigma}}\tilde{\mathbf{V}}^T, \quad (6.68)$$

where $\tilde{\mathbf{\Sigma}}$ is a diagonal matrix in which the diagonal entries are the singular values of $\tilde{\mathbf{R}}$, and the columns of $\tilde{\mathbf{U}}$ and $\tilde{\mathbf{V}}$ are the left and right singular vectors of $\tilde{\mathbf{R}}$, respectively. Then a solution to (6.67) can be obtained as

$$\hat{\mathbf{R}} = \tilde{\mathbf{U}} \begin{bmatrix} 1 & 0 & 0 \\ 0 & 1 & 0 \\ 0 & 0 & \det(\tilde{\mathbf{U}})\det(\tilde{\mathbf{V}}) \end{bmatrix} \tilde{\mathbf{V}}^T. \quad (6.69)$$

It can be readily seen that $\hat{\mathbf{R}}$ is an orthogonal matrix, i.e, it satisfies all the required constraints. However, this is only a sub-optimal estimate of the rotation matrix; hence, a refinement is required.

Similar to the single-baseline set-up, if the unambiguous phase Φ is known, we can consider the following optimization

$$\min_{\mathbf{R} \in \mathbb{O}^{3 \times q}} \left\| \begin{bmatrix} \text{vec}(\Phi - \mathbf{H}\mathbf{R}\mathbf{X}_b) \\ \text{vec}(\mathbf{P} - \mathbf{H}\mathbf{R}\mathbf{X}_b) \end{bmatrix} \right\|_{\mathbf{Q}^{-1}}^2. \quad (6.70)$$

Again, we directly take advantage of the ambiguous phase by using $\hat{\mathbf{R}}$ as the initial solution and applying the substitution

$$\Phi = \Psi + \text{round}(\mathbf{H}\mathbf{R}\mathbf{X}_b - \Psi). \quad (6.71)$$

The entire process to estimate the rotation matrix and resolve the carrier-phase ambiguity is summarized in Algorithm 6.3.

6.3 Performance Evaluation

In this section, we first present simulation results. Next, we evaluate the performance of the proposed method experimentally. Our tests focus on the most challenging single-frequency and single-epoch scenarios, with only GPS constellation utilized. To demonstrate the performance of the proposed approach, we benchmark against the AFM-based [41] and LAMBDA-based search algorithms (the C-LAMBDA method [68] for single-baseline set-ups and the MC-LAMBDA method [118] in multi-baseline scenarios). A 10-degree cut-off elevation mask is used in all cases, as is usually recommended to protect against severe multi-path effects.

6.3.1 Simulation Results

Simulations are implemented based on the Visual software [119] using the assumed antenna position and real GPS constellation information on November 7, 2021. We evaluate the performance of the proposed approach under different noise levels by adding Gaussian noise with different standard deviations to both the pseudo-range and carrier-phase measurements. We also examine the feasibility of the proposed method under adverse satellite geometry conditions, namely scenarios with a poor position dilution of precision (PDOP) due to limited satellite visibility. A pseudo-range to carrier-phase variance ratio $\sigma_\rho^2/\sigma_\psi^2 = 10^4$ is adopted [54]. We consider setups involving one, two, and three baselines with a 1-meter baseline length. In the multi-baseline cases, the baselines are perpendicular to each other, so the baseline matrices in the body frame are

$$\mathbf{X}_b^1 = \begin{bmatrix} 1 & 0 \\ 0 & 1 \end{bmatrix}, \quad \mathbf{X}_b^2 = \begin{bmatrix} 1 & 0 & 0 \\ 0 & 1 & 0 \\ 0 & 0 & 1 \end{bmatrix}. \quad (6.72)$$

For each simulated scenario, the tests are repeated 10^4 times. Each time the attitude angles are generated randomly.

Table 6.1: Success rate (%) versus phase noise σ_ψ (mm), number of satellites (#Sat), and number of baselines.

C-LAMBDA/MC-LAMBDA

AFM

Proposed

| #Sat | σ_ψ | Single Baseline | | | | | Two Baselines | | | | | Three Baselines | | | | |
|------|---------------|-----------------|--------------|--------------|--------------|--------------|---------------|--------------|--------------|--------------|--------------|-----------------|--------------|--------------|--------------|---|
| | | 9 | 7 | 5 | 3 | 1 | 9 | 7 | 5 | 3 | 1 | 9 | 7 | 5 | 3 | 1 |
| 4 | 6.43 | 9.11 | 14.54 | 29.23 | 82.74 | 0 | 0.11 | 1.72 | 22.43 | 99.02 | 0 | 0 | 0 | 0.25 | 88.52 | |
| | 3.33 | 4.01 | 6.23 | 9.37 | 23.78 | 2.08 | 3.12 | 6.55 | 14.56 | 37.75 | 15.67 | 33.22 | 62.61 | 94.09 | 99.01 | |
| | 6.48 | 9.11 | 14.54 | 29.23 | 82.74 | 3.43 | 8.35 | 19.45 | 54.87 | 98.81 | 22.02 | 43.18 | 72.37 | 96.08 | 99.76 | |
| 5 | 13.47 | 21.46 | 37.51 | 70.11 | 99.11 | 1.22 | 6.95 | 40.27 | 96.09 | 99.97 | 0 | 0.15 | 1.13 | 43.54 | 100 | |
| | 7.24 | 11.21 | 19.45 | 39.72 | 83.94 | 7.23 | 21.09 | 45.76 | 78.22 | 95.21 | 52.88 | 81.09 | 95.67 | 99.31 | 99.99 | |
| | 13.47 | 21.47 | 37.51 | 70.11 | 99.11 | 16.54 | 36.82 | 69.44 | 96.27 | 99.97 | 66.47 | 89.45 | 99.1 | 100 | 100 | |
| 6 | 26.97 | 43.88 | 70.40 | 94.48 | 100 | 16.35 | 50.46 | 93.41 | 99.85 | 100 | 0.45 | 4.17 | 43.76 | 100 | 100 | |
| | 17.97 | 31.71 | 51.74 | 80.59 | 98.83 | 26.55 | 58.77 | 76.33 | 98.31 | 99.23 | 84.12 | 94.36 | 98.59 | 99.92 | 100 | |
| | 26.97 | 43.88 | 70.40 | 94.48 | 100 | 47.95 | 76.96 | 96.16 | 99.85 | 100 | 93.19 | 99.36 | 99.99 | 100 | 100 | |
| 7 | 46.42 | 69.04 | 91.22 | 99.38 | 100 | 50.59 | 90.13 | 99.59 | 99.99 | 100 | 6.18 | 42.16 | 97.87 | 100 | 100 | |
| | 37.53 | 57.11 | 79.58 | 95.73 | 99.82 | 48.87 | 78.59 | 92.67 | 99.89 | 100 | 88.31 | 97.31 | 99.31 | 99.99 | 100 | |
| | 46.42 | 69.05 | 91.22 | 99.38 | 100 | 78.16 | 95.12 | 99.59 | 99.99 | 100 | 99.24 | 99.97 | 100 | 100 | 100 | |
| 8 | 67.63 | 87.26 | 98.01 | 99.96 | 100 | 85.51 | 99.16 | 99.96 | 100 | 100 | 37.39 | 89.89 | 100 | 100 | 100 | |
| | 58.02 | 78.06 | 92.68 | 98.69 | 99.94 | 85.01 | 91.13 | 98.11 | 99.89 | 100 | 95.13 | 98.78 | 99.95 | 100 | 100 | |
| | 67.64 | 87.27 | 98.01 | 99.96 | 100 | 93.29 | 99.16 | 99.96 | 100 | 100 | 99.84 | 99.98 | 100 | 100 | 100 | |

Table 6.2: Average number of integers in the search space of the C-LAMBDA or MC-LAMBDA method versus phase noise σ_ψ (mm), number of satellites (#Sat), and number of baselines.

| #Sat | σ_ψ | Single Baseline | | | | | Two Baselines | | | | | Three Baselines | | | | |
|------|---------------|-----------------|--------|--------|-------|------|---------------|---------|---------|---------|--------|-----------------|---------|---------|---------|---------|
| | | 9 | 7 | 5 | 3 | 1 | 9 | 7 | 5 | 3 | 1 | 9 | 7 | 5 | 3 | 1 |
| 4 | | 14203.3 | 6619.9 | 2536.8 | 595.7 | 40.5 | 99916.2 | 99965.5 | 99675.1 | 95971.5 | 4175.6 | 100000 | 100000 | 100000 | 100000 | 73607.3 |
| 5 | | 3656.1 | 1483.7 | 492.3 | 94.6 | 3.8 | 99626.3 | 99255.3 | 89286.8 | 25015.6 | 12.1 | 100000 | 100000 | 100000 | 95734.4 | 49.9 |
| 6 | | 1239.4 | 463.4 | 127.1 | 16.1 | 2.1 | 96414.6 | 81804.9 | 33112.7 | 599.7 | 2.0 | 100000 | 100000 | 93842.6 | 9697.9 | 2.1 |
| 7 | | 533.4 | 166.8 | 34.5 | 3.8 | 2.0 | 80451.1 | 36197.0 | 2107.1 | 10.6 | 2.0 | 99839.2 | 93376.0 | 32230.0 | 40.9 | 2.0 |
| 8 | | 216.4 | 54.8 | 8.6 | 2.3 | 2.0 | 40763.2 | 6298.8 | 76.3 | 2.3 | 2.0 | 93682.6 | 49282.2 | 1020.4 | 2.7 | 2.0 |

Table 6.1 reports the success rates of ambiguity resolution for the proposed method and the benchmark methods. These results are obtained for a number of different scenarios involving different numbers of baselines, different numbers of satellites, and various noise levels. The success rate is calculated as the percentage of trials in which all the integer ambiguities are retrieved correctly. Note that success cases can provide accurate attitude estimation, whereas failure cases tend to produce outliers or estimates that are meaningless. This underscores the pertinence of success rate as a performance indicator.

Based on the search-and-shrink or search-and-expand algorithm, the C-LAMBDA and MC-LAMBDA methods can adaptively adjust the search space in the integer domain. Theoretically, they could find the global optimum of the optimization (2.24). However, the performance of the C-LAMBDA and MC-LAMBDA meth-

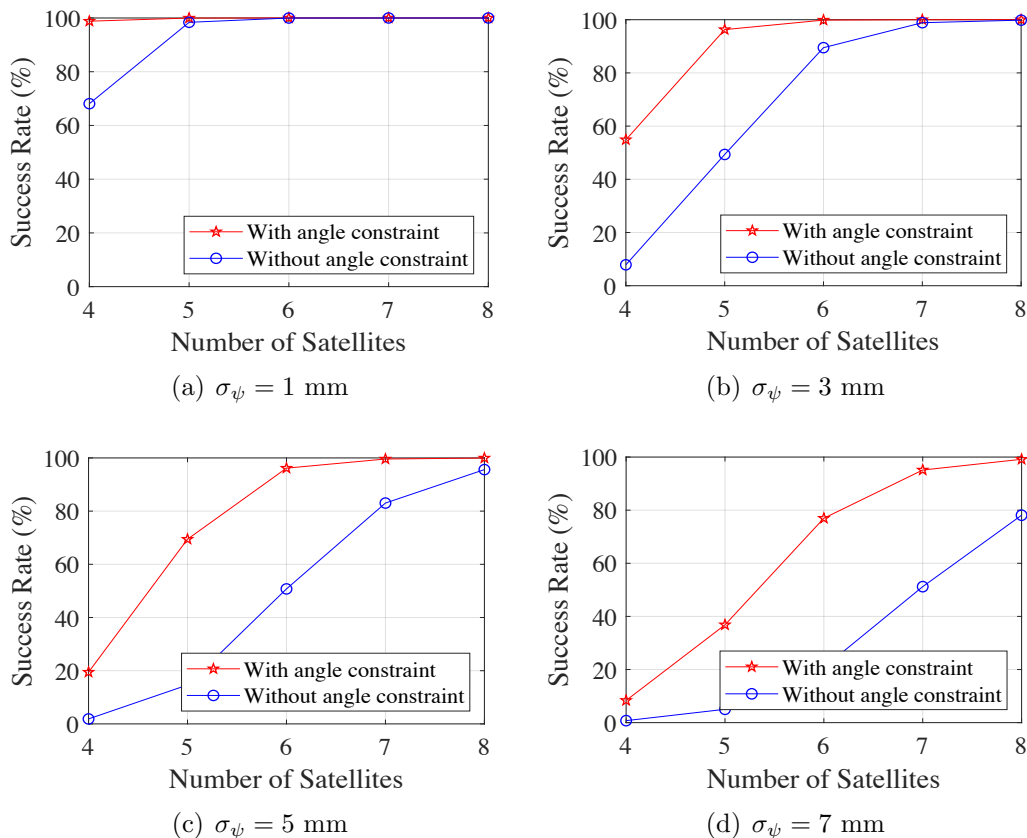


Figure 6.5: Success rate with and without the angle constraint for dual-baseline set-up.

ods dramatically depends on the accuracy of the float solutions. In challenging scenarios, the inadequacy of the float solutions results in an extensive set of potential integer vectors to be evaluated by these two approaches. The set can grow even larger as the number of baselines increases and the dimensionality of the ambiguity vectors/matrices grows. To avoid computational issues due to prohibitively large search spaces, we force the adaptive adjustment strategies of the C-LAMBDA and MC-LAMBDA methods to stop after a search limit of 10^5 integer searches.

As shown in Table 6.1, the proposed approach and the C-LAMBDA method have almost the same success rates in single-baseline configurations, both outperforming the AFM method. In the multiple baseline case, the proposed method utilizes the angle constraint to evaluate and improve the single-baseline estimates; hence, its performance improves as more baselines are used. This should be the

Table 6.3: Computational Complexity of Different Algorithms.

| Algorithms | Complexity |
|-----------------------|--|
| Proposed | $O\left(\mathcal{A}^3 \frac{\mathcal{S}^3(\mathcal{S}-1)}{2} K_w^2\right)$ |
| AFM | $O(\mathcal{A}\mathcal{S}K_a^n)$ |
| C-LAMBDA MC-LAMBDA | $O(\mathcal{A}^2\mathcal{S}^2K_sK_l)$ |

case, more or less, with the MC-LAMBDA method if a search limit is not imposed. However, without the search limit, an unacceptable computational complexity results in the case of the MC-LAMBDA algorithm. As shown in Table 6.2, the C-LAMBDA and MC-LAMBDA methods need to evaluate just a few integer candidates in ideal scenarios. However, an enormous number of integers need to be evaluated in many challenging setups. The application of a search limit to the C-LAMBDA and MC-LAMBDA methods explains their low success rate in Table 6.1, but it makes the two algorithms computationally feasible.

Fig. 6.5 demonstrates how the angle constraint affects the success rate for a dual-baseline set-up. Table 6.1 and Fig. 6.5 demonstrate that the proposed approach provides the highest success rate in almost all scenarios, which illustrates that this method is remarkably effective. In contrast with the AFM-based methods, the C-WLS approach jointly utilizes pseudo-range and carrier-phase measurements instead of only carrier-phase observation. Besides, we strengthen the proposed C-WLS model by incorporating the high correlations of double-difference observations. On the other hand, the proposed approach outperforms the C-LAMBDA and MC-LAMBDA methods, which is attributed to the additional constraint on the carrier-phase residual errors and the proposed search strategy. The superiority of the proposed method is more pronounced in scenarios with fewer satellites and higher noise levels.

Table 6.3 summarizes the computational complexity of different algorithms. We characterize the computational complexity based on the required number of operations. For simplicity, we count each addition, subtraction, multiplication, division, and square root calculation as one arithmetic operation. The complexity

of each method depends on the two parameters \mathcal{A} and \mathcal{S} in addition to a third algorithm-specific parameter K . The computational complexity of the proposed method depends on the parameter K_w , which represents the average number of possible integer ambiguities for each element of Ψ . For the AFM method, we assume that an identical search step is applied for each Euler angle. The parameter K_a represents the number of potential attitude angles, which is practically much greater than K_w . The symbol n denotes the number of Euler angles, i.e., $n = 2$ for a single baseline or $n = 3$ for multiple baselines. Since $\mathcal{A}, \mathcal{S}, K_w \ll K_a$, the complexity of the proposed method is much lower than that of the AFM method, especially in multi-baseline scenarios. Note that K_w and K_a are proportionate to the baseline length. Hence, the proposed approach and the AFM method are more adequate for short-baseline set-ups (meter level). The C-LAMBDA and MC-LAMBDA methods include three steps: shrink the search space, enumerate the integer vectors/matrices, and minimize the objective function [120]. The first step dominates the complexity of these methods as it accounts for at least 60% of the total arithmetic operations [120]. The parameters K_s and $\mathcal{A}^2 \mathcal{S}^2 K_l$ denote the number of iterations in the shrinking process and the required operations in each iteration, respectively. K_s , as shown in Table 6.2, is extremely sensitive to various parameters, such as \mathcal{A} , \mathcal{S} , \mathbf{H} , Ξ , and $\mathbf{\Pi}$; nevertheless, K_l depends on the value of K_s . In ideal environments, the product $K_s K_l$ can be smaller than $\mathcal{A} \frac{\mathcal{S}(\mathcal{S}-1)}{2} K_w^2$ such that the C-LAMBDA and MC-LAMBDA algorithms are more computationally efficient than the proposed approach. However, in challenging scenarios such as those with poor PDOP, high noise levels, and severe multi-path, $K_s K_l$ can be much greater than $\mathcal{A} \frac{\mathcal{S}(\mathcal{S}-1)}{2} K_w^2$ ($K_s K_l$ could reach $10 \mathcal{A} \frac{\mathcal{S}(\mathcal{S}-1)}{2} K_w^2$, $100 \mathcal{A} \frac{\mathcal{S}(\mathcal{S}-1)}{2} K_w^2$, or even more), making the computational complexity of the C-LAMBDA and MC-LAMBDA methods being far worse than that of the proposed method. For instance, consider the antenna geometry described by \mathbf{X}_b^1 in (6.72), i.e., $\mathcal{A} = 2$, with $\sigma_\psi = 3$ mm and $\sigma_\rho = 30$ cm. For $\mathcal{S} = 6$, we have $K_w = 10.19$, $K_a = 180$, $K_s = 10.60$, and $K_l = 35.03$, then $\mathcal{A}^2 \mathcal{S}^2 K_s K_l < \mathcal{A}^3 \frac{\mathcal{S}^3(\mathcal{S}-1)}{2} K_w^2 < \mathcal{A} \mathcal{S} K_a^3$. For

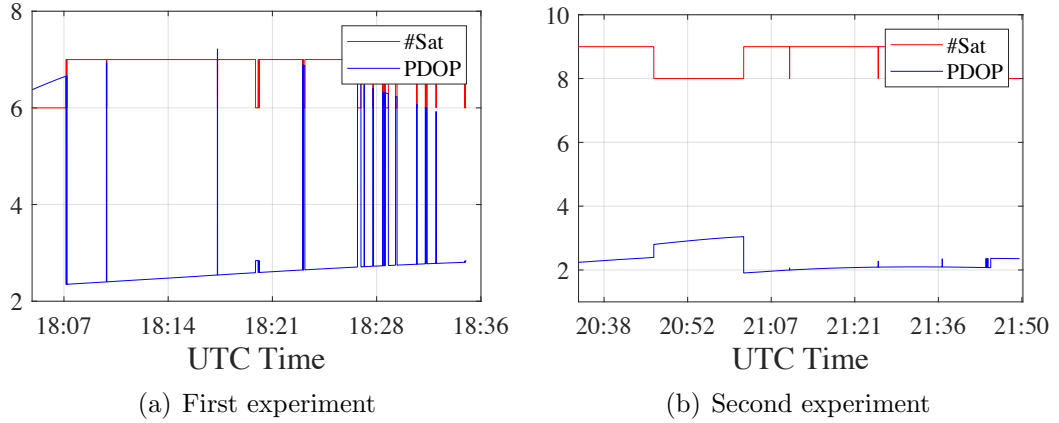


Figure 6.6: The number of tracked satellites and PDOP values.

$\mathcal{S} = 4$, we have $K_w = 8.33$, $K_a = 180$, $K_s = 25015.6$, and $K_l = 14.01$, then we obtain $\mathcal{A}^3 \frac{\mathcal{S}^3(\mathcal{S}-1)}{2} K_w^2 < \mathcal{A}^2 \mathcal{S}^2 K_s K_l < \mathcal{A} \mathcal{S} K_a^3$.

6.3.2 Experimental Results

In this section, we provide performance evaluation based on experimental tests. Three ANAVS multi-sensor modules were used [121], which include a multi-GNSS receiver, an inertial measurement unit (IMU), and a barometer. To be able to measure the ground truth with reasonable accuracy, we consider two static experiments performed on the campus of King Abdullah University of Science and Technology, Thuwal, Saudi Arabia. The receivers were firmly attached to a fixed platform and remained stationary throughout the experiments. The baseline matrix in the body frame used in both tests is described by

$$\mathbf{X}_b^3 = \begin{bmatrix} 0.63 & 0.315 \\ 0 & 0.545 \end{bmatrix}.$$

Two datasets were collected with 5 Hz sampling on 6 April 2021 (between 18:05 and 18:35, UTC time) and 25 May 2021 (from 20:34 to 21:50, UTC time), respectively. The first experiment collected around 9000 epochs of data within 30 minutes, and the other test collected 25500 epochs of observations. We apply the elevation-dependent model to characterize the GNSS observation variance

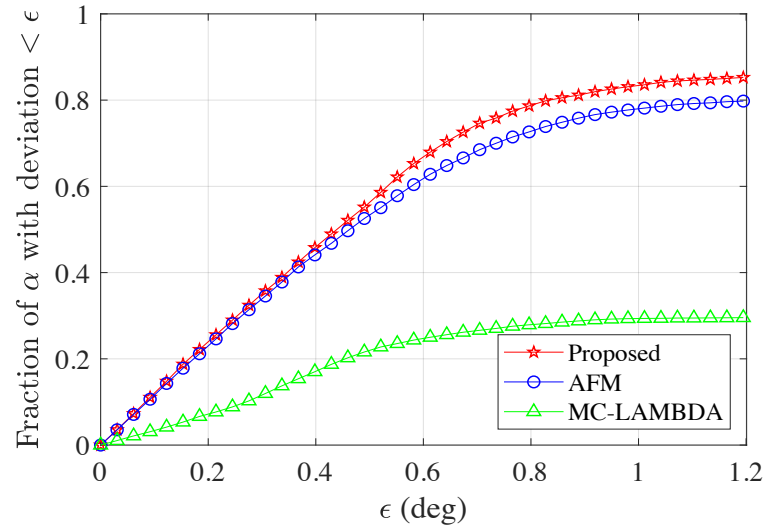
Table 6.4: Success rate (%) and RMSE (deg.) based on the experimental data.

| | Success rate | | | RMSE | | |
|--------|--------------|-------|----------|----------|---------|----------|
| | MC-LAMBDA | AFM | Proposed | α | β | γ |
| Data 1 | 25.85 | 76.20 | 83.18 | 0.13 | 0.92 | 1.27 |
| Data 2 | 99.28 | 97.64 | 99.33 | 0.03 | 0.42 | 0.45 |

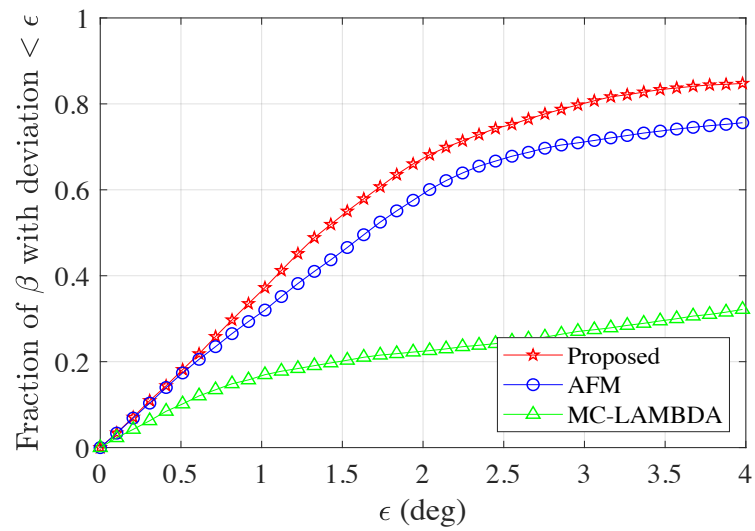
components [122] and consider the correlation introduced by differencing operations. Note that in our comparison of various methods, we utilize only GPS observations, with the number of tracked satellites and the corresponding PDOP values shown in Fig. 6.6. In contrast, the ground truth is estimated by leveraging observations from two GNSS constellations (GPS and GLONASS), IMU measurements, and barometer data integrated over the whole observation time.

Table 6.4 summarizes the experimental results by listing the success rate and the root-mean-square error (RMSE) of attitude angles for the two experiments. Only success cases are considered in calculating the RMSE to eliminate the contribution of outliers. As stated earlier, the constrained search space (at most 10^5 integers) in the integer domain explains the low ambiguity resolution success rate of the MC-LAMBDA method in the first experiment. Data 1 was measured in a particular area with trees, buildings, and other obstructions, which results in signal blockage and multipath errors. Data 2 was collected with good satellite visibility. Hence, the results of data 2 are remarkably better than those obtained from Data 1. From Table 6.4, we see that the proposed method has the best success-rate performance, and the advantage is more significant in challenging environments, which indicates its notable reliability.

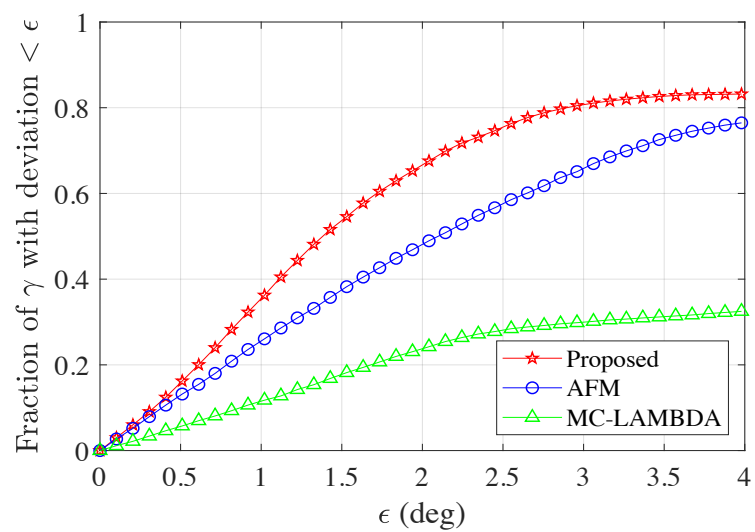
Fig. 6.7 and Fig. 6.8 shows the distribution of attitude angle estimation error for two experiments. From the plots, it can be readily seen that the proposed method obtains the largest fraction of Euler angle estimates with an error smaller than a given value. This is more visible with data 1. These figures indicate that the proposed approach can provide better attitude angle estimates compared with the AFM-based and the MC-LAMBDA methods.



(a) Yaw

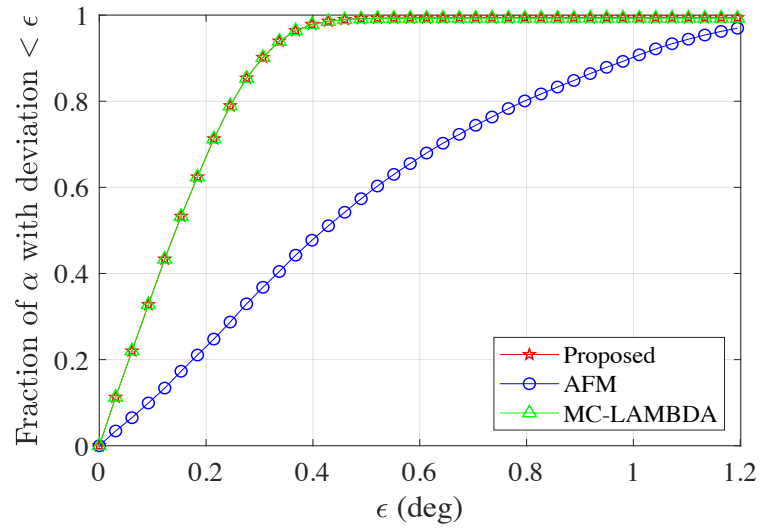


(b) Pitch

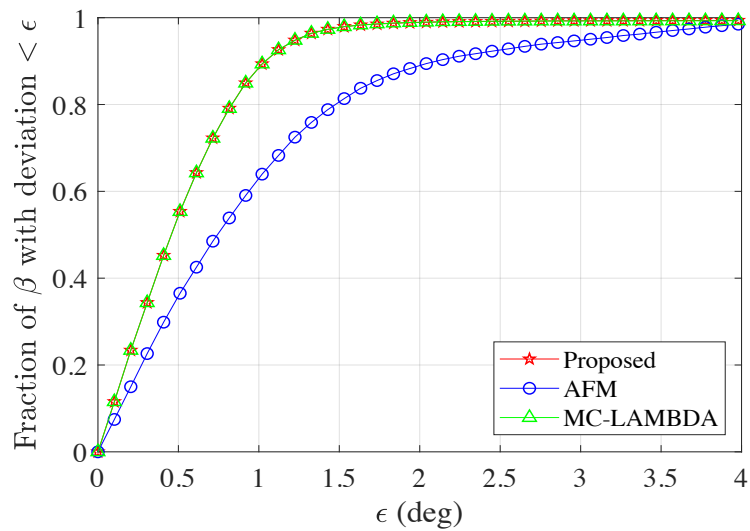


(c) Roll

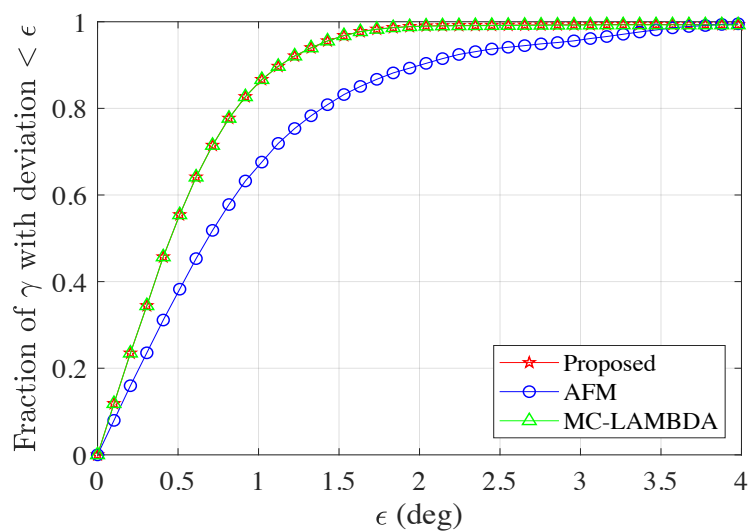
Figure 6.7: Attitude angle error distribution for data 1.



(a) Yaw



(b) Pitch



(c) Roll

Figure 6.8: Attitude angle error distribution for data 2.

6.4 Chapter Summary

A constrained wrapped least-squares (C-WLS) method for attitude determination using multiple GNSS antennas is presented. Unlike existing attitude determination methods, the proposed approach allows the attitude determination problem to be tackled directly—without initially estimating the integer ambiguities—while respecting the antenna array constraints and the integer property of the carrier-phase ambiguities. Given a stated assumption on the double-difference carrier-phase noise, the proposed approach includes an additional constraint on the residual phase to strengthen the optimization model. We solve the C-WLS problem by searching the potential candidates on the unit sphere and obtaining an improved solution through a refinement process. The proposed method targets the estimation of the attitude parameters but inherently returns the integer ambiguities. Simulation and experimental results demonstrate the effectiveness of the proposed approach.

Chapter 7

Integrated Solution for Real-time Kinematic Positioning and Attitude Determination

RTK positioning and attitude determination are usually treated as two independent problems. However, many dynamic systems demand not only precise position but also attitude information, motivating an effort to develop an integrated solution for RTK positioning and attitude determination. Although there are no common parameters in both problems, committing to a joint solution is necessary because of the correlation between the two datasets [90].

Several methods have been proposed to solve RTK positioning and attitude determination simultaneously. It has been reported that the RTK performance improves with the assistance of multi-antenna configuration. In [123, 124], a sequential C-LAMBDA method is adopted to enhance the relative positioning performance using multi-antenna setups. However, it does not manage to do full justice to the given antenna-array information. More recently, the array-aided precise point positioning (A-PPP) concept has been developed to enable faster and improved positioning using the data from multiple antennas on the platform [90], which is extended to the RTK application [125]. A-PPP concept utilizes a decorrelating transformation to decouple the positioning and attitude parameters so that one can first solve the attitude determination problem, whose solution is used to enhance positioning performance subsequently. In [126], the same objective function is used as in the A-PPP model, which is decomposed to maintain only the terms regarding the constraints. The MC-LAMBDA method is used to solve the simplified objective function after decomposition. The methods discussed in the literature [90, 125, 126] can rigorously take advantage of the

orthonormality constraint concerning the antenna array with an integer least-squares formulation.

The unknown parameters and observation errors are usually time-varying for practical GNSS applications [2]. In such scenarios, it is critical to estimate the states of the dynamic system of interest recursively. Kalman filter and its variants are the most prominent of the various recursive techniques, which can minimize the mean squared prediction errors [127, 128]. The main contribution of this work is to design a Kalman-based filter suitable for the integrated RTK positioning and attitude determination (IRTKAD).

Generally, a Kalman filter implementation produces a float solution, that is, a solution without integer constraints, followed by ambiguity resolution. The float solution improves as the GNSS data accumulates. Once sufficient epochs are available, the fixed solution with the integer ambiguities resolved correctly can be achieved. To further enhance the success rate of ambiguity resolution or shorten the required time to fix estimations, we should strengthen the system model so as to improve the float solution as much as possible. Given the prior knowledge concerning the antenna geometry, one can take the orthonormality constraint into account in the process of designing the filter. The difficulty is how to integrate the orthonormality constraint into the filter in a rigorous manner. Due to the presence of the attitude parameters, the state vector of the joint model of RTK and attitude determination lives on a manifold [129, 130, 131]. It has been reported that confining (parts of) the model to a Riemannian manifold often provides better metrics, which benefit the statistical models. Therefore, an unscented Kalman filter on the Riemannian manifold is applied rather than a filter in Euclidean space.

7.1 System Model

Consider a single-antenna GNSS reference station and a rover vehicle equipped with $\mathcal{A}+1$ GNSS antennas. All the antennas track a total of $\mathcal{S}+1$ satellites simul-

taneously. For the sake of simplicity, this contribution focuses on a short-baseline RTK system. However, the proposed methodology can be readily extended to long-baseline RTK positioning as well as other GNSS localization techniques.

For the k -th ($k = 0, 1, 2, \dots, \mathcal{A}$) antenna on the vehicle and the reference station (symbolized as r), we can construct the standard RTK positioning model based on a differential positioning procedure. The single-frequency double-difference (DD) observation equation reads

$$\mathbf{y}_{kr} = \mathbf{H}\mathbf{x}_{kr} + \mathbf{G}\mathbf{n}_{kr} + \mathbf{e}_{kr}, \quad (7.1)$$

where $\mathbf{y}_{kr} \in \mathbb{R}^{2\mathcal{S}}$ represents the DD observation vector consisting of DD carrier phase and pseudo-range, $\mathbf{x}_{kr} \in \mathbb{R}^3$ denotes the unknown relative position between the antenna and reference station, $\mathbf{n}_{kr} \in \mathbb{R}^{\mathcal{S}}$ is the DD carrier-phase ambiguity vector, $\mathbf{H} \in \mathbb{R}^{2\mathcal{S} \times 3}$ and $\mathbf{G} \in \mathbb{R}^{2\mathcal{S} \times \mathcal{S}}$ are the design matrices, and the DD observation noise is given by \mathbf{e}_{kr} .

Taking all the $\mathcal{A} + 1$ GNSS antennas into account, we have the following compact formulation

$$\mathbf{Y} = \mathbf{H}\mathbf{X} + \mathbf{G}\mathbf{N} + \mathbf{E}, \quad (7.2)$$

where

$$\begin{aligned} \mathbf{Y} &= \begin{bmatrix} \mathbf{y}_{0r} & \mathbf{y}_{1r} & \cdots & \mathbf{y}_{\mathcal{A}r} \end{bmatrix} \in \mathbb{R}^{2\mathcal{S} \times (\mathcal{A}+1)}, \\ \mathbf{X} &= \begin{bmatrix} \mathbf{x}_{0r} & \mathbf{x}_{1r} & \cdots & \mathbf{x}_{\mathcal{A}r} \end{bmatrix} \in \mathbb{R}^{3 \times (\mathcal{A}+1)}, \\ \mathbf{N} &= \begin{bmatrix} \mathbf{n}_{0r} & \mathbf{n}_{1r} & \cdots & \mathbf{n}_{\mathcal{A}r} \end{bmatrix} \in \mathbb{Z}^{\mathcal{S} \times (\mathcal{A}+1)}, \\ \mathbf{E} &= \begin{bmatrix} \mathbf{e}_{0r} & \mathbf{e}_{1r} & \cdots & \mathbf{e}_{\mathcal{A}r} \end{bmatrix} \in \mathbb{R}^{2\mathcal{S} \times (\mathcal{A}+1)}. \end{aligned}$$

The vehicle's orientation with respect to the reference coordinate frame, i.e., attitude information, can be determined using the relative position of the GNSS antennas on the vehicle. Given that these antennas are firmly fixed on the vehicle, their relative position in the body coordinate system, \mathbf{X}_b , can be precisely

measured in advance and used as prior knowledge. Without loss of generality, let the antenna 0 be a reference and the others be auxiliary. Based on the known geometry of the antenna array, we can express the auxiliary antennas' positions as a function of platform attitude and the position of the main antenna. The unknown position matrix can be expressed as

$$\mathbf{X} = \begin{bmatrix} \mathbf{x}_{0r}, & \mathbf{1}_{\mathcal{A}}^T \otimes \mathbf{x}_{0r} + \mathbf{R}\mathbf{X}_b \end{bmatrix}, \quad (7.3)$$

where $\mathbf{1}_{\mathcal{A}}$ is an \mathcal{A} -dimensional all-one column vector, \otimes denotes the Kronecker product, \mathbf{T} indicates the matrix, the orthogonal matrix $\mathbf{R} \in \mathbb{O}^{3 \times q}$ represents the rotation from the body coordinate frame to the reference coordinate frame, and $q = \min(3, \mathcal{A})$.

If we assume to have the same type of antennas, the observations of various antennas have the identical stochastic model. The DD observation covariance matrices are formulated as

$$\begin{aligned} \mathbf{Q} &= \text{Cov}(\mathbf{y}_{kr}) \\ &= \mathbb{E} \left[(\mathbf{y}_{kr} - \mathbb{E}(\mathbf{y}_{kr})) (\mathbf{y}_{kr} - \mathbb{E}(\mathbf{y}_{kr}))^T \right], \quad k = 0, 1, 2, \dots, \mathcal{A}, \end{aligned} \quad (7.4)$$

where $\mathbb{E}(\cdot)$ represents the expectation operator, and $\text{Cov}(\cdot)$ produces the covariance matrix. Then, we have

$$\mathbf{Q}_{\mathbf{Y}} = \text{Cov}(\text{vec}(\mathbf{Y})) = \mathbf{P} \otimes \mathbf{Q}, \quad (7.5)$$

where $\text{vec}(\cdot)$ denotes the vectorization operator, and \mathbf{P} is a square matrix of order $\mathcal{A} + 1$ that is defined as

$$\mathbf{P} = \begin{bmatrix} 1 & 0.5 & \cdots & 0.5 \\ 0.5 & 1 & \cdots & 0.5 \\ & & \ddots & \\ 0.5 & 0.5 & \cdots & 1 \end{bmatrix}. \quad (7.6)$$

Combining (7.2)–(7.6), we can establish the integrated model for RTK positioning and attitude determination. The covariance matrix \mathbf{Q}_Y shows the correlation that exists between \mathbf{y}_{kr} , revealing the GNSS positioning and attitude determination are not independent. This correlation has to be taken into account to rigorously estimate the unknown parameters, inclusive of \mathbf{x}_{0r} , \mathbf{R} , and \mathbf{N} . It should be noted that the DD carrier-phase ambiguities satisfy

$$\mathbf{n}_{kr} = \mathbf{n}_{0r} + \mathbf{n}_{k0}, \quad k = 1, 2, \dots, \mathcal{A}. \quad (7.7)$$

When the attitude has already been estimated reliably using traditional methods based on GNSS or other techniques, \mathbf{n}_{k0} can be treated as known parameters if no cycle slip occurs. As a consequence of that, the unknown variables are \mathbf{x}_{0r} , \mathbf{R} , and \mathbf{n}_{0r} in the ensuing motions.

A Kalman filter (KF) or its variants can be used to precisely estimate the unknowns and recursively update the solution using the GNSS data received. The difficulty derives from the presence of the integer and orthonormality constraints. It is challenging to incorporate the integer constraint into the filter directly. Therefore, the integer constraint is generally ignored to apply the filters to produce the so-called float solution, followed by the ambiguity resolution. The fixed solution is available if the carrier-phase ambiguities are resolved to the correct integer values.

On the other hand, as will be stated later, one can leverage the orthonormality constraint to strengthen the filter. Note that \mathbf{R} lies on Riemannian manifolds, as does the whole unknown state vector. Thus, we can integrate the Kalman-based filter with Riemannian optimization. In this paper, a variant of the unscented Kalman filter (UKF) on the Riemannian manifold is utilized to estimate GNSS parameters recursively, with the solutions satisfying the orthonormality constraint inherently.

7.2 Classical Unscented Kalman Filter

The UKF is a non-linear version of the KF that works on the systems with non-linear dynamics and observation models. In contrast to the extended Kalman filter (EKF), UKF utilizes an unscented transformation instead of a linearization of non-linear system equations. The linearization considers only the first-order Taylor expansion with higher-order terms omitted, which degrades estimation accuracy in highly non-linear systems. For UKF, the usage of unscented transformation can avoid the drawbacks of linearization, leading to higher estimation accuracy. Before stating the generalized UKF on Riemannian manifolds, we first review the classical version in Euclidean space.

Consider a dynamics system with the process and measurement models given by

$$\mathbf{x}_t = f(\mathbf{x}_{t-1}) + \boldsymbol{\delta}_t, \quad (7.8)$$

$$\mathbf{y}_t = h(\mathbf{x}_t) + \boldsymbol{\varepsilon}_t, \quad (7.9)$$

where $\mathbf{x}_t \in \mathbb{R}^n$ and $\mathbf{y}_t \in \mathbb{R}^m$ are the state and observation vectors at time point t , respectively, the function $f: \mathbb{R}^n \rightarrow \mathbb{R}^n$ and $h: \mathbb{R}^n \rightarrow \mathbb{R}^m$ are assumed known, and $\boldsymbol{\delta}_t \sim \mathcal{N}(0, \mathbf{Q}_{\boldsymbol{\delta}_t})$ and $\boldsymbol{\varepsilon}_t \sim \mathcal{N}(0, \mathbf{Q}_{\boldsymbol{\varepsilon}_t})$ denote independent Gaussian noise.

Let $\boldsymbol{\mu}_{t-1}$ and $\mathbf{Q}_{\mathbf{x}_{t-1}}$ be the mean and covariance of the variable \mathbf{x}_{t-1} . We can define $2n + 1$ sigma points as following

$$\begin{aligned} \boldsymbol{\sigma}_{t-1}^{(0)} &= \boldsymbol{\mu}_{t-1}, \\ \boldsymbol{\sigma}_{t-1}^{(k)} &= \boldsymbol{\mu}_{t-1} + \left(\sqrt{(n + \xi) \mathbf{Q}_{\mathbf{x}_{t-1}}} \right)_k, \\ \boldsymbol{\sigma}_{t-1}^{(k+n)} &= \boldsymbol{\mu}_{t-1} - \left(\sqrt{(n + \xi) \mathbf{Q}_{\mathbf{x}_{t-1}}} \right)_k, \quad k = 1, \dots, n, \end{aligned} \quad (7.10)$$

where $(\sqrt{\cdot})_k$ represents the k -th column of the Cholesky decomposition of a matrix, and the parameter ξ controls the distance between the sigma points and the mean value.

Based on the sigma points, the state vector can be predicted using

$$\hat{\mathbf{x}}_t = \hat{\boldsymbol{\mu}}_t = \sum_{k=0}^{2n} \omega_k^{(m)} f\left(\boldsymbol{\sigma}_{t-1}^{(k)}\right), \quad (7.11)$$

with the covariance matrix

$$\hat{\mathbf{Q}}_{\mathbf{x}_t} = \sum_{k=0}^{2n} \omega_k^{(c)} \left[f\left(\boldsymbol{\sigma}_{t-1}^{(k)}\right) - \hat{\mathbf{x}}_t \right] \left[f\left(\boldsymbol{\sigma}_{t-1}^{(k)}\right) - \hat{\mathbf{x}}_t \right]^T + \mathbf{Q}_{\boldsymbol{\delta}_t}, \quad (7.12)$$

where $\omega_k^{(m)}$ and $\omega_k^{(c)}$ denote the weights defined as

$$\begin{aligned} \omega_0^{(m)} &= \frac{\xi}{n + \xi}, \\ \omega_0^{(c)} &= \frac{\xi}{n + \xi} + (1 - \alpha^2 + \beta), \\ \omega_k^{(m)} &= \omega_k^{(c)} = \frac{1}{2(n + \xi)}, \quad k = 1, \dots, 2n, \end{aligned} \quad (7.13)$$

where α represents the spread of the sigma points around the mean value, and β demonstrates the prior distribution knowledge of the state.

According to (7.10), one can use $\hat{\boldsymbol{\mu}}_t$ and $\hat{\mathbf{Q}}_{\mathbf{x}_t}$ to achieve another $2n + 1$ sigma points, i.e., $\hat{\boldsymbol{\sigma}}_t^{(0)}$, $\hat{\boldsymbol{\sigma}}_t^{(1)}$, \dots , $\hat{\boldsymbol{\sigma}}_t^{(2n)}$. Subsequently, the predicted observation and the corresponding covariance are given by

$$\hat{\mathbf{y}}_t = \sum_{k=0}^{2n} \omega_k^{(m)} h\left(\hat{\boldsymbol{\sigma}}_t^{(k)}\right), \quad (7.14)$$

$$\hat{\mathbf{Q}}_{\mathbf{y}_t} = \sum_{k=0}^{2n} \omega_k^{(c)} \left[h\left(\hat{\boldsymbol{\sigma}}_t^{(k)}\right) - \hat{\mathbf{y}}_t \right] \left[h\left(\hat{\boldsymbol{\sigma}}_t^{(k)}\right) - \hat{\mathbf{y}}_t \right]^T + \mathbf{Q}_{\boldsymbol{\varepsilon}_t}. \quad (7.15)$$

Once the real observation \mathbf{y}_t is available, the correction step can be carried out using

$$\mathbf{x}_t = \boldsymbol{\mu}_t = \hat{\mathbf{x}}_t + \mathbf{K}_t (\mathbf{y}_t - \hat{\mathbf{y}}_t), \quad (7.16)$$

$$\mathbf{Q}_{\mathbf{x}_t} = \hat{\mathbf{Q}}_{\mathbf{x}_t} - \mathbf{K}_t \hat{\mathbf{Q}}_{\mathbf{y}_t} \mathbf{K}_t^T, \quad (7.17)$$

where \mathbf{K}_t represents the so-called Kalman gain

$$\mathbf{K}_t = \hat{\mathbf{Q}}_{\mathbf{x}_t \mathbf{y}_t} \left(\hat{\mathbf{Q}}_{\mathbf{y}_t} \right)^{-1}, \quad (7.18)$$

and $\hat{\mathbf{Q}}_{\mathbf{x}_t \mathbf{y}_t}$ is the cross-covariance of $\hat{\mathbf{x}}_t$ and $\hat{\mathbf{y}}_t$

$$\hat{\mathbf{Q}}_{\mathbf{x}_t \mathbf{y}_t} = \sum_{k=0}^{2n} \omega_k^{(c)} \left[f \left(\hat{\boldsymbol{\sigma}}_t^{(k)} \right) - \hat{\mathbf{x}}_t \right] \left[h \left(\hat{\boldsymbol{\sigma}}_t^{(k)} \right) - \hat{\mathbf{y}}_t \right]^T. \quad (7.19)$$

7.3 Unscented Kalman Filter on Riemannian Manifolds

If the state and observation are on manifolds, one can treat this characteristic as a constraint to obtain a high-quality estimation. The key to generalizing the UKF to Riemannian manifolds is to force the estimates to fall in the corresponding space. It is also essential to define the covariance appropriately. In this section, we first present the structure of the generalized UKF on Riemannian manifolds [132, 133], which is named as the Riemannian manifold-based UKF (RieMUKF). Then, we will address the required Riemannian manifold-related terminology elements to apply the RieMUKF to this work.

7.3.1 The Structure of RieMUKF

Assume that the process and measurement models are formulated as

$$\mathbf{x}_t = \bar{f}(\mathbf{x}_{t-1}) \boxplus \boldsymbol{\delta}_t, \quad (7.20)$$

$$\mathbf{y}_t = \bar{h}(\mathbf{x}_t) \boxplus \boldsymbol{\varepsilon}_t, \quad (7.21)$$

where the state \mathbf{x}_t and observation \mathbf{y}_t are on the manifold \mathcal{M} and \mathcal{M}_{obs} , respectively, $\bar{f} : \mathcal{M} \rightarrow \mathcal{M}$ and $\bar{h} : \mathcal{M} \rightarrow \mathcal{M}_{\text{obs}}$ are the known functions that map the variables from a manifold to a possibly different manifold, and $\boldsymbol{\delta}_t \sim \mathcal{N}(0, \mathbf{Q}_{\boldsymbol{\delta}_t})$ and $\boldsymbol{\varepsilon}_t \sim \mathcal{N}(0, \mathbf{Q}_{\boldsymbol{\varepsilon}_t})$ represent independent Gaussian noise. The box-plus operator is defined as $\boxplus : \mathcal{M} \times \mathbb{R}^n \rightarrow \mathcal{M}$, which represents a generalized addition mov-

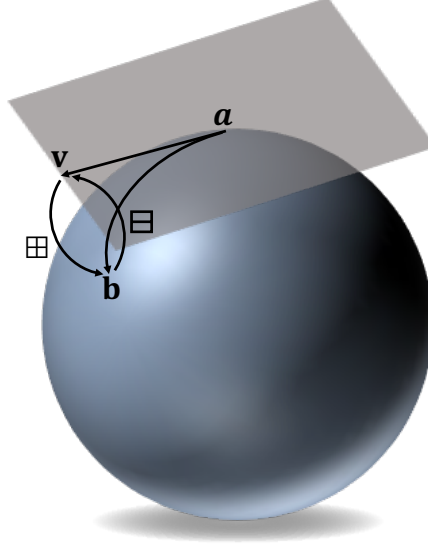


Figure 7.1: Graphical illustration of the operators \boxplus and \boxminus .

ing the point on \mathcal{M} to another point on the same manifold \mathcal{M} according to the associated perturbation in Euclidean space. Likewise, we define the box-minus operator as $\boxminus : \mathcal{M} \times \mathcal{M} \rightarrow \mathbb{R}^n$, which is a generalized subtraction measuring the difference, expressed in Euclidean space, between two points on the manifold. The operators \boxplus and \boxminus are illustrated in Figure 7.1, where \mathbf{a} and \mathbf{b} are on a manifold (a sphere), $\mathbf{b} = \mathbf{a} \boxplus \mathbf{v}$, and $\mathbf{v} = \mathbf{b} \boxminus \mathbf{a}$.

If the mean $\boldsymbol{\mu}_{t-1} \in \mathcal{M}$ and the covariance matrix $\mathbf{Q}_{\mathbf{x}_{t-1}}$ of the state \mathbf{x}_{t-1} are known, we can define $2n + 1$ sigma points on \mathcal{M} as

$$\begin{aligned} \boldsymbol{\sigma}_{t-1}^{(0)} &= \boldsymbol{\mu}_{t-1}, \\ \boldsymbol{\sigma}_{t-1}^{(k)} &= \boldsymbol{\mu}_{t-1} \boxplus \left(\sqrt{(n + \xi) \mathbf{Q}_{\mathbf{x}_{t-1}}} \right)_k, \\ \boldsymbol{\sigma}_{t-1}^{(k+n)} &= \boldsymbol{\mu}_{t-1} \boxplus \left(-\sqrt{(n + \xi) \mathbf{Q}_{\mathbf{x}_{t-1}}} \right)_k, \quad k = 1, \dots, n. \end{aligned} \quad (7.22)$$

Based on the definition of \boxplus , all the sigma points lie on the manifold \mathcal{M} .

The predicted state is defined as the mean value of the sigma points on the manifold, that is

$$\hat{\mathbf{x}}_t = \hat{\boldsymbol{\mu}}_t = \arg \min_{\mathbf{x} \in \mathcal{M}} \sum_{k=0}^{2n} \omega_k^{(m)} d^2 \left[\bar{f} \left(\boldsymbol{\sigma}_{t-1}^{(k)} \right), \mathbf{x} \right], \quad (7.23)$$

with the covariance matrix

$$\hat{\mathbf{Q}}_{\mathbf{x}_t} = \sum_{k=0}^{2n} \omega_k^{(c)} \left[\bar{f}(\boldsymbol{\sigma}_{t-1}^{(k)}) \ominus \hat{\mathbf{x}}_t \right] \left[\bar{f}(\boldsymbol{\sigma}_{t-1}^{(k)}) \ominus \hat{\mathbf{x}}_t \right]^T + \mathbf{Q}_{\delta_t}, \quad (7.24)$$

where $d(\cdot, \cdot)$ denotes geodesic distance on the manifold \mathcal{M} . Let $\gamma : [0, 1] \rightarrow \mathcal{M}$ be a continuously differentiable curve connecting $\mathbf{a} \in \mathcal{M}$ and $\mathbf{b} \in \mathcal{M}$ ($\gamma(0) = \mathbf{a}$ and $\gamma(1) = \mathbf{b}$). The length of γ is formulated as

$$L(\gamma) = \int_0^1 \langle \gamma'(t), \gamma'(t) \rangle_{\gamma(t)} dt, \quad (7.25)$$

with the Riemannian metric $\langle \cdot, \cdot \rangle_{\mathbf{x}}$ at point $\mathbf{x} \in \mathcal{M}$. The geodesic distance $d(\cdot, \cdot)$ refers to the infimum of the length $L(\gamma)$ for all continuous, piecewise continuously differentiable curves γ .

Using $\hat{\boldsymbol{\mu}}_t \in \mathcal{M}$ and $\hat{\mathbf{Q}}_{\mathbf{x}_t}$, we can obtain another set of the sigma points, i.e., $\hat{\boldsymbol{\sigma}}_t^{(0)}, \hat{\boldsymbol{\sigma}}_t^{(1)}, \dots, \hat{\boldsymbol{\sigma}}_t^{(2n)}$. The predicted observation and covariance matrix can be calculated using

$$\hat{\mathbf{y}}_t = \arg \min_{\mathbf{y} \in \mathcal{M}_{\text{obs}}} \sum_{k=0}^{2n} \omega_k^{(m)} d^2 \left[\bar{h}(\hat{\boldsymbol{\sigma}}_t^{(k)}), \mathbf{y} \right], \quad (7.26)$$

$$\hat{\mathbf{Q}}_{\mathbf{y}_t} = \sum_{k=0}^{2n} \omega_k^{(c)} \left[h(\hat{\boldsymbol{\sigma}}_t^{(k)}) \ominus \hat{\mathbf{y}}_t \right] \left[h(\hat{\boldsymbol{\sigma}}_t^{(k)}) \ominus \hat{\mathbf{y}}_t \right]^T + \mathbf{Q}_{\epsilon_t}. \quad (7.27)$$

Similar to the UFK in Euclidean space, we can also define the cross-covariance and the Kalman gain as following

$$\hat{\mathbf{Q}}_{\mathbf{x}_t \mathbf{y}_t} = \sum_{k=0}^{2n} \omega_k^{(c)} \left[f(\hat{\boldsymbol{\sigma}}_t^{(k)}) \ominus \hat{\mathbf{x}}_t \right] \left[h(\hat{\boldsymbol{\sigma}}_t^{(k)}) \ominus \hat{\mathbf{y}}_t \right]^T, \quad (7.28)$$

$$\mathbf{K}_t = \hat{\mathbf{Q}}_{\mathbf{x}_t \mathbf{y}_t} \left(\hat{\mathbf{Q}}_{\mathbf{y}_t} \right)^{-1}. \quad (7.29)$$

The real observation is utilized to correct the estimation as follows. We cal-

culate the correction term in Euclidean space and update the covariance

$$\Delta_{\mathbf{x}_t} = \mathbf{K}_t (\mathbf{y}_t \boxminus \hat{\mathbf{y}}_t), \quad (7.30)$$

$$\bar{\mathbf{Q}}_{\mathbf{x}_t} = \hat{\mathbf{Q}}_{\mathbf{x}_t} - \mathbf{K}_t \hat{\mathbf{Q}}_{\mathbf{y}_t} \mathbf{K}_t^T, \quad (7.31)$$

which are use to construct a new sigma point set

$$\begin{aligned} \bar{\boldsymbol{\sigma}}_t^{(0)} &= \hat{\boldsymbol{\mu}}_t \boxplus \Delta_{\mathbf{x}_t}, \\ \bar{\boldsymbol{\sigma}}_t^{(k)} &= \hat{\boldsymbol{\mu}}_t \boxplus \left(\Delta_{\mathbf{x}_t} + \sqrt{(n + \xi) \bar{\mathbf{Q}}_{\mathbf{x}_t}} \right)_k, \\ \bar{\boldsymbol{\sigma}}_t^{(k+n)} &= \hat{\boldsymbol{\mu}}_t \boxplus \left(\Delta_{\mathbf{x}_t} - \sqrt{(n + \xi) \bar{\mathbf{Q}}_{\mathbf{x}_t}} \right)_k, \quad k = 1, \dots, n. \end{aligned} \quad (7.32)$$

Finally, we have

$$\mathbf{x}_t = \boldsymbol{\mu}_t = \arg \min_{\mathbf{x} \in \mathcal{M}} \sum_{k=0}^{2n} \omega_k^{(m)} d^2 \left[\bar{f} \left(\bar{\boldsymbol{\sigma}}_t^{(k)} \right), \mathbf{x} \right], \quad (7.33)$$

$$\mathbf{Q}_{\mathbf{x}_t} = \sum_{k=0}^{2n} \omega_k^{(c)} \left[\bar{f} \left(\bar{\boldsymbol{\sigma}}_t^{(k)} \right) \boxminus \mathbf{x}_t \right] \left[\bar{f} \left(\bar{\boldsymbol{\sigma}}_t^{(k)} \right) \boxminus \mathbf{x}_t \right]^T + \mathbf{Q}_{\delta_t}. \quad (7.34)$$

7.3.2 Required Riemannian Manifold-related Terminology

In this work, the GNSS observation matrix is in Euclidean space, that is, $\mathbf{Y} \in \mathbb{R}^{2S \times (A+1)}$. We just need to study the required Riemannian manifold-related terminology elements for the unknown state. As discussed in Section 7.1, the unknown parameters include $\mathbf{x}_{0r} \in \mathbb{R}^3$, $\mathbf{R} \in \mathbb{O}^{3 \times q}$, and $\mathbf{N} \in \mathbb{Z}^{S \times (A+1)}$. Besides, to accurately describe the vehicle's motions, we can also take the velocity, acceleration, and change of the rotation matrix into account, with the corresponding variables $\mathbf{v}_{0r} \in \mathbb{R}^3$, $\mathbf{a}_{0r} \in \mathbb{R}^3$, and $\boldsymbol{\Omega} \in \mathbb{O}^{3 \times 3}$, respectively.

Similar to the standard RTK positioning routine, we first ignore the integer constraint to get the float solutions. Then, a search is performed around the float solution to resolve the integer unknowns and compute the fixed solution. However, maintaining the orthonormality constraint, forcing the state on the

manifolds, distinguish the proposed algorithm from the existing methods. The RieMUFK stated in Section 7.3.1 is used to process multi-epoch GNSS data to improve the quality of the float solutions over time. Therefore, the state lies in the following set

$$\mathbb{S} = \mathbb{R}^3 \times \mathbb{R}^3 \times \mathbb{R}^3 \times \mathbb{R}^{\mathcal{S} \times (\mathcal{A}+1)} \times \mathbb{O}^{3 \times q} \times \mathbb{O}^{3 \times 3}. \quad (7.35)$$

Since the Cartesian product of the manifolds yields another, the state in this work is also a manifold, namely, a compound manifold. To deal with a compound manifold, the definition of \boxplus and \boxminus satisfies that if $\mathbf{x}_1, \mathbf{y}_1 \in \mathcal{M}_1$ and $\mathbf{x}_2, \mathbf{y}_2 \in \mathcal{M}_2$, we have

$$\begin{pmatrix} \mathbf{x}_1, \mathbf{x}_2 \end{pmatrix} \boxplus \begin{pmatrix} \boldsymbol{\delta}_1 \\ \boldsymbol{\delta}_2 \end{pmatrix} = \begin{pmatrix} \mathbf{x}_1 \boxplus_{\mathcal{M}_1} \boldsymbol{\delta}_1, \mathbf{x}_2 \boxplus_{\mathcal{M}_2} \boldsymbol{\delta}_2 \end{pmatrix}, \quad (7.36)$$

$$\begin{pmatrix} \mathbf{y}_1, \mathbf{y}_2 \end{pmatrix} \boxminus \begin{pmatrix} \mathbf{x}_1, \mathbf{x}_2 \end{pmatrix} = \begin{pmatrix} \mathbf{y}_1 \boxminus_{\mathcal{M}_1} \mathbf{x}_1 \\ \mathbf{y}_2 \boxminus_{\mathcal{M}_2} \mathbf{x}_2 \end{pmatrix}, \quad (7.37)$$

where the subscripts indicate the corresponding manifolds on which to use the \boxplus and \boxminus operators.

The operators \boxplus and \boxminus can be defined using different forms. Here we use the retraction and inverse retraction mapping to define \boxplus and \boxminus , respectively. At each point $\mathbf{x} \in \mathcal{M}$, the manifold \mathcal{M} locally resembles a linear space, i.e., a Euclidean space, which is known as the tangent space $\mathcal{T}_{\mathbf{x}}\mathcal{M}$. The retraction and inverse retraction map points back and forth between the manifold \mathcal{M} and the tangent space $\mathcal{T}_{\mathbf{x}}\mathcal{M}$. The retraction operation at a point $\mathbf{x} \in \mathcal{M}$ maps a tangent vector $\mathbf{v} \in \mathcal{T}_{\mathbf{x}}\mathcal{M}$ to the point $\mathbf{y} = \mathfrak{R}_{\mathbf{x}}(\mathbf{v}) \in \mathcal{M}$. The inverse retraction mapping is expressed as $\mathbf{v} = \mathfrak{R}_{\mathbf{x}}^{-1}(\mathbf{y}) \in \mathcal{T}_{\mathbf{x}}\mathcal{M}$. It is readily seen that the covariance is calculated in the tangent space. The cross-covariance is measured for the variables in two different tangent spaces.

According to (7.36) and (7.37), we can just establish the required operators for each single manifold component ($\mathbf{R} \in \mathbb{O}^{3 \times q}$ and $\mathbf{\Omega} \in \mathbb{O}^{3 \times 3}$) and extend the results to the compound manifold. If there are four or more antennas on each platform, both \mathbf{R} and $\mathbf{\Omega}$ are in $\mathbb{O}^{3 \times 3}$, which is a three-dimensional orientation, i.e., $\text{SO}(3)$. However, it is not valid when the number of antennas is less than four. To express the solution in a compact form for different number of antennas, the potential solution set \mathcal{M} for \mathbf{R} and $\mathbf{\Omega}$ are in $\mathbb{O}^{3 \times 3}$ is given by

$$\mathcal{M} = \{ \mathbf{x} \in \mathbb{R}^{3 \times q} \mid \mathbf{x}^T \mathbf{x} = \mathbf{I}_q \}, \quad q = 1, 2, 3, \quad (7.38)$$

which is well known as the Stiefel manifold.

The tangent space of the the Stiefel manifold \mathcal{M} , a subspace of $\mathbb{R}^{3 \times q}$, is given by

$$\mathcal{T}_x \mathcal{M} = \{ \mathbf{v} \in \mathbb{R}^{3 \times q} \mid \mathbf{x}^T \mathbf{v} + \mathbf{v}^T \mathbf{x} = \mathbf{0} \}. \quad (7.39)$$

With $\mathbf{x} \in \mathcal{M}$ and $\mathbf{v} \in \mathcal{T}_x \mathcal{M}$, the retraction mapping can be formulated as [104]

$$\begin{aligned} \mathfrak{R}_x(\mathbf{v}) &= (\mathbf{x} + \mathbf{v}) \left((\mathbf{x} + \mathbf{v})^T (\mathbf{x} + \mathbf{v}) \right)^{-\frac{1}{2}} \\ &= (\mathbf{x} + \mathbf{v}) (\mathbf{I}_q + \mathbf{v}^T \mathbf{v})^{-\frac{1}{2}}, \end{aligned} \quad (7.40)$$

where $(\cdot)^{-\frac{1}{2}}$ denotes the inverse square root of matrix, and \mathbf{I}_q is an identity matrix of size q . (7.40) is known as the polar retraction for the Stiefel manifold. Given $\mathbf{x}, \mathbf{y} \in \mathcal{M}$, the inverse of the polar retraction reads

$$\mathfrak{R}_x^{-1}(\mathbf{y}) = \mathbf{y} \mathbf{z} - \mathbf{x}, \quad (7.41)$$

where \mathbf{z} is an upper triangular matrix as the solution of the following equation

$$2\mathbf{I}_q = (\mathbf{x}^T \mathbf{y}) \mathbf{z} + \mathbf{z}^T (\mathbf{x}^T \mathbf{y})^T. \quad (7.42)$$

Based on (7.35)–(7.42), we can obtain all the necessary terminology ingredients to apply the UKF on Riemannian manifolds. More detailed information about manifolds can be found in [107, 94, 108].

7.4 Performance Evaluation

In this section, we evaluate the performance of the proposed method for different scenarios using simulated and experimental GNSS data. Here we use the traditional RTK positioning technique with a single antenna as a benchmark. For the multi-antenna scenarios, we solve the problem using the UKFs in Euclidean space and on the Riemannian manifold. The former takes advantage of only the linear constraint introduced by $\mathbf{R} \in \mathbb{R}^{3 \times q}$, which is defined as the loose IRTKAD method because of partially losing the geometry information of the antenna array. In contrast, the latter stands for the proposed IRTKAD, which can fully leverage the orthonormality constraint.

7.4.1 Simulation

Simulations were conducted to investigate the proposed method under controlled environments. We consider 6 GPS satellites, a single reference station, and a rover with four antennas. These antennas are firmly mounted on the vehicle in a configuration with three perpendicular 2-meter baselines. With dual, triple, and quadruple antennas employed, the associated coordinates in the body frame system can be expressed as

$$\mathbf{x}_b^{(1)} = 2, \quad \mathbf{x}_b^{(2)} = \begin{bmatrix} 2 & 0 \\ 0 & 2 \end{bmatrix}, \quad \mathbf{x}_b^{(3)} = \begin{bmatrix} 2 & 0 & 0 \\ 0 & 2 & 0 \\ 0 & 0 & 2 \end{bmatrix}.$$

The vehicle was assumed to move at constant speed in a circular horizontal track with a 1-kilometer radius around the base station. It took 20 minutes to make a round of the circle. We obtained the vehicle’s position and attitude associated

with the assumed movement. We generated the GNSS data with a 1-Hz sampling rate, wherein additive zero mean Gaussian noise with 3-millimeter and 0.3-meter standard deviation are added to the carrier phase and pseudo-range, respectively. Moreover, we assume no cycle slip happened during the test such that the carrier-phase ambiguities were constant integers. Finally, the previous state deemed to be known that is used for initialization.

Figure 7.2 demonstrates the position errors of the float solutions versus epochs for a different number of antennas. According to Figure 7.2, the RTK technique and loose IRTKAD method achieve comparable positioning accuracy using dual, triple, or quadruple antennas. In contrast to the other two approaches, the proposed method can enhance the positioning accuracy by leveraging the geometry information of the antenna array to the filtering, whose performance improves as the number of GNSS antennas increases.

As shown in Figure 7.3, we also computed the positioning root mean square error (RMSE) of the float and fixed solutions. The proposed method can significantly reduce the float positioning RMSE compared with RTK and the loose IRTKAD, indicating the function of the orthonormality constraint. With dual, triple, and quadruple antennas applied, the positioning RMSEs of the float solutions of the proposed method are 11.4 cm, 7.5 cm, and 5.9 cm, respectively. On the other hand, the fixed solutions can achieve much higher positioning accuracy than the float solutions due to the presence of integer constraints. The RTK technique and the loose IRTKAD method with two to four antennas obtain the same fixed position RMSE. By contrast, the proposed method can still improve the positioning accuracy of the fixed solutions.

In addition to position estimations, the loose IRTKAD and the tight IRTKAD can also determine the vehicle's attitude. In a dual-antenna configuration, we can estimate the vehicle's pointing direction, depicted using the yaw and pitch angles. The complete attitude information, i.e., the three Euler angles, can be estimated with three or more non-linear antennas. Figure 7.4 shows the Euler

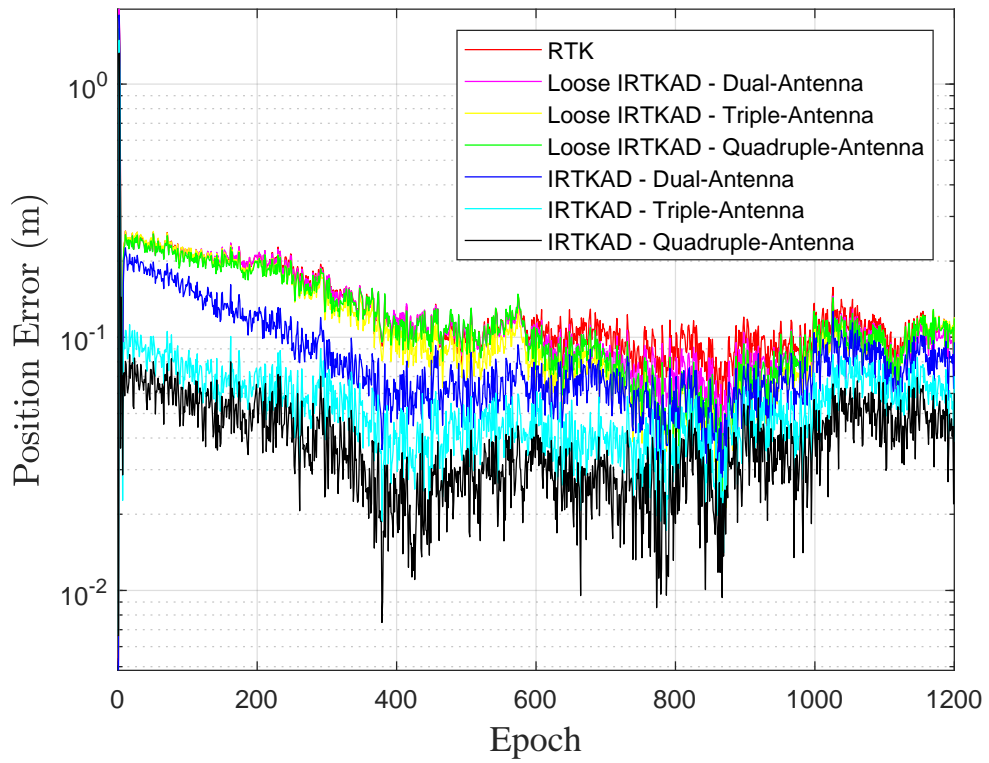


Figure 7.2: Position errors vs. epoch.

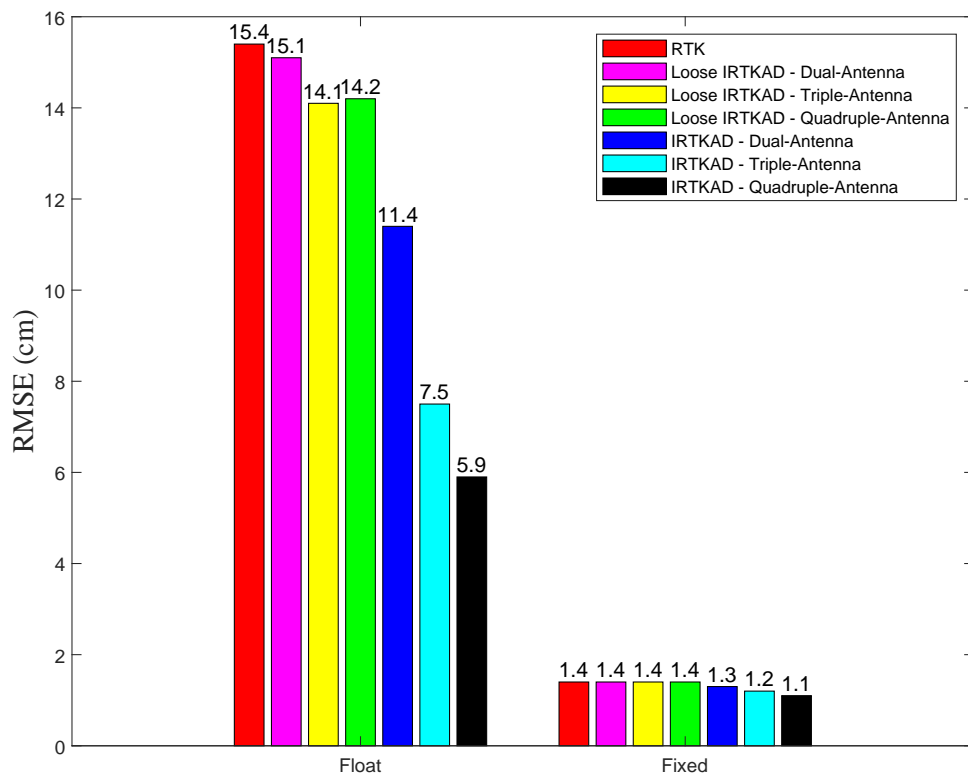
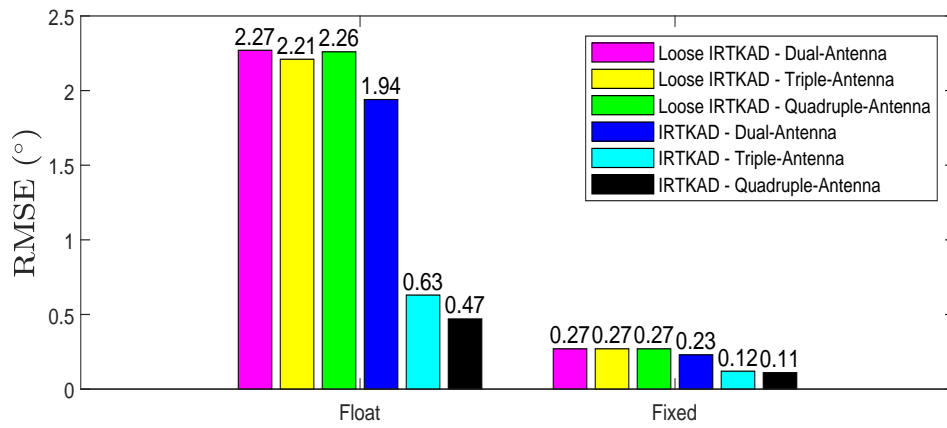
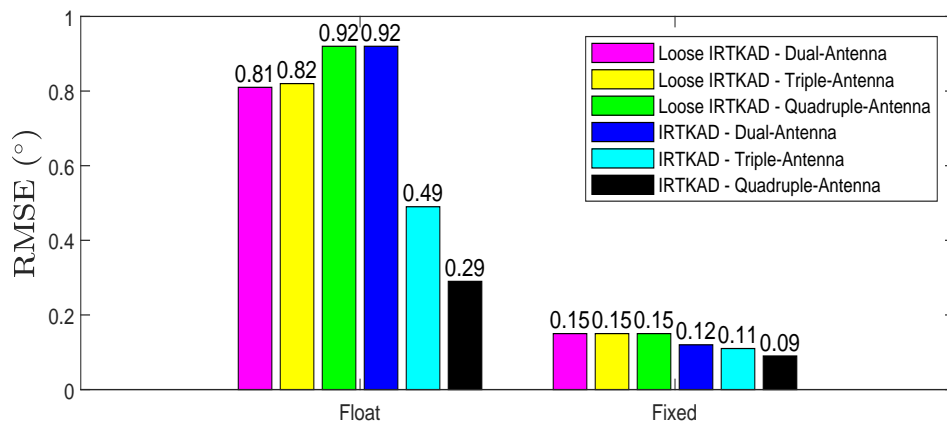


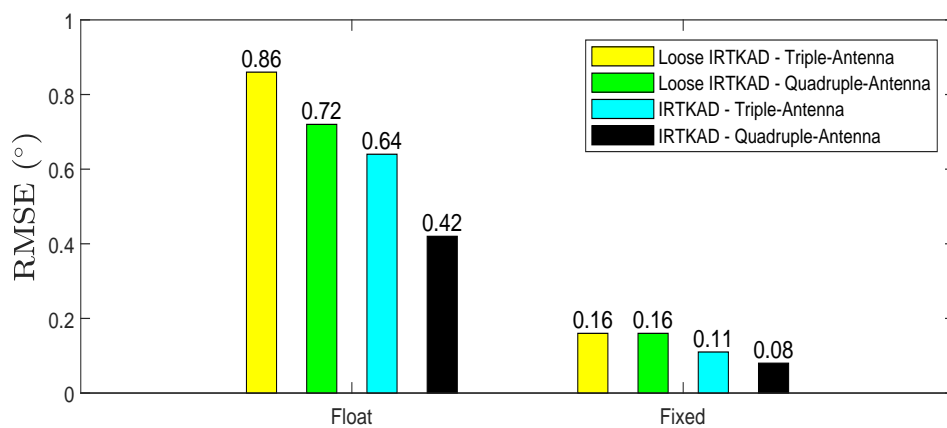
Figure 7.3: Positioning RMSE of the float and fixed solutions.



(a) Yaw



(b) Pitch



(c) Roll

Figure 7.4: Euler angle RMSE of the float and fixed solutions.

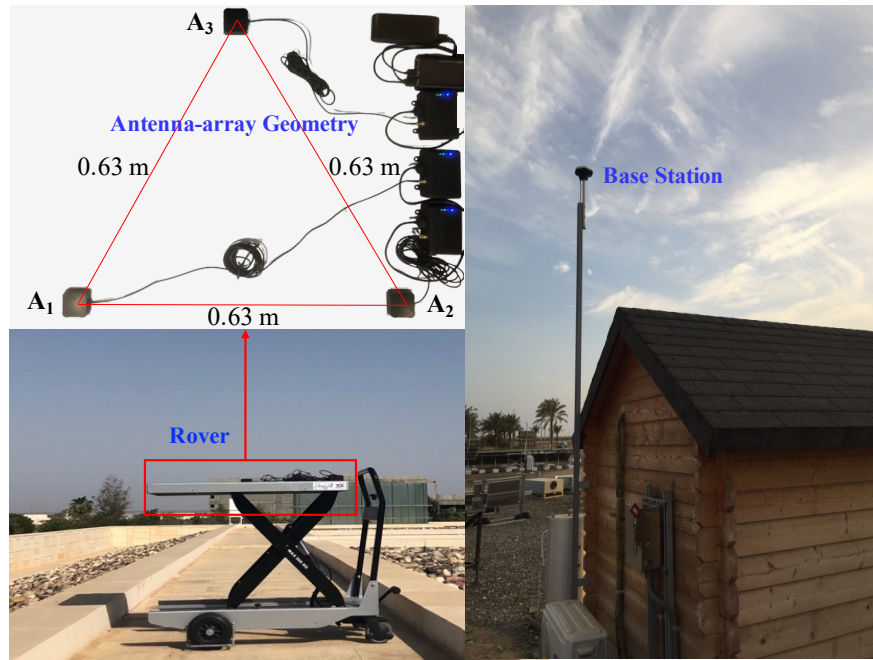


Figure 7.5: Experimental set-up.

angle RMSE of both the float and fixed estimations using a different number of antennas. There are no apparent differences in the attitude estimation accuracy of the loose IRTKAD method when we use two, three, or four antennas. The proposed IRTKAD method can reduce the RMSE of the Euler angles compared to the loose solutions, no matter the float and fixed estimations. Figure 7.4 indicates that the more antennas we use, the attitude determination performance of the proposed method better.

7.4.2 Experiment

A static experiment was implemented to test the performance of the proposed method with real GNSS data. As shown in Figure 7.5, a set of three ANAVS multi-sensor modules [121] and a single base station were placed on the campus of the King Abdullah University of Science and Technology, Thuwal, Saudi Arabia. The GNSS antennas were on the three vertices of an equilateral triangle with 0.63-meter sides, which were around 550 meters away from the base station. The correction information is transferred using the 4G connection as described in

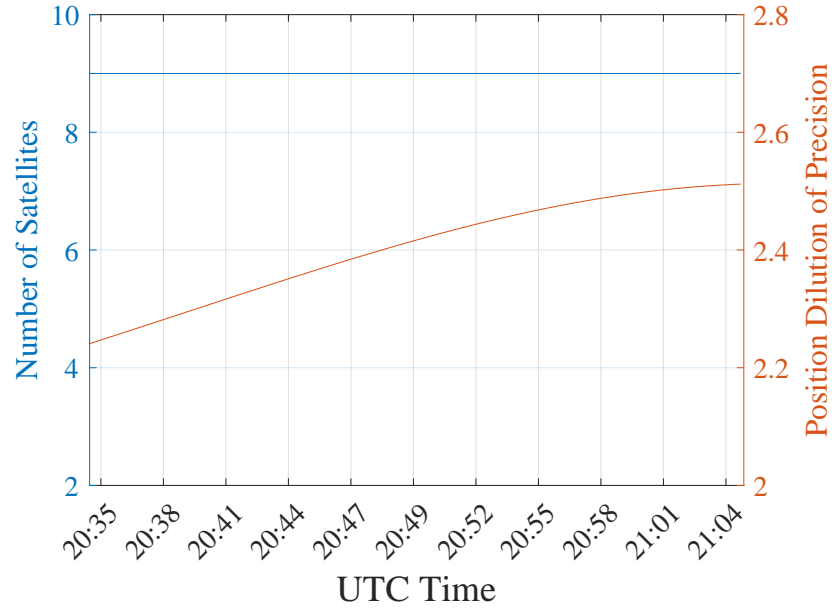


Figure 7.6: The number of tracked satellites and the corresponding position dilution of precision.

[134]. The geometry of the antenna array is addressed by

$$\mathbf{X}_b = \begin{bmatrix} 0.63 & 0.315 \\ 0 & 0.545 \end{bmatrix}.$$

We collected 1800 epochs of GNSS observations at 1 Hz on 25 May 2021 (UTC time 20:35 to 21:05). The number of tracked satellites and the associated value of position dilution of precision are shown in Figure 7.6. The results based on post-processing with the carrier-phase ambiguities successfully fixed are used as ground truth. For state initialization, we made use of the first epoch data to estimate the position, attitude, and carrier-phase ambiguities based on the integer least-squares estimation and Riemannian optimization. In this experiment, the ambiguities associated with attitude determination, i.e., \mathbf{n}_{k0} with $k = 1, 2$, can be fixed successfully. Besides, there is no cycle slip. Therefore, we treated the \mathbf{n}_{0r} to be the only integer unknown to be resolved.

Table 7.1 displays the percentage that the carrier-phase ambiguities are fixed and the positioning RMSE for the fixed solutions. The fix ratios of loose IRTKAD and IRTKAD are higher than that of the standard RTK technique, indicating the

Table 7.1: Fix ratio (%) of ambiguity resolution and positioning RMSE (cm) of the fixed solutions based on experimental data.

| | Fix Ratio (%) | Positioning RMSE (cm) |
|--------------|---------------|-----------------------|
| RTK | 96.83 | 4.26 |
| Loose IRTKAD | 99.22 | 4.26 |
| IRTKAD | 99.22 | 2.86 |

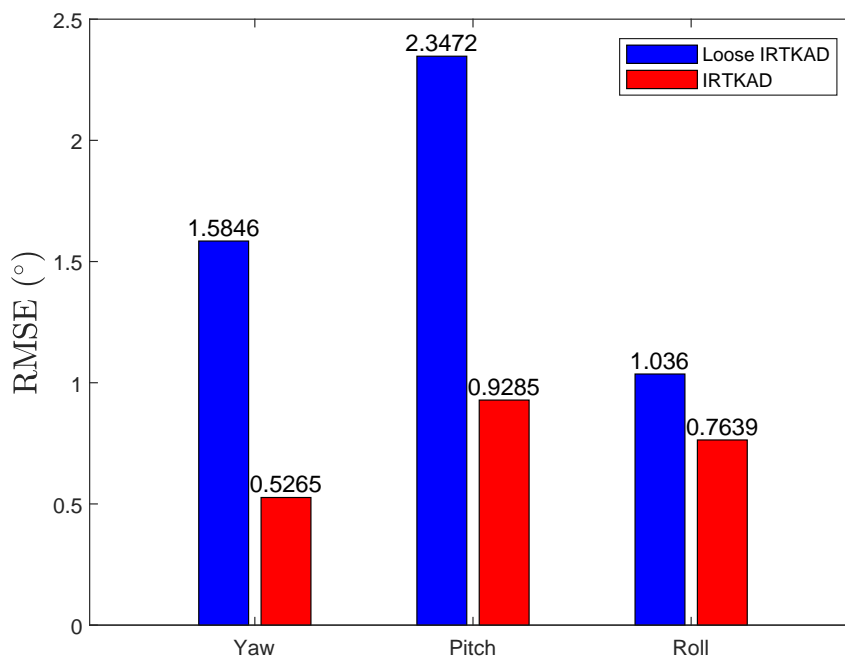


Figure 7.7: Euler angle RMSE based on experimental data.

enhancement of the integrated solution concerning carrier-phase ambiguity resolution. The values of positioning RMSE demonstrate that the RTK and loose IRTKAD provide the same positioning accuracy based on the employed antenna configuration. Benefiting from leveraging the antenna-array geometry, the positioning accuracy of IRTKAD significantly outperforms the other two methods.

Figure 7.7 demonstrates the RMSE of the Euler angle estimations based on the experimental data. We can see that the IRTKAD can remarkably reduce the angular RMSE compared with the loose IRTKAD. The improvement of attitude determination shows the effects of leveraging the orthonormality constraint by forcing the state to the Riemannian manifolds. Table 7.1 and Figure 7.7 prove the capability of the proposed IRTKAD and the RieMUKF in improving GNSS

parameter estimates inclusive of position, attitude, and ambiguities.

Chapter 8

Conclusion

8.1 Summary

In this thesis, we study GNSS localization and attitude determination problems based on optimization techniques on Riemannian manifolds. As the solution set of the attitude matrix is a manifold, we formulate GNSS attitude determination as an optimization over Riemannian manifolds. We develop three different attitude determination methods:

- **Array-aided attitude determination based on an oriented sphere manifold**

Given a specific antenna configuration, the unwrapped phase difference is recovered by an efficient state-of-the-art ambiguity resolution method. Subsequently, this unwrapped phase difference is used to formulate 3-D attitude determination as a non-convex optimization problem that incorporates all the available baseline length and angle constraints. The non-convex problem is solved by introducing a novel Riemannian manifold and investigating its geometry. The resulting first and second order optimization algorithms are not only efficient for their clever use of the geometry of the problem, but are also guaranteed to converge to an extreme point. The performance of the proposed framework is assessed through extensive numerical simulations under various setup conditions, with particular a focus on challenging scenarios. Simulation results demonstrate that the proposed Riemannian optimization based scheme largely outperforms the least squares and the LAMBDA benchmark approaches in all test scenarios with a lower com-

plexity than generic non-convex solvers.

- **Riemannian-manifold-based orthonormality-constrained attitude determination**

By modeling the GNSS attitude problem as an optimization on the Stiefel manifold, we alleviate the difficulties of resolving the unknown carrier-phase ambiguities. First, to replace the widely used least-squares solution, we calculate a constrained float solution using Riemannian manifold optimization as an improved starting point for the integer search process. To take advantage of the improved intermediate solution, we propose a new decomposition of the objective function at an arbitrary point to replace the widely used orthogonal decomposition appropriate for the least-squares approach. By leveraging Riemannian optimization, the improved float solution, and the proposed decomposition, we are able to search for the carrier-phase ambiguities in the integer domain with high efficiency and reliability. The presented algorithm has two variants: a loose form and a tight form abbreviated as RieMOCAD-LF and RieMOCAD-TF, respectively. The proposed algorithms are compared to relevant state-of-the-art methods using both simulation and experimental data. We evaluate performance in terms of key performance indicators such as success rate, search space size, and attitude error distribution. The results confirm the feasibility and effectiveness of the proposed approach, especially in reducing the computational complexity while maintaining high success rates.

- **Constrained wrapped least squares method**

A constrained wrapped least-squares (C-WLS) method for attitude determination using multiple GNSS antennas is presented. Unlike existing attitude determination methods, the proposed approach allows the attitude determination problem to be tackled directly—without initially estimating the integer ambiguities—while respecting the antenna array constraints and the

integer property of the carrier-phase ambiguities. Given a stated assumption on the double-difference carrier-phase noise, the proposed approach includes an additional constraint on the residual phase to strengthen the optimization model. We solve the C-WLS problem by searching the potential candidates on the unit sphere and obtaining an improved solution through a refinement process. The proposed method targets the estimation of the attitude parameters but inherently returns the integer ambiguities.

Since the GNSS data of the positioning and attitude determination problems are correlated, we introduce a joint solution for these two problems using the fused data from multiple GNSS antennas, that is,

- **Integrated RTK positioning and attitude determination**

The correlation between GNSS positioning and attitude determination problems is considered to strengthen the system model rather than treating them independently. The known geometry of the antennas on the vehicle is utilized to enhance GNSS parameter estimates, i.e., position, attitude, and ambiguities, based on the suggested UKF on Riemannian manifolds. The Riemannian extension of UKF and the associated terminology ingredients are studied, fitting the joint problem of RTK positioning and attitude determination well. Finally, the proposed method is numerically evaluated and compared with the traditional techniques based on simulations and experiments, verifying its feasibility and advantages.

8.2 Future Research Work

This section presents the future research plan that extends the current work. Based on the techniques we have studied previously, we propose several research directions as follows:

- **Extend the work regarding the integrated GNSS localization and attitude determination**

We have verified that the known geometry of the antenna array can be used to improve RTK positioning accuracy. In the future, we will theoretically analyze the effects of the antenna array on the positioning accuracy using Cramér–Rao bound (CRB).

- **Multipath Detection and Mitigation from GNSS Observations**

We consider the problem of detecting and mitigating the effect of multipath on GNSS observations. We can exploit the antenna-array geometry and an attitude estimate provided by an attitude filter or an IMU to develop a technique to identify the satellite observations that are contaminated with multipath. The antenna geometry can be leveraged to estimate the attitude parameters for various satellite combinations rapidly. Then, a dedicated decision-making algorithm can be utilized to identify the satellite observations affected by multipath. By rejecting the multipath-affected observations, remarkable performance gains can be expected.

- **Joint localization and attitude determination based on sensor fusion**

Our current research focuses on pure GNSS positioning or attitude determination. However, the performance of GNSS-based techniques degrades significantly in deep urban environments. In such scenarios, buildings can block, weaken, reflect, and diffract the GNSS signals, which may result in insufficiently visible satellites and observations with severe multipath effects. Therefore, we will extend our work to a multi-sensor navigation system to overcome the drawbacks of GNSS.

REFERENCES

- [1] M. M. Miller, A. Soloviev, M. Uijt de Haag, M. Veth, J. Raquet, T. J. Klausutis, and J. E. Touma, “Navigation in GPS denied environments: Feature-aided inertial systems,” AIR FORCE RESEARCH LAB EGLIN AFB FL MUNITIONS DIRECTORATE, Tech. Rep., 2010.
- [2] P. Teunissen and O. Montenbruck, *Springer handbook of global navigation satellite systems*. Springer, 2017.
- [3] D. Bevly, X. Cao, M. Gordon, G. Ozbilgin, D. Kari, B. Nelson, J. Woodruff, M. Barth, C. Murray, A. Kurt, K. Redmill, and U. Ozguner, “Lane change and merge maneuvers for connected and automated vehicles: A survey,” *IEEE Trans. Intell. Veh.*, vol. 1, no. 1, pp. 105–120, 2016.
- [4] N. Joubert, T. G. Reid, and F. Noble, “Developments in modern GNSS and its impact on autonomous vehicle architectures,” in *2020 IEEE Intelligent Vehicles Symposium (IV)*. IEEE, 2020, pp. 2029–2036.
- [5] L. Xiong, R. Kang, J. Zhao, P. Zhang, M. Xu, R. Ju, C. Ye, and T. Feng, “G-VIDO: A vehicle dynamics and intermittent GNSS-aided visual-inertial state estimator for autonomous driving,” *IEEE Trans. Intell. Transp. Syst.*, 2021.
- [6] —, “G-VIDO: A vehicle dynamics and intermittent GNSS-aided visual-inertial state estimator for autonomous driving,” *IEEE Trans. Intell. Transp. Syst.*, vol. 23, no. 8, pp. 11 845–11 861, 2022.
- [7] J. V. Stafford, “Implementing precision agriculture in the 21st century,” *Journal of agricultural engineering research*, vol. 76, no. 3, pp. 267–275, 2000.
- [8] M. Pérez Ruiz and S. Upadhyaya, *GNSS in precision agricultural operations*. Intech, 2012.
- [9] G. Aifadopoulou, G. Tsaples, J. M. S. Grau, and P. Tzenos, “Autonomous port vehicles fleet management: analyzing the effect of GNSS limitations,” in *2020 IEEE 23rd International Conference on Intelligent Transportation Systems (ITSC)*. IEEE, 2020, pp. 1–6.
- [10] R. Skulstad, C. Syversen, M. Merz, N. Sokolova, T. Fossen, and T. Johansen, “Autonomous net recovery of fixed-wing UAV with single-

- frequency carrier-phase differential GNSS,” *IEEE Aerosp. Electron. Syst. Mag.*, vol. 30, no. 5, pp. 18–27, 2015.
- [11] S. Pullen, P. Enge, and J. Lee, “Local-area differential GNSS architectures optimized to support unmanned aerial vehicles (UAVs),” in *Proceedings of the International Technical Meeting of the Institute of Navigation (ION ITM 2013)*, San Diego, CA, USA, 2013, pp. 28–30.
- [12] O. Kutsenko, S. Ilnytska, V. Kondratyuk, and V. Konin, “Unmanned aerial vehicle position determination in GNSS landing system,” in *2017 IEEE 4th International Conference Actual Problems of Unmanned Aerial Vehicles Developments (APUAVD)*. IEEE, 2017, pp. 79–83.
- [13] Y.-T. Tranchant, L. Testut, C. Chupin, V. Ballu, and P. Bonnefond, “Near-coast tide model validation using GNSS unmanned surface vehicle (USV), a case study in the Pertuis Charentais (France),” *Remote Sensing*, vol. 13, no. 15, p. 2886, 2021.
- [14] D. M. Bevly and S. Cobb, *GNSS for vehicle control*. Artech House, 2010.
- [15] C. Ruf, R. Backhus, T. Butler, C.-C. Chen, S. Gleason, E. Loria, D. McKague, R. Miller, A. O’Brien, and L. van Nieuwstadt, “Next generation GNSS-R instrument,” in *IGARSS 2020 - 2020 IEEE International Geoscience and Remote Sensing Symposium*, 2020, pp. 3353–3356.
- [16] F. Diani, F. Sbardellati, and M. Lisi, “GNSS user technology: next generation GNSS-based location technologies,” in *2019 European Microwave Conference in Central Europe (EuMCE)*, 2019, pp. 319–322.
- [17] R. Linnabary, A. O’Brien, C. Ruf, S. Musko, and D. Moller, “Analysis of GNSS-R coverage by a regional aircraft fleet,” in *IGARSS 2020 - 2020 IEEE International Geoscience and Remote Sensing Symposium*, 2020, pp. 6270–6273.
- [18] H. Cui and S. Zhang, “Satellite availability and service performance evaluation for next-generation GNSS, RNSS and LEO augmentation constellation,” *Remote Sensing*, vol. 13, no. 18, p. 3698, 2021.
- [19] Z. Yao and M. Lu, *Next-Generation GNSS Signal Design*. Springer, 2021.
- [20] M. Shen, J. Sun, H. Peng, and D. Zhao, “Improving localization accuracy in connected vehicle networks using Rao-Blackwellized particle filters: Theory, simulations, and experiments,” *IEEE Trans. Intell. Transp. Syst.*, 2018.
- [21] R. J. P. van Bree and C. C. J. M. Tiberius, “Real-time single-frequency precise point positioning: accuracy assessment,” *GPS Solut.*, vol. 16, no. 2, pp. 259–266, Apr 2012.

- [22] J. Wang, “Stochastic modeling for real-time kinematic GPS/GLONASS positioning,” *Navigation*, vol. 46, no. 4, pp. 297–305, 1999.
- [23] D. Kozlov and M. Tkachenko, “Centimeter-level, real-time kinematic positioning with GPS+ GLONASS C/A receivers,” *Navigation*, vol. 45, no. 2, pp. 137–147, 1998.
- [24] B. Li, Y. Feng, W. Gao, and Z. Li, “Real-time kinematic positioning over long baselines using triple-frequency BeiDou signals,” *IEEE Trans. Aerosp. Electron. Syst.*, vol. 51, no. 4, pp. 3254–3269, 2015.
- [25] X. Luo, S. Li, and H. Xu, “Results of real-time kinematic positioning based on real GPS L5 data,” *IEEE Geoscience and Remote Sensing Letters*, vol. 13, no. 8, pp. 1193–1197, 2016.
- [26] H.-F. Ng and L.-T. Hsu, “3D mapping database-aided GNSS RTK and its assessments in urban canyons,” *IEEE Trans. Aerosp. Electron. Syst.*, vol. 57, no. 5, pp. 3150–3166, 2021.
- [27] L. Wang, Z. Li, J. Zhao, K. Zhou, Z. Wang, and H. Yuan, “Smart device-supported BDS/GNSS real-time kinematic positioning for sub-meter-level accuracy in urban location-based services,” *Sensors*, vol. 16, no. 12, p. 2201, 2016.
- [28] N. Zhu, J. Marais, D. Bétaille, and M. Berbineau, “GNSS position integrity in urban environments: A review of literature,” *IEEE Trans. Intell. Transp. Syst.*, vol. 19, no. 9, pp. 2762–2778, 2018.
- [29] Y. Wu, X. Hu, D. Hu, T. Li, and J. Lian, “Strapdown inertial navigation system algorithms based on dual quaternions,” *IEEE Trans. Aerosp. Electron. Syst.*, vol. 41, no. 1, pp. 110–132, 2005.
- [30] J. K. Lee, E. J. Park, and S. N. Robinovitch, “Estimation of attitude and external acceleration using inertial sensor measurement during various dynamic conditions,” *IEEE Trans. Instrum. Meas.*, vol. 61, no. 8, pp. 2262–2273, 2012.
- [31] M. Grewal, V. Henderson, and R. Miyasako, “Application of Kalman filtering to the calibration and alignment of inertial navigation systems,” *IEEE Trans. Autom. Control*, vol. 36, no. 1, pp. 3–13, 1991.
- [32] B. Hofmann-Wellenhof, H. Lichtenegger, and J. Collins, *Global positioning system: theory and practice*. Springer Science & Business Media, 2012.
- [33] B. Hofmann-Wellenhof, H. Lichtenegger, and E. Wasle, *GNSS—global navigation satellite systems: GPS, GLONASS, Galileo, and more*. Springer Science & Business Media, 2007.

- [34] J. Madsen and E. G. Lightsey, “Robust spacecraft attitude determination using global positioning system receivers,” *J. Spacec. Rockets*, vol. 41, no. 4, pp. 635–644, 2004.
- [35] J. L. Crassidis and F. L. Markley, “New algorithm for attitude determination using global positioning system signals,” *J. Guid. Control Dyn.*, vol. 20, no. 5, pp. 891–896, 1997.
- [36] F. Causa and G. Fasano, “Improving navigation in GNSS-Challenging environments: Multi-UAS cooperation and generalized dilution of precision,” *IEEE Trans. Aerosp. Electron. Syst.*, vol. 57, no. 3, pp. 1462–1479, 2021.
- [37] L. Xiong, X. Xia, Y. Lu, W. Liu, L. Gao, S. Song, and Z. Yu, “Imu-based automated vehicle body sideslip angle and attitude estimation aided by GNSS using parallel adaptive kalman filters,” *IEEE Trans. Veh. Technol.*, vol. 69, no. 10, pp. 10 668–10 680, 2020.
- [38] A. A. Ardalan and M. H. Rezvani, “An iterative method for attitude determination based on misaligned GNSS baselines,” *IEEE Trans. Aerosp. Electron. Syst.*, vol. 51, no. 1, pp. 97–107, 2015.
- [39] F. Aghili and A. Salerno, “Driftless 3-D attitude determination and positioning of mobile robots by integration of IMU with two RTK GPSs,” *IEEE/ASME Trans. Mechatronics*, vol. 18, no. 1, pp. 21–31, Feb. 2013.
- [40] M. Farkas, B. Vanek, and S. Rozsa, “Small UAV’s position and attitude estimation using tightly coupled multi baseline multi constellation GNSS and inertial sensor fusion,” in *2019 IEEE 5th Int. Workshop Metrol. AeroSp. (MetroAeroSpace)*, June 2019, pp. 176–181.
- [41] Y. Li, K. Zhang, C. Roberts, and M. Murata, “On-the-fly GPS-based attitude determination using single- and double-differenced carrier phase measurements,” *GPS Solut.*, vol. 8, no. 2, pp. 93–102, Jul. 2004.
- [42] N. O. Leite and F. Walter, “Flight test evaluation of a new GPS attitude determination algorithm,” *IEEE Aerosp. Electron. Syst. Mag.*, vol. 22, no. 12, pp. 3–10, 2007.
- [43] S. Dahiya, V. Saini, and A. K. Singh, “GNSS signal processing based attitude determination of spinning projectiles,” *IEEE Trans. Aerosp. Electron. Syst.*, pp. 1–1, 2022.
- [44] L. Lau, P. Cross, and M. Steen, “Flight tests of error-bounded heading and pitch determination with two GPS receivers,” *IEEE Trans. Aerosp. Electron. Syst.*, vol. 48, no. 1, pp. 388–404, 2012.

- [45] K. Chiang, M. Psiaki, S. Powell, R. Miceli, and B. O. Hanlon, "GPS-based attitude determination for a spinning rocket," *IEEE Trans. Aerosp. Electron. Syst.*, vol. 50, no. 4, pp. 2654–2663, Oct. 2014.
- [46] G. Giorgi, P. J. G. Teunissen, and T. P. Gourlay, "Instantaneous global navigation satellite system (GNSS)-based attitude determination for maritime applications," *IEEE J. Ocean. Eng.*, vol. 37, no. 3, pp. 348–362, 2012.
- [47] S. Bijjahalli, S. Ramasamy, and R. Sabatini, "A novel vehicle-based GNSS integrity augmentation system for autonomous airport surface operations," *J. Intell. Robot. Syst.*, vol. 87, no. 2, pp. 379–403, 2017.
- [48] A. Vetrella, G. Fasano, D. Accardo, and A. Moccia, "Differential GNSS and vision-based tracking to improve navigation performance in cooperative multi-UAV systems," *Sensors*, vol. 16, no. 12, p. 2164, 2016.
- [49] H. Wang, N. Liu, Z. Su, and Q. Li, "Research on low-cost attitude estimation for MINS/dual-antenna GNSS integrated navigation method," *Micro-machines*, vol. 10, no. 6, p. 362, 2019.
- [50] X. Liu, T. Ballal, and T. Y. Al-Naffouri, "GNSS-based localization for autonomous vehicles: Prospects and challenges," in *2019 27th Eur. Signal Process. Conf. (EUSIPCO)*, Sep. 2019, pp. 2–6.
- [51] G. Blewitt, "Basics of the GPS technique: observation equations," *Geodetic applications of GPS*, pp. 10–54, 1997.
- [52] W. Chen and X. Li, "Success rate improvement of single epoch integer least-squares estimator for the GNSS attitude/short baseline applications with common clock scheme," *Acta Geod. Geophys.*, vol. 49, no. 3, pp. 295–312, Sep. 2014.
- [53] W. Chen, C. Yu, D. Dong, M. Cai, F. Zhou, Z. Wang, L. Zhang, and Z. Zheng, "Formal uncertainty and dispersion of single and double difference models for GNSS-based attitude determination," *Sensors*, vol. 17, no. 2, p. 408, Feb. 2017.
- [54] G. Giorgi and P. J. G. Teunissen, "Low-complexity instantaneous ambiguity resolution with the affine-constrained GNSS attitude model," *IEEE Trans. Aerosp. Electron. Syst.*, vol. 49, no. 3, pp. 1745–1759, 2013.
- [55] J. L. Crassidis, F. L. Markley, and E. G. Lightsey, "Global positioning system integer ambiguity resolution without attitude knowledge," *J. Guid. Control Dyn.*, vol. 22, no. 2, pp. 212–218, 1999.

- [56] C. Chun and F. C. Park, “Dynamics-based attitude determination using the global positioning system,” *J. Guid. Control Dyn.*, vol. 24, no. 3, pp. 466–473, May. 2001.
- [57] B. Wang, Z. Deng, S. Wang, and M. Fu, “A motion-based integer ambiguity resolution method for attitude determination using the global positioning system (GPS),” *Meas. Sci. Technol.*, vol. 21, no. 6, p. 065102, 2010.
- [58] M. L. Psiaki, “Batch algorithm for global-positioning-system attitude determination and integer ambiguity resolution,” *J. Guid. Control Dyn.*, vol. 29, no. 5, pp. 1070–1079, 2006.
- [59] T.-H. Hsu and T.-L. Chen, “A new instantaneous method for attitude determination using GPS phase measurement,” *IEEE Trans. Instrum. Meas.*, vol. 71, pp. 1–13, 2022.
- [60] P. J. G. Teunissen, “The least-squares ambiguity decorrelation adjustment: a method for fast GPS integer ambiguity estimation,” *J. Geod.*, vol. 70, no. 1, p. 65–82, 1995.
- [61] M. Ziebart and P. Cross, “LEO GPS attitude determination algorithm for a micro-satellite using boom-arm deployed antennas,” *GPS Solut.*, vol. 6, no. 4, pp. 242–256, 2003.
- [62] S. Purivigraipong, S. Hodgart, M. Unwin, and S. Kuntanapreeda, “Resolving integer ambiguity of GPS carrier phase difference,” *IEEE Trans. Aerosp. Electron. Syst.*, vol. 46, no. 2, pp. 832–847, 2010.
- [63] C. Gunther and P. Henkel, “Integer ambiguity estimation for satellite navigation,” *IEEE Trans. Signal Process.*, vol. 60, no. 7, pp. 3387–3393, Jul. 2012.
- [64] T. Ballal and C. J. Bleakley, “GNSS instantaneous ambiguity resolution and attitude determination exploiting the receiver antenna configuration,” *IEEE Trans. Aerosp. Electron. Syst.*, vol. 50, no. 3, pp. 2061–2069, 2014.
- [65] X. Liu, T. B. K. Ahmed, and T. Y. Al-Naffouri, “Attitude determination based on global navigation satellite system information,” Dec. 23 2021, US Patent App. 17/269,390.
- [66] J. L. Crassidis, F. L. Markley, and E. G. Lightsey, “Global Positioning System integer ambiguity resolution without attitude knowledge,” *J. Guid. Control Dyn.*, vol. 22, no. 2, pp. 212–218, Mar. 1999.
- [67] B. Wang, Z. Deng, S. Wang, and M. Fu, “A motion-based integer ambiguity resolution method for attitude determination using the Global Positioning System (GPS),” *Meas. Sci. Technol.*, vol. 21, no. 6, p. 065102, Apr. 2010.

- [68] P. J. G. Teunissen, “Integer least-squares theory for the GNSS compass,” *J. Geod.*, vol. 84, no. 7, pp. 433–447, 2010.
- [69] C. Park, I. Kim, J. G. Lee, and G.-I. Jee, “Efficient ambiguity resolution using constraint equation,” in *In Proceedings of IEEE Position Locat. Navig. Symp.*, Atlanta, Georgia, USA, Apr. 1996, pp. 277–284.
- [70] J.-C. Juang and G.-S. Huang, “Development of GPS-based attitude determination algorithms,” *IEEE Trans. Aerosp. Electron. Syst.*, vol. 33, no. 3, pp. 968–976, Jul. 1997.
- [71] P. J. Teunissen, “Least-squares estimation of the integer GPS ambiguities,” in *Invited lecture, section IV theory and methodology, IAG general meeting, Beijing, China*, 1993, pp. 1–16.
- [72] ———, “A new method for fast carrier phase ambiguity estimation,” in *Proceedings of 1994 IEEE Position Locat. Navig. Symp.-PLANS’94*. IEEE, 1994, pp. 562–573.
- [73] B. Wang, L. Miao, S. Wang, and J. Shen, “A constrained LAMBDA method for GPS attitude determination,” *GPS Solut.*, vol. 13, no. 2, pp. 97–107, Mar. 2009.
- [74] P. Teunissen, “The affine constrained GNSS attitude model and its multivariate integer least-squares solution,” *J. Geod.*, vol. 86, no. 7, pp. 547–563, 2012.
- [75] N. Nadarajah, P. J. G. Teunissen, and N. Raziq, “Instantaneous GPS–Galileo attitude determination: Single-frequency performance in satellite-deprived environments,” *IEEE Trans. Veh. Technol.*, vol. 62, no. 7, pp. 2963–2976, 2013.
- [76] P. J. Teunissen, “An optimality property of the integer least-squares estimator,” *J. Geod.*, vol. 73, no. 11, pp. 587–593, 1999.
- [77] ———, “A general multivariate formulation of the multi-antenna GNSS attitude determination problem,” *Artif. Satell.*, vol. 42, no. 2, pp. 97–111, 2007.
- [78] G. Giorgi and P. J. Teunissen, “Carrier phase GNSS attitude determination with the multivariate constrained LAMBDA method,” in *2010 IEEE Aerosp. Conf.* IEEE, 2010, pp. 1–12.
- [79] L.-T. Hsu, “Analysis and modeling GPS NLOS effect in highly urbanized area,” *GPS Solut.*, vol. 22, no. 1, p. 7, 2018.
- [80] S. Pullen, J. Kilfeather, J. Goddard, T. Nowitzky, B. Shah, W. Doong, A. Welton, and D. Kagan, “Enhanced navigation, robustness, and safety

- assurance for autonomous vehicles as part of the Globalstar connected car program,” in *Proc. 31st Int. Tech. Meet. Satell. Div. Inst. Navig. (ION GNSS+ 2018)*, Miami, Florida, Sep. 2018, pp. 1538–1565.
- [81] X. Liu, T. Ballal, H. Chen, and T. Y. Al-Naffouri, “Constrained wrapped least squares: A tool for high-accuracy GNSS attitude determination,” *IEEE Trans. Instrum. Meas.*, vol. 71, pp. 1–15, 2022.
- [82] P. J. Teunissen and A. Kleusberg, *GPS for Geodesy*. Springer Science & Business Media, 2012.
- [83] Y. Feng and J. Wang, “GPS RTK performance characteristics and analysis,” *J. Glob. Position. Syst.*, vol. 7, no. 1, pp. 1–8, 2008.
- [84] J. Zhang and G. Lachapelle, “Precise estimation of residual tropospheric delays using a regional GPS network for real-time kinematic applications,” *J. Geod.*, vol. 75, no. 5-6, pp. 255–266, 2001.
- [85] P. Teunissen, “GPS double difference statistics: with and without using satellite geometry,” *J. Geod.*, vol. 71, no. 3, pp. 137–148, 1997.
- [86] L. Zhao, N. Li, L. Li, Y. Zhang, and C. Cheng, “Real-time GNSS-based attitude determination in the measurement domain,” *Sensors*, vol. 17, no. 2, p. 296, 2017.
- [87] T. Ballal and C. Bleakley, “Phase-difference ambiguity resolution for a single-frequency signal,” *IEEE Signal Process. Lett.*, vol. 15, pp. 853–856, 2008.
- [88] T. Ballal and C. J. Bleakley, “Phase-difference ambiguity resolution for a single-frequency signal in the near-field using a receiver triplet,” *IEEE Trans. Signal Process.*, vol. 58, no. 11, pp. 5920–5926, Aug. 2010.
- [89] S. Alban, “Design and performance of a robust GPS/INS attitude system for automobile applications,” Ph.D. dissertation, Stanford University, Standford, CA, USA, 2004.
- [90] P. J. G. Teunissen, “A-PPP: Array-aided precise point positioning with global navigation satellite systems,” *IEEE Trans. Signal Process.*, vol. 60, no. 6, pp. 2870–2881, 2012.
- [91] P. J. G. Teunissen and G. Giorgi, “Testing of a new single-frequency GNSS carrier phase attitude determination method: land, ship and aircraft experiments,” *GPS Solut.*, vol. 15, no. 1, pp. 15–28, 2011.
- [92] Y. Yang, “Attitude determination using newton’s method on riemannian manifold,” *Proceedings of the Institution of Mechanical Engineers, Part G: Journal of Aerospace Engineering*, vol. 229, no. 14, pp. 2737–2742, 2015.

- [93] J. Wu, Z. Zhou, B. Gao, R. Li, Y. Cheng, and H. Fourati, “Fast linear quaternion attitude estimator using vector observations,” *IEEE Transactions on Automation Science and Engineering*, vol. 15, no. 1, pp. 307–319, Jan 2018.
- [94] P.-A. Absil, R. Mahony, and R. Sepulchre, *Optimization algorithms on matrix manifolds*. Princeton University Press, 2009.
- [95] A. Douik and B. Hassibi, “A riemannian approach for Graph-Based clustering by doubly stochastic matrices,” in *Proc. of IEEE Stat. Signal Process. Workshop (SSP 2018)*, Freiburg im Breisgau, Germany, Jun. 2018.
- [96] P. J. Buist, P. J. G. Teunissen, G. Giorgi, and S. Verhagen, “Multiplatform instantaneous GNSS ambiguity resolution for triple-and quadruple-antenna configurations with constraints,” *Int. J. Navig. Obs.*, 2009.
- [97] S. Verhagen, B. Li, and M. Geodesy, *LAMBDA software package: MATLAB implementation, Version 3.0*, Delft University of Technology and Curtin University, 2012.
- [98] P. Cederholm, “Statistical characteristics of L1 carrier phase observations from four low-cost GPS receivers,” *Nordic Journal of Surveying and Real Estate Research*, vol. 7, no. 1, pp. 58–75, 2010.
- [99] D. Medina, V. Centrone, R. Ziebold, and J. García, “Attitude determination via GNSS carrier phase and inertial aiding,” in *Proceedings of the 32nd International Technical Meeting of the Satellite Division of The Institute of Navigation (ION GNSS+ 2019)*, 2019, pp. 2964–2979.
- [100] J. Kuang and S. Tan, “GPS-based attitude determination of gyrostatt satellite by quaternion estimation algorithms,” *Acta Astronautica*, vol. 51, no. 11, pp. 743–759, 2002.
- [101] N. Lovren and J. Pieper, “Error analysis of direction cosines and quaternion parameters techniques for aircraft attitude determination,” *IEEE Trans. Aerosp. Electron. Syst.*, vol. 34, no. 3, pp. 983–989, 1998.
- [102] G. Giorgi, “GNSS carrier phase-based attitude determination: Estimation and applications,” 2011.
- [103] M. D. Shuster, “Constraint in attitude estimation part II: Unconstrained estimation,” *The Journal of the Astronautical Sciences*, vol. 51, no. 1, pp. 75–101, 2003.
- [104] N. Boumal, “An introduction to optimization on smooth manifolds,” *Available online*, Aug. 2020.
- [105] H. Sato, *Riemannian Optimization and Its Applications*. Springer, 2021.

- [106] W. Ring and B. Wirth, “Optimization methods on Riemannian manifolds and their application to shape space,” *SIAM Journal on Optimization*, vol. 22, no. 2, pp. 596–627, 2012.
- [107] S. T. Smith, “Optimization techniques on Riemannian manifolds,” *Fields Inst. Commun.*, vol. 3, no. 3, pp. 113–135, 1994.
- [108] C. Liu and N. Boumal, “Simple algorithms for optimization on Riemannian manifolds with constraints,” *Appl. Math. Optim.*, vol. 82, no. 3, pp. 949–981, 2020.
- [109] N. Boumal, B. Mishra, P.-A. Absil, and R. Sepulchre, “Manopt, a Matlab toolbox for optimization on manifolds,” *J. Mach. Learn. Res.*, vol. 15, no. 42, pp. 1455–1459, 2014. [Online]. Available: <https://www.manopt.org>
- [110] C. Park and P. J. Teunissen, “Integer least squares with quadratic equality constraints and its application to GNSS attitude determination systems,” *Int. J. Control. Autom. Syst.*, vol. 7, no. 4, pp. 566–576, 2009.
- [111] C. C. Counselman and S. A. Gourevitch, “Miniature interferometer terminals for earth surveying: Ambiguity and multipath with global positioning system,” *IEEE Trans. Geosci. Remote Sens.*, vol. GE-19, no. 4, pp. 244–252, 1981.
- [112] S. Han and C. Rizos, “Improving the computational efficiency of the ambiguity function algorithm,” *J. Geod.*, vol. 70, no. 6, pp. 330–341, 1996.
- [113] Y. Yang, X. Mao, and W. Tian, “Rotation matrix method based on ambiguity function for GNSS attitude determination,” *Sensors*, vol. 16, no. 6, p. 841, 2016.
- [114] Y. Li, M. Murata, and B. Sun, “New approach to attitude determination using global positioning system carrier phase measurements,” *J. Guid. Control Dyn.*, vol. 25, no. 1, pp. 130–136, 2002.
- [115] J. Cheng, J. Wang, and L. Zhao, “A direct attitude determination approach based on GPS double-difference carrier phase measurements,” *J. Appl. Math.*, vol. 2014, 2014.
- [116] G. Wahba, “Problem 65-1: A least square estimate of spacecraft attitude,” *SIAM Rev.*, vol. 7, no. 3, p. 409, 1965.
- [117] F. L. Markley, “Attitude determination using vector observations and the singular value decomposition,” *J. Astronaut. Sci.*, vol. 36, no. 3, pp. 245–258, 1988.

- [118] G. Giorgi, P. J. Teunissen, S. Verhagen, and P. J. Buist, “Testing a new multivariate GNSS carrier phase attitude determination method for remote sensing platforms,” *Adv. Space Res.*, vol. 46, no. 2, pp. 118–129, 2010.
- [119] S. Verhagen, *Visualization of GNSS-related design parameters: manual for the MATLAB user interface VISUAL*, Delft University of Technology, 2006.
- [120] G. Giorgi, P. Teunissen, and P. Buist, “A search and shrink approach for the baseline constrained LAMBDA method: Experimental results,” in *Proc. Int. Symposium GPS/GNSS*. Curran Associates, 2008.
- [121] *ANavS® Multi-Sensor Modules*, ANavS GmbH – Advanced Navigation Solutions, Munich, Germany. [Online]. Available: <https://anavs.com/multi-sensor-rtk-module/>
- [122] X. X. Jin and C. D. de Jong, “Relationship between satellite elevation and precision of GPS code observations,” *J. Navig.*, vol. 49, no. 2, pp. 253–265, 1996.
- [123] P. Buist, P. Teunissen, G. Giorgi, and S. Verhagen, “Multiplatform instantaneous GNSS ambiguity resolution for triple-and quadruple-antenna configurations with constraints,” *International Journal of Navigation and Observation*, vol. 2009, 2009.
- [124] —, “Instantaneous GNSS-based kinematic relative positioning and attitude determination using multi-antenna configurations,” in *Proc. Int. Symp. GPS/GNSS*, 2009, pp. 1–11.
- [125] B. Li and P. J. Teunissen, “Real-time kinematic positioning using fused data from multiple GNSS antennas,” in *2012 15th International Conference on Information Fusion*. IEEE, 2012, pp. 933–938.
- [126] S. Wu, X. Zhao, C. Pang, L. Zhang, Z. Xu, and K. Zou, “Improving ambiguity resolution success rate in the joint solution of GNSS-based attitude determination and relative positioning with multivariate constraints,” *GPS Solutions*, vol. 24, no. 1, pp. 1–14, 2020.
- [127] G. Welch, G. Bishop *et al.*, “An introduction to the Kalman filter,” 1995.
- [128] R. J. Meinhold and N. D. Singpurwalla, “Understanding the Kalman filter,” *The American Statistician*, vol. 37, no. 2, pp. 123–127, 1983.
- [129] A. Douik, X. Liu, T. Ballal, T. Y. Al-Naffouri, and B. Hassibi, “Precise 3-D GNSS attitude determination based on Riemannian manifold optimization algorithms,” *IEEE Trans. Signal Process.*, vol. 68, pp. 284–299, 2020.

- [130] X. Liu, T. Ballal, M. Ahmed, and T. Y. Al-Naffouri, “Instantaneous GNSS ambiguity resolution and attitude determination via Riemannian manifold optimization,” *IEEE Trans. Aerosp. Electron. Syst.*, pp. 1–16, 2022.
- [131] —, “A GNSS attitude determination algorithm using optimization techniques on Riemannian manifolds,” in *Proceedings of the 35th International Technical Meeting of the Satellite Division of The Institute of Navigation (ION GNSS+ 2022)*, 2022, pp. 2064–2073.
- [132] C. Hertzberg, R. Wagner, U. Frese, and L. Schröder, “Integrating generic sensor fusion algorithms with sound state representations through encapsulation of manifolds,” *Inf. Fusion*, vol. 14, no. 1, pp. 57–77, 2013.
- [133] S. Hauberg, F. Lauze, and K. S. Pedersen, “Unscented Kalman filtering on Riemannian manifolds,” *J. Math. Imaging Vis.*, vol. 46, no. 1, pp. 103–120, 2013.
- [134] X. Liu, T. Ballal, M. Bruvelis, and T. Y. Al-Naffouri, “Deployment and evaluation of a real-time kinematic system using tinc-VPN software,” in *2020 IEEE/ION Position, Location and Navigation Symposium (PLANS)*, 2020, pp. 1155–1159.

APPENDICES

A Proof of Lemma 5.1

We first vectorize all the unknown parameters in a single vector $\boldsymbol{\theta} = \text{vec}([\mathbf{R} \ \mathbf{N}])$ and define the objective function as

$$\mathcal{F}(\boldsymbol{\theta}) = \|\text{vec}(\mathbf{Y} - \mathbf{A}\mathbf{R}\mathbf{X}_b - \mathbf{B}\mathbf{N})\|_{\mathbf{Q}_Y^{-1}}^2. \quad (\text{A.1})$$

To achieve the LS solution $\hat{\boldsymbol{\theta}} = \text{vec}\left(\begin{bmatrix} \hat{\mathbf{R}}_{AC} & \hat{\mathbf{N}}_{AC} \end{bmatrix}\right)$, we let the first order derivative equal to zero [90]

$$\mathcal{F}'(\hat{\boldsymbol{\theta}}) = \mathbf{0}, \quad (\text{A.2})$$

that is

$$\mathbf{M} \cdot \hat{\boldsymbol{\theta}} = \begin{bmatrix} \mathbf{X}_b \mathbf{P}^{-1} \otimes \mathbf{A}^T \mathbf{Q}_y^{-1} \\ \mathbf{P}^{-1} \otimes \mathbf{B}^T \mathbf{Q}_y^{-1} \end{bmatrix} \text{vec}(\mathbf{Y}), \quad (\text{A.3})$$

with

$$\mathbf{M} = \begin{bmatrix} \mathbf{X}_b \mathbf{P}^{-1} \otimes \mathbf{A}^T \mathbf{Q}_y^{-1} \mathbf{B} & \mathbf{X}_b \mathbf{P}^{-1} \mathbf{X}_b^T \otimes \mathbf{A}^T \mathbf{Q}_y^{-1} \mathbf{A} \\ \mathbf{P}^{-1} \otimes \mathbf{B}^T \mathbf{Q}_y^{-1} \mathbf{B} & \mathbf{P}^{-1} \mathbf{X}_b^T \otimes \mathbf{B}^T \mathbf{Q}_y^{-1} \mathbf{A} \end{bmatrix}, \quad (\text{A.4})$$

$$\mathbf{Q}_Y = \mathbf{P} \otimes \mathbf{Q}_y = \begin{bmatrix} 1 & 0.5 & \cdots & 0.5 \\ 0.5 & 1 & \cdots & 0.5 \\ & & \ddots & \\ 0.5 & 0.5 & \cdots & 1 \end{bmatrix} \otimes \mathbf{Q}_y, \quad (\text{A.5})$$

where \mathbf{Q}_y is the covariance matrix of GNSS observations for a single baseline, and \otimes indicates the Kronecker product.

Since $\mathcal{F}(\boldsymbol{\theta})$ is a quadratic form of $\boldsymbol{\theta}$, its third or higher order derivatives are

all equal to zero, i.e., $\mathcal{F}^{(3)}(\boldsymbol{\theta}) = \mathcal{F}^{(4)}(\boldsymbol{\theta}) = \dots = \mathcal{F}^{(n)}(\boldsymbol{\theta}) = \mathbf{0}$. Then, we can expand $\mathcal{F}(\boldsymbol{\theta})$ as a Taylor series at $\hat{\boldsymbol{\theta}}$

$$\mathcal{F}(\boldsymbol{\theta}) = \mathcal{F}(\hat{\boldsymbol{\theta}}) + \frac{1}{2} (\boldsymbol{\theta} - \hat{\boldsymbol{\theta}})^{\text{T}} \mathcal{F}''(\hat{\boldsymbol{\theta}}) (\boldsymbol{\theta} - \hat{\boldsymbol{\theta}}), \quad (\text{A.6})$$

with

$$\mathcal{F}''(\hat{\boldsymbol{\theta}}) = 2\mathbf{M}.$$

To rewrite the second term on the right-hand side of (A.6) as a sum of squares terms, we define the block-triangular transformation

$$\mathbf{T}_1 = \begin{bmatrix} \mathbf{I} & \mathbf{O} \\ \mathbf{I} \otimes \mathbf{B}^+ \mathbf{A} & \mathbf{I} \end{bmatrix}. \quad (\text{A.7})$$

Then we obtain

$$\mathbf{T}_1 (\boldsymbol{\theta} - \hat{\boldsymbol{\theta}}) = \begin{bmatrix} \text{vec}(\mathbf{R} - \hat{\mathbf{R}}_{\text{AC}}) \\ \text{vec}(\mathbf{N} - \hat{\mathbf{N}}_{\text{AC}}(\mathbf{R})) \end{bmatrix}, \quad (\text{A.8})$$

and

$$\mathbf{T}_1^{-\text{T}} \mathbf{M} \mathbf{T}_1^{-1} = \begin{bmatrix} \mathbf{Q}_{\hat{\mathbf{R}}_{\text{AC}} \hat{\mathbf{R}}_{\text{AC}}}^{-1} & \mathbf{O} \\ \mathbf{O} & \mathbf{Q}_{\hat{\mathbf{N}}_{\text{AC}}(\mathbf{R}) \hat{\mathbf{N}}_{\text{AC}}(\mathbf{R})}^{-1} \end{bmatrix}. \quad (\text{A.9})$$

Based on the transformation, we have

$$\begin{aligned} \mathcal{F}(\boldsymbol{\theta}) &= \mathcal{F}(\hat{\boldsymbol{\theta}}) + (\boldsymbol{\theta} - \hat{\boldsymbol{\theta}})^{\text{T}} \mathbf{M} (\boldsymbol{\theta} - \hat{\boldsymbol{\theta}}) \\ &= \mathcal{F}(\hat{\boldsymbol{\theta}}) + (\boldsymbol{\theta} - \hat{\boldsymbol{\theta}})^{\text{T}} \mathbf{T}_1^{\text{T}} \mathbf{T}_1^{-\text{T}} \mathbf{M} \mathbf{T}_1^{-1} \mathbf{T}_1 (\boldsymbol{\theta} - \hat{\boldsymbol{\theta}}) \\ &= \mathcal{F}(\hat{\boldsymbol{\theta}}) + \left\| \text{vec}(\mathbf{R} - \hat{\mathbf{R}}_{\text{AC}}) \right\|_{\mathbf{Q}_{\hat{\mathbf{R}}_{\text{AC}} \hat{\mathbf{R}}_{\text{AC}}}^{-1}}^2 + \left\| \text{vec}(\mathbf{N} - \hat{\mathbf{N}}_{\text{AC}}(\mathbf{R})) \right\|_{\mathbf{Q}_{\hat{\mathbf{N}}_{\text{AC}}(\mathbf{R}) \hat{\mathbf{N}}_{\text{AC}}(\mathbf{R})}^{-1}}^2. \end{aligned} \quad (\text{A.10})$$

B Proof of Lemma 5.2

Consider an arbitrary point $\bar{\boldsymbol{\theta}} = \text{vec}([\bar{\mathbf{R}} \ \bar{\mathbf{N}}])$. According to (A.6), we have

$$\begin{aligned} \mathcal{F}(\boldsymbol{\theta}) &= \mathcal{F}(\hat{\boldsymbol{\theta}}) + (\boldsymbol{\theta} - \bar{\boldsymbol{\theta}} + \bar{\boldsymbol{\theta}} - \hat{\boldsymbol{\theta}})^{\text{T}} \mathbf{M} (\boldsymbol{\theta} - \bar{\boldsymbol{\theta}} + \bar{\boldsymbol{\theta}} - \hat{\boldsymbol{\theta}}) \\ &= \mathcal{F}(\hat{\boldsymbol{\theta}}) + (\bar{\boldsymbol{\theta}} - \hat{\boldsymbol{\theta}})^{\text{T}} \mathbf{M} (\bar{\boldsymbol{\theta}} - \hat{\boldsymbol{\theta}}) + (\boldsymbol{\theta} - \bar{\boldsymbol{\theta}})^{\text{T}} \mathbf{M} (\boldsymbol{\theta} - \bar{\boldsymbol{\theta}}) + 2 (\boldsymbol{\theta} - \bar{\boldsymbol{\theta}})^{\text{T}} \mathbf{M} (\bar{\boldsymbol{\theta}} - \hat{\boldsymbol{\theta}}) \quad (\text{B.1}) \\ &= \mathcal{F}(\bar{\boldsymbol{\theta}}) + (\boldsymbol{\theta} - \bar{\boldsymbol{\theta}})^{\text{T}} \mathbf{M} (\boldsymbol{\theta} - \bar{\boldsymbol{\theta}}) + 2 (\boldsymbol{\theta} - \bar{\boldsymbol{\theta}})^{\text{T}} \mathbf{M} (\bar{\boldsymbol{\theta}} - \hat{\boldsymbol{\theta}}). \end{aligned}$$

Again, we define the block-triangular transformation

$$\mathbf{T}_2 = \begin{bmatrix} \mathbf{I} & (\mathbf{X}_b^+)^{\text{T}} \otimes \mathbf{A} + \mathbf{B} \\ \mathbf{O} & \mathbf{I} \end{bmatrix}. \quad (\text{B.2})$$

Then we have

$$\mathbf{T}_2 (\boldsymbol{\theta} - \bar{\boldsymbol{\theta}}) = \begin{bmatrix} \text{vec}(\mathbf{R} - \bar{\mathbf{R}}(\mathbf{N})) \\ \text{vec}(\mathbf{N} - \bar{\mathbf{N}}) \end{bmatrix}, \quad (\text{B.3})$$

$$\mathbf{T}_2 (\bar{\boldsymbol{\theta}} - \hat{\boldsymbol{\theta}}) = \begin{bmatrix} \text{vec}(\bar{\mathbf{R}} - \hat{\mathbf{R}}_{\text{AC}}(\bar{\mathbf{N}})) \\ \text{vec}(\bar{\mathbf{N}} - \hat{\mathbf{N}}_{\text{AC}}) \end{bmatrix}, \quad (\text{B.4})$$

$$\mathbf{T}_2^{-\text{T}} \mathbf{M} \mathbf{T}_2^{-1} = \begin{bmatrix} \mathbf{Q}_{\hat{\mathbf{R}}_{\text{AC}}(\mathbf{N}) \hat{\mathbf{R}}_{\text{AC}}(\mathbf{N})}^{-1} & \mathbf{O} \\ \mathbf{O} & \mathbf{Q}_{\hat{\mathbf{N}}_{\text{AC}} \hat{\mathbf{N}}_{\text{AC}}}^{-1} \end{bmatrix}. \quad (\text{B.5})$$

Therefore, we obtain

$$\begin{aligned} & (\boldsymbol{\theta} - \bar{\boldsymbol{\theta}})^{\text{T}} \mathbf{M} (\boldsymbol{\theta} - \bar{\boldsymbol{\theta}}) \\ &= (\boldsymbol{\theta} - \bar{\boldsymbol{\theta}})^{\text{T}} \mathbf{T}_2^{\text{T}} \mathbf{T}_2^{-\text{T}} \mathbf{M} \mathbf{T}_2^{-1} \mathbf{T}_2 (\boldsymbol{\theta} - \bar{\boldsymbol{\theta}}) \quad (\text{B.6}) \\ &= \|\text{vec}(\mathbf{N} - \bar{\mathbf{N}})\|_{\mathbf{Q}_{\hat{\mathbf{N}}_{\text{AC}} \hat{\mathbf{N}}_{\text{AC}}}^{-1}}^2 + \|\text{vec}(\mathbf{R} - \bar{\mathbf{R}}(\mathbf{N}))\|_{\mathbf{Q}_{\hat{\mathbf{R}}_{\text{AC}}(\mathbf{N}) \hat{\mathbf{R}}_{\text{AC}}(\mathbf{N})}^{-1}}^2, \end{aligned}$$

and

$$\begin{aligned}
& (\boldsymbol{\theta} - \bar{\boldsymbol{\theta}})^\top \mathbf{M} (\bar{\boldsymbol{\theta}} - \hat{\boldsymbol{\theta}}) \\
&= (\boldsymbol{\theta} - \bar{\boldsymbol{\theta}})^\top \mathbf{T}_2^\top \mathbf{T}_2^{-\top} \mathbf{M} \mathbf{T}_2^{-1} \mathbf{T}_2 (\bar{\boldsymbol{\theta}} - \hat{\boldsymbol{\theta}}) \\
&= \text{vec}(\mathbf{N} - \bar{\mathbf{N}})^\top \mathbf{Q}_{\hat{\mathbf{N}}_{\text{AC}} \hat{\mathbf{N}}_{\text{AC}}}^{-1} \text{vec}(\bar{\mathbf{N}} - \hat{\mathbf{N}}_{\text{AC}}) \\
&\quad + \text{vec}(\mathbf{R} - \bar{\mathbf{R}}(\mathbf{N}))^\top \mathbf{Q}_{\hat{\mathbf{R}}_{\text{AC}}(\mathbf{N}) \hat{\mathbf{R}}_{\text{AC}}(\mathbf{N})}^{-1} \text{vec}(\bar{\mathbf{R}} - \hat{\mathbf{R}}_{\text{AC}}(\bar{\mathbf{N}})).
\end{aligned} \tag{B.7}$$

The combination of (B.1), (B.6) and (B.7) concludes the proof.

C Proof of Lemma 5.3

According to Lemma 5.2, $\mathcal{F}(\boldsymbol{\theta})$ can be expressed as

$$\begin{aligned}
\mathcal{F}(\boldsymbol{\theta}) &= \mathcal{F}(\bar{\boldsymbol{\theta}}) + \left\| \text{vec}(\mathbf{N} - \bar{\mathbf{N}}) \right\|_{\mathbf{Q}_{\hat{\mathbf{N}}_{\text{AC}} \hat{\mathbf{N}}_{\text{AC}}}^{-1}}^2 + \left\| \text{vec}(\mathbf{R} - \bar{\mathbf{R}}(\mathbf{N})) \right\|_{\mathbf{Q}_{\hat{\mathbf{R}}_{\text{AC}}(\mathbf{N}) \hat{\mathbf{R}}_{\text{AC}}(\mathbf{N})}^{-1}}^2 \\
&\quad + 2 \text{vec}(\mathbf{N} - \bar{\mathbf{N}})^\top \mathbf{Q}_{\hat{\mathbf{N}}_{\text{AC}} \hat{\mathbf{N}}_{\text{AC}}}^{-1} \text{vec}(\bar{\mathbf{N}} - \hat{\mathbf{N}}_{\text{AC}}) \\
&\quad + 2 \text{vec}(\mathbf{R} - \bar{\mathbf{R}}(\mathbf{N}))^\top \mathbf{Q}_{\hat{\mathbf{R}}_{\text{AC}}(\mathbf{N}) \hat{\mathbf{R}}_{\text{AC}}(\mathbf{N})}^{-1} \text{vec}(\bar{\mathbf{R}} - \hat{\mathbf{R}}_{\text{AC}}(\bar{\mathbf{N}})) \\
&\quad + \left\| \text{vec}(\bar{\mathbf{R}} - \hat{\mathbf{R}}(\bar{\mathbf{N}})) \right\|_{\mathbf{Q}_{\hat{\mathbf{R}}_{\text{AC}}(\mathbf{N}) \hat{\mathbf{R}}_{\text{AC}}(\mathbf{N})}^{-1}}^2 - \left\| \text{vec}(\bar{\mathbf{R}} - \hat{\mathbf{R}}(\bar{\mathbf{N}})) \right\|_{\mathbf{Q}_{\hat{\mathbf{R}}_{\text{AC}}(\mathbf{N}) \hat{\mathbf{R}}_{\text{AC}}(\mathbf{N})}^{-1}}^2.
\end{aligned} \tag{C.1}$$

Note that

$$\begin{aligned}
& \left\| \text{vec}(\mathbf{R} - \hat{\mathbf{R}}_{\text{AC}}(\mathbf{N})) \right\|_{\mathbf{Q}_{\hat{\mathbf{R}}_{\text{AC}}(\mathbf{N}) \hat{\mathbf{R}}_{\text{AC}}(\mathbf{N})}^{-1}}^2 \\
&= \left\| \text{vec}(\mathbf{R} - \bar{\mathbf{R}}(\mathbf{N}) + \bar{\mathbf{R}}(\mathbf{N}) - \hat{\mathbf{R}}_{\text{AC}}(\mathbf{N})) \right\|_{\mathbf{Q}_{\hat{\mathbf{R}}_{\text{AC}}(\mathbf{N}) \hat{\mathbf{R}}_{\text{AC}}(\mathbf{N})}^{-1}}^2 \\
&= \left\| \text{vec}(\mathbf{R} - \bar{\mathbf{R}}(\mathbf{N})) \right\|_{\mathbf{Q}_{\hat{\mathbf{R}}_{\text{AC}}(\mathbf{N}) \hat{\mathbf{R}}_{\text{AC}}(\mathbf{N})}^{-1}}^2 + \left\| \text{vec}(\bar{\mathbf{R}}(\mathbf{N}) - \hat{\mathbf{R}}_{\text{AC}}(\mathbf{N})) \right\|_{\mathbf{Q}_{\hat{\mathbf{R}}_{\text{AC}}(\mathbf{N}) \hat{\mathbf{R}}_{\text{AC}}(\mathbf{N})}^{-1}}^2 \\
&\quad + 2 \text{vec}(\mathbf{R} - \bar{\mathbf{R}}(\mathbf{N}))^\top \mathbf{Q}_{\hat{\mathbf{R}}_{\text{AC}}(\mathbf{N}) \hat{\mathbf{R}}_{\text{AC}}(\mathbf{N})}^{-1} \text{vec}(\bar{\mathbf{R}}(\mathbf{N}) - \hat{\mathbf{R}}_{\text{AC}}(\mathbf{N})).
\end{aligned} \tag{C.2}$$

Since

$$\bar{\mathbf{R}} - \hat{\mathbf{R}}_{\text{AC}}(\bar{\mathbf{N}}) = \bar{\mathbf{R}}(\mathbf{N}) - \hat{\mathbf{R}}_{\text{AC}}(\mathbf{N}), \tag{C.3}$$

we have

$$\begin{aligned}
& \left\| \text{vec}(\mathbf{R} - \hat{\mathbf{R}}_{\text{AC}}(\mathbf{N})) \right\|_{\mathbf{Q}_{\hat{\mathbf{R}}_{\text{AC}}(\mathbf{N})\hat{\mathbf{R}}_{\text{AC}}(\mathbf{N})}^{-1}}^2 \\
= & \left\| \text{vec}(\mathbf{R} - \bar{\mathbf{R}}(\mathbf{N})) \right\|_{\mathbf{Q}_{\hat{\mathbf{R}}_{\text{AC}}(\mathbf{N})\hat{\mathbf{R}}_{\text{AC}}(\mathbf{N})}^{-1}}^2 + \left\| \text{vec}(\bar{\mathbf{R}} - \hat{\mathbf{R}}(\bar{\mathbf{N}})) \right\|_{\mathbf{Q}_{\hat{\mathbf{R}}_{\text{AC}}(\mathbf{N})\hat{\mathbf{R}}_{\text{AC}}(\mathbf{N})}^{-1}}^2 \\
& + 2 \text{vec}(\mathbf{R} - \bar{\mathbf{R}}(\mathbf{N}))^T \mathbf{Q}_{\hat{\mathbf{R}}_{\text{AC}}(\mathbf{N})\hat{\mathbf{R}}_{\text{AC}}(\mathbf{N})}^{-1} \text{vec}(\bar{\mathbf{R}} - \hat{\mathbf{R}}(\bar{\mathbf{N}})),
\end{aligned} \tag{C.4}$$

which combining with (C.1) will conclude the proof.

D Papers Published and Under Preparation

Publications

- **X. Liu**, T. Ballal, M. Ahmed and T. Y. Al-Naffouri, "Instantaneous GNSS Ambiguity Resolution and Attitude Determination via Riemannian Manifold Optimization," in IEEE Transactions on Aerospace and Electronic Systems, 2022.
- **X. Liu**, T. Ballal, H. Chen, and T. Y. Al-Naffouri, "Constrained Wrapped Least Squares: A Tool for High Accuracy GNSS Attitude Determination," in IEEE Transactions on Instrumentation and Measurement, vol. 71, pp. 1-15, 2022.
- A. Douik, **X. Liu**, T. Ballal, T. Y. Al-Naffouri and B. Hassibi, "Precise 3-D GNSS Attitude Determination Based on Riemannian Manifold Optimization Algorithms," in IEEE Transactions on Signal Processing, vol. 68, pp. 284-299, 2020.
- **X. Liu**, T. Ballal, M. Ahmed, and T. Y. Al-Naffouri, "A GNSS Attitude Determination Algorithm Using Optimization Techniques on Riemannian Manifolds," in Proc. 2022 Int. Tech. Meet. Satell. Div. Inst. Navig. (ION GNSS+ 2022), Denver, Colorado, Sep. 2022.
- **X. Liu**, T. Ballal, M. Bruvelis and T. Y. Al-Naffouri, "Deployment and Evaluation of a Real-time Kinematic System Using tinc-VPN Software," in Proc. 2020 IEEE/ION Position Locat. Navig. Symp. (PLANS), 2020, pp. 1155-1159.
- **X. Liu**, T. Ballal and T. Y. Al-Naffouri, "GNSS Attitude Determination Using a Constrained Wrapped Least Squares Approach," in Proc. 2020 IEEE/ION Position Locat. Navig. Symp. (PLANS), 2020, pp. 1135-1139.
- **X. Liu**, T. Ballal, and T. Y. Al-Naffouri, "GNSS-based localization for autonomous vehicles: Prospects and challenges," in Proc. 2019 27th Eur. Signal

Process. Conf. (EUSIPCO), A Coruña, Spain, Sep. 2019, pp. 2–6.

- **X. Liu**, T. Ballal, and T. Y. Al-Naffouri, "GNSS Ambiguity Resolution and Attitude Determination by Leveraging Relative Baseline and Frequency Information," in Proc. 31st Int. Tech. Meet. Satell. Div. Inst. Navig. (ION GNSS+ 2018), Miami, Florida, Sep. 2018, pp. 1647-1660.
- M. Alsaif, T. Ballal, **X. Liu**, T. Y. Al-Naffouri, "Precise Multiple-Receiver GNSS SPP Algorithm Based on Constrained Optimization Techniques," in Proc. 2022 ITM/PTTI, Long Beach, California, Jan. 2022, pp. 753-767.
- H. Chen, T. Ballal, **X. Liu** and T. Y. Al-Naffouri, "Realtime 2-D DOA Estimation using Phase-Difference Projection (PDP)," in Proc. 2019 27th Eur. Signal Process. Conf. (EUSIPCO), A Coruña, Spain, Sep. 2019, pp. 1-5.
- P. Zheng, **X. Liu**, T. Ballal, and T. Y. Al-Naffouri, "5G-Aided RTK Positioning in GNSS-Deprived Environments," in Eur. Signal Process. Conf. (EUSIPCO) 2023, Helsinki, Finland, Sep. 2023.
- M. Ahmed, T. Ballal, **X. Liu**, and T. Y. Al-Naffouri, "Multipath Detection and Mitigation from GNSS Observations Using Antenna Arrays," in IEEE/ION Position Locat. Navig. Symp. (PLANS), Monterey, California, Apr. 2023, pp. 875 - 882.

Papers Under Preparation

- **X. Liu**, M. Alsharif, T. Ballal, M. Ahmed, and T. Y. Al-Naffouri, "Joint Solution for Real-Time Kinematic Positioning and Attitude Determination," (draft available).
- **X. Liu**, T. Ballal, and T. Y. Al-Naffouri, "Constrained Cramér–Rao Bound for Joint Real-Time Kinematic Positioning and Attitude Determination," (draft available).
- P. Zheng, **X. Liu**, T. Ballal, and T. Y. Al-Naffouri, "Attitude Determination in Urban Canyons: A Synergy between GNSS and 5G/6G Observations,"

(Submitted to Int. Tech. Meet. Satell. Div. Inst. Navig. (ION GNSS+ 2023)).